

Gdańsk University of Technology  
Faculty of Civil and Environmental Engineering

---



mgr inż. Łukasz Skarżyński

# Macroscopic and mesoscopic modelling of strain localization in concrete

Doctoral thesis

Supervisor: prof. dr hab. inż. Jacek Tejchman

Gdańsk, 2010



## Summary

The doctoral thesis presents the results of investigations of strain localization in concrete. An understanding of the mechanism of the formation of localized zones is of a crucial importance since they act as a precursor to ultimate fracture and failure of concrete specimens. A realistic description of the width and spacing of localized zones is also important to evaluate material strength at the peak and post-peak regime and ensure safety to civil engineering structures.

The laboratory experiments were carried out to determine the width and shape of a localized zone on the surface of notched concrete beams during quasi-static three-point bending. To measure two-dimensional displacements on the surface of concrete beams, a non-invasive Digital Image Correlation technique was used. Beams with different geometry were tested.

The numerical calculations using the finite element method were performed with concrete and reinforced concrete elements at macro-, meso- and macro-meso-scale. To capture strain localization in long concrete beams under tensile failure and short reinforced concrete beams under shear failure at macro-scale, three different constitutive continuum models for concrete were used: an elasto-plastic with isotropic hardening and softening using the Drucker-Prager criterion in compression and the Rankine criterion in tension, an isotropic continuum damage describing the degradation with the aid of one damage scalar parameter and an anisotropic smeared-crack approach with fixed cracks or one rotating crack. To properly describe strain localization, the continuum models were enhanced by a characteristic length of micro-structure by means of a non-local theory. Thus, underlying boundary value problems were mathematically well-posed.

The mesoscopic FE calculations were carried out with a concrete element subjected to uniaxial tension. Concrete was described as a random heterogeneous three-phase material composed of cement matrix, aggregate and interfacial transition zones (ITZ) between the cement matrix and aggregate. An isotropic damage model with non-local softening was used. The concept of a Representative Volume Element (RVE) in concrete using a standard approach was analysed. In addition, two alternative non-standard strategies to determine RVE in concrete under uniaxial tension were proposed.

Finally, comprehensive FE calculations at a combined macro-meso-scale were performed with notched concrete beams under bending. An isotropic damage model with non-local softening was used again. The effect of the beam size, aggregate distribution, aggregate density, aggregate shape, aggregate size and characteristic length on the width and shape of a localized zone and the load-displacement curve was numerically investigated. The

macro–meso computations showed a satisfactory agreement with corresponding own laboratory tests.

# Contents

<b>Summary</b> . . . . .	3
<b>List of Figures</b> . . . . .	7
<b>List of Tables</b> . . . . .	15
<b>List of important symbols</b> . . . . .	17
Latin symbols . . . . .	17
Greek symbols . . . . .	18
<b>Chapter 1. Introduction</b> . . . . .	21
1.1. Phenomenon and problem . . . . .	21
1.2. Aims . . . . .	21
1.3. Outline . . . . .	22
1.4. Literature review . . . . .	23
<b>Chapter 2. Continuum modelling of concrete and reinforcement</b> . . . . .	27
2.1. Mechanical properties of concrete . . . . .	27
2.2. Constitutive models for concrete . . . . .	30
2.2.1. Elasto–plastic model . . . . .	30
2.2.2. Damage model . . . . .	35
2.2.3. Smearred–crack model . . . . .	39
2.3. Non–local theory . . . . .	40
2.4. Constitutive model for reinforcement . . . . .	44
2.5. Bond between concrete and reinforcement . . . . .	44
<b>Chapter 3. Laboratory tests on strain localization</b> . . . . .	49
3.1. Digital Image Correlation technique . . . . .	49
3.2. Experimental set–up . . . . .	55
3.3. Experimental results . . . . .	57
3.4. Conclusions . . . . .	62
<b>Chapter 4. Macroscopic modelling of strain localization in concrete and reinforced concrete</b> . . . . .	65
4.1. Concrete beams . . . . .	65
4.2. Reinforced concrete beams . . . . .	67
4.3. Conclusions . . . . .	75
<b>Chapter 5. Mesoscopic modelling of strain localization in concrete</b> . . . . .	85
5.1. Determination of RVE with standard averaging approach . . . . .	85
5.2. Determination of RVE with non–standard averaging approaches . . . . .	91
5.3. Conclusions . . . . .	102
<b>Chapter 6. Macroscopic – mesoscopic modelling of strain localization</b> . . . . .	113
6.1. Input data . . . . .	114
6.2. Numerical results . . . . .	115

---

6.3. Conclusions . . . . .	129
<b>Chapter 7. Final conclusions and future work . . . . .</b>	<b>133</b>
<b>Bibliography . . . . .</b>	<b>135</b>
<b>List of publications . . . . .</b>	<b>145</b>
<b>Streszczenie . . . . .</b>	<b>147</b>
<b>Acknowledgements . . . . .</b>	<b>149</b>

## List of Figures

2.1.	Stress–strain curve for concrete in uniaxial compression . . . . .	27
2.2.	Stress–strain curves for concrete in uniaxial compression for various compressive strength $f_c$ . . . . .	28
2.3.	Evolution of Poisson’s ratio $\nu$ during deformation . . . . .	28
2.4.	Stress–strain curve for concrete in uniaxial tension . . . . .	28
2.5.	Envelope of principal compressive stresses $\sigma_i$ under biaxial conditions ( <i>Kupfer et al.</i> [96]) . . . . .	29
2.6.	Stress–strain curves in biaxial compression ( <i>Kupfer et al.</i> [96]) . . . . .	29
2.7.	Stress–strain curves in triaxial compression ( <i>Kotsovos and Newman</i> [90]) . . . . .	30
2.8.	Shape of triaxial surface in the space of principal stresses $\sigma_i$ . . . . .	30
2.9.	Linear Drucker–Prager criterion (a) in the space of principal stresses $\sigma_i$ and (b) on the $p - q$ surface . . . . .	32
2.10.	Rankine criterion: (a) in the space of principal stresses, (b) for plane stress, (c) in the octahedral space, (d) on the $\xi - \rho$ surface . . . . .	34
2.11.	Evolution of tensile yield stress $\sigma_t$ : (a) linear law, (b) exponential law by Hordijk ( <i>Hordijk</i> [74]) . . . . .	34
2.12.	Uniaxial tension. Evolution of damage parameter $D$ and corresponding $\sigma - \varepsilon$ curves: (a) linear law, (b) exponential by Peerlings ( <i>Peerlings et al.</i> [134]) and (c) exponential law by Geers ( <i>Geers</i> [60]) . . . . .	37
2.13.	Distribution of: (b) strain and (c) stress in (a) aggregates and cement matrix according to experiments by Dantu ( <i>Godycki–Ćwirko</i> [68]) . . . . .	40
2.14.	Region of the influence of a characteristic length $l_c$ and the weighting function $\omega$ in the non–local approach. . . . .	41
2.15.	Stress–strain relationship in uniaxial tension for (a) real steel, (b) constitutive model . . . . .	44
2.16.	Bond stress–relative displacement relationship ( $\tau - \delta$ ) according to (a) Dörr ( <i>Dörr</i> [51]) and (b) CEB–FIP [34] . . . . .	45
2.17.	Displacement $\delta$ – radial stress $\sigma_r$ relationship ( $\tau - \delta$ ) according to den Uijl and Bigaj ( <i>den Uijl and Bigaj</i> [46]) for two types of bond failures (a) splitting (b) pull–out . . . . .	46
2.18.	Bond stress – relative displacement relationship ( $\tau - \delta$ ) according to Haskett et al. ( <i>Haskett et al.</i> [70]) . . . . .	47
3.1.	Two successive digital images with the marked square pixel subsets (white squares) and other overlapping pixel subsets (hashed squares) from Digital Image Correlation (DIC) analysis . . . . .	50
3.2.	Comparison between search patch sizes using Pearson’s formula (Eq. 3.2) with (a) 10 pixels, (b) 50 pixels and (c) 200 pixels . . . . .	51
3.3.	Interpolation function sinc256 used to achieve sub–pixel precision . . . . .	51
3.4.	Correlation plane with correlation peak ( $16 \times 16$ pixel area): (a) surface before sub–pixel interpolation (b) surface after sub–pixel interpolation . . . . .	52
3.5.	Standard deviation from expected zero strain versus search patch size . . . . .	52
3.6.	Images used to validate experiments: (a) two subsequent images, (b) random image with $3 \times 3$ ‘grains’, (c) single image, (d) random image with $1 \times 1$ ‘grains’ . . . . .	52

3.7.	Precision of DIC against the search patch size for strain equal zero for images of Fig. 3.6: (a) two subsequent images, (b) random image with $3 \times 3$ 'grains', (c) single image, (d) random image with $1 \times 1$ 'grains'	53
3.8.	Precision of DIC against the search patch size for strain oscillating between 0 and 0.0033 every 300 pixels for images of Fig. 3.6: (a) two subsequent images, (b) random image with $3 \times 3$ 'grains', (c) single image, (d) random image with $1 \times 1$ 'grains'	54
3.9.	Strain fluctuations along single line of the image for the point 'A' of Fig. 3.7 (pixel subset size has 40 pixels, standard deviation from the expected zero strain is 0.0012)	54
3.10.	Geometry of experimental concrete beams subjected to three-point bending	55
3.11.	Grading curve of sand and gravel used for concrete mixes	56
3.12.	Measurement instrumentation: (a) digital camera Canon EOS-1Ds Mark II in front of a small size beam, (b) induction displacement gauge at the beam covered with the black-yellow pattern inside the image area of interest	56
3.13.	Nominal strength $1.5Pl/bD^2$ versus normalised beam deflection $u/D$ (where $u$ – beam deflection, $b$ – beam width, $D$ – beam height, $l$ – beam span, $P$ – vertical force) from experiments: (A) with gravel concrete: (a) small-size beam $80 \times 320$ mm <sup>2</sup> , (b) small-size long beam $80 \times 640$ mm <sup>2</sup> , (c) medium-size beam $160 \times 640$ mm <sup>2</sup> and (B) with sand concrete: (a) small-size beam $80 \times 320$ mm <sup>2</sup> , (b) small-size long beam $80 \times 640$ mm <sup>2</sup> , (c) medium-size beam $160 \times 640$ mm <sup>2</sup> , (d) medium-size long beam $160 \times 1280$ mm <sup>2</sup> , (e) long-size beam $320 \times 1280$ mm <sup>2</sup>	57
3.14.	Evolution of a localized zone from DIC during experiments (vertical and horizontal axes denote coordinates in [mm], colour scales denote the strain intensity in [-]) and experimental load-deflection curves for gravel concrete medium size beam (points correspond to images)	58
3.15.	Formation of a localized zone from DIC in gravel concrete: (a) small-size beam $80 \times 320$ mm <sup>2</sup> , (b) small-size long beam $80 \times 640$ mm <sup>2</sup> , (c) medium-size beam $160 \times 640$ mm <sup>2</sup> (vertical and horizontal axes denote coordinates in [mm], colour scales denote the strain intensity [-])	59
3.16.	Formation of a localized zone from DIC in sand concrete: (a) small-size beam $80 \times 320$ mm <sup>2</sup> , (b) small-size long beam $80 \times 640$ mm <sup>2</sup> , (c) medium-size beam $160 \times 640$ mm <sup>2</sup> , (d) medium-size long beam $160 \times 1280$ mm <sup>2</sup> , (e) long-size beam $320 \times 1280$ mm <sup>2</sup> (vertical and horizontal axes denote coordinates in [mm], colour scales denote the strain intensity [-])	60
3.17.	Evolution of the width of a localized zone from DIC versus normalised beam deflection $u/D$ ( $u$ – beam deflection, $D$ – beam height): (A) gravel concrete: (a) small-size beam $80 \times 320$ mm <sup>2</sup> , (b) small-size long beam $80 \times 640$ mm <sup>2</sup> , (c) medium-size beam $160 \times 640$ mm <sup>2</sup> and (B) with sand concrete: (a) small-size beam $80 \times 320$ mm <sup>2</sup> , (b) small-size long beam $80 \times 640$ mm <sup>2</sup> , (c) medium-size beam $160 \times 640$ mm <sup>2</sup> , (d) medium-size long beam $160 \times 1280$ mm <sup>2</sup> , (e) long-size beam $320 \times 1280$ mm <sup>2</sup>	61
3.18.	Measurements of the width of a localized zone by: (a) an induction displacement gauge and (b) DIC technique (A) large-size gravel beam, (B) small-size sand beam	61
3.19.	Calculated and measured size effect in nominal strength $1.5Pl/(bD^2)$ versus beam height $D$ for concrete beams of similar geometry (beams '1', '2' and '3': (a) own laboratory experiments, (b) size effect law by Bažant (Bažant [7]), Eq. 3.5, (c) experiments by Le Bellégo et al. (Le Bellégo et al. [97])	62
4.1.	Calculated nominal strength $1.5Pl/(bD^2)$ versus normalised beam deflection $u/D$ ( $u$ – beam deflection, $D$ – beam height): (sand concrete): (A) elasto-plasticity, (B) damage mechanics, (a) FE results, (b) experiments by Le Bellégo et al. (Le Bellégo et al. [97]): (1) small-size beam, (2) medium-size beam, (3) large-size beam, (4) small-size long beam, (5) medium-size long beam	66

4.2.	Distribution of the non-local: (A) softening parameter $\bar{\kappa}$ (elasto-plasticity) and (B) strain measure $\bar{\epsilon}$ (damage mechanics) above the notch from numerical calculations for: (1) small-size beam, (2) medium-size beam, (3) large-size beam, (4) small-size long beam, (5) medium-size long beam . . . . .	69
4.3.	Geometry of reinforced concrete beams used in laboratory tests by Walraven and Lehwalter ( <i>Walraven and Lehwalter</i> [168]) . . . . .	70
4.4.	Assumed hardening/softening functions for FE-calculations: (a) $\sigma_t = f(\kappa_2)$ in tension, (b) $\sigma_c = f(\kappa_1)$ in compression ( $\sigma_t$ – tensile stress, $\sigma_c$ – compressive stress, $\kappa_i$ – hardening/softening parameter) . . . . .	71
4.5.	Calculated force-displacement curves within elasto-plasticity (as compared to the experimental maximum vertical force) for different beams: (A) $h = 200$ mm, (B) $h = 400$ mm, (C) $h = 600$ mm, (D) $h = 800$ mm ( $P$ – resultant vertical force, $u$ – vertical displacement) . . . . .	72
4.6.	Distribution of calculated non-local tensile softening parameter within elasto-plasticity in beams at failure for different beams: (a) $h=200$ mm, (b) $h=400$ mm, (c) $h = 600$ mm, (d) $h = 800$ mm (note that the beams are not proportionally scaled) . . . . .	73
4.7.	Comparison of distribution of the non-local tensile softening parameter within elasto-plasticity in short reinforced concrete beams at the normalised vertical force $V/(bdfc) = 0.10$ with experimental crack patterns for different beams: (a) $h = 200$ mm, (b) $h = 400$ mm, (c) $h = 600$ mm, (d) $h = 800$ mm (note that the beams are not proportionally scaled) . . . . .	74
4.8.	Calculated force-displacement curves with smeared crack approach (as compared to the experimental maximum vertical force) for different beams: (a) $h = 200$ mm, (b) $h = 400$ mm, (c) $h = 600$ mm, (d) $h = 800$ mm ( $P$ – resultant vertical force, $u$ – vertical displacement) . . . . .	76
4.9.	Distribution of calculated non-local strain measure with smeared crack approach in different beams at failure: (a) $h = 200$ mm, (b) $h = 400$ mm, (c) $h = 600$ mm, (d) $h = 800$ mm (note that the beams are not proportionally scaled) . . . . .	77
4.10.	Calculated force-displacement curves within damage mechanics (as compared to the experimental maximum vertical force) for two beams: (A) $h = 400$ mm, (B) $h = 600$ mm ( $P$ – resultant vertical force, $u$ – vertical displacement): (a) equivalent strain measure by Eq. 2.42, (b) equivalent strain measure by Eq. 2.44 . . . . .	78
4.11.	Distribution of the calculated non-local strain measure within damage mechanics in two beams at failure: (A) $h = 400$ mm, (B) $h = 600$ mm, (a) equivalent strain measure by Eq. 2.42, (b) equivalent strain measure by Eq. 2.44 (note that the beams are not proportionally scaled) . . . . .	78
4.12.	Calculated and measured size effect in nominal strength $1.5Pl/(bD^2)$ versus beam height $D$ for concrete beams of similar geometry (beams '1', '2' and '3': (a) own laboratory experiments, (b) own FE-calculations (elasto-plasticity), (c) size effect law by Bažant ( <i>Bažant</i> [7]), Eq. 3.5, (d) experiments by Le Bellėgo et al. ( <i>Le Bellėgo et al.</i> [97]) . . . . .	79
4.13.	Calculated size effect in reinforced concrete beams from FE-analyses compared to experiments ( <i>Walraven and Lehwalter</i> [168]) and to the size effect law by Bažant ( <i>Bažant and Planas</i> [16]) ( $b$ – beam width, $d$ – effective beam height, $f_c$ – compressive strength of concrete, $V_u$ – ultimate vertical force): (a) experiments, (b) FE-calculations (elasto-plasticity), (c) FE-calculations (smeared crack model), (d) FE-calculations (damage mechanics), (e) size effect law by Bažant . . . . .	80
5.1.	Approximation of the grading curve with discrete number of aggregate sizes . . . . .	86
5.2.	Periodically deformed unit cell with boundaries $\Gamma_R$ and nodes $v_i$ ( <i>van der Sluis</i> [164]) . . . . .	87
5.3.	Distribution of different unit cells in a concrete specimen ( <i>Gitman</i> [65]) . . . . .	87
5.4.	Simulation of material periodicity . . . . .	88

5.5. Uniaxial tension test (schematically) . . . . .	88
5.6. Concrete specimens of a different size: (a) $10 \times 10 \text{ mm}^2$ , (b) $15 \times 15 \text{ mm}^2$ , (c) $20 \times 20 \text{ mm}^2$ , (d) $25 \times 25 \text{ mm}^2$ (aggregate density $\rho = 30\%$ ) . . . . .	88
5.7. Different distributions of aggregate for a concrete specimen of $15 \times 15 \text{ mm}^2$ (aggregate density $\rho = 30\%$ ) . . . . .	88
5.8. Concrete specimens for different aggregate density $\rho$ : (a) $\rho = 30\%$ , (b) $\rho = 45\%$ , (c) $\rho = 60\%$ . . . . .	89
5.9. Stress–strain curves with various sizes of concrete specimen and random distributions of aggregate: (a) $10 \times 10 \text{ mm}^2$ , (b) $15 \times 15 \text{ mm}^2$ , (c) $20 \times 20 \text{ mm}^2$ , (d) $25 \times 25 \text{ mm}^2$ (characteristic length $l_c = 0.5 \text{ mm}$ , aggregate density $\rho = 30\%$ ) . . . . .	90
5.10. Stress–strain curves with various sizes of concrete specimen and random distributions of aggregate: (a) $10 \times 10 \text{ mm}^2$ , (b) $15 \times 15 \text{ mm}^2$ , (c) $20 \times 20 \text{ mm}^2$ , (d) $25 \times 25 \text{ mm}^2$ (characteristic length $l_c = 0.5 \text{ mm}$ , aggregate density $\rho = 45\%$ ) . . . . .	91
5.11. Stress–strain curves with various sizes of concrete specimen and random distributions of aggregate: (a) $10 \times 10 \text{ mm}^2$ , (b) $15 \times 15 \text{ mm}^2$ , (c) $20 \times 20 \text{ mm}^2$ , (d) $25 \times 25 \text{ mm}^2$ (characteristic length $l_c = 0.5 \text{ mm}$ , aggregate density $\rho = 60\%$ ) . . . . .	92
5.12. Stress–strain curves with various sizes of concrete specimen and aggregate densities $\rho$ : (a) $\rho = 30\%$ , (b) $\rho = 45\%$ , (c) $\rho = 60\%$ (characteristic length $l_c = 0.5 \text{ mm}$ ) . . . . .	92
5.13. Distribution of non–local softening strain measure for two different random distributions of aggregate: (a) $10 \times 10 \text{ mm}^2$ , (b) $15 \times 15 \text{ mm}^2$ , (c) $20 \times 20 \text{ mm}^2$ , (d) $25 \times 25 \text{ mm}^2$ (characteristic length $l_c = 0.5 \text{ mm}$ , aggregate density $\rho = 30\%$ ) . . . . .	93
5.14. Stress–strain curves for different values of a characteristic length: (a) $l_c = 0.1 \text{ mm}$ , (b) $l_c = 0.25 \text{ mm}$ , (c) $l_c = 0.5 \text{ mm}$ , (d) $l_c = 1.0 \text{ mm}$ , (e) $l_c = 2.0 \text{ mm}$ (specimen size $10 \times 10 \text{ mm}^2$ , aggregate density $\rho = 30\%$ ) . . . . .	93
5.15. Distribution of non–local softening strain measure for different values of a characteristic length: (a) $l_c = 0.1 \text{ mm}$ , (b) $l_c = 0.25 \text{ mm}$ , (c) $l_c = 0.5 \text{ mm}$ , (d) $l_c = 1.0 \text{ mm}$ , (e) $l_c = 2.0 \text{ mm}$ (specimen size $10 \times 10 \text{ mm}^2$ , aggregate density $\rho = 30\%$ ) . . . . .	94
5.16. Stress–strain curves for different values of a characteristic length: (a) $l_c = 0.1 \text{ mm}$ , (b) $l_c = 0.25 \text{ mm}$ , (c) $l_c = 0.5 \text{ mm}$ , (d) $l_c = 1.0 \text{ mm}$ , (e) $l_c = 2.0 \text{ mm}$ (specimen size $25 \times 25 \text{ mm}^2$ , aggregate density $\rho = 30\%$ ) . . . . .	94
5.17. Distribution of non–local softening strain measure for different values of a characteristic length: (a) $l_c = 0.1 \text{ mm}$ , (b) $l_c = 0.25 \text{ mm}$ , (c) $l_c = 0.5 \text{ mm}$ , (d) $l_c = 1.0 \text{ mm}$ , (e) $l_c = 2.0 \text{ mm}$ (specimen size $25 \times 25 \text{ mm}^2$ , aggregate density $\rho = 30\%$ ) . . . . .	94
5.18. Stress–strain curves for different aggregate densities: (a) $\rho = 30\%$ , (b) $\rho = 45\%$ , (c) $\rho = 60\%$ and cell sizes (A) $20 \times 20 \text{ mm}^2$ , (B) $25 \times 25 \text{ mm}^2$ ( $l_c = 0.5 \text{ mm}$ ) . . . . .	95
5.19. Distribution of non–local softening strain measure for two different aggregate densities: (a) $\rho = 30\%$ , (b) $\rho = 45\%$ , (c) $\rho = 60\%$ and cell sizes (A) $20 \times 20 \text{ mm}^2$ , (B) $25 \times 25 \text{ mm}^2$ ( $l_c = 0.5 \text{ mm}$ ) . . . . .	95
5.20. Stress–strain curves for two different specimen sizes: (A) $15 \times 15 \text{ mm}^2$ , (B) $25 \times 25 \text{ mm}^2$ with (a) non–locality prescribed to three phases and (b) non–locality prescribed to cement matrix (aggregate density $\rho = 30\%$ , characteristic length $l_c = 0.5 \text{ mm}$ ) . . . . .	96
5.21. Distribution of non–local softening strain measure for two different specimen sizes: (A) $15 \times 15 \text{ mm}^2$ , (B) $25 \times 25 \text{ mm}^2$ with (a) non–locality prescribed to three phases and (b) non–locality prescribed to cement matrix (aggregate density $\rho = 30\%$ , characteristic length $l_c = 0.5 \text{ mm}$ ) . . . . .	96
5.22. Deformed three–phase concrete with periodicity of boundary conditions and material periodicity . . . . .	97
5.23. Concrete specimens of different size: (a) $5 \times 5 \text{ mm}^2$ , (b) $10 \times 10 \text{ mm}^2$ , (c) $15 \times 15 \text{ mm}^2$ , (d) $20 \times 20 \text{ mm}^2$ , (e) $25 \times 25 \text{ mm}^2$ , (f) $30 \times 30 \text{ mm}^2$ (aggregate density $\rho = 30\%$ ) . . . . .	98

5.24. Stress–strain curves for various sizes of concrete specimens and two different random distributions of aggregate (a) and (b) using standard averaging procedure (characteristic length $l_c = 1.5$ mm, aggregate density $\rho = 30\%$ ) . . . . .	99
5.25. Distribution of non–local softening strain measure for various specimen sizes and stress–strain curves of Fig. 5.24a using standard averaging procedure (characteristic length $l_c = 1.5$ mm, aggregate density $\rho = 30\%$ ) . . . . .	100
5.26. Distribution of non–local softening strain measure for various specimen sizes and stress–strain curves of Fig. 5.24b using standard averaging procedure (characteristic length $l_c = 1.5$ mm, aggregate density $\rho = 30\%$ ) . . . . .	101
5.27. Expected value and standard deviation of fracture energy using standard averaging (aggregate density $\rho = 30\%$ ) . . . . .	102
5.28. Stress–strain curves for various sizes of concrete specimens and two different random distributions of aggregate (a) and (b) using failure averaging procedure (characteristic length $l_c = 1.5$ mm, aggregate density $\rho = 30\%$ ) . . . . .	103
5.29. Expected value and standard deviation of fracture energy using failure averaging (aggregate density $\rho = 30\%$ ) . . . . .	104
5.30. Stress–strain curves for various sizes of concrete specimens and two different random distributions of aggregate (a) and (b) using varying characteristic length averaging approach (reference size $15 \times 15$ mm <sup>2</sup> , characteristic length according to Eq. 5.8, aggregate density $\rho = 30\%$ ) . . . . .	105
5.31. Stress–strain curves for various sizes of concrete specimens and two different random distributions of aggregate (a) and (b) using varying characteristic length averaging approach (reference size $30 \times 30$ mm <sup>2</sup> , characteristic length according to Eq. 5.9, aggregate density $\rho = 30\%$ ) . . . . .	106
5.32. Distribution of non–local softening strain measure for various specimen sizes and stress–strain curves of Fig. 5.30a using varying characteristic length averaging approach (reference size $15 \times 15$ mm <sup>2</sup> , characteristic length according to Eq. 5.8, aggregate density $\rho = 30\%$ ) . . . . .	107
5.33. Distribution of non–local softening strain measure for various specimen sizes and stress–strain curves of Fig. 5.30b using varying characteristic length averaging approach (reference size $15 \times 15$ mm <sup>2</sup> , characteristic length according to Eq. 5.8, aggregate density $\rho = 30\%$ ) . . . . .	108
5.34. Distribution of non–local softening strain measure for various specimen sizes and stress–strain curves of Fig. 5.31a using varying characteristic length averaging approach (reference size $30 \times 30$ mm <sup>2</sup> , characteristic length according to Eq. 5.9, aggregate density $\rho = 30\%$ ) . . . . .	109
5.35. Distribution of non–local softening strain measure for various specimen sizes and stress–strain curves of Fig. 5.31b using varying characteristic length averaging approach (reference size $30 \times 30$ mm <sup>2</sup> , characteristic length according to Eq. 5.9, aggregate density $\rho = 30\%$ ) . . . . .	110
5.36. Expected value and standard deviation of fracture energy using standard averaging: (a) reference size $15 \times 15$ mm <sup>2</sup> , (b) reference size $30 \times 30$ mm <sup>2</sup> (aggregate density $\rho = 30\%$ )	111
6.1. Three–phase concrete in the neighbourhood of the notch: aggregate of round shape, cement matrix and interfacial transition zones (ITZ) . . . . .	114
6.2. Calculated and experimental nominal strength $1.5Pl/(bD^2)$ versus normalised beam deflection $u/D$ ( $u$ –beam deflection, $D$ –beam height): (a) FE–results, (b) experiments by Le Bellėgo et al. ( <i>Le Bellėgo et al.</i> [97]): (1) small–size beam, (2) medium–size beam, (3) large–size beam (homogeneous one–phase material, $l_c^M = 2$ mm) . . . . .	115
6.3. Distribution of non–local strain measure above the notch from numerical calculations (at $u/D = 0.005$ ): (a) small–size beam, (b) medium–size beam, (c) large–size beam (homogeneous one phase material, $l_c^M = 2$ mm) . . . . .	116

6.4.	Deformed FE mesh for a small-size beam $80 \times 320 \text{ mm}^2$ with random spatially correlated distribution of tensile strength ( <i>Bobinski et.al</i> [28]) . . . . .	117
6.5.	Calculated force-deflection curves for two different random distributions of aggregate in small-size beam of gravel concrete ( $d_{50} = 2 \text{ mm}$ , $d_{max} = 8 \text{ mm}$ , $l_c^m = 1.5 \text{ mm}$ ): (a) entirely heterogeneous, (b) partially heterogeneous beam with width of meso-scale section of $b_{ms} = 80 \text{ mm}$ , (c) partially heterogeneous beam with width of the meso-scale section of $b_{ms} = 40 \text{ mm}$ . . . . .	117
6.6.	FE-mesh used for calculations (small-size beam $80 \times 320 \text{ mm}^2$ ) in the meso-scale region ( $b_{ms} = D$ , $\rho = 30\%$ ) . . . . .	118
6.7.	Calculated distribution of non-local strain measure above the notch (small-size beam $80 \times 320 \text{ mm}$ , $l_c^m = 1.5 \text{ mm}$ ) for gravel concrete ( $d_{50} = 2 \text{ mm}$ , $d_{max} = 8 \text{ mm}$ ): (a) entirely heterogeneous beam, (b) partially heterogeneous beam with width of meso-scale section of $b_{ms} = 80 \text{ mm}$ , (c) partially heterogeneous beam with width of the meso-scale section of $b_{ms} = 40 \text{ mm}$ . . . . .	120
6.8.	Calculated load-deflection curves for two concrete mixes and three random distributions of aggregate (curves (a), (b), (c)) in a small-size beam $80 \times 320 \text{ mm}^2$ ( $l_c^m = 1.5 \text{ mm}$ , $\rho = 30\%$ ): (A) sand concrete ( $d_{50} = 0.5 \text{ mm}$ , $d_{max} = 3 \text{ mm}$ ), (B) gravel concrete ( $d_{50} = 2 \text{ mm}$ , $d_{max} = 8 \text{ mm}$ ) . . . . .	121
6.9.	Calculated distribution of non-local strain measure for various concrete mixes and three random distributions of aggregate: (a), (b), (c) in small-size beam corresponding to load-deflection curves of Fig. 6.8 ( $l_c^m = 1.5 \text{ mm}$ , $\rho = 30\%$ ): (A) sand concrete ( $d_{50} = 0.5 \text{ mm}$ , $d_{max} = 3 \text{ mm}$ ), (B) gravel concrete ( $d_{50} = 2 \text{ mm}$ , $d_{max} = 8 \text{ mm}$ ) . . . . .	121
6.10.	Calculated load-deflection curves for two concrete mixes and three random distributions of aggregate (curves (a), (b), (c)) in a small-size beam $80 \times 320 \text{ mm}^2$ ( $l_c^m = 1.5 \text{ mm}$ , $\rho = 45\%$ ): (A) sand concrete ( $d_{50} = 0.5 \text{ mm}$ , $d_{max} = 3 \text{ mm}$ ), (B) gravel concrete ( $d_{50} = 2 \text{ mm}$ , $d_{max} = 8 \text{ mm}$ ) . . . . .	122
6.11.	Calculated distribution of non-local strain measure for various concrete mixes and three random distributions of aggregate: (a), (b), (c) in small-size beam corresponding to load-deflection curves of Fig. 6.10 ( $l_c^m = 1.5 \text{ mm}$ , $\rho = 45\%$ ): (A) sand concrete ( $d_{50} = 0.5 \text{ mm}$ , $d_{max} = 3 \text{ mm}$ ), (B) gravel concrete ( $d_{50} = 2 \text{ mm}$ , $d_{max} = 8 \text{ mm}$ ) . . . . .	122
6.12.	Calculated load-deflection curves for different aggregate densities (small-size beam $80 \times 320 \text{ mm}^2$ ): (A) $\rho = 30\%$ , (B) $\rho = 45\%$ , (C) $\rho = 60\%$ , (a) sand concrete ( $d_{50} = 0.5 \text{ mm}$ , $d_{max} = 3 \text{ mm}$ ), (b) gravel concrete ( $d_{50} = 2 \text{ mm}$ , $d_{max} = 8 \text{ mm}$ ) . . . . .	123
6.13.	Calculated load-deflection curves (small-size beam $80 \times 320 \text{ mm}^2$ ): (A) sand concrete ( $d_{50} = 0.5 \text{ mm}$ , $d_{max} = 3 \text{ mm}$ ), (B) gravel concrete ( $d_{50} = 2 \text{ mm}$ , $d_{max} = 8 \text{ mm}$ ), (a) $\rho = 30\%$ , (b) $\rho = 45\%$ , (c) $\rho = 60\%$ . . . . .	123
6.14.	Calculated distribution of non-local strain measure for different aggregate densities (small-size beam $80 \times 320 \text{ mm}^2$ ): (a) $\rho = 30\%$ , (b) $\rho = 45\%$ , (c) $\rho = 60\%$ , (A) sand concrete ( $d_{50} = 0.5 \text{ mm}$ , $d_{max} = 3 \text{ mm}$ ), (B) gravel concrete ( $d_{50} = 2 \text{ mm}$ , $d_{max} = 8 \text{ mm}$ ) . . . . .	124
6.15.	Calculated load-deflection diagrams (small-size beam $80 \times 320 \text{ mm}^2$ ): (a) aggregate of circular shape, (b) aggregate of angular shape for different aggregate densities: (A) $\rho = 30\%$ , (B) $\rho = 45\%$ , (C) $\rho = 60\%$ ( $l_c^m = 1.5 \text{ mm}$ ) . . . . .	125
6.16.	Shape of aggregate used in calculations ( $\rho = 30\%$ ): (a) circular aggregate, (b) angular aggregate . . . . .	125
6.17.	Calculated distribution of non-local strain measure above notch (small-size beam $80 \times 320 \text{ mm}^2$ ): (A) aggregate of circular shape, (B) aggregates of angular shape, (a) $\rho = 30\%$ , (b) $\rho = 45\%$ , (c) $\rho = 60\%$ ( $l_c = 1.5 \text{ mm}$ ) . . . . .	126
6.18.	Calculated load-deflection curves for different characteristic lengths: (a) $l_c^m = 0.1 \text{ mm}$ , (b) $l_c^m = 0.5 \text{ mm}$ , (c) $l_c^m = 1.5 \text{ mm}$ , (d) $l_c^m = 2.5 \text{ mm}$ , (e) $l_c^m = 5.0 \text{ mm}$ (small-size beam $80 \times 320 \text{ mm}^2$ , sand concrete $d_{50} = 0.5 \text{ mm}$ , $d_{max} = 3 \text{ mm}$ , aggregate density $\rho = 30\%$ ) . . . . .	127

- 
- 6.19. Calculated distribution of non–local strain measure for different characteristic lengths: (a)  $l_c^m = 0.1$  mm, (b)  $l_c^m = 0.5$  mm, (c)  $l_c^m = 1.5$  mm, (d)  $l_c^m = 2.5$  mm, (e)  $l_c^m = 5.0$  mm (small–size beam  $80 \times 320$  mm<sup>2</sup>, sand concrete  $d_{50} = 0.5$  mm,  $d_{max} = 3$  mm, aggregate density  $\rho = 30\%$ ) . . . . . 127
- 6.20. Calculated load–deflection curves for different characteristic lengths: (a)  $l_c^m = 0.5$  mm, (b)  $l_c^m = 1.5$  mm, (c)  $l_c^m = 2.5$  mm, (d)  $l_c^m = 5.0$  mm (small–size beam  $80 \times 320$  mm<sup>2</sup>, gravel concrete  $d_{50} = 2$  mm,  $d_{max} = 8$  mm, aggregate density  $\rho = 45\%$ ) . . . . . 128
- 6.21. Calculated distribution of non–local strain measure for different characteristic lengths: (a)  $l_c^m = 0.5$  mm, (b)  $l_c^m = 1.5$  mm, (c)  $l_c^m = 2.5$  mm, (d)  $l_c^m = 5.0$  mm (small–size beam  $80 \times 320$  mm<sup>2</sup>, gravel concrete  $d_{50} = 2$  mm,  $d_{max} = 8$  mm, aggregate density  $\rho = 45\%$ ) . . . . . 128
- 6.22. Calculated nominal strength  $1.5Pl/(bD^2)$  versus normalised beam deflection  $u/D$  ( $u$  – beam deflection,  $D$  – beam height): (A) FE–results, (B) experiments by Le Bellęgo et al. (*Le Bellęgo et al.* [97]): (1) small–size beam, (2) medium–size beam, 3) large–size beam (three–phase random heterogeneous material close to notch  $b_{ms} = D$ ,  $\rho = 30\%$ ,  $l_c^m = 1.5$  mm) . . . . . 129
- 6.23. Calculated distribution of non–local strain measure above the notch from numerical calculations (at  $u/D = 0.0005$ ): (a) small–size beam, (b) medium–size beam, (c) large–size beam (three–phase random heterogeneous material close to notch  $b_{ms} = D$ ,  $\rho = 30\%$ ,  $l_c^m = 1.5$  mm) . . . . . 130
- 6.24. Calculated and measured size effect in nominal strength  $1.5Pl/(bD^2)$  versus beam height  $D$  for concrete beams of a similar geometry (small–, medium–and large–size beam): (a) own laboratory experiments, (b) own FE–calculations (homogeneous one–phase material), (c) own FE–calculations (heterogeneous material close to the notch  $b_{ms} = D$ ), (d) size effect law by Bařant (*Bařant* [7]), (e) experiments by Le Bellęgo et al. (*Le Bellęgo et al.* [97]) . . . . . 130



# List of Tables

3.1.	Contents of concrete mixes: (a) with sand, (b) with gravel . . . . .	55
3.2.	Data summary of own laboratory experiments and corresponding laboratory tests by <i>Le Bellęgo et al.</i> [97] . . . . .	63
4.1.	Maximum vertical failure forces obtained in laboratory tests and numerical FE calculations . . . . .	66
4.2.	Beams' properties and failure loads . . . . .	68
4.3.	Data summary of own laboratory experiments, FE-results and corresponding laboratory tests by <i>Le Bellęgo et al.</i> [97] . . . . .	81
4.4.	Summary of FE-input data . . . . .	82
4.5.	Data summary of experiments, FE-results and analytical formulae (crack spacing) . . .	83
5.1.	Material properties assumed for FE calculations . . . . .	86
6.1.	Material properties assumed for FE calculations of concrete beams on meso-scale . . .	115



# List of important symbols

## Latin symbols

$A_z$  – localized zone area

$b$  – width of the specimen

$b_{ms}$  – meso–scale section width

$d_{max}$  – maximum size of the aggregate in concrete

$d_{min}$  – minimum size of the aggregate in concrete

$d_{50}$  – mean size of the aggregate in concrete

$\mathbf{C}^e$  – initial stiffness tensor

$\mathbf{D}^e$  – initial compliance tensor

$D$  – damage parameter (or distance between two neighbouring particle centres or beam height)

$E$  – Young modulus for concrete

$\mathbf{e}$  – total strain tensor deviator

$f$  – plastic function, loading activation function

$f_1$  – plasticity condition for linear Drucker–Prager criterion

$f_2$  – plasticity condition for linear Rankine criterion

$f_s$  – plasticity condition for Huber–Mises criterion

$f_c$  – uniaxial compressive strength of concrete

$f_{bc}$  – biaxial compressive strength of concrete

$f_t$  – uniaxial tensile strength of concrete

$f_{bt}$  – biaxial tensile strength of concrete

$G$  – shear modulus

$G_c$  – compressive fracture energy

$G_f$  – tensile fracture energy

$g$  – plastic potential

$g_1$  – plastic potential for Drucker–Prager criterion

$h$  – height of a specimen

$\mathbf{I}$  – second–order elementary tensor

$\mathbf{I}$  – fourth–order elementary tensor

$I_1$  – first invariant of stress tensor

$l_c^m$  – mesoscopic characteristic length

$l_c^M$  – macroscopic characteristic length

$l_c^v$  – characteristic length for the reference unit cell

$m$  – non–local parameter

$P$  – vertical force

$p$  – mean stress

$q$  – effective von Mises stress

$RGB$  – colour space ( $R$  – red,  $G$  – green,  $B$  – blue)

$R(x,y)$  – the Pearson’s product–moment correlation function  
 $r$  – distance between two material points  
 $\mathbf{S}$  – stress tensor deviator  
 $s_a$  – aggregate triangular finite element size  
 $s_{ITZ}$  – interface triangular finite element size  
 $s_{cm}$  – cement matrix triangular finite element size  
 $t$  – time  
 $\mathbf{u}$  – point displacement vector  
 $V$  – body (element) volume  
 $v_u$  – normalised shear strength  
 $w_c$  – width of the localized zone  
 $\mathbf{x}$  – actual coordinates of a material point (non–local theory)  
 $\xi$  – actual coordinates of neighbouring points (non–local theory)  
 $Y$  – elastic strain energy  
 $YC_bC_r$  – colour components of the image ( $Y$  – luminosity,  $C_b$  – blueness,  $C_r$  – redness)  
 $w(a)$  – sinc256 correlation function

## Greek symbols

$\alpha$  – exponential softening law parameter (residual level)  
 $\alpha_1$  – ratio between uniaxial tensile ( $f_t$ ) and uniaxial compressive ( $f_c$ ) strength in Häußler–Combe and Pröchtel criterion  
 $\alpha_2$  – ratio between biaxial tensile ( $f_{bt}$ ) and biaxial compressive ( $f_{bc}$ ) strength in Häußler–Combe and Pröchtel criterion  
 $\alpha_3$  – multiplier of material strength in triaxial compression Häußler–Combe and Pröchtel criterion  
 $\beta$  – internal friction angle (or exponential softening law parameter (slope of softening) or shear retention factor)  
 $\gamma$  – multiplier of material strength in triaxial compression Häußler–Combe and Pröchtel criterion  
 $\eta$  – coefficient relating  $\kappa$  and  $\lambda$  in plasticity  
 $\boldsymbol{\varepsilon}$  – total strain tensor  
 $\varepsilon_i$  – principal strains ( $i=1, 2, 3$ )  
 $\boldsymbol{\varepsilon}^e$  – elastic strain tensor  
 $\varepsilon_m$  – meso strain  
 $\boldsymbol{\varepsilon}^p$  – plastic strain tensor  
 $\varepsilon_{nu}$  – ultimate cracked strain in tension (smeared–crack model)  
 $\varepsilon_{su}$  – ultimate cracked strain in shear (smeared–crack model)  
 $\bar{\varepsilon}$  – equivalent strain measure  
 $\bar{\varepsilon}$  – non–local equivalent strain  
 $\delta$  – relative displacement (slip) between concrete and reinforcement steel  
 $\delta_u$  – ultimate value when bond stress  $\tau$  reaches its residual value (perfect slip occurs)  
 $\kappa$  – hardening / softening parameter, load history parameter  
 $\bar{\kappa}$  – non–local hardening / softening parameter, non–local load history parameter  
 $\kappa_0$  – initial value of load history hardening/softening parameter  
 $\kappa_1$  – hardening / softening parameter for Drucker–Prager criterion  
 $\kappa_2$  – hardening / softening parameter for Rankine criterion  
 $\kappa_u$  – ultimate value of softening parameter for Rankine criterion

---

$\kappa_s$  – hardening / softening parameter for Huber–Mises criterion  
 $\lambda$  – plastic multiplier, Lamé’s constant  
 $\mu$  – Lamé’s constant  
 $\nu$  – Poisson’s ratio  
 $\rho$  – aggregate density  
 $\sigma$  – Cauchy strain tensor  
 $\sigma_c$  – uniaxial compression yield stress for concrete  
 $\sigma_i$  – principal stresses (i=1, 2, 3)  
 $\sigma_m$  – meso stress  
 $\sigma_N$  – nominal tensile strength  
 $\sigma_s$  – yield stress for reinforcement steel  
 $\sigma_t$  – uniaxial tensile yield stress for concrete  
 $\sigma_y$  – yield stress for concrete  
 $\tau$  – Kirchhoff stress tensor  
 $\tau$  – bond stress between concrete and reinforcement steel  
 $\phi_s$  – reinforcement bar diameter  
 $\varphi$  – internal friction angle  
 $\psi$  – dilatancy angle  
 $\omega$  – weighting function



## Chapter 1

# Introduction

### 1.1. Phenomenon and problem

Fracture process is a fundamental phenomenon in cementitious materials (*Bažant and Planas* [16], *Lilliu and van Mier* [99]). An analysis of this process is very complex due to occurrence of main cracks with various branches, secondary cracks and micro-cracks. It is a major reason of damage in concrete material under mechanical loading contributing to a significant degradation of material strength. Fracture is always preceded by the occurrence of narrow zones of intense deformation which have a certain volume being not negligible as compared to the specimen size. The localization of deformation can occur as tensile zones (failure mode I), shear zones (failure mode II) or mixed zones (failure mode III) An understanding of the mechanism of the formation of localized zone is thus of a crucial importance since they act as a precursor to ultimate fracture and failure. A realistic description of the width and spacing of localized zones is also crucial to evaluate material strength at peak- and post-peak regime and ensure safety to the civil engineering structures. The mechanism of strain localization strongly depends upon a heterogeneous structure of materials over many different length scales, changing e.g. in concrete from the few nanometres (hydrated cement) to the millimetres (aggregate particles). Therefore, to realistically model strain localization, concrete should be considered at meso-scale by distinguishing at least cement matrix, aggregate and bond. However, when modelling the structure of concrete at meso-scale using the FEM, a huge number of finite elements and computational effort is needed which pose a big problem. To practically solve this problem, a direct macroscopic-mesoscopic approach can be used, where a mesoscopic approach is applied to the region with strain localization only, and a macroscopic approach to the remaining region. A meso-region has to be large enough to not influence numerical results. To obtain mesh-independent FE results for concrete specimens with localized zones and to describe their width and spacing, constitutive models have to be equipped with a characteristic length of micro-structure.

### 1.2. Aims

The intention of the thesis is to numerically analyse quasi-static localization of deformation in concrete specimens by means of enhanced constitutive models formulated within continuum mechanics using a macroscopic, mesoscopic and macroscopic-mesoscopic approach. The macroscopic FE analyses of concrete elements were performed using three different continuum models: isotropic elasto-plastic, isotropic damage and smeared-crack one. The models were enhanced by a characteristic length of micro-structure by means of a non-local theory. So they could describe both: the formation of localized zones with a certain thickness and spacing and a related deterministic size effect. The FE-contours of localized zones converged to a finite size upon mesh refinement, initial and boundary value problems became mathematically well-posed at the onset of localization. The 2D finite element analyses were

performed with notched concrete beams and unnotched slender reinforced concrete beams under bending. The numerical results were compared with the corresponding experiments. The meso–scopic studies on concrete specimens under uniaxial tension were carried out with an isotropic damage model with non–local softening. The size of a Representative Volume Element (RVE) was studied using a standard averaging approach. Two novel non–standard methods to determine RVE in concrete were also proposed. The macroscopic–mesoscopic studies on concrete specimens under bending were performed again with a damage model with non–local softening, where a mesoscopic approach was applied to the region with strain localization only. The effect of different material parameters was carefully analysed: beam size, aggregate distribution, aggregate density, aggregate shape, aggregate size, characteristic length and width of a meso–region. The numerical results were compared with the corresponding own experiments. The advantages and disadvantages of the approach were outlined as compared to usual multi–scale models.

The innovative research points concern:

1. FE analyses of strain localization in concrete described as a heterogeneous three–phase material,
2. a determination of RVE using non–standard averaging methods,
3. identification of a characteristic length of macro–structure with calculations and experiments.

### 1.3. Outline

The thesis consists of 7 chapters. After Introduction (Chapter 1), Chapter 2 presents the most important mechanical properties of concrete and describes shortly continuum constitutive models for concrete used in this thesis to simulate strain localization. In addition, a model for reinforcement and bond between concrete and reinforcement is depicted. In Chapter 3, the results of own experimental tests on strain localization are described. To measure two–dimensional displacements on the surface of notched concrete beams during quasi–static bending, a non–invasive Digital Image Correlation (DIC) technique was used. Chapter 4 summarises macroscopic numerical FE results of strain localization on notched concrete beams and unnotched slender reinforced concrete beams without shear reinforcement. The results of a mesoscopic modelling of strain localization in concrete under uniaxial tension are listed in Chapter 5. Concrete was modelled as a random heterogeneous three–phase material. The simulations were carried out with FEM using an isotropic damage constitutive model enhanced by a characteristic length of micro–structure by means of a non–local theory. The existence of a Representative Volume Element (RVE) was discussed using a standard approach. Alternative two non–standard approaches of the RVE determination were proposed. Chapter 6 describes FE investigations on strain localization at a combined macro–meso–scale in notched concrete beams subjected to quasi–static three–point bending. The simulations were carried out with FEM using an isotropic damage constitutive model with non–local softening. The effect of different material parameters was carefully analysed: beam size, aggregate distribution, aggregate density, aggregate shape, aggregate size and characteristic length. The numerical meso–macro results were compared with own laboratory tests results using a Digital Image Correlation and own numerical results using a direct macroscopic–mesoscopic approach. Chapter 7 includes final conclusions and future work perspectives.

## 1.4. Literature review

A fracture process in concrete can be modelled with continuous and discrete models. Continuum models describing the mechanical behaviour of concrete were formulated within, among others, non-linear elasticity (*Kompfner* [89], *Liu et al.* [100], *Palaniswamy and Shah* [128]), rate-independent plasticity (*Bobiński and Tejchman* [25], *Menetrey and Willam* [113], *Mróz* [120], *Pietruszczak et al.* [135]) damage theory (*Bobiński and Tejchman* [24], *Dragon and Mróz* [52], *di Prisco and Mazars* [49], *Peerlings et al.* [134]), endochronic approach (*Bažant and Bhat* [8], *Bažant and Shieh* [17]), coupled damage and plasticity (*de Borst et al.* [44], *Ibrahimbegović et al.* [77], *Klisiński and Mróz* [87]), micro-plane theory (*Bažant and Ožbolt* [13]) and smeared-crack approach (*de Borst and Nauta* [42], *Jirasek and Zimmermann* [81]). The continuum models were also used at meso-level (*Gitman et al.* [67]). Within discrete methods, the most popular ones are classical particle discrete models (*Donze et al.* [50], *D'Addetta et al.* [40]), interface element models with constitutive laws based on elasto-plasticity and fracture mechanics (*Caballero et al.* [32]) and linear and non-linear lattice models (*Schlangen and Garboczi* [145], *Cusatis et al.* [39], *Kozicki and Tejchman* [95]).

Classical FE-simulations of the behaviour of materials with strain localization within continuum mechanics are not able to describe properly both the thickness of localization and distance between them. They suffer from mesh sensitivity (its size and alignment) and produce unreliable results. The strains concentrate in one element wide zones and the computed force-displacement curves are mesh-dependent (especially in a post-peak regime). The reason is that differential equations of motion change their type (from elliptic to hyperbolic in static problems) and the rate boundary value problem becomes ill-posed (*de Borst et al.* [41]). Thus, classical constitutive continuum models require an extension in the form of a characteristic length to properly model the thickness of localized zones. Such extension can be by done within different theories: a micro-polar (*Mühlhaus* [121], *Sluys* [153], *Tejchman and Wu* [159], *Tejchman et al.* [158]), a strain gradient (*Zbib and Aifantis* [172], *Mühlhaus and Aifantis* [122], *Pamin* [129], *de Borst and Pamin* [43], *Pamin* [130], *Sluys and de Borst* [154], *Peerlings et al.* [134], *Meftah and Reynouard* [112], *Pamin and de Borst* [131], *Chen et al.* [37], *Zhou et al.* [174], *Askes and Sluys* [5]), a viscous (*Sluys* [153], *Sluys and de Borst* [154], *Neddleman* [123], *Loret and Prevost* [102], *Lodygowski and Perzyna* [101], *Winnicki et al.* [171], *Pedersen et al.* [132], *Winnicki* [170]) and a non-local (*Pijaudier-Cabot and Bažant* [136], *Bažant and Lin* [10], *Brinkgreve* [31], *de Vree et al.* [45], *Strömberg and Ristinmaa* [156], *Marcher and Vermeer* [108], *Maier* [106, 107], *di Prisco et al.* [48], *Bažant and Jirasek* [9], *Jirasek and Rolshoven* [80], *Tejchman* [157]). Other numerical technique which also enables to remedy the drawbacks of a standard FE-method and to obtain mesh-independency during formation of cracks, are approaches with strong discontinuities which enrich continuous displacement modes of the standard finite elements with additional discontinuous displacements (*Belytschko et al.* [20, 19], *Simone et al.* [148], *Asferg et al.* [4], *Oliver et al.* [126]) or approaches with cohesive (interface) elements (*Ortiz and Pandolfi* [127], *Zhou and Molinari* [173]). In the first approaches, discontinuity paths are placed inside the elements irrespective of the size and specific orientation. In the latter approaches, discontinuity paths are defined at the edges between standard finite elements. The most realistic continuous-discontinuous approach was used by Moonen et al. (*Moonen et al.* [119]). The enhanced continuum models were also used at meso-level of concrete (*Gitman et al.*

[67]).

To experimentally determine the width of the fracture process zone on the surface of concrete specimens, a non-invasive method called Digital Image Correlation (DIC) can be used. It is a powerful optical surface-displacement measuring tool (originally developed in the field of experimental fluid and gas mechanics (*Adrian [2], Raffael et al. [140]*)) to visualise two-dimensional displacements by successive post-processing of digital images (*White et al. [169], Bhandari and Inoue [21], Rechenmacher [141], Słomiński et al. [152], Kozicki and Tejchman [94], Skarżyński et al. [150]*). To investigate strain localization inside specimens, a three-dimensional acoustic emission technique (*Pijaudier-Cabot et al. [137], Mihashi and Nomura [118]*) can be also applied. Another non-invasive method to detect damage in concrete is the elastic wave technique (*Skarżyński et al. [149], Rucka and Wilde [144]*).

To realistically capture numerically the mechanism of strain localization, material micro-structure should be taken into account (*Nilsen et al. [125], Bažant and Planas [16], Sengul et al. [146], Lilliu and van Mier [99], Kozicki and Tejchman [95], He [72]*). The mechanism strongly depends upon a heterogeneous structure of materials over many different length scales, changing e.g. in concrete from the few nanometres (hydrated cement) to the millimetres (aggregate particles). In particular, the presence of aggregate is important since its volume fraction can be as high as 0.70–0.75 in concrete. However, when modelling micro-structure, a huge number of finite elements and computational effort are needed. A directly combined macroscopic-mesoscopic model for strain localization can be used where the material is modelled as partially homogeneous (within the area without strain localization) and partially heterogeneous (within the area where strain localization occurs). A mesoscopic region can be switched on only if strain localization is created (*Eckardt and Könke [54]*). Alternatively, an adaptive FEM solution can be implemented in the region of strain localization (*Ehlers et al. [55], Cecot [35], Cecot and Rachowicz [36]*). Usually, a multi-scale approach is used, aimed to predict a macroscopic constitutive behavior of materials with heterogeneous micro-structure. Different levels can be distinguished: level of quantum mechanics (information about electrons), level of molecular mechanics (information about individual atoms), level of meso-scale or nano-scale mechanics (information about different phases) and level of continuum mechanics. Each level addresses a phenomenon over a specific length and time. To predict a macroscopic behaviour of materials on the basis of micro-structure, several analytical and computational homogenization techniques were developed. A general framework to link material properties at two different levels of the description, incorporating both physical and geometrical nonlinearities, was suggested in 1984 by Hill (*Hill [73]*). He described the material as heterogeneous one on one level, whereas a macroscopic behaviour was assumed to be homogeneous. In 1980s and 1990s, multi-scale techniques were applied to quasi-brittle materials (*Zimmermann et al. [175]*), polycrystalline materials (*Miehe et al. [117]*) and porous media (*Trukozko and Zijl [162]*). An increasing complexity of a microstructural mechanical and physical behaviour corresponding with the development of computational methods, contributed to the development of so-called unit cell methods (e.g. *Christman et al. [38], Bao et al. [6], van der Sluis [163, 164]*). The unit cell methods provided valuable information on local microstructural fields as well as effective material properties. These properties were generally determined by fitting the averaged microscopic stress-strain fields (resulting from the analysis of a microstructural representative cell subjected to certain loading paths) to macroscopic closed-form phenomenological constitutive

equations established ‘a priori’. Once a constitutive behaviour became non-linear (geometrically and physically), it was difficult to make an assumption on a suitable macroscopic constitutive format. Lately, multi-scale computational homogenization techniques (also called hierarchical analyses) were laid down (*Guedes and Kikuchi* [69], *Terada and Kikuchi* [160], *Ghosh et al.* [62, 63]). Further developments and improvements have been done by Smit et al. (*Smit et al.* [155]), Miehe et al. (*Miehe et al.* [116, 117]), Michel et al. (*Michel et al.* [114]), Feyel and Chaboche (*Feyel and Chaboche* [59]), Terada and Kikuchi (*Terada and Kikuchi* [161]), Ghosh et al. (*Ghosh et al.* [64]), Kouznetsova (*Kouznetsova* [92]), *Kouznetsova et al.* (*Kouznetsova et al.* [91]), Miehe and Koch (*Miehe and Koch* [115]) and Maasart (*Maasart* [105]). During computational homogenization (*Gitman* [65], *Kouznetsova et al.* [93], *Kaczmarczyk* [84], *Kaczmarczyk et al.* [83]), the material behaviour is simultaneously studied at two different scales: (1) at the meso-level where strain localization is created and the material is composed of different phases (e.g. aggregate, cement matrix and bond zones for concrete) and (2) at the macro-level where the material is treated as a homogeneous one (*Gitman et al.* [67]). These two different scales interact by coupling kinematics, various stresses and forces. A macroscopic constitutive relation is implicitly provided by a macro-meso connection in the following way: a material is described as homogeneous with any constitutive assumption at macro-level, a meso-level cell is assigned then in each integration of the discretised macro-level (a macro-level strain field is translated into meso-level displacement boundary conditions), later a boundary value problem is solved for each meso-level cell, homogenization is performed on a meso-level response in terms of local reaction forces and local stiffness relations and finally a homogeneous material is transferred to a macro-level. Different modelling techniques were applied at micro-level, e.g. the finite element method (*Smit et al.* [155], *Feyel and Chaboche* [59], *Terada and Kikuchi* [161], *Kouznetsova* [92], *Kouznetsova et al.* [91]), the Voronoi cell method (*Ghosh et al.* [62, 63]) or numerical methods based on Fast Fourier Transforms (*Michel et al.* [114]). However, a local homogenization concept indicates a macro-level size dependence (due to a lack of a characteristic length at macro-level by local considerations) and meso-level size dependence (due to the lack of RVE in a softening regime). A second-order homogenization scheme overcomes a dependence on a macro-level discretisation by considering non-local values (*Kouznetsova* [92]) but suffers from a meso-level size dependence. To avoid both a macro- and meso-level dependence, a Coupled Volume approach can be used (*Gitman et al.* [67]), where a size of a macro-level element equals a meso-level cell size. A realistic assumption of a meso-level region is of an importance. This approach is similar to a directly combined macro-meso calculation scheme (Chapter 6).

As it was mentioned, the most important parameter in a multi-scale approach is a cell size at meso-level, called a Representative Volume Element (RVE) which includes effective properties of a homogenized macroscopic model. RVE was originally defined by Hill (*Hill* [73]) as “a sample that is structurally entirely typical of the whole mixture on average and contains a sufficient number of inclusions for the apparent overall moduli to be effectively independent of the surface values of traction and displacement, as long as these values are macroscopically uniform”. Thus, the size of RVE should be large enough with respect to an individual grain size in order to define overall quantities such as stress and strain, but this size should also be small enough in order not to hide macroscopic heterogeneity (*Evesque* [56]). Many researchers attempted to define the size of RVE in heterogeneous materials with a softening response in a post-peak regime (*Hill* [73], *Bažant and Pijauder-Cabot* [15], *Drugan and Willis* [53], *Evesque* [56], *van Mier* [165], *Bažant and Novak* [11], *Kanit et al.*

[86]). In the majority of different applications of multi-scale approaches, it is assumed that a RVE has a certain specified size. Van Mier (*van Mier* [165]) suggested that the RVE in concrete was approximately equal to 3–8 times the largest particle size. In turn, Bažant and Pijauder–Cabot (*Bažant and Pijauder–Cabot* [15]), Bažant and Novak (*Bažant and Novak* [11]) proposed the size of the RVE to be  $V = l^n$  where  $n$  is the number of spatial dimensions and  $l$  denotes a characteristic length of the material which equals to 2.7–3.0 times the maximum inclusion size. However, the authors did not take into account strain localization. (see Chapter 5).

## Chapter 2

# Continuum modelling of concrete and reinforcement

This chapter presents the most important mechanical quasi-static properties of concrete and briefly describes continuum constitutive models for concrete used in this thesis to simulate strain localization. Next, a regularisation technique in the form of an integral-type non-local theory is summarised. In addition, a model for reinforcement and model for bond between concrete and reinforcement are depicted.

### 2.1. Mechanical properties of concrete

In a Stress-strain diagram under uniaxial compression (Fig. 2.1) one can distinguish several regimes of the concrete behaviour. The behaviour is linear-elastic until approximately 30% of its uniaxial compressive strength  $f_c$  of concrete. Above this point, concrete starts to behave non-linearly (it hardens) up to the peak. Later, the stress decreases, with increasing strain, in a softening regime to the failure. With increasing compressive strength  $f_c$ , concrete becomes brittle (Fig. 2.2). The strain corresponding to  $f_c$  is about value  $\varepsilon_c = 0.0022$ . The Young modulus  $E$  increases with increasing  $f_c$  as well. Poisson's ratio  $\nu$  ranges from 0.15 to 0.22 and is constant up to 80% of  $f_c$ . Afterwards, it increases up to 0.5 during cracking (Fig. 2.3). Under uniaxial tension concrete behaves linearly up to 60% of the uniaxial tension strength  $f_t$ . After the strength is reached, a stress-strain curve falls down again (Fig. 2.4).

During biaxial compression, the concrete strength is higher than in uniaxial compression (Kupfer *et al.* [96]), Fig. 2.5. The maximum increase of 25% is obtained with the ratio of the principal compressive stresses  $\sigma_1, \sigma_2$  equal to 0.5 (Figure 2.6). The tensile strength  $f_t$  is very similar in the case of biaxial and uniaxial tension.

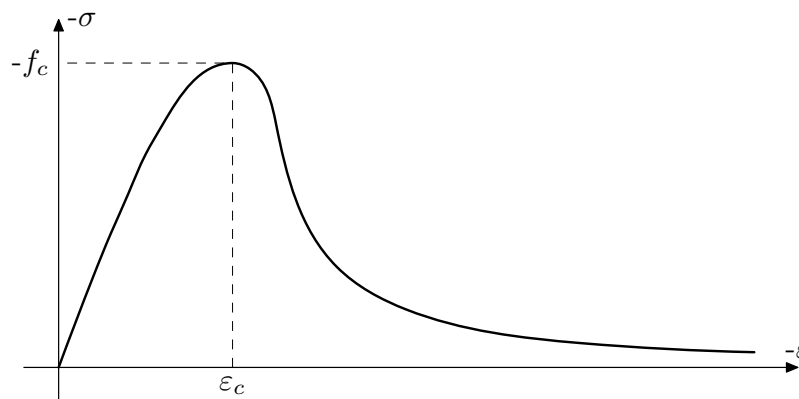


Figure 2.1. Stress-strain curve for concrete in uniaxial compression

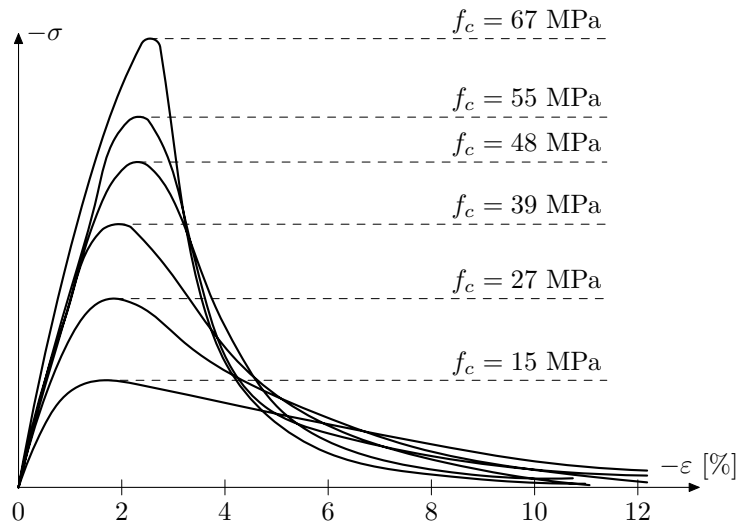


Figure 2.2. Stress–strain curves for concrete in uniaxial compression for various compressive strength  $f_c$

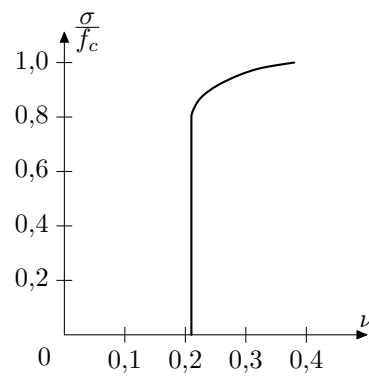


Figure 2.3. Evolution of Poisson's ratio  $\nu$  during deformation

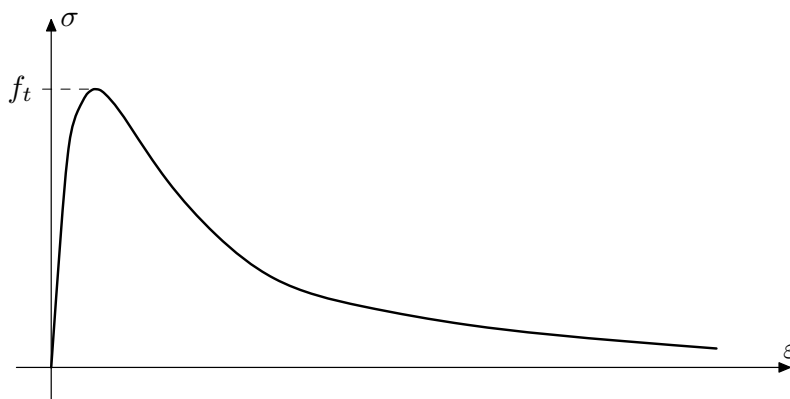


Figure 2.4. Stress–strain curve for concrete in uniaxial tension

The usual triaxial compression laboratory tests were carried out by Kotsovos and Newman (Kotsovos and Newman [90]) (Fig. 2.7). Fig. 2.14 demonstrates the results of these experiments. The cylindrical specimens were initially loaded under hydrostatic confining pressure till the required value is reached. After that, horizontal confining pressure was kept constant and the specimen was subjected to increasing vertical loading. With increasing lateral pressure, a pronounced increase of compressive strength  $f_c$  was obtained. An approximate shape of a failure surface for concrete in the space of principal stresses based on experiments is shown in Fig. 2.8. The failure surface of concrete is symmetric against the hydrostatic line  $\sigma_1 = \sigma_2 = \sigma_3$ . The shape of the surface in a principal stress space is paraboloidal. In deviatoric planes, the surface shape is approximately circular (during compression) and approximately elliptic (during tension); thus it changes from a curvilinear triangle with smoothly rounded corners to nearly circular with increasing pressure.

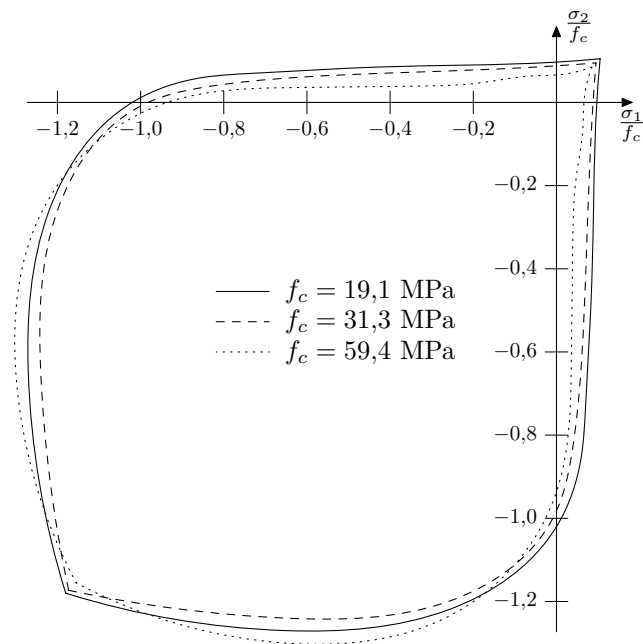


Figure 2.5. Envelope of principal compressive stresses  $\sigma_i$  under biaxial conditions (Kupfer *et al.* [96])

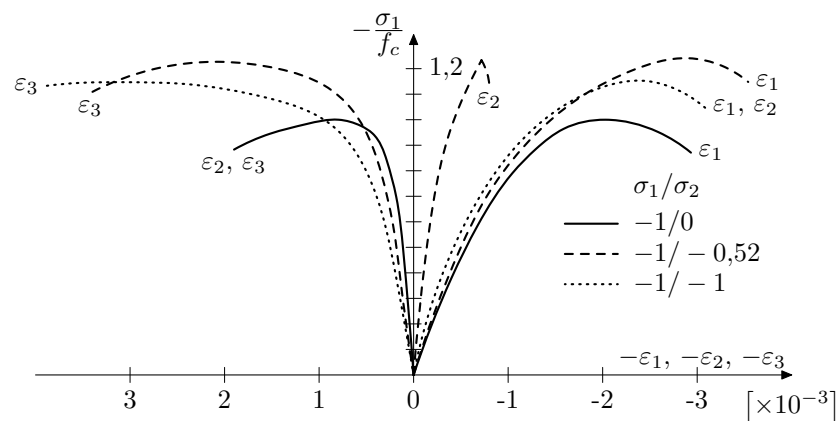


Figure 2.6. Stress–strain curves in biaxial compression (Kupfer *et al.* [96])

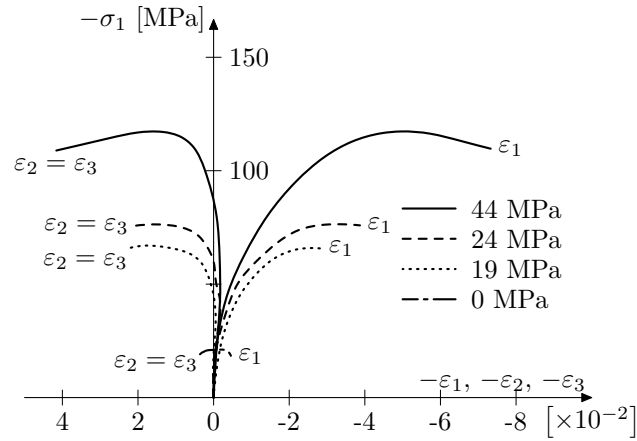


Figure 2.7. Stress–strain curves in triaxial compression (*Kotsovos and Newman [90]*)

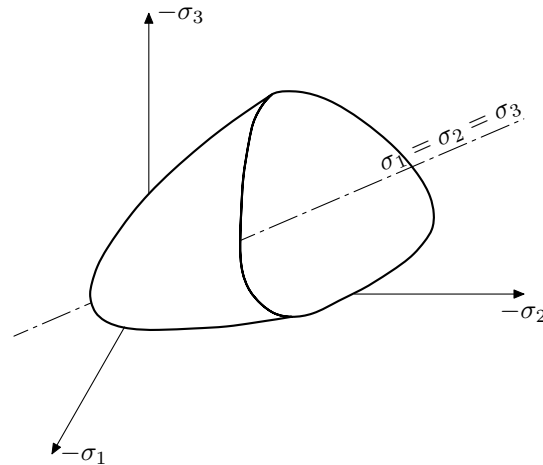


Figure 2.8. Shape of triaxial surface in the space of principal stresses  $\sigma_i$

## 2.2. Constitutive models for concrete

### 2.2.1. Elasto–plastic model

Elasto–plastic models describe plastic deformations in the material connected with energy dissipation (originally introduced by Tresca in 1864). To loading–unloading stages can be distinguished: (a) elasto–plastic loading, (b) elastic unloading. The simplest plastic surface for elasto–plastic materials is:

$$f(\boldsymbol{\sigma}, \kappa) = 0, \quad (2.1)$$

where  $\boldsymbol{\sigma}$  is the Cauchy stress tensor and  $\kappa$  is the hardening / softening parameter. If  $f = 0$  material is in a plastic regime and if  $f < 0$  material is in an elastic regime. Plastic criterion can be re–written as:

$$f(\boldsymbol{\sigma}, \kappa) = F(\boldsymbol{\sigma}) - \sigma_y(\kappa) = 0, \quad (2.2)$$

where  $F$  – the function including tensor invariants and  $\sigma_y$  – the yield stress. Total strains  $d\boldsymbol{\varepsilon}$  can be decomposed into elastic strains  $d\boldsymbol{\varepsilon}^e$  and plastic strains  $d\boldsymbol{\varepsilon}^p$ :

$$d\boldsymbol{\varepsilon} = d\boldsymbol{\varepsilon}^e + d\boldsymbol{\varepsilon}^p. \quad (2.3)$$

The Stress increment  $d\boldsymbol{\sigma}$  depends on the elastic strain increment  $d\boldsymbol{\varepsilon}^e$ :

$$d\boldsymbol{\sigma} = \mathbf{C}^e : d\boldsymbol{\varepsilon}^e, \quad (2.4)$$

where  $\mathbf{C}^e$  denotes the elastic stiffness tensor:

$$\mathbf{C}^e = \lambda \mathbf{I} \otimes \mathbf{I} + 2\mu \mathbf{I}, \quad (2.5)$$

with  $\lambda$  and  $\mu$  are the Lamé's constants,  $\mathbf{I}$  – second–order tensor and  $\mathbf{I}$  – fourth–order tensor. The plastic strain increment is derived on the basis of a flow rule:

$$d\boldsymbol{\varepsilon}^p = d\lambda \frac{\partial g(\boldsymbol{\sigma})}{\partial \boldsymbol{\sigma}}, \quad (2.6)$$

where  $g$  is the plastic potential and  $d\lambda$  stands for the non–negative scalar multiplier (proportionality factor). Loading and unloading conditions can be defined as follows:

$$d\lambda \geq 0 \quad f(\boldsymbol{\sigma}, \boldsymbol{\kappa}) \leq 0 \quad d\lambda f(\boldsymbol{\sigma}, \boldsymbol{\kappa}) = 0. \quad (2.7)$$

Usually, the following relation between the increment of the hardening / softening parameter  $d\boldsymbol{\kappa}$  and the plastic multiplier  $d\lambda$  is valid:

$$d\boldsymbol{\kappa} = \eta d\lambda, \quad (2.8)$$

where  $\eta$  is the constant dependent on the assumed model. The plastic criterion  $f$  and plastic potential  $g$  are described with the help of stress tensor invariants. The first invariant is:

$$I_1 = \text{tr} \boldsymbol{\sigma} = \sigma_{11} + \sigma_{22} + \sigma_{33}, \quad (2.9)$$

and the second invariant is:

$$J_2 = \frac{1}{2} \boldsymbol{S} : \boldsymbol{S} = \frac{1}{6} \left[ (\sigma_{11} - \sigma_{22})^2 + (\sigma_{22} - \sigma_{33})^2 + (\sigma_{33} - \sigma_{11})^2 \right] + \sigma_{12}^2 + \sigma_{13}^2 + \sigma_{23}^2. \quad (2.10)$$

The stress deviator is equal to:

$$\boldsymbol{S} = \boldsymbol{\sigma} - \frac{I_1}{3} \mathbf{I}, \quad (2.11)$$

the the mean stress  $p$  to:

$$p = \frac{\text{tr} \boldsymbol{\sigma}}{3} = \frac{\sigma_{11} + \sigma_{22} + \sigma_{33}}{3}, \quad (2.12)$$

and the effective von Mises stress  $q$  to:

$$q = \sqrt{\frac{3}{2} \boldsymbol{S} : \boldsymbol{S}}. \quad (2.13)$$

One of the most popular approaches realistically simulating the concrete behaviour in compression and tension is the two–surface model based on the Drucker–Prager criterion (in compression) and the Rankine criterion (in tension) (*Feenstra and de Borst [57]*), *Bobiński*

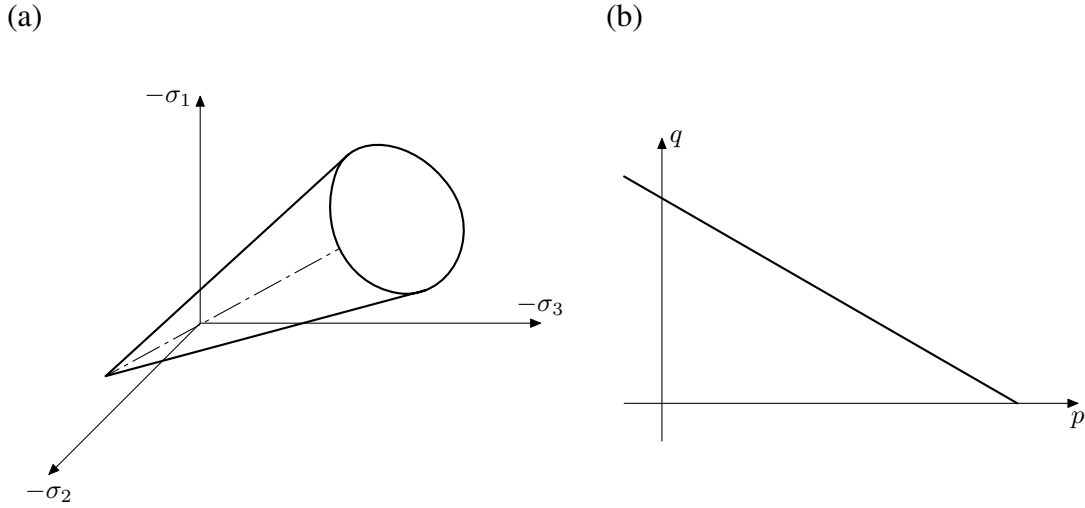


Figure 2.9. Linear Drucker–Prager criterion (a) in the space of principal stresses  $\sigma_i$  and (b) on the  $p - q$  surface

(Bobiński [22]) and Marzec (Marzec [109]). In a compression regime, a linear Drucker–Prager criterion with isotropic hardening and softening used in this thesis is expressed as (Fig. 2.9) :

$$f_1(\boldsymbol{\sigma}, \kappa_1) = q + p \tan \beta - \left(1 - \frac{1}{3} \tan \beta\right) \sigma_c(\kappa_1) = 0, \quad (2.14)$$

where  $\beta$  – the internal friction angle,  $\sigma_c$  – the uniaxial compression yield stress and  $\kappa_1$  – the parameter corresponding to plastic normal stress during uniaxial compression. The flow function is expressed by:

$$d\varepsilon^p = d\lambda_c \frac{\partial g_1(\boldsymbol{\sigma})}{\partial \boldsymbol{\sigma}}, \quad (2.15)$$

where  $d\lambda_c$  is the plastic multiplier in the compression,  $g_1$  is the plastic potential assumed as:

$$g_1 = q + p \tan \psi, \quad (2.16)$$

where  $\psi$  is the dilatancy angle ( $\psi \neq \beta$ ). Using Eq. 2.16 and the derivatives of  $p$  and  $q$  invariants, the flow function becomes:

$$d\varepsilon^p = d\lambda_c \left( \frac{3\mathcal{S}}{2q} + \frac{1}{3} \mathbf{I} \tan \psi \right). \quad (2.17)$$

For the uniaxial compression, the relationship between the hardening parameter and the strain multiplier can be written as:

$$d\kappa_1 = -d\varepsilon_{11}^p = \left(1 - \frac{1}{3} \tan \psi\right). \quad (2.18)$$

A hypothesis by Bednarski (Bednarski [18]) assumes that the increment of the hardening parameter  $\kappa$  is equal to the increment of the equivalent strain measure  $\tilde{\varepsilon}$ :

$$d\tilde{\varepsilon} = 2\sqrt{\frac{1}{3} \mathbf{II}_{de}}, \quad (2.19)$$

where  $\mathbf{II}_{de}$  denotes the second invariant of the strain increment deviator:

$$\mathbf{II}_{de} = \sqrt{\frac{2}{3}} \sqrt{de_{11}^2 + de_{22}^2 + de_{33}^2 + 2(de_{12}^2 + de_{23}^2 + de_{31}^2)} \quad (2.20)$$

$$d\mathbf{e} = d\boldsymbol{\varepsilon} - \frac{tr(d\boldsymbol{\varepsilon})}{3} \mathbf{I}.$$

On the basis of Eq. 2.17 one obtains:

$$d\tilde{\boldsymbol{\varepsilon}} = d\lambda_c = \frac{d\kappa_1}{1 - \frac{1}{3} \tan \psi}. \quad (2.21)$$

An alternative definition of the hardening parameter increment can be also used (Sluys [153], Pamin [130]):

$$d\kappa_1' = \sqrt{\frac{2}{3}} d\boldsymbol{\varepsilon}^p : d\boldsymbol{\varepsilon}^p, \quad (2.22)$$

and the following relationship is obtained:

$$d\kappa_1' = \frac{\sqrt{1 + \frac{2}{9} (\tan \psi)^2}}{1 - \frac{1}{3} \tan \psi} d\kappa_1. \quad (2.23)$$

After scaling of the  $\sigma_c(\kappa_1)$  curve, the both formulae are equivalent.

In FE calculations, different hardening / softening curves are used.

In the tensile regime a Rankine criterion with isotropic softening is used:

$$f_2(\boldsymbol{\sigma}, \kappa_2) = \max\{\sigma_1, \sigma_2, \sigma_3\} - \sigma_t(\kappa_2) = 0, \quad (2.24)$$

where  $\sigma_1, \sigma_2, \sigma_3$  – the principal stresses,  $\sigma_t$  – the uniaxial tensile yield stress and  $\kappa_2$  – the hardening / softening parameter. A geometric interpretation of this condition are three planes perpendicular to the  $\sigma_1, \sigma_2$  and  $\sigma_3$  axes (Fig. 2.10). Eq. 2.24 can be re-written in the following way:

$$\begin{aligned} f_{2,1}(\boldsymbol{\sigma}, \kappa_2) &= \sigma_1 - \sigma_t(\kappa_2) = 0 \\ f_{2,2}(\boldsymbol{\sigma}, \kappa_2) &= \sigma_2 - \sigma_t(\kappa_2) = 0 \\ f_{2,3}(\boldsymbol{\sigma}, \kappa_2) &= \sigma_3 - \sigma_t(\kappa_2) = 0. \end{aligned} \quad (2.25)$$

The singularities in the Rankine criterion occur where individual planes cross each other (edge and vertex). The increments of plastic strains are calculated according to the Koiter's formula (Eq. 2.15):

$$d\boldsymbol{\varepsilon}^p = \sum_{i=1}^3 d\lambda_{2,i} \frac{\partial f_{2,i}}{\partial \boldsymbol{\sigma}}, \quad (2.26)$$

where  $d\lambda_{2,i}$  is a plastic multiplier connected with plane  $f_{2,i}$  ( $i = 1, 2, 3$ ). Using Eq. 2.25, the following formula is obtained:

$$d\boldsymbol{\varepsilon}_i^p = d\lambda_{2,i} \frac{\partial f_{2,i}}{\partial \boldsymbol{\sigma}_i} = d\lambda_{2,i} \quad i = 1, 2, 3. \quad (2.27)$$

The softening parameter  $\kappa_2$  is defined as:

$$\kappa_2 = \boldsymbol{\varepsilon}_1^p + k_{RK} (\boldsymbol{\varepsilon}_2^p + \boldsymbol{\varepsilon}_3^p), \quad (2.28)$$

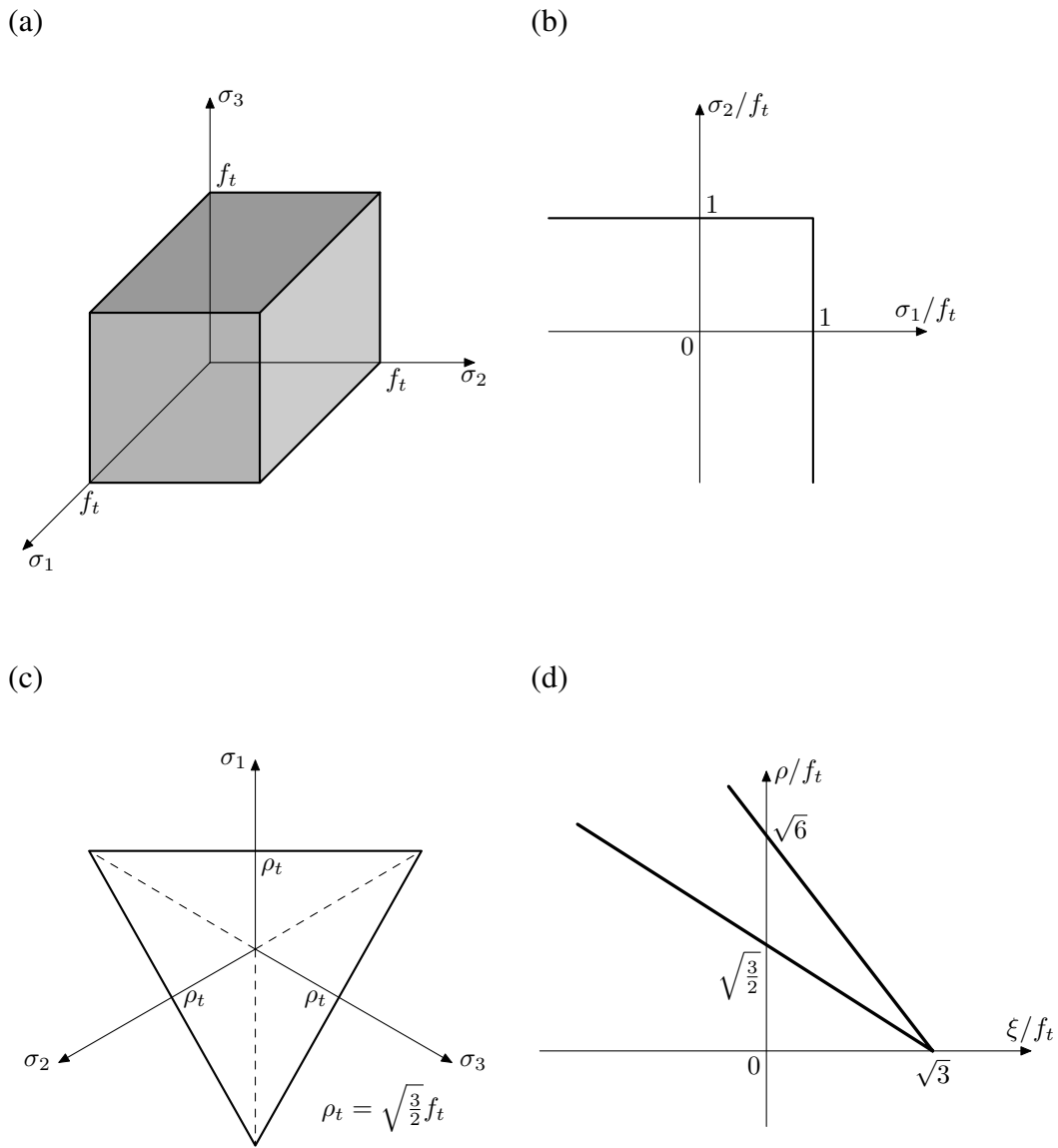


Figure 2.10. Rankine criterion: (a) in the space of principal stresses, (b) for plane stress, (c) in the octahedral space, (d) on the  $\xi - \rho$  surface

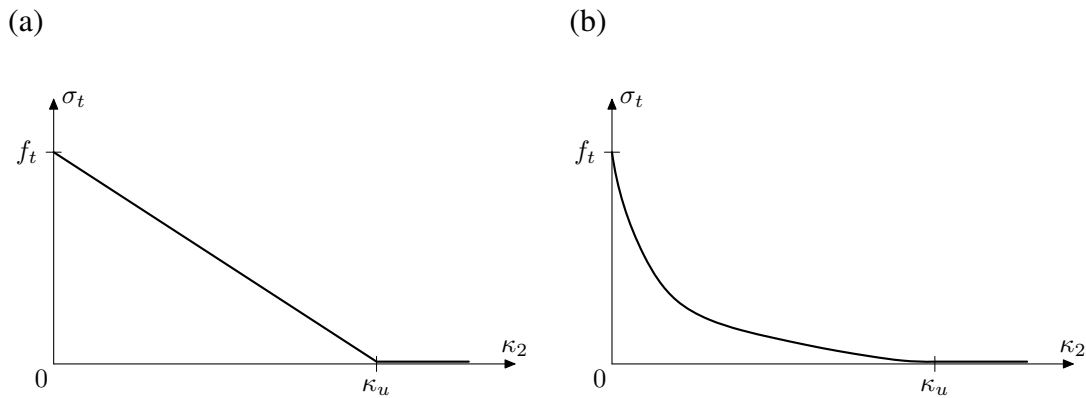


Figure 2.11. Evolution of tensile yield stress  $\sigma_t$ : (a) linear law, (b) exponential law by Hordijk (Hordijk [74])

where  $\varepsilon_i^p$  ( $i = 1, 2, 3$ ) are the principal plastic strains,  $k_{RK}$  denotes the coefficient taking into account the influence of plasticity in the areas of a singularity. It is equal to 0 or to 1 (Lourenco [104], Pivonka et al. [138]). On the basis of Eqs. 2.27 and 2.28 the increment of the softening parameter is equal:

$$d\kappa_2 = d\lambda_{2,1} + k_{RK} (d\lambda_{2,2} + d\lambda_{2,3}). \quad (2.29)$$

To define the evolution of the tensile yield stress  $\sigma_t$ , a linear softening law can be introduced (Fig. 2.11):

$$\sigma_t(\kappa_2) = f_t \left( 1 - \frac{\kappa_2}{\kappa_u} \right), \quad (2.30)$$

or a non-linear exponential curve proposed by Hordijk (Hordijk [74]) can be used:

$$\sigma_t(\kappa_2) = f_t \left\{ \left[ 1 + \left( c_1 \frac{\kappa_2}{\kappa_u} \right)^3 \right] \exp \left( -c_2 \frac{\kappa_2}{\kappa_u} \right) - \frac{\kappa_2}{\kappa_u} (1 + c_1^3) \exp(-c_2) \right\}, \quad (2.31)$$

where  $c_1 = 3.0$ ,  $c_2 = 6.93$  (constants are based on the experimental investigations) and  $\kappa_u$  denotes the ultimate value of  $\kappa$ . In the numerical calculations of the reinforced concrete beams the second curve was mainly used.

This simple isotropic elasto-plastic model for concrete (Eqs. 4.4 – 2.31) requires two elastic constants: modulus of elasticity  $E$  and Poisson's ratio  $\nu$ , two plastic constants: internal friction angle  $\varphi$  and dilatancy angle  $\psi$ , one compressive yield stress function  $\sigma_c = f(\kappa_1)$  with softening and one tensile yield stress function  $\sigma_t = f(\kappa_2)$  with softening. The disadvantages of the model are following: the shape of the failure surface in a principal stress space is linear (not paraboloidal as in reality). In deviatoric planes, the shape is circular (during compression) and triangular (during tension); thus it does not gradually change from a curvilinear triangle with smoothly rounded corners to nearly circular with increasing pressure. The strength is similar for triaxial compression and extension, and the stiffness degradation due to strain localization and non-linear volume changes during loading are not taken into account.

The constitutive law was implemented in the commercial finite element code Abaqus (Abaqus [1]) with the aid of subroutine UMAT (user constitutive law definition) by Bobiński (Bobiński and Tejchman [23]).

### 2.2.2. Damage model

A simple isotropic damage continuum model which describes the degradation with the aid of only a single scalar damage parameter  $D$  growing monotonically from zero (undamaged material) to one (completely damaged material) was used. A damage variable  $D$  is associated with a degradation of the material due to the propagation and coalescence of micro-cracks and micro-voids. It is defined as the ratio between the damage area and the overall material area (Kachanov [82], Simo and Ju [147]). The stress-strain function is represented by the following relationship:

$$\sigma_{ij} = (1 - D) C_{ijkl}^e \varepsilon_{kl}, \quad (2.32)$$

where:  $C_{ijkl}^e$  – the linear elastic material stiffness matrix and  $\varepsilon_{kl}$  – the strain tensor. The damage parameter  $D$  acts as a stiffness reduction factor (the Poisson ratio  $\nu$  is not affected

by damage) that changes from 0 to 1. A general isotropic damage model takes into account two scalar parameters corresponding to two independent elastic constants. To control a degradation of the material a loading function of damage was introduced:

$$f(\tilde{\varepsilon}, \kappa) = \tilde{\varepsilon} - \kappa, \quad (2.33)$$

where the damage threshold parameter  $\kappa$  was defined as:

$$\kappa(t) = \max \left\{ \max_{\tau \leq t} \tilde{\varepsilon}(\tau), \kappa_0 \right\}, \quad (2.34)$$

with  $\kappa_0$  – the initial value of  $\kappa$  when damage begins. If the loading function  $f$  is negative, damage does not develop. During monotonic loading, the parameter  $\kappa$  grows (it coincides with  $\tilde{\varepsilon}$ ) and during unloading and reloading it remains constant. The growth of the damage is controlled by a damage threshold parameter  $\kappa$  which is defined as a maximum of the equivalent strain measure  $\tilde{\varepsilon}$  reached during the load history up to time  $t$ .

The general function controlling growth of a degradation process is defined as follows:

$$\dot{D} = \begin{cases} g(D, \tilde{\varepsilon}) \dot{\tilde{\varepsilon}} & \text{for } f = 0 \text{ and } \dot{f} = 0 \text{ and } D < 1 \\ 0 & \text{for other cases} \end{cases} \quad (2.35)$$

The damage evolution law determines the shape of the softening curve, i.e. material brittleness. The material softening starts when the strain reaches the initial threshold  $\kappa_0$  (material hardening is neglected). The parameter  $\beta$  determines the rate of the damage growth (larger value of  $\beta$  a faster damage growth). The simplest function describing the evolution of the damage parameter  $D$  is a linear softening one (Fig. 2.12a):

$$D = \begin{cases} \frac{\kappa_c}{\kappa} \frac{\kappa - \kappa_0}{\kappa_c - \kappa_0} & \text{for } \kappa < \kappa_c \\ 1 & \text{for } \kappa \geq \kappa_c \end{cases} \quad (2.36)$$

The drawback of this approach is the linear relationship  $\sigma - \varepsilon$  in a softening regime what does not reflect the real behaviour of concrete. Other alternative solution to this problem is an exponential softening law (*Mazars and Pijauder-Cabot* [111], *Peerlings* [133], *Peerlings et al.* [134]) (Fig. 2.12b):

$$D = 1 - \frac{\kappa_0}{\kappa} \left( 1 - \alpha + \alpha e^{-\beta(\kappa - \kappa_0)} \right) \quad (2.37)$$

where  $\alpha$  and  $\beta$  are the material constants describing growth of a degradation process. In one dimensional problems, for  $\varepsilon \rightarrow \infty$  (uniaxial tension) the stress approaches the value of  $(1 - \alpha) E \kappa_0$ . The damage parameter  $D$  grows asymptotically to 1 (it means that material can not be totally damaged). Due to that, for  $\varepsilon \rightarrow \infty$ , a residual value of the stresses is obtained. A different evolution law was proposed by Geers (*Geers* [60]) (Fig. 2.12c):

$$D = \begin{cases} 1 - \left( \frac{\kappa_0}{\kappa} \right)^\beta \left( \frac{\kappa_c - \kappa}{\kappa_c - \kappa_0} \right)^\alpha & \text{for } \kappa < \kappa_c \\ 1 & \text{for } \kappa \geq \kappa_c \end{cases}, \quad (2.38)$$

where  $\alpha$  and  $\beta$  are the material constants describing the growth of a degradation process.

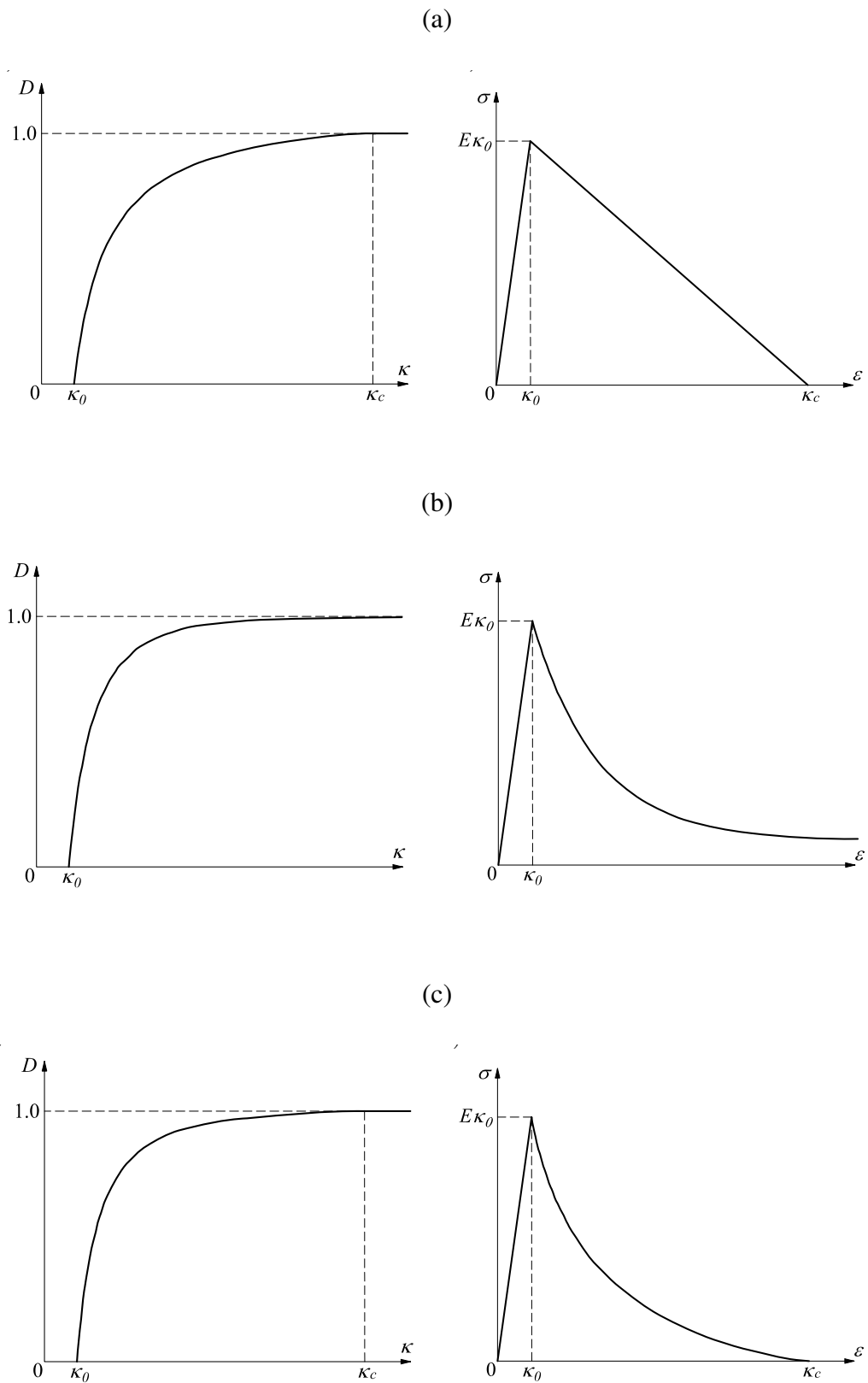


Figure 2.12. Uniaxial tension. Evolution of damage parameter  $D$  and corresponding  $\sigma - \varepsilon$  curves: (a) linear law, (b) exponential by Peerlings (Peerlings *et al.* [134]) and (c) exponential law by Geers (Geers [60])

To define the equivalent strain measure  $\tilde{\varepsilon}$ , the elastic strain energy can be used (*Lemaitre and Chaboche* [98]):

$$\tilde{\varepsilon} = \sqrt{\frac{2Y}{E}}, \quad Y = \frac{1}{2} \boldsymbol{\varepsilon} : \mathbf{C}^e : \boldsymbol{\varepsilon}. \quad (2.39)$$

This approach does not distinguish a different ratio between the compressive and tensile strength of the material. Another definition was proposed by Mazars and Pijauder–Cabot (*Mazars and Pijauder–Cabot* [111]):

$$\tilde{\varepsilon} = \sqrt{\sum_{i=1}^3 \langle \varepsilon_i \rangle^2}, \quad (2.40)$$

where  $\varepsilon_i$  denotes the principal strains for  $i=1, 2, 3$ . The modified von Mises equivalent strain measure  $\tilde{\varepsilon}$  was also proposed by de Vree et al. (*de Vree et al.* [45]) and Peerlings et al. (*Peerlings et al.* [134]):

$$\tilde{\varepsilon} = \frac{k-1}{2k(1-2\nu)} I_1^e + \frac{1}{2k} \sqrt{\frac{(k-1)^2}{(1-2\nu)^2} (I_1^e)^2 + \frac{12k}{(1+\nu)^2} J_2^e}, \quad (2.41)$$

where  $I_1^e = \text{tr}(\boldsymbol{\varepsilon})$  is the first invariant of the total strain tensor,  $J_2^e = \mathbf{II}_{de}$  is the second invariant of the deviatoric strain tensor,  $\nu$  denotes the Poisson's ratio and  $k$  stands for the ratio between the compressive and tensile strength of the material.

Alternatively, a Rankine failure type criterion (*Jirasek and Marfia* [79]) may be used:

$$\tilde{\varepsilon} = \frac{1}{E} \max(\sigma_i^{eff}), \quad (2.42)$$

where  $E$  denotes the modulus of elasticity and  $\sigma_i^{eff}$  are principal values of the effective stress for  $i=1, 2, 3$ :

$$\sigma_i^{eff} = \sigma_{ijkl}^e \varepsilon_{kl}. \quad (2.43)$$

Finally, a failure criterion following Hübler–Combe and Pröchtel (*Hübler–Combe and Pröchtel* [71]), based on the failure criterion by Hsieh–Ting–Chen (*Hsieh et al.* [75]), can be chosen:

$$\tilde{\varepsilon} = \frac{1}{2} \left( a_2 \sqrt{J_2^e} + a_3 \varepsilon_{max} + a_4 I_1^e + \sqrt{\left( a_2 \sqrt{J_2^e} + a_3 \varepsilon_{max} + a_4 I_1^e \right)^2 + 4a_1 J_2^e} \right), \quad (2.44)$$

where  $\varepsilon_{max}$  is the maximum principal total strain,  $a_1, a_2, a_3$  and  $a_4$  are the coefficients depending on  $\alpha_1 = f_t/f_c$  (ratio between the uniaxial tensile strength and the uniaxial compressive strength),  $\alpha_2 = f_{bt}/f_{bc}$  (ratio between biaxial and uniaxial compressive strength),  $\alpha_3, \gamma$  – multipliers of the material strength in triaxial compression.

The constitutive isotropic damage model for concrete requires 5 material parameters:  $E, \nu, \kappa_0, \alpha$  and  $\beta$  (Eq. 2.42), 6 material parameters:  $E, \nu, \kappa_0, \alpha, \beta$  and  $k$  (Eq. 2.41) or 9 material parameters  $E, \nu, \kappa_0, \alpha, \beta, \alpha_1, \alpha_2, \alpha_3$  and  $\gamma$  (Eq. 2.44).

The constitutive law was implemented in the commercial finite element code Abaqus (*Abaqus* [1]) with the aid of subroutine UMAT (user constitutive law definition) by Marzec (*Marzec* [109]).

### 2.2.3. Smeared–crack model

An anisotropic smeared–crack approach was used wherein a discrete crack was represented by cracking strain distributed over a finite volume (*de Borst and Nauta* [42], *Rots and Blaauwendraad* [143]). The total strains were decomposed into the elastic and inelastic strains (coupled with cracks) (*Bobiński* [26]):

$$\boldsymbol{\varepsilon}_{ij} = \boldsymbol{\varepsilon}_{ij}^e + \boldsymbol{\varepsilon}_{ij}^{cr}. \quad (2.45)$$

The stresses were related to elastic strains by the following relationship:

$$\boldsymbol{\sigma}_{ij} = \mathbf{C}_{ijkl}^e \boldsymbol{\varepsilon}_{kl}^e, \quad (2.46)$$

where  $\mathbf{C}_{ijkl}^e$  is the elastic stiffness matrix. Between stresses and cracked strains, the following relationship is held (in a local coordinate system):

$$\boldsymbol{\sigma}_{ij} = \mathbf{C}_{ijkl}^{cr} \boldsymbol{\varepsilon}_{kl}^{cr}, \quad (2.47)$$

with the secant cracked stiffness matrix  $\mathbf{C}_{ijkl}^{cr}$  (defined only for open cracks). The matrix was assumed to be diagonal. A crack was created when the maximum tensile stress exceeded tensile strength  $f_t$ . To define softening in a normal direction under tension, a Hordijk's curve (*Hordijk* [74]) was adopted:

$$\sigma_t(\kappa) = f_t \left[ (1 + A_1 \kappa^3) \exp(-A_2 \kappa) - A_3 \kappa \right], \quad (2.48)$$

with

$$A_1 = \frac{b_1}{\varepsilon_{nu}}, \quad A_2 = \frac{b_2}{\varepsilon_{nu}}, \quad A_3 = \frac{1}{\varepsilon_{nu}} (1 + b_1^3) \exp(-b_2), \quad (2.49)$$

$\varepsilon_{nu}$  is the ultimate cracked strain in tension and the material constants are  $b_1 = 3.0$  and  $b_2 = 6.93$ . The shear modulus  $G$  was reduced by the shear retention factor  $\beta$  according to *Rots and Blaauwendraad* (*Rots and Blaauwendraad* [143]):

$$\beta = \left( 1 - \frac{\varepsilon_i^{cr}}{\varepsilon_{su}} \right)^p, \quad (2.50)$$

where  $\varepsilon_{su}$  is the ultimate cracked strain in shear (usually  $\varepsilon_{su} = \varepsilon_{nu}$ ) and  $p$  is the material parameter. Combining Eqs. 2.45 – 2.47, the following relationship between stresses and total strains (in local coordinate system) is derived:

$$\boldsymbol{\sigma}_{ij} = \mathbf{C}_{ijkl}^s \boldsymbol{\varepsilon}_{kl}^s, \quad (2.51)$$

with the secant stiffness matrix  $\mathbf{C}_{ijkl}^s$  as:

$$\mathbf{C}_{ijkl}^s = \mathbf{C}_{ijkl}^e - \mathbf{C}_{ijrs}^e (\mathbf{C}_{rstu}^e + \mathbf{C}_{rstu}^{cr})^{-1} \mathbf{C}_{tukl}^e. \quad (2.52)$$

After cracking, the isotropic elastic stiffness matrix is replaced by the orthotropic one. In this thesis two different formulations are investigated: a rotating crack model and a multi–fixed orthogonal crack model. In the first approach (rotating crack), only one crack is created which can rotate during deformation. To keep the principal axis of total strains and stresses aligned, the secant stiffness coefficient is calculated according to:

$$C_{ijij}^s = \frac{\sigma_{ii} - \sigma_{jj}}{2(\varepsilon_{ii} - \varepsilon_{jj})}. \quad (2.53)$$

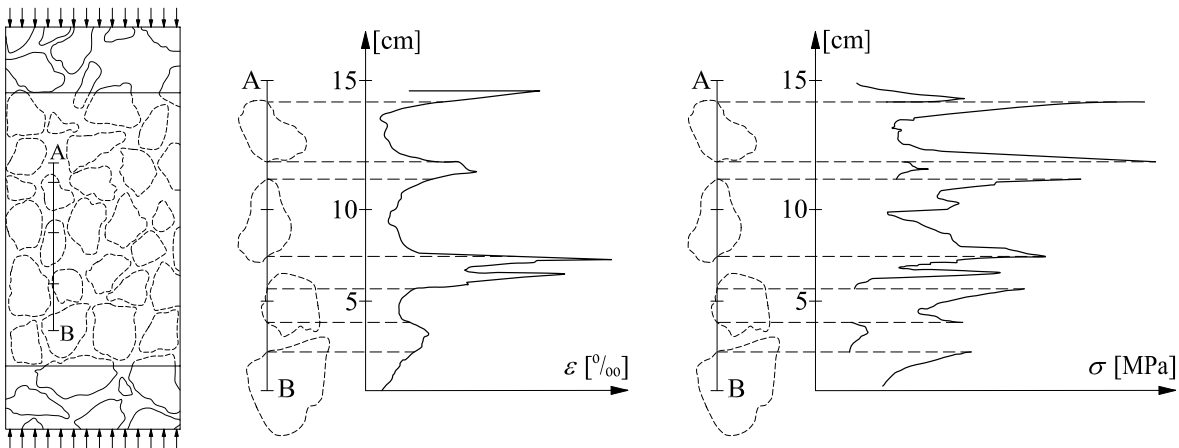


Figure 2.13. Distribution of: (b) strain and (c) stress in (a) aggregates and cement matrix according to experiments by Dantu (*Godycki-Ćwirko* [68])

The second formulation (fixed crack) is allowed for a creation of three mutually orthogonal cracks in 3D problems (or two cracks in plane simulations, respectively). The orientation of the crack is described by its primary inclination at the onset, i.e. the crack cannot rotate during loading.

The constitutive smeared crack model for concrete requires the following 8 material parameters:  $E$ ,  $\nu$ ,  $p$ ,  $b_1$ ,  $b_2$ ,  $f_t$ ,  $\varepsilon_{su}$  and  $\varepsilon_{nu}$ . The constitutive law was implemented in the commercial finite element code Abaqus (*Abaqus* [1]) with the aid of subroutine UMAT (user constitutive law definition) by Bobiński (*Bobiński and Tejchman* [26]).

### 2.3. Non-local theory

Concrete is still the most widely used construction material in terms of volume since it has the lowest ratio between cost and strength as compared to other available materials. It is a composite phase material consisting mainly of aggregate, cement matrix and voids containing water or air. As a consequence, the concrete structure is strongly heterogeneous and the stress and strain distribution is very non-uniform. (Fig. 2.13).

A non-local model of the integral type (so called “strongly non-local model”) was used as a regularisation technique:

1. to properly describe strain localization (width and spacing),
2. to preserve the well-posedness of the boundary value problem,
3. to obtain mesh-independent results,
4. to take into account material heterogeneity and
5. to include a characteristic length of micro-structure for simulations of a deterministic size effect (*Pijauder-Cabot and Bažant* [136], *Bažant and Jirasek* [9], *Bobiński and Tejchman* [23]).

It is based on a spatial averaging of tensor or scalar state variables in a certain neighborhood of a given point (i.e. material response at a point depends both on the state of its neighborhood and the state of the point itself). The idea of non-local models is thus based on averaging procedures due to occurring non-uniformities in concrete (one or several state

variables can be replaced by their non-local equivalents). Thus, a characteristic length  $l_c$  can be incorporated and softening can spread over material points. It is in contrast to classical continuum mechanics, wherein the principle of local action holds (i.e. the dependent variables in each material point depend only upon the values of the independent variables at the same point), and softening at one material point does not affect directly the yield surfaces of other points. Polizzotto et al. (*Polizzotto et. al.* [139]) laid down a thermodynamic consistent formulation of non-local plasticity.

The averaging procedure for local field of body volume  $V$  can be presented as follows:

$$\bar{f}(\mathbf{x}) = \int_V \omega(\mathbf{x}, \boldsymbol{\xi}) f(\boldsymbol{\xi}) d\boldsymbol{\xi}, \quad (2.54)$$

where  $V$  is the integration volume,  $\omega$  is the weighting function,  $\mathbf{x}$  denotes coordinates of material point and  $\boldsymbol{\xi}$  denotes coordinates of neighbouring material points. In general, it is required that the weighting function  $\omega$  should not alter a uniform field which means that it must satisfy the normalising condition (*Bažant and Jirasek* [9]):

$$\int_V \omega(\mathbf{x}, \boldsymbol{\xi}) d\boldsymbol{\xi} = 1 \quad \forall \mathbf{x} \in V. \quad (2.55)$$

The most popular weighting function  $\omega$  is the Gauss distribution function (*Brinkgreve* [31], *Borino et al.* [29]):

$$\omega_0^g(r) = \frac{1}{c_g} \exp\left(-\frac{r^2}{l_c^2}\right) \quad r \geq 0, \quad (2.56)$$

where  $c_g$  is the coefficient and the parameter  $r$  denotes the distance between two material points. The averaging in Eq. 2.56 is restricted to a small representative area around each material point (the influence of points at the distance of  $r = 3l_c$  is only 0.01% (Fig. 2.14)).

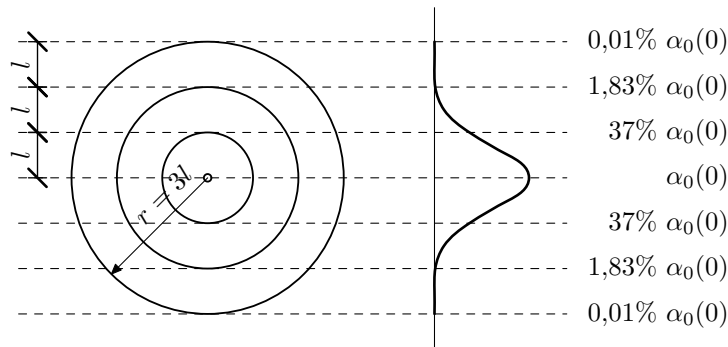


Figure 2.14. Region of the influence of a characteristic length  $l_c$  and the weighting function  $\omega$  in the non-local approach.

A characteristic length is usually related to the micro-structure of the material and is usually determined with an inverse identification process of experimental data (*Le Bellège et al.* [97]). However, the determination of a representative characteristic length of micro-structure is very complex in concrete since the strain localization can include mixed mode (cracks, shear zones) and the characteristic length (which is a scalar value) is related to the localized zone with a certain area of volume which increases during deformation (*Bažant and Jirasek*

[9]). It depends also on the choice of the weighting function. In turn, other researches conclude that the characteristic length depends upon the boundary value problem (*Ferrara and di Prisco* [58]). In general, the Gauss can also have the following representation (*Jirasek* [78]):

$$\omega_0^g(r) = \frac{1}{c_g} \exp\left(-\frac{r^2}{2l_c^2}\right) \quad r \geq 0, \quad (2.57)$$

or (*Bažant and Pijauder–Cabot* [15], *Rodriguez–Ferran et al.* [142]):

$$\omega_0^g(r) = \frac{1}{c_g} \exp\left(-\frac{4r^2}{l_c^2}\right) \quad r \geq 0. \quad (2.58)$$

In this thesis only Gauss distribution according to Eq. 2.56 is used.

Other representation can also be used for the function  $\omega$ , e.g. the bell–shape function (*Bažant and Ožbolt* [13], *Jirasek and Marfia* [79]):

$$\omega_0^b(r) = \begin{cases} \frac{1}{c_b} \left(1 - \frac{r^2}{R^2}\right)^2 & \text{if } r \leq R \\ 0 & \text{if } r > R \end{cases} \quad r \geq 0, \quad (2.59)$$

where  $c_b$  is the coefficient and  $R$  is the characteristic length. In the calculations within the elasto–plastic model, the softening parameters  $\kappa_i$  ( $i = 1, 2$ ) are assumed to be non–local (independently for both yield surfaces):

$$\bar{\kappa}_i(\mathbf{x}) = \frac{\int_V \omega(\|\mathbf{x} - \boldsymbol{\xi}\|) \kappa_i(\boldsymbol{\xi}) d\boldsymbol{\xi}}{\int_V \omega(\|\mathbf{x} - \boldsymbol{\xi}\|) d\boldsymbol{\xi}} \quad i = 1, 2, \quad (2.60)$$

where  $\bar{\kappa}_i(\mathbf{x})$  is the non–local softening parameter,  $V$  – the volume of the body,  $\mathbf{x}$  – the coordinates of the considered (actual) point,  $\boldsymbol{\xi}$  – the coordinates of the surrounding points and  $\omega$  – the weighting function (Gauss distribution according to Eq. 2.56). The softening non–local parameters  $\kappa_i$  near boundaries were also calculated on the basis of Eq. 2.60 (which satisfies the normalising condition). The FE–analyses show that a classical non–local assumption (Eq. 2.60) does not fully regularise a boundary value problem in elasto–plasticity (*Bobiński and Tejchman* [23], *Bažant and Jirasek* [9]). Therefore, a modified formula (*Brinkgreve* [31]) was used to calculate the non–local parameters:

$$\bar{\kappa}_i(\mathbf{x}) = (1 - m) \kappa_i(\mathbf{x}) + m \frac{\int_V \omega(\|\mathbf{x} - \boldsymbol{\xi}\|) \kappa_i(\boldsymbol{\xi}) d\boldsymbol{\xi}}{\int_V \omega(\|\mathbf{x} - \boldsymbol{\xi}\|) d\boldsymbol{\xi}} \quad i = 1, 2, \quad (2.61)$$

where  $m$  denotes the additional non–local parameter controlling the size of the localized plastic zone and the distribution of the plastic strain. For  $m = 0$ , a local approach is obtained and for  $m = 1$ , a classical non–local model is recovered. If the parameter  $m > 1$ , the influence of the non–locality increases and the localized plastic region reaches a finite mesh–independent size (*Bobiński and Tejchman* [23], *Bažant and Jirasek* [9]). To simplify the calculations, the non–local rates were replaced by their approximation  $\Delta \kappa_i^{est}$  calculated on the basis of the known total strain increment values (*Brinkgreve* [31]):

$$\Delta \bar{\kappa}_i(\mathbf{x}) \approx \Delta \kappa_i(\mathbf{x}) + m \left( \frac{\int_V \omega(\|\mathbf{x} - \boldsymbol{\xi}\|) \kappa_i^{est}(\boldsymbol{\xi}) d\boldsymbol{\xi}}{\int_V \omega(\|\mathbf{x} - \boldsymbol{\xi}\|) d\boldsymbol{\xi}} - \Delta \kappa_i^{est}(\mathbf{x}) \right) \quad i = 1, 2. \quad (2.62)$$

Eq. 2.62 enables to ‘freeze’ the non–local influence of the neighbouring points and to determine the actual values of the softening parameters using the same procedures as in a local

formulation.

In the damage model, the equivalent strain measure  $\tilde{\varepsilon}$  was replaced by its non-local definition (*Pijauder–Cabot and Bažant* [136]) to evaluate the loading function (Eq. 2.33) and to calculate the damage threshold parameter  $\kappa$ :

$$\tilde{\varepsilon}(\mathbf{x}) = \frac{\int_V \omega(\|\mathbf{x} - \boldsymbol{\xi}\|) \tilde{\varepsilon}(\boldsymbol{\xi}) d\boldsymbol{\xi}}{\int_V \omega(\|\mathbf{x} - \boldsymbol{\xi}\|) d\boldsymbol{\xi}}, \quad (2.63)$$

where  $V$  – the volume of the body,  $\mathbf{x}$  – the coordinates of the considered (actual) point,  $\boldsymbol{\xi}$  – the coordinates of the surrounding points and  $\omega$  – the weighting function. As a weighting function  $\omega$ .

In the smeared crack approach, the secant matrix was calculated with the non-local strain tensor defined (independently for all tensor components) as (*Jirasek and Zimmermann* [81]):

$$\tilde{\varepsilon}_{kl}(\mathbf{x}) = \frac{\int \omega(\|\mathbf{x} - \boldsymbol{\xi}\|) \varepsilon_{kl}(\boldsymbol{\xi}) d\boldsymbol{\xi}}{\int \omega(\|\mathbf{x} - \boldsymbol{\xi}\|) d\boldsymbol{\xi}}. \quad (2.64)$$

Thus, the resulting stresses were calculated from the following relationship:

$$\sigma_{ij} = C_{ijkl}^s(\tilde{\varepsilon}_{kl}) \varepsilon_{kl}. \quad (2.65)$$

The 2D and 3D non-local models were implemented in the commercial finite element code Abaqus [1] for efficient computations (*Bobiński and Tejchman* [23] *Marzec et al.* [110]). Such implementation was performed using two identical overlapping FE-meshes (with the same nodes). The first mesh allows to gather information about coordinates of integration points in the entire specimen, area of all finite elements and total strain rates in each element. The mentioned elements are defined by the user in the UEL procedure (user element definition) and they do not influence the results of stresses in the specimen since they have no stiffness. The stored information is needed to calculate non-local variables with the aid of the second mesh which includes standard elements from the Abaqus library [1]. The constitutive law is defined by the UMAT procedure (user constitutive law definition). During odd iterations, information is gathered in the elements of the first mesh. During even iterations, stresses in the elements of the second mesh (including standard elements) are determined taking into account non-local variables. Afterwards for a solution of a non-linear equation of motion governing the response of a system of finite elements, the initial stiffness method was used with a symmetric elastic global stiffness matrix. The following convergence criteria were assumed:

$$r_{max} \leq 0.01\tilde{q} \quad \text{and} \quad c_{max} \leq 0.01\Delta u_{max}, \quad (2.66)$$

where  $r_{max}$  – the largest residual out-of-balance force,  $\tilde{q}$  – spatial averaged force over the entire body,  $c_{max}$  – the largest correction of the displacement between two consecutive iterations and  $\Delta u_{max}$  – the largest change of the displacement in the increment. The procedure yielded sufficiently accurate and fast convergence. The magnitude of the maximum out-of-balance force at the end of each calculation step was smaller than 1% of the calculated total force on the specimen. The calculations with smaller tolerances (Eq. 2.66) did not influence the FE-results. The integration was performed at one sample point of each element (centroid).

The calculations were carried out using a large-displacement analysis available in the Abaqus

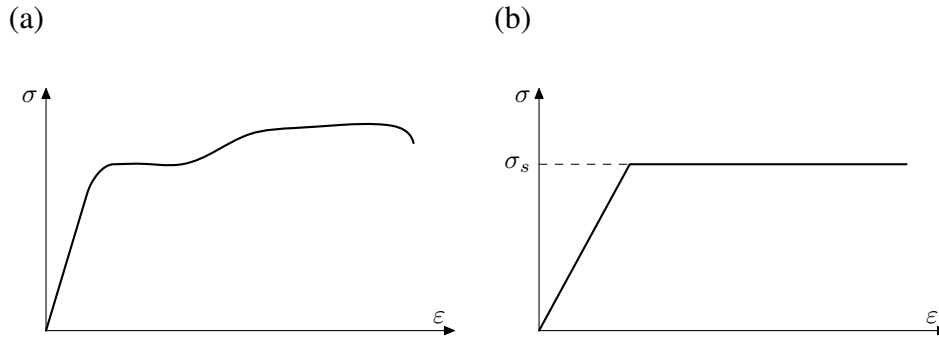


Figure 2.15. Stress–strain relationship in uniaxial tension for (a) real steel, (b) constitutive model

finite element code [1]. According to this method, the current configuration of the body was taken into account. The Cauchy stress was assumed to be the stress measure. The conjugate strain rate was the rate of deformation. The rotation of the stress and strain tensor were calculated with the Hughes–Winget method (*Hughes and Winget* [76]). The non–local averaging was performed in the current configuration. For the solution of a non–linear equation of motion governing the response of a system of finite elements, the initial stiffness method was used with a symmetric elastic global stiffness matrix.

The more detailed information about non–local theory can be found in the doctoral theses by Bobiński (*Bobiński* [22]) and Marzec (*Marzec* [109]).

## 2.4. Constitutive model for reinforcement

The reinforcement cooperates with concrete during loading by carrying principal tensile and compressive stresses. To simulate the behaviour of the reinforcement, the Huber–Mises criterion was assumed:

$$f_s = (\boldsymbol{\sigma}, \boldsymbol{\kappa}_s) = q - \sigma_s(\boldsymbol{\kappa}_s), \quad (2.67)$$

where  $\sigma_s$  is the yield stress for steel and  $\boldsymbol{\kappa}_s$  is the hardening parameter. This law describes an elasto–perfect plastic material (in tensile and compressive experiments, usual steel behaves linearly until its yield limit is reached, Fig. 2.15).

## 2.5. Bond between concrete and reinforcement

Bond between concrete and reinforcement plays a crucial role in a structural behaviour (*den Uijl and Bigaj* [46], *Dörr* [51]). It embraces three major mechanisms: adhesion and friction between concrete and steel surface, and the bearing of reinforcement ribs against concrete. It depends on many factors such as: bar diameter, bar type (smooth or ribbed), dimensions of ribs, concrete type and stress state perpendicular to bars. Usually, two types of bond failures can occur, namely, a pull–out failure or splitting failure (*den Uijl and Bigaj* [46]).

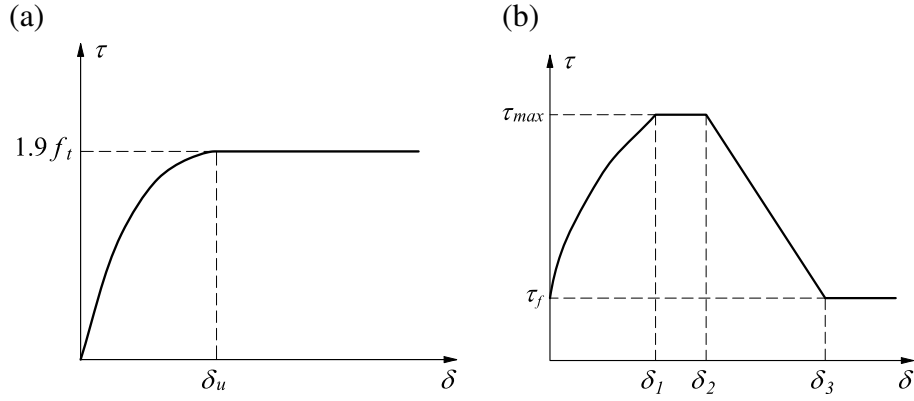


Figure 2.16. Bond stress–relative displacement relationship ( $\tau - \delta$ ) according to (a) Dörr (Dörr [51]) and (b) CEB–FIP [34]

There are many proposed bond models for bars embedded in concrete. One of the oldest is the bond–slip law according to Dörr (Dörr [51]):

$$\tau(\delta) = \begin{cases} f_t \left[ 5.0 \left( \frac{\delta}{\delta_u} \right) - 4.5 \left( \frac{\delta}{\delta_u} \right)^2 + 1.4 \left( \frac{\delta}{\delta_u} \right)^3 \right] & \text{if } 0 \leq \delta \leq \delta_u \\ 1.9f_t & \text{if } \delta > \delta_u \end{cases} \quad (2.68)$$

This is a simple relationship between the bond stress  $\tau(\delta)$  and slip  $\delta$  (Fig. 2.16a). In the Eq. 2.68  $\delta_u$  is the limit displacement during which bond stress reaches its residual value equal to  $\tau(\delta) = 1.9f_t$ . Different values of  $\delta_u$  were proposed: 0.06 mm (Dörr [51]) or 1.0 mm (Haskett *et al.* [70]).

Other possibility is the CEB–FIP [34] (Fig. 2.16b) formula:

$$\tau(\delta) = \begin{cases} \tau_{max} \left( \frac{\delta}{\delta_1} \right)^\alpha & 0 \leq \delta \leq \delta_1 \\ \tau_{max} & \delta_1 \leq \delta \leq \delta_2 \\ \tau_{max} - (\tau_{max} - \tau_f) \frac{\delta - \delta_2}{\delta_3 - \delta_2} & \delta_2 \leq \delta \leq \delta_3 \\ \tau_f & \delta_3 \leq \delta \end{cases}, \quad (2.69)$$

where  $\delta_i$  denotes various bar displacements for different bond zones,  $\tau_{max}$  and  $\tau_f$  are the maximum and residual tangential stress respectively,  $\alpha$  is a parameter.

An alternative concept was proposed by den Uijl and Bigaj (den Uijl and Bigaj [46]). This model presents the relationship between the radial stresses  $\sigma_{r,r_s}$  and the radial strains  $\epsilon_{r,r_s}$  for the concrete cylinder. Different loading stages are analysed. In the first phase (non–cracked concrete cylinder), the radial stresses are defined as follows:

$$\sigma_{r,r_s,I} = \frac{E}{\frac{c_1^2 + r_s^2}{c_1^2 - r_s^2} + \nu} \epsilon_{r,r_s}, \quad (2.70)$$

where  $E$  denotes the modulus of elasticity,  $\nu$  denotes Poisson's ratio,  $r_s$  is the radius of reinforcement bar and  $c_1 = r_s + c_{eff}$  ( $c_{eff}$  – effective radius of concrete cover).

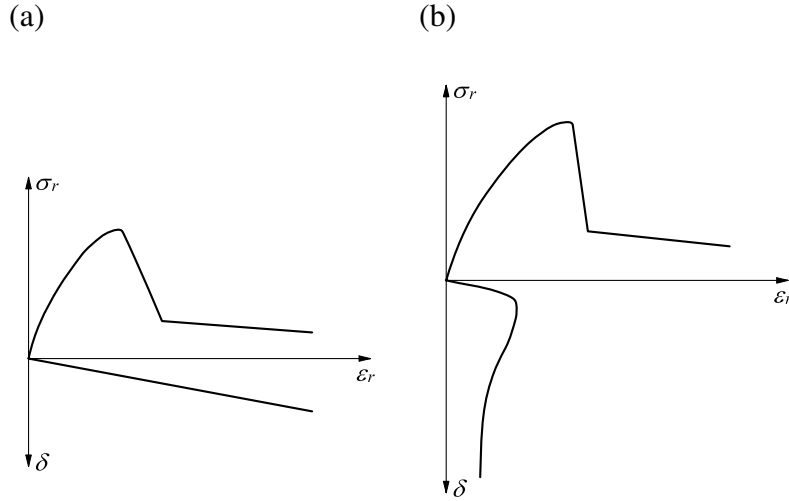


Figure 2.17. Displacement  $\delta$  – radial stress  $\sigma_r$  relationship ( $\tau - \delta$ ) according to den Uijl and Bigaj (*den Uijl and Bigaj* [46]) for two types of bond failures (a) splitting (b) pull-out

In the second phase (partially cracked concrete cylinder), the following expression is assumed:

$$\sigma_{r,r_s,II} = f_{ct} C_1 \frac{r_{cr}}{r_s} + f_{ct} \left( \frac{C_2 r_s}{2} \left( \frac{r_{cr}}{r_s} - 1 \right)^2 + \frac{r_{cr}}{r_s} - 1 \right), \quad (2.71)$$

where  $r_{cr}$  describes the location of the crack start against the axis of the reinforcement (in the II phase  $r_s \leq r_{cr} \leq c_1$ ).

In the third phase (totally cracked concrete cylinder), the radial stresses are equal:

$$\sigma_{r,r_s,III} = f_{ct} \left[ (aC_3 + b) \left( \frac{c_1}{r_s} - 1 \right) - \frac{aC_4 r_s}{2} \left( \left( \frac{c_1}{r_s} \right)^2 - 1 \right) \right]. \quad (2.72)$$

The coefficients  $C_1 - C_4$  and  $a$  and  $b$  are defined by other equations. They depend on concrete properties in tension / compression and number of radial cracks along the bar perimeter. This bond law (*den Uijl and Bigaj* [46]) distinguishes two types of bond failures: a pull-out failure and splitting failure (Fig. 2.17). The first one characterises with developing cracks parallel to the reinforcement bar. The second one appears when the reinforcement bar is pull-out of concrete. For the splitting failure, the radial strains  $\epsilon_r$  are linearly dependent on the slip  $\delta$ , and for the pull-out failure, they are nonlinearly dependent. If the radial stresses  $\sigma_r$  are smaller than the maximum slip stresses  $\tau^{max} = 5f_t$ , a splitting failure takes place. Otherwise a pull-out failure occurs ( $\tau^{max} / \sigma_{r,r_s} \leq 1$ ). A splitting failure is often caused by an insufficient concrete cover.

Akkerman (*Akkerman* [3]) modified bond law by den Uijl and Bigaj (*den Uijl and Bigaj* [46]) by applying relations between radial stress and strain for various limit deformations  $\epsilon_{r,r_s}$ :

$$\sigma_{r,r_s}(\epsilon_{r,r_s}) = \begin{cases} \sigma_{r,r_s,max} \frac{k\eta - \eta^2}{1 + (k-2)\eta} & 0 \leq \epsilon_{r,r_s} \leq \epsilon_{r,r_s,max} \\ \sigma_{r,r_s,max} [1 + h(\epsilon_{r,r_s} - \epsilon_{r,r_s,max})] & \epsilon_{r,r_s,max} \leq \epsilon_{r,r_s} \leq \epsilon_{r,r_s,res} \\ \sigma_{r,r_s,res} & \epsilon_{r,r_s,res} \leq \epsilon_{r,r_s} \end{cases}, \quad (2.73)$$

where  $k$ ,  $\eta$  and  $h$  are calculated as follows:

$$k = \frac{E_r \varepsilon_{r,s,max}}{\sigma_{r,s,max}} \quad \eta = \frac{\varepsilon_{r,s}}{\varepsilon_{r,s,max}} \quad h = -\frac{1 - \beta_t}{\varepsilon_{r,s,res} - \varepsilon_{r,s,max}}, \quad (2.74)$$

where  $E_r$  is the initial stiffness in the radial direction,  $\beta_t$  is usually equal to 0.2,  $\sigma_{r,s,max}$  and  $\varepsilon_{r,s,max}$  denote maximum stress and strain during the failure.

Finally a relationship between bond stress and relative displacement ( $\tau - \delta$ ) according to Haskett et al. ((Haskett et al. [70]) was tested (Fig. 2.18). It assumes that until the limit displacement ( $\delta_u = 1.5$  mm) is reached, bond stress is as follows:

$$\tau(\delta) = \tau_{max} \left( \frac{\delta}{\delta_u} \right)^{0.4}, \quad (2.75)$$

where  $\tau_{max}$  denotes the maximum bond stress equal to  $2.5\sqrt{f_t}$ . After the maximum value is reached, a linear decrease of stress occurs. Haskett et al. (Haskett et al. [70]) assumed that bond stress decreases to 0 for the limit displacement  $\delta_{max} = 1.5$  mm.

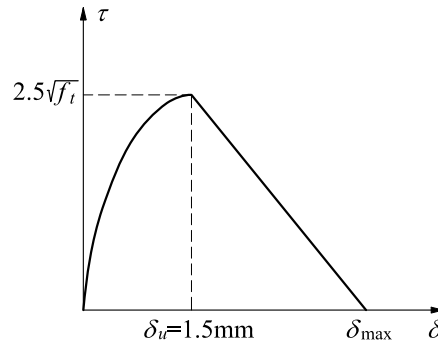


Figure 2.18. Bond stress – relative displacement relationship ( $\tau - \delta$ ) according to Haskett et al. (Haskett et al. [70])

It has to be noted that a universal bond law does not exist since it depends on boundary conditions of the entire system (specimen size, concrete type, reinforcement diameter, reinforcement roughness and confining pressure).



## Chapter 3

# Laboratory tests on strain localization

This chapter presents the results of experimental investigations of the width of a localized zone on the surface of notched concrete beams under quasi-static three-point bending (*Skarżyński et al.* [150]) which were a continuation of similar tests performed by Kozicki and Tejchman (*Kozicki and Tejchman* [94]). To experimentally measure two-dimensional displacements on the surface of beams, a non-invasive Digital Image Correlation (DIC) technique was used. The laboratory experiments were performed with several notched concrete beams of a different geometry. The specimens were prepared using two concrete mixes: sand and gravel. Obtained results were also compared with a deterministic size effect law by Bažant (*Bažant* [7]) for notched specimens.

### 3.1. Digital Image Correlation technique

The Digital Image Correlation was originally developed in the field of experimental fluid and gas mechanics (*Adrian* [2], *Raffael et al.* [140]). It is an optical method to visualise surface displacements by successive post-processing of digital images taken with a constant time between frames from a professional digital camera (*Kozicki and Tejchman* [94]). The coloured surface serves as the tracer in concrete elements. The digital camera sensors are comprised of tiny, light-sensitive elements called pixels. When an image is captured, each pixel reflects three numbers (called the colour components  $Y C_b C_r$ ) in proportion to the amount of the light reflected from the imaged object, where  $Y$  is the luminosity (brightness),  $C_b$  is the blueness and  $C_r$  is the redness. The DIC system interprets differences in light intensity as a grey-scale pattern recorded at each pixel on CCD-camera (Charge Coupled Device). Three functions are of a major importance for DIC: (a) image field intensity, (b) cross-correlation function and (c) interpolation function. The image intensity field assigns to each point in the image plane a scalar value which reflects the light intensity ( $Y$ -colour component) of the corresponding point in the physical space (it maps simply the light energy of an individual particle in a physical space). The grey levels range numerically between 0 (black) and 255 (white) for an 8-bit image. A so-called area of interest is cut out of the digital image and small overlapping sub-areas called search patches are chosen (Fig. 3.1). The search patch ranges in size from  $15 \times 15$  pixels up to  $240 \times 240$  pixels. If the deformation between two images is sufficiently small, the patterns of the interrogation cells are supposed not to change their characteristics (only their locations). A displacement pattern is detected by comparing two consecutive images captured by a camera which remains in a fixed position with its axis oriented perpendicularly to the plane of deformation. To find a local displacement between images '1' and '2', a search zone is extracted from the second image (Fig. 3.1). A correct local displacement vector for each interrogation cell is accomplished by means of a cross-correlation function between two consecutive brightness distributions ( $Y$ -colour component) in two digital images. The function calculates simply possible displacements by correlating all grey values from the first image with all grey values from the

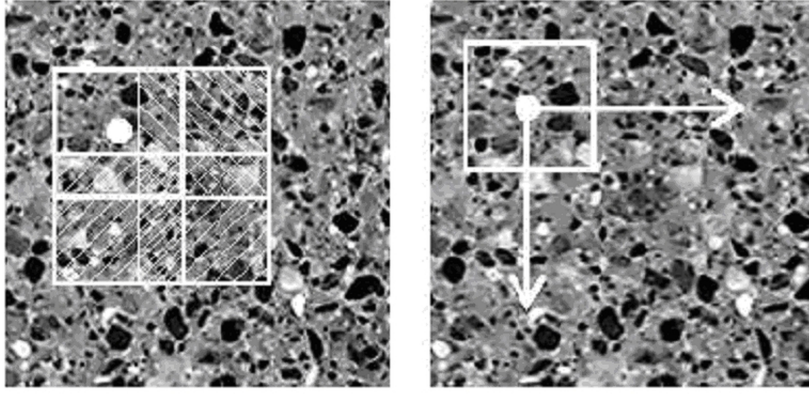


Figure 3.1. Two successive digital images with the marked square pixel subsets (white squares) and other overlapping pixel subsets (hashed squares) from Digital Image Correlation (DIC) analysis

second image. The correlation plane is evaluated at single pixel intervals, what means that the resolution is equal to one pixel. By fitting an interpolation function to the region close to the peak, the displacement vector is established with a high accuracy (equal to the correlation offset). The peak in the correlation function indicates that two images are overlying each other (thus, it indicates the “degree of match” between two images). The Charged Coupled Device operates in the colour space  $Y, C_b, C_r$  in opposition to widely known colour space  $RGB$  ( $R$  is red,  $G$  is green,  $B$  is blue). The first step in the image pre-processing is to convert the  $RGB$  colour space into  $Y, C_b, C_r$  colour space according to the ISO/TC42N 4378 TIFF/EP standard, assuming  $R, G, B$  in the range  $\langle 0, 255 \rangle$  and  $Y, C_b, C_r$  in the range  $\langle 0, 255 \rangle$ :

$$\begin{aligned}
 Y &= 0.2989R + 0.5866G + 0.1145B \\
 C_b &= 128 - 0.168736R - 0.331264G + 0.5B \\
 C_r &= 128 + 0.5R - 0.418688G - 0.081312B
 \end{aligned} \tag{3.1}$$

To calculate a strain field on the specimen surface, two successive digital images were compared with each other. First, one pixel was selected on the first digital image, then a square pixel subset of a certain size was chosen around it. Next, a search for this pixel subset on the second damage was done by using correlation function (Fig. 3.1). The Person’s product-moment correlation function was used (Fig. 3.2) which was obtained by dividing the covariance of the two variables by the product of their standard deviations (*Kozicki and Tejchman* [94]):

$$R(x, y) = \frac{n \sum x_i y_i - \sum x_i \sum y_i}{\sqrt{n \sum x_i^2 - (\sum x_i)^2} \sqrt{n \sum y_i^2 - (\sum y_i)^2}}, \tag{3.2}$$

where  $x$  refers to the first image,  $y$  refers to the second image,  $n$  is the number of pixels in the pixel subset and indexes  $i$  are  $Y$  channel values of subsequent pixels from pixel subset. The top of a correlation function is usually not clearly distinguished as the correlation function produces results for each pixel of image. To precisely locate the top of the peak, a sub-pixel interpolation was performed. As an interpolation function, the function sinc256 was used (*Kozicki and Tejchman* [94]) (Figs. 3.3 and 3.4) which was the most effective among other interpolation functions (*Dersh* [47]) tested in preliminary calculations:

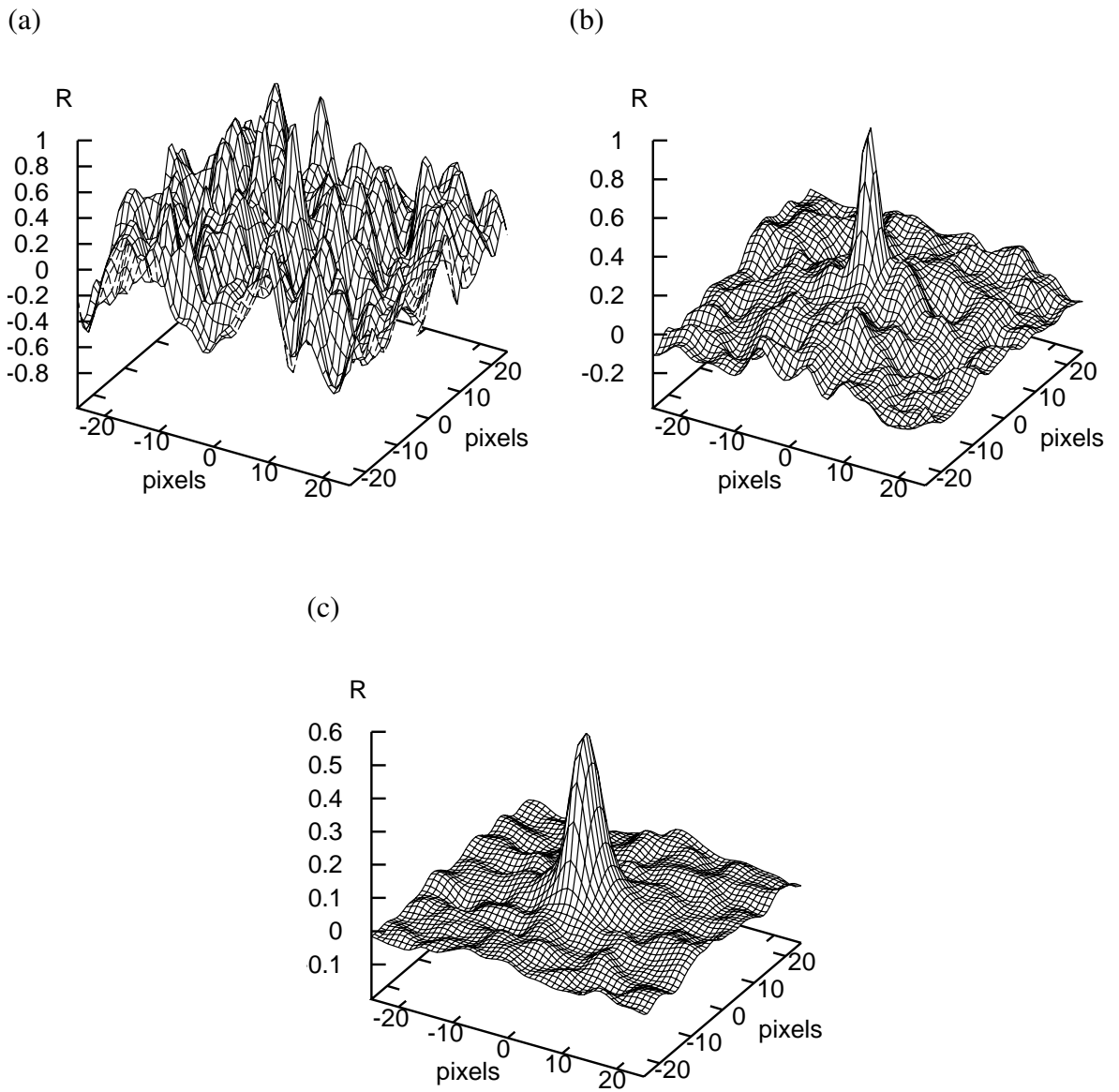


Figure 3.2. Comparison between search patch sizes using Pearson’s formula (Eq. 3.2) with (a) 10 pixels, (b) 50 pixels and (c) 200 pixels

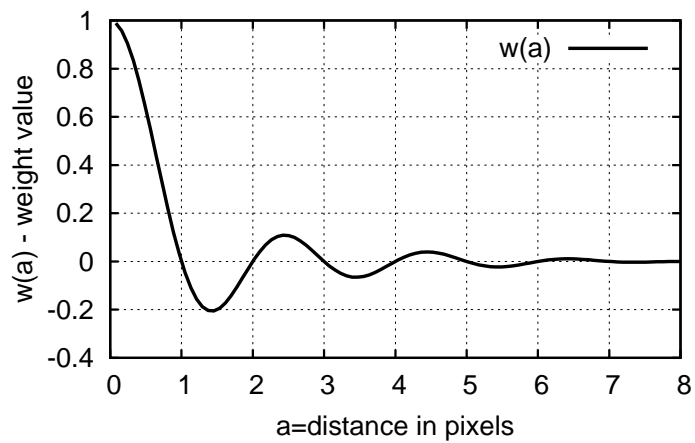


Figure 3.3. Interpolation function sinc256 used to achieve sub-pixel precision

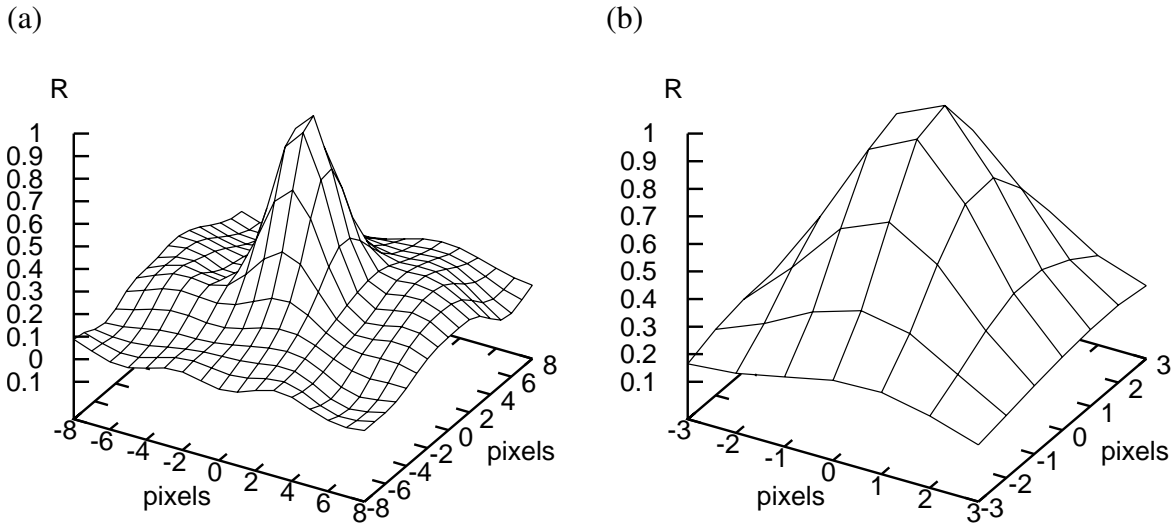


Figure 3.4. Correlation plane with correlation peak (16×16 pixel area): (a) surface before sub-pixel interpolation (b) surface after sub-pixel interpolation

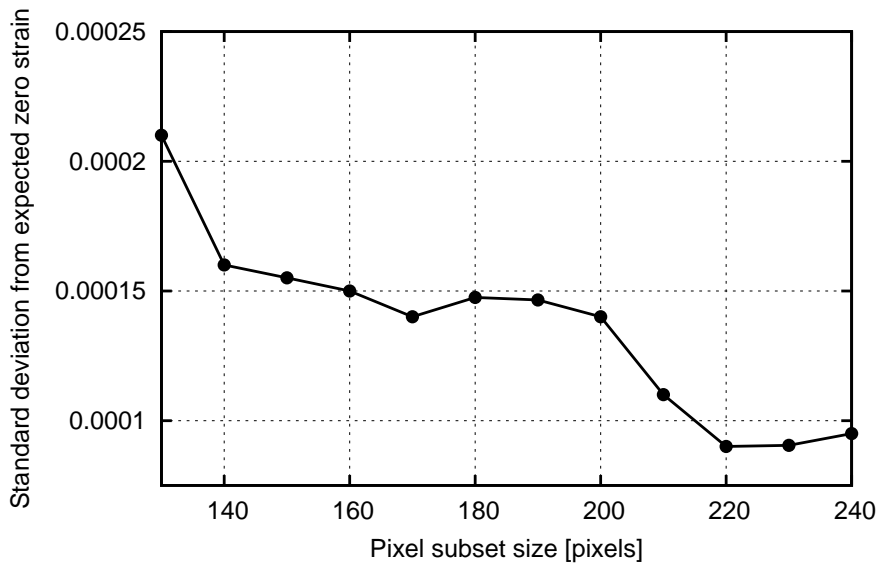


Figure 3.5. Standard deviation from expected zero strain versus search patch size

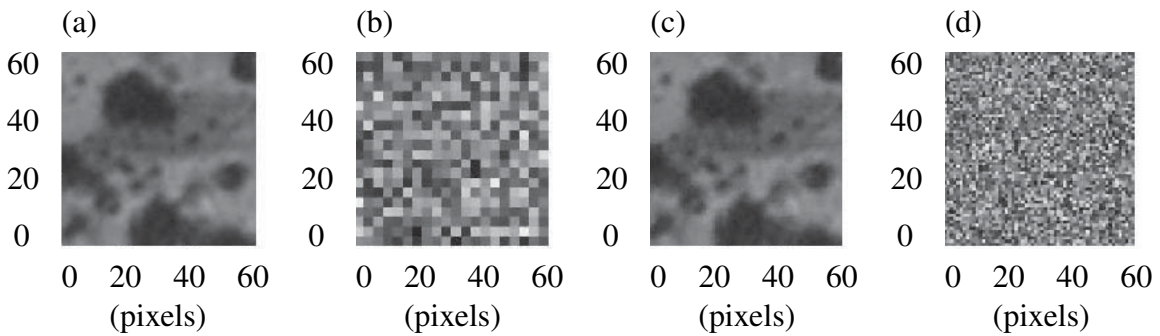


Figure 3.6. Images used to validate experiments: (a) two subsequent images, (b) random image with 3×3 'grains', (c) single image, (d) random image with 1×1 'grains'

$$w(a) = \begin{cases} 1 & \text{for } a = 0 \\ \frac{\sin(\pi a)}{\pi a} \frac{\sin(\pi a/8)}{\pi a/8} & \text{for } a > 0 \end{cases}, \quad (3.3)$$

where  $a$  denotes the distance in pixels. The interpolation was evaluated at  $1/500^{\text{th}}$  pixel intervals, yielding a system resolution of 0.002 pixels. The programme written in C++ by Kozicki (*Kozicki and Tejchman* [94]) was applied for DIC tests.

A series of preliminary tests were conducted to assess the precision of the DIC technique (according to the procedure proposed by White et al. (*White et al.* [169])). Figure 3.5 shows the standard deviation of the measured strain on the basis of two successive digital images versus the assumed strain equal to zero against the search patch size. In turn, Figs. 3.6–3.9 show the results for the following digital image pairs: (a) two subsequent images of the concrete specimen, (b) random image with  $3 \times 3$  'grains', (c) single image of the concrete specimen compared with itself, (d) random image with  $1 \times 1$  'grains' (Fig. 3.6). For those four cases, the DIC precision was better than 0.0005 for the search patches larger than 60 pixels (Fig. 3.7). The precision errors were associated with the asymmetry of the correlation peak. In the case of the random image with  $1 \times 1$  'grains' (Fig. 3.6d), the highest precision was found. For  $3 \times 3$  'grains' and two subsequent, no perfect match was found, since the correlation peak was asymmetric. The strain value fluctuations along a single line of the image are shown in Fig. 3.9 for the point 'A' of Fig. 3.7. Next, the second image for all four cases (Fig. 3.6) was artificially modified, so strain oscillated between 0 and 0.0033 every 300 pixels. Figure 3.8 reveals a higher precision for the real case (Figs. 3.6a and 3.6c) than for the random pixel pattern (Figs. 3.6b and 3.6d). In the randomly generated pixel pattern, the noise had a high amplitude in the frequency domain. Thus, by stretching it (to achieve the strain of 0.0033), an image interference occurred. The real images had a small amplitude in the frequency domain. In this way, the artefacts were not generated. Moreover, a large

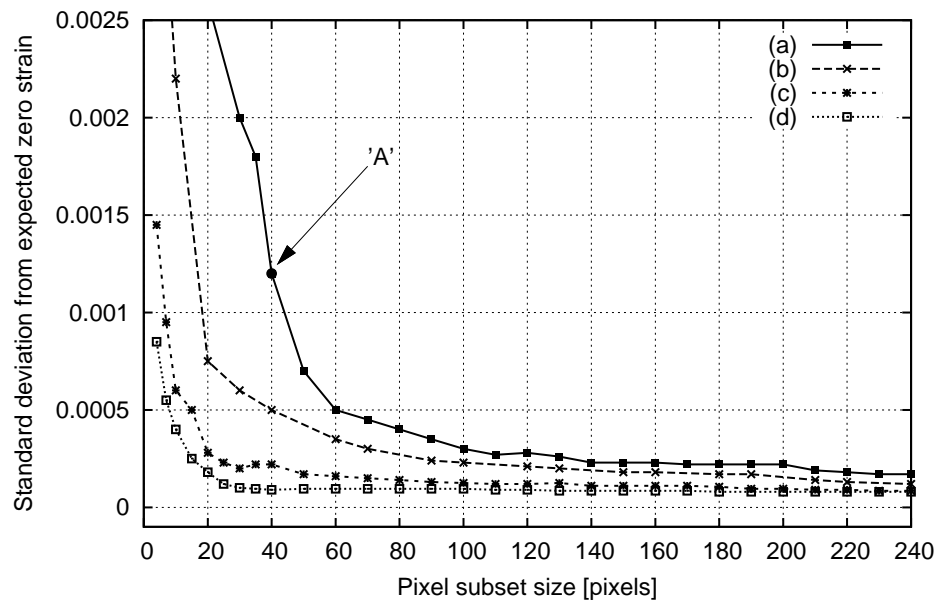


Figure 3.7. Precision of DIC against the search patch size for strain equal zero for images of Fig. 3.6: (a) two subsequent images, (b) random image with  $3 \times 3$  'grains', (c) single image, (d) random image with  $1 \times 1$  'grains'

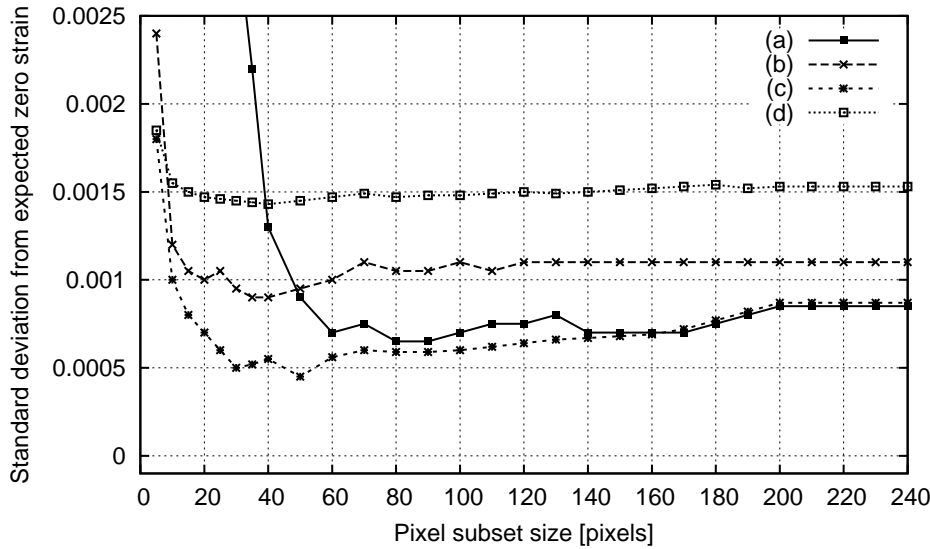


Figure 3.8. Precision of DIC against the search patch size for strain oscillating between 0 and 0.0033 every 300 pixels for images of Fig. 3.6: (a) two subsequent images, (b) random image with  $3 \times 3$  'grains', (c) single image, (d) random image with  $1 \times 1$  'grains'

search patch size blurred the boundaries between oscillating strain values whereas a smaller search patch size yielded a more accurate result. Thus, the precision of DIC strongly depends on the search patch size and the quality of a random pattern in the image. The speckle pattern on the concrete surface should include 4–10 pixels on the captured image. The selection of an optimum search patch size in the analysis requires two conflicting parameters to be balanced. The larger search patch improves accuracy (Figs. 3.7 and 3.8) but it blurs the boundary between strain values. In turn, a too small pixel subset produces noise (*Kozicki and Tejchman* [94]). The number of measurement points depends only on the computational time since the distance between the search patch centres can be as small as one pixel. In the calculations, this distance was assumed to lie between 10 and 40 pixels. It was small enough to have no influence on the resolution of results.

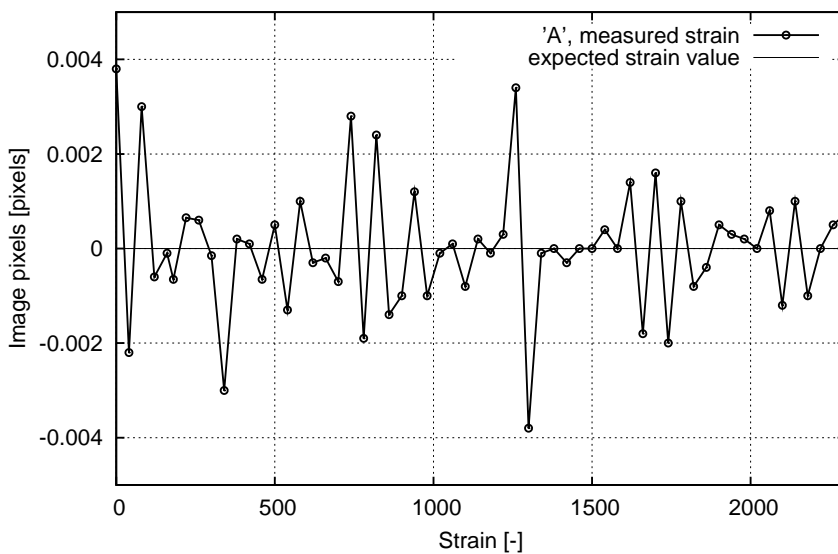


Figure 3.9. Strain fluctuations along single line of the image for the point 'A' of Fig. 3.7 (pixel subset size has 40 pixels, standard deviation from the expected zero strain is 0.0012)

### 3.2. Experimental set-up

The three-point bending laboratory tests were carried out on concrete specimens of five different sizes  $D \times L$  ( $D$  – beam height,  $L = 4D$  – beam length) with free ends (Fig. 3.10). Three beams were geometrically similar:

- small-size beams  $80 \times 320 \text{ mm}^2$  (beam '1'),
- medium-size beam  $160 \times 640 \text{ mm}^2$  (beam '2'),
- large-size beam  $320 \times 1280 \text{ mm}^2$  (beam '3').

The beams were geometrically similar in two dimensions only to avoid differences in hydration heat effects being proportional to the thickness of the member (*Bažant and Planas* [16]).

The remaining two types had the same cross-section as the beams '1' and '2' but they were longer:

- small-size long beam  $80 \times 640 \text{ mm}^2$  (beam '4'),
- medium-size long beam  $160 \times 1280 \text{ mm}^2$  (beam '5').

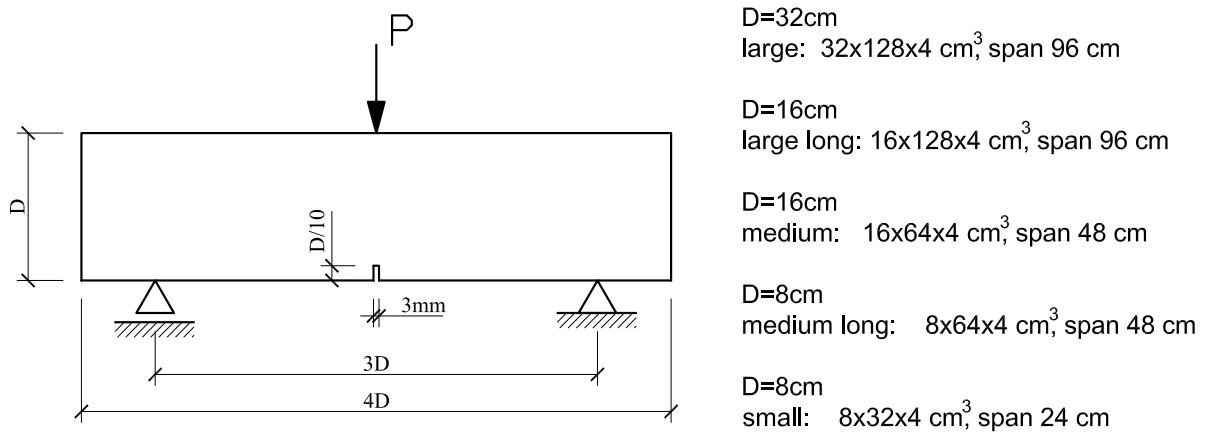


Figure 3.10. Geometry of experimental concrete beams subjected to three-point bending

Table 3.1. Contents of concrete mixes: (a) with sand, (b) with gravel

(a)			(b)		
No.	Material	Volume	No.	Material	Volume
1.	Sand	62%	1.	Gravel	76%
2.	Cement	27%	2.	Cement	17%
3.	Water	11%	3.	Water	7%

The beam thickness was always  $b = 40 \text{ mm}$ . The beam span was equal to  $3D$ . A notch of the height of  $D/10 \text{ mm}$  and the width of  $3 \text{ mm}$  was located in the middle of each beam bottom. The quasi-static deformation in beams was induced by a vertical displacement  $u$  prescribed at the beam mid-span with a rate of  $0.001 \text{ mm/min}$ . The geometry of the first three beams was the same as that assumed in laboratory tests by Le Bellęgo et al. (*Le Bellęgo et al.* [97]) which were carried out using Crack Mouth Opening Displacement (CMOD) control. In the tests by Le Bellęgo et al. (*Le Bellęgo et al.* [97]), no snap-back behaviour was observed

during beam deformations.

Two different concrete mixes were composed of ordinary Portland cement (CEM II/B–S 32.5R), water and: sand (mean aggregate diameter  $d_{50} = 0.5$  mm, maximum aggregate diameter  $d_{max} = 3.0$  mm) or gravel (mean aggregate diameter  $d_{50} = 2.0$  mm, maximum aggregate diameter  $d_{max} = 8.0$  mm) (Tab. 3.1 and Fig. 3.11). The beams were cut out from the same mix block. The uniaxial compression strength obtained on cubes  $10 \times 10 \times 10$  cm<sup>3</sup> was about  $f_c = 64$  MPa (sand concrete) and  $f_c = 52$  MPa (gravel concrete). In experiments, the digital camera Canon EOS–1Ds Mark II (Fig. 3.12a) with a powerful 16.7 megapixels CMOS sensor was applied. It was mounted on a tripod with its axis perpendicular to the photographed specimen surface. The concrete beams were initially carefully polished. Then a speckle pattern (serving as a tracer) was put on this surface using to colour sprays: black and yellow (Fig. 3.12b). During the experiments, the width of a localized zone was also measured with an induction displacement gauge placed under the notch (Fig. 3.12b).

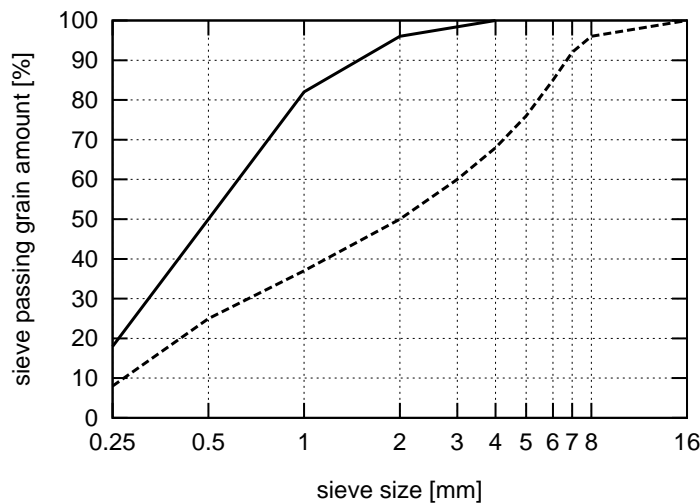


Figure 3.11. Grading curve of sand and gravel used for concrete mixes

(a)



(b)



Figure 3.12. Measurement instrumentation: (a) digital camera Canon EOS–1Ds Mark II in front of a small size beam, (b) induction displacement gauge at the beam covered with the black–yellow pattern inside the image area of interest

Since the assumed photographed region did not cover the entire beam height (Fig. 3.12b), the length of a localized zone could not be determined. The digital photos were shot every 30s. Totally, 44 tests were carried out (24 with sand concrete specimens and 20 with gravel concrete specimens).

### 3.3. Experimental results

The typical evolutions of the nominal tensile strength  $\sigma_N = 1.5Pl/(bD^2)$  versus the normalised deflection  $u/D$  ( $P$  – vertical force,  $u$  – beam deflection,  $D$  – beam height,  $b$  – beam width,  $l = 3D$  – beam span) for sand and gravel concrete beams during three–point bending are shown in Fig. 3.13.

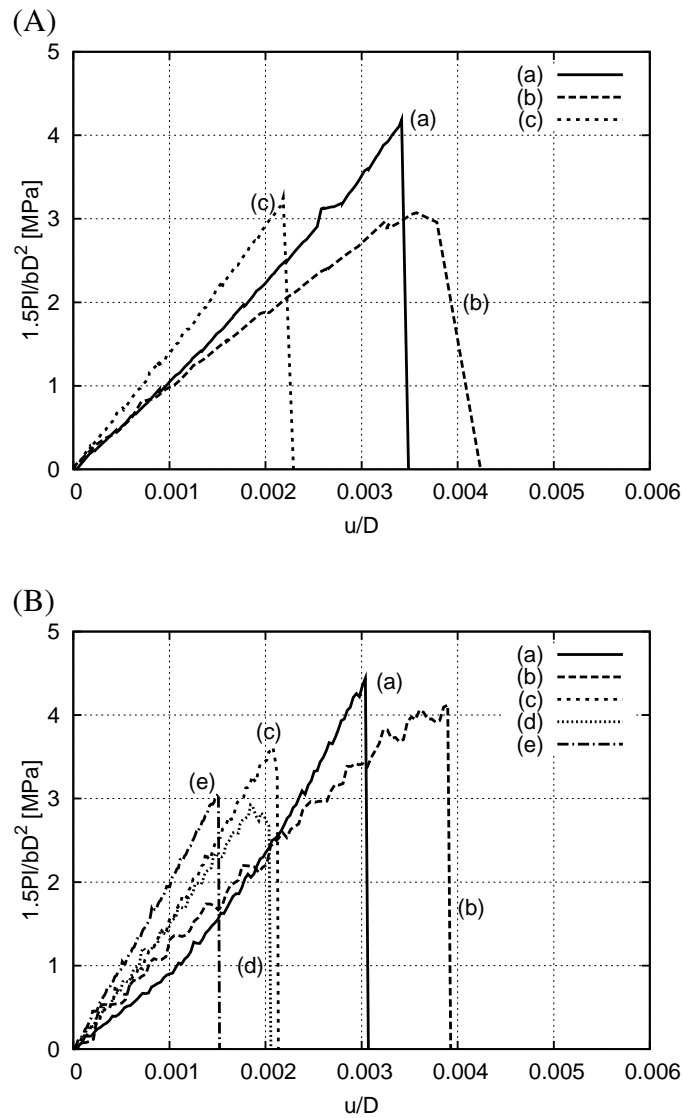


Figure 3.13. Nominal strength  $1.5Pl/bD^2$  versus normalised beam deflection  $u/D$  (where  $u$  – beam deflection,  $b$  – beam width,  $D$  – beam height,  $l$  – beam span,  $P$  – vertical force) from experiments: (A) with gravel concrete: (a) small–size beam  $80 \times 320 \text{ mm}^2$ , (b) small–size long beam  $80 \times 640 \text{ mm}^2$ , (c) medium–size beam  $160 \times 640 \text{ mm}^2$  and (B) with sand concrete: (a) small–size beam  $80 \times 320 \text{ mm}^2$ , (b) small–size long beam  $80 \times 640 \text{ mm}^2$ , (c) medium–size beam  $160 \times 640 \text{ mm}^2$ , (d) medium–size long beam  $160 \times 1280 \text{ mm}^2$ , (e) long–size beam  $320 \times 1280 \text{ mm}^2$

For beams of a similar geometry (beams '1', '2' and '3'), the nominal strength increases with decreasing specimen height indicating a pronounced deterministic size effect (caused by a different ratio between a characteristic length of micro-structure and beam height) similarly as in experiments by Le Bellégo et al. (*Le Bellégo et al.* [97]). In the case of beams with the same cross-section but with a different length ('4' and '5'), the nominal strength is smaller for a longer beam span indicating a statistical size effect (the longer the beam, the higher the probability of encountering in it a material element of a given low strength; *Bažant and Planas* [16], *Koide et al.* [88], *Bažant et al.* [14]). The tensile strength of sand concrete beams is higher than of gravel concrete ones independently on the size (similarly as the compressive strength). The vertical normal strain corresponding to the maximum vertical force increases with decreasing specimen size. The response of beams after peak is purely brittle in spite of a very small vertical deformation rate prescribed in experiments.

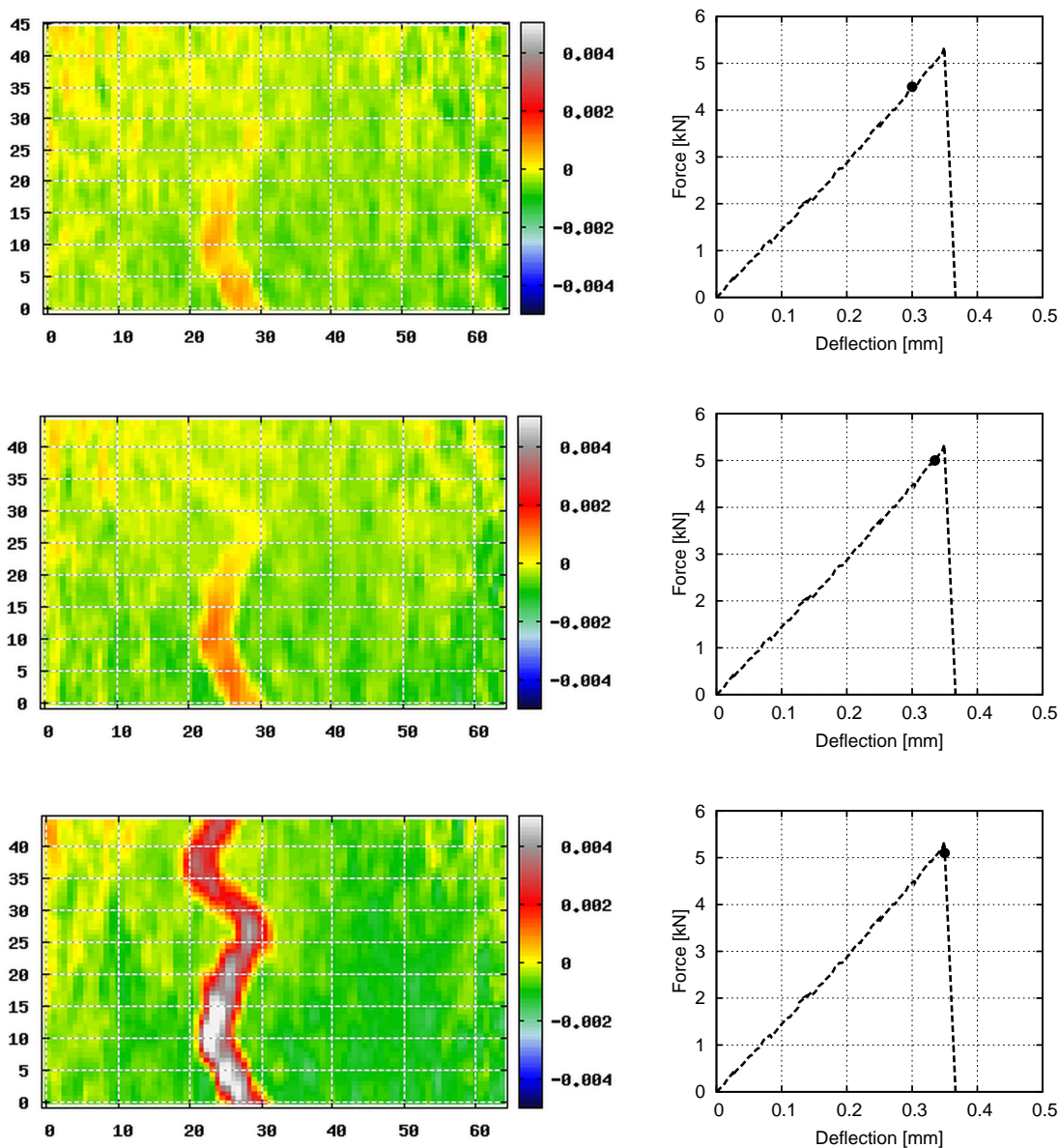


Figure 3.14. Evolution of a localized zone from DIC during experiments (vertical and horizontal axes denote coordinates in [mm], colour scales denote the strain intensity in [-]) and experimental load-deflection curves for gravel concrete medium size beam (points correspond to images)

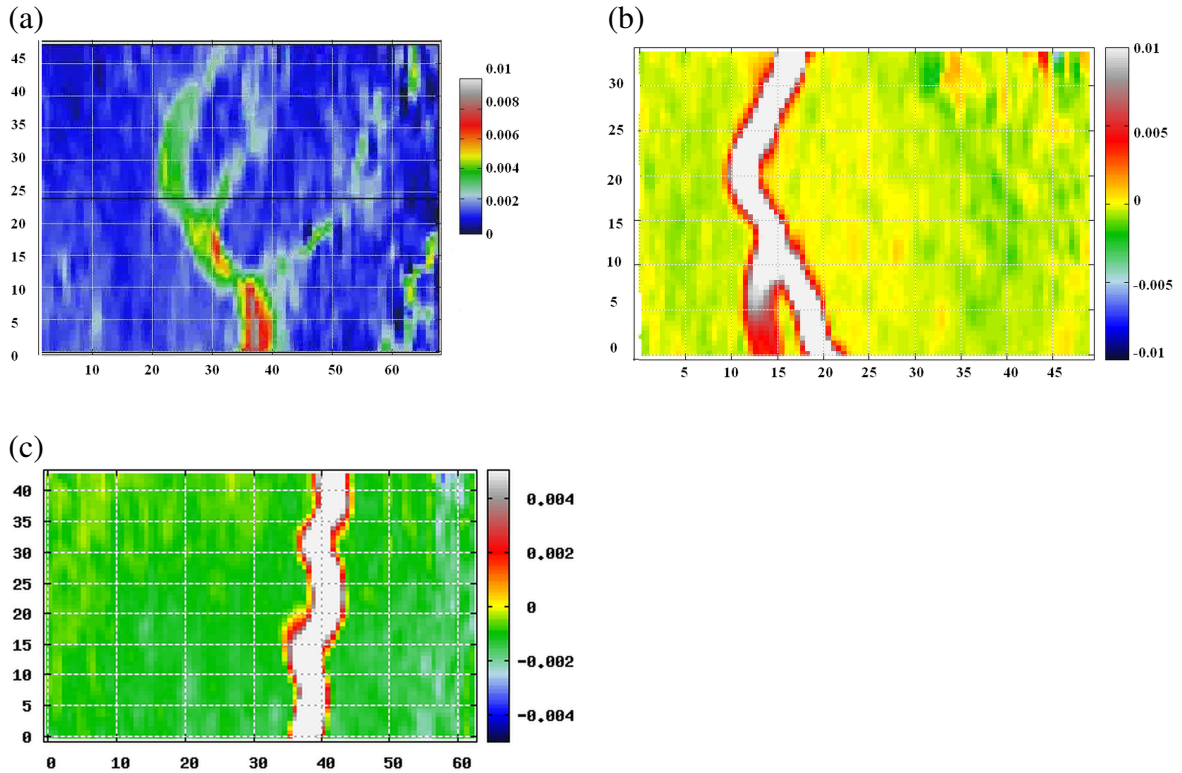


Figure 3.15. Formation of a localized zone from DIC in gravel concrete: (a) small-size beam  $80 \times 320 \text{ mm}^2$ , (b) small-size long beam  $80 \times 640 \text{ mm}^2$ , (c) medium-size beam  $160 \times 640 \text{ mm}^2$  (vertical and horizontal axes denote coordinates in [mm], colour scales denote the strain intensity [-])

Figure 3.14 presents the typical evolution of the horizontal normal strain on the surface of a concrete beam above the notch from DIC measurements. The localized zone occurs before the peak on the load–deflection diagram (Fig. 3.14). The zone can be almost straight or it can be significantly curved. In some cases, the localized zones can branch (Figs. 3.15a and 3.15b).

The localized zone above the notch occurs before the peak on the load–deflection diagram (Fig. 3.14). At peak, it is already well developed (Figs. 3.14 and 3.16). The width of a localized zone increases during deformation (Fig. 3.17) due to concrete dilatancy. The maximum width of a localized zone on the surface of concrete specimens is small and is equal to 3.5 mm–5.5 mm. It does not surprisingly depend upon the mix type and beam size. It means that the characteristic length of micro-structure may not always be related to the aggregate size. This outcome is in contrast to statements by Pijauder–Cabot and Bažant (*Pijauder–Cabot and Bažant* [136]), Bažant and Oh (*Bažant and Oh* [12]) where the width of a localized zone (also called fracture process zone (FPZ)) was estimated to be  $3 \times d_{max}$ . The experiments by Mihashi and Nomura (*Mihashi and Nomura* [118]) using the three-dimensional acoustic emission technique have also shown that the width of a localized zone in the case of normal concrete increases with the aggregate size. The width may be related e.g. to the aggregate spacing or cement particle size. It is also possible that the width of a localized zone (which was measured on the concrete surface in experiments) is significantly larger inside the concrete specimen. Further experimental investigations (under CMOD control) are necessary to correlate the characteristic length with micro-structural parameters of concrete.

The horizontal displacement measured with the induction gauge was used as a verification of the localized zone width obtained from DIC (Fig. 3.18). It was assumed that the measured displacement was equal to the strain integral over the width of a localized zone:

$$U_x = \int \boldsymbol{\varepsilon} dl \approx \sum \boldsymbol{\varepsilon} d, \quad (3.4)$$

where  $d$  is a distance between pixel subsets. Before the beam failure, a perfect fit occurred between two curves. After the failure, a small discrepancy could be noticed due to the fact that the displacement was not exactly measured at the same height where the width of the localized zone was determined with DIC.

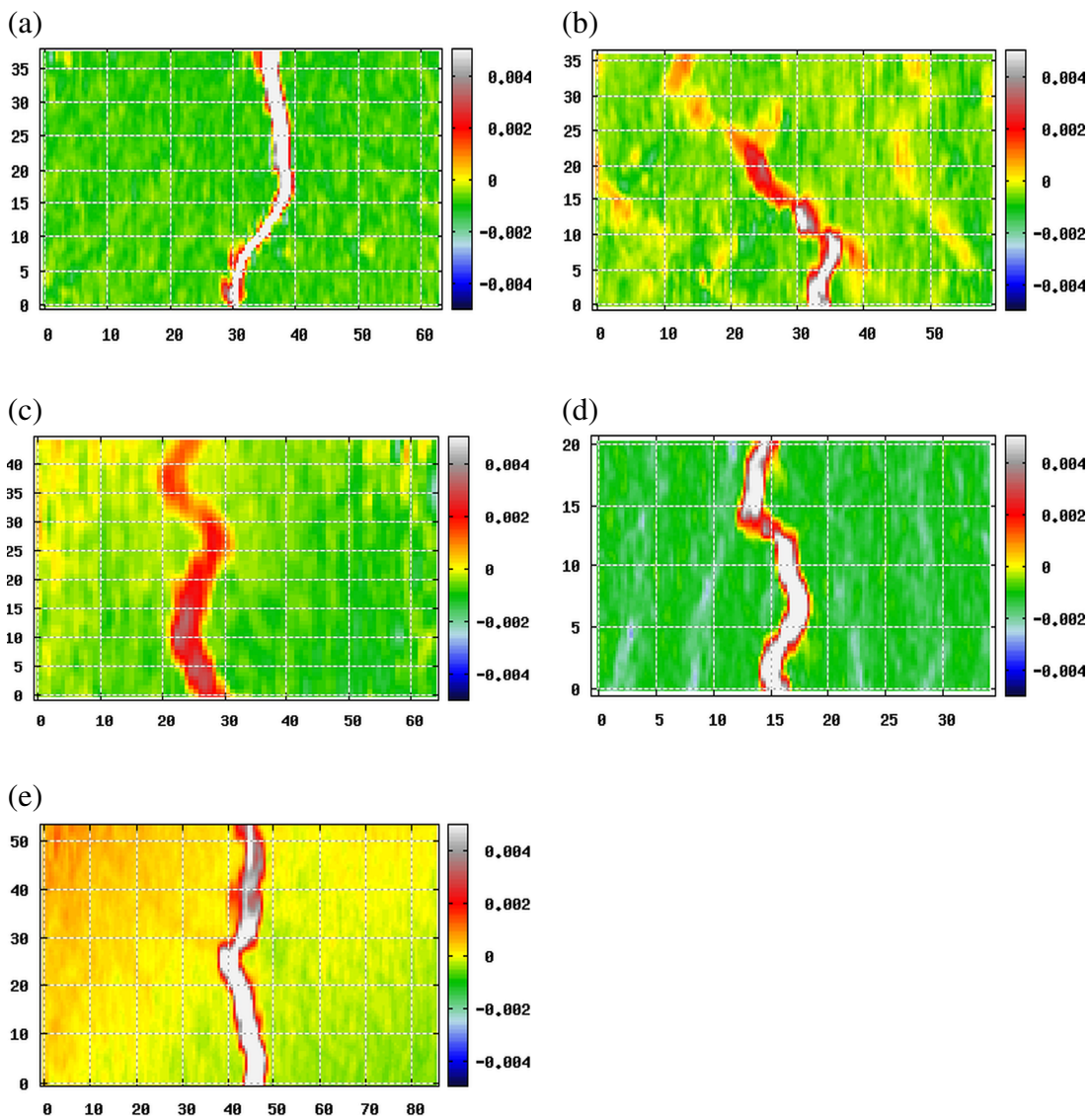


Figure 3.16. Formation of a localized zone from DIC in sand concrete: (a) small-size beam  $80 \times 320 \text{ mm}^2$ , (b) small-size long beam  $80 \times 640 \text{ mm}^2$ , (c) medium-size beam  $160 \times 640 \text{ mm}^2$ , (d) medium-size long beam  $160 \times 1280 \text{ mm}^2$ , (e) long-size beam  $320 \times 1280 \text{ mm}^2$  (vertical and horizontal axes denote coordinates in [mm], colour scales denote the strain intensity [-])

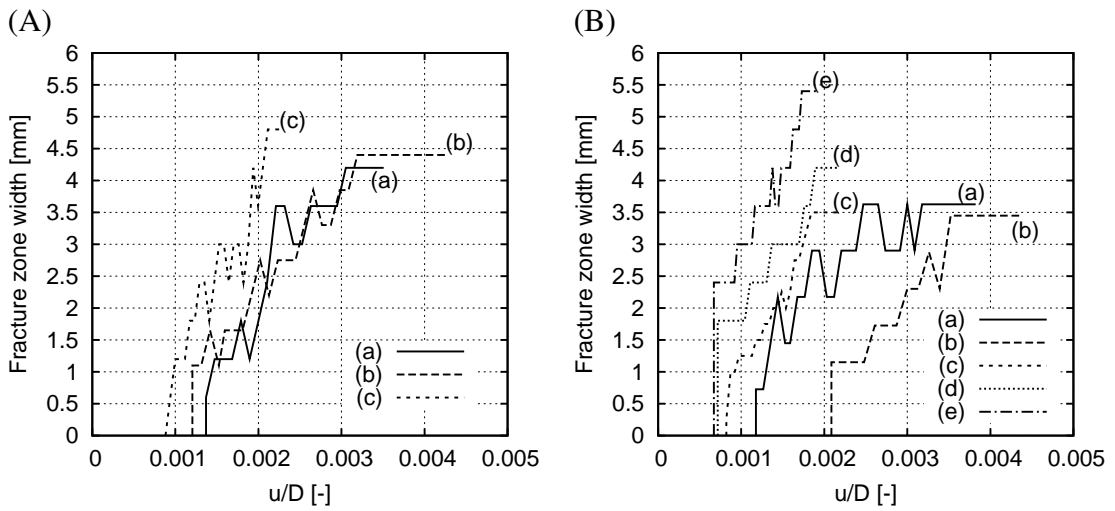


Figure 3.17. Evolution of the width of a localized zone from DIC versus normalised beam deflection  $u/D$  ( $u$  – beam deflection,  $D$  – beam height): (A) gravel concrete: (a) small-size beam  $80 \times 320 \text{ mm}^2$ , (b) small-size long beam  $80 \times 640 \text{ mm}^2$ , (c) medium-size beam  $160 \times 640 \text{ mm}^2$  and (B) with sand concrete: (a) small-size beam  $80 \times 320 \text{ mm}^2$ , (b) small-size long beam  $80 \times 640 \text{ mm}^2$ , (c) medium-size beam  $160 \times 640 \text{ mm}^2$ , (d) medium-size long beam  $160 \times 1280 \text{ mm}^2$ , (e) long-size beam  $320 \times 1280 \text{ mm}^2$

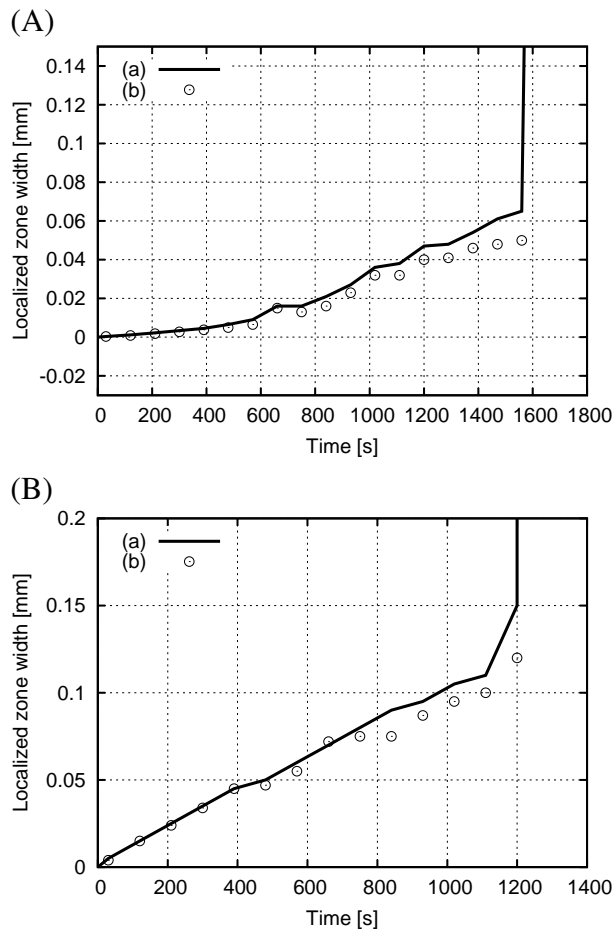


Figure 3.18. Measurements of the width of a localized zone by: (a) an induction displacement gauge and (b) DIC technique (A) large-size gravel beam, (B) small-size sand beam

Figure 3.19 shows a measured size effect for beams of a similar geometry (beams '1', '2' and '3'). In addition, the results following the deterministic size effect law by Bažant (Bažant [7]) (being valid for structures of a similar geometry with pre-existing notches or large cracks) are enclosed where the nominal strength was calculated as:

$$\sigma_N = \frac{Bf_t}{\sqrt{1 + (D/D_0)}}, \quad (3.5)$$

where  $f_t$  – the tensile strength,  $B$  – the dimensionless geometry dependent parameter which depends on the geometry of the structure and of the crack,  $D$  – the specimen size (beam height in this case) and  $D_0$  – the size dependent parameter called transitional size. To find the parameters  $B$  and  $D_0$  a non-linear least-squares Marquardt–Levenberg algorithm was used. The measured data with concrete beams of a similar geometry match well the size effect law of Eq. 3.5. In turn, the nominal strength of long beams ('4' and '5') was significantly below the size effect curve.

The summary of vertical failure forces from own laboratory experiments and corresponding laboratory tests by Le Bellégo et al. (Le Bellégo et al. [97]) is attached in Tab. 4.3.

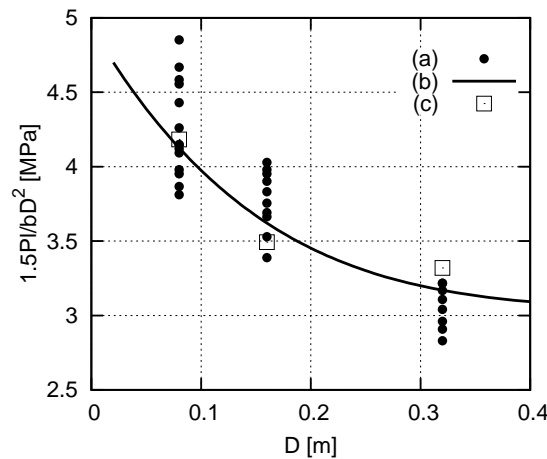


Figure 3.19. Calculated and measured size effect in nominal strength  $1.5Pl/(bD^2)$  versus beam height  $D$  for concrete beams of similar geometry (beams '1', '2' and '3': (a) own laboratory experiments, (b) size effect law by Bažant (Bažant [7]), Eq. 3.5, (c) experiments by Le Bellégo et al. (Le Bellégo et al. [97])

### 3.4. Conclusions

The Digital Image Correlation technique is a very effective optical technique to determine the displacement field on the surface of concrete with a high accuracy and without any physical contact with the surface.

The width of the localized zone on the concrete surface of notched beams does not depend on the beam dimensions and concrete mix. Its maximum size (on the concrete surface) lies between 3.5 mm and 5.5 mm (on the basis of experimental results obtained using DIC technique). It means that the characteristic length of micro-structure may not always be related to the aggregate size. It can be supposed that  $l_c$  may be more related to the aggregate spacing or cement particle size than to the aggregate size.

The nominal strength of notched concrete beams during three–point bending increases with decreasing beam height and beam span.

Table 3.2. Data summary of own laboratory experiments and corresponding laboratory tests by *Le Bellęgo et al.* [97]

No.	Force small beam ( $D = 0.08$ m) [kN]	Force medium beam ( $D = 0.16$ m) [kN]	Force large beam ( $D = 0.32$ m) [kN]	Force small long beam ( $D = 0.08$ m) [kN]	Force medium long beam ( $D = 0.16$ m) [kN]
Experiments for sand concrete beams by Le Bellęgo et al. ( <i>Le Bellęgo et al.</i> [97])					
1	2.96	4.97	9.44	-	-
Own experiments with gravel (g) and sand (s) concrete beams					
1	2.81 (g)	5.21 (g)	8.42 (g)	1.12 (g)	1.74 (g)
2	2.83 (g)	4.62 (g)	8.27 (g)	1.41 (g)	1.95 (s)
3	2.95 (g)	5.07 (g)	8.84 (g)	1.20 (g)	1.82 (s)
4	2.75 (g)	5.45 (g)	8.05 (g)	1.25 (s)	-
5	2.71 (g)	5.25 (g)	9.15 (s)	1.08 (s)	-
6	2.93 (g)	5.55 (s)	8.65 (s)	1.15 (s)	-
7	2.87 (g)	5.34 (s)	9.01 (s)	1.18 (s)	-
8	2.91 (s)	5.62 (s)	9.15 (s)	1.51 (s)	-
9	3.26 (s)	5.66 (s)	-	-	-
10	3.03 (s)	5.73 (s)	-	-	-
11	3.24 (s)	-	-	-	-
12	3.45 (s)	-	-	-	-
13	3.15 (s)	-	-	-	-
14	3.32 (s)	-	-	-	-
15	2.95 (s)	-	-	-	-



## Chapter 4

# Macroscopic modelling of strain localization in concrete and reinforced concrete

This chapter presents macroscopic numerical FE results of strain localization on notched concrete beams subjected to quasi-static three-point bending and unnotched short reinforced concrete beams without shear reinforcement under mixed shear-tension failure. Three different constitutive continuum models for concrete (Chapter 2) were used (isotropic elasto-plastic model with a Rankine criterion in tension, isotropic damage and anisotropic smeared-crack one). All models were enhanced in a softening regime by a characteristic length of micro-structure by means of a non-local theory. To simulate the behaviour of reinforcement in reinforced concrete beams, an associated elasto-perfect plastic constitutive law by von Mises was assumed. A bond-slip (*den Uijl and Bigaj* [46], *Dörr* [51], *Haskett et al.* [70]) between concrete and reinforcement was also considered. The numerical results for concrete beams were compared with the corresponding laboratory tests performed by Le Bellégo (*Le Bellégo et al.* [97]) and for reinforced concrete beams with corresponding laboratory tests by Walraven and Lehwalter (*Walraven and Lehwalter* [168]). In addition, the numerical results were confronted with the and deterministic size effect law by Bažant (*Bažant* [7]).

### 4.1. Concrete beams

Laboratory tests on notched concrete beams described in Chapter 3 were simulated with two different continuum crack models for concrete: an elasto-plastic and a damage one with non-local softening. In the first case, a Rankine criterion was used with a yield function  $f$  with isotropic softening. A non-linear exponential tensile softening curve proposed by Hordijk (*Hordijk* [74]) (Eq. 2.31) was assumed (with:  $c_1 = 3.0$ ,  $c_2 = 6.93$  and  $\kappa_u = 0.005$ ). In the second case, an isotropic damage model was used. To define the equivalent strain measure, the Rankine failure type criterion was assumed (Eq. 2.42). To describe the evolution of the damage parameter, an exponential softening function was used by Eq. 2.37 with  $\kappa_0 = 7 \times 10^{-5}$ ,  $\alpha = 0.99$  and  $\beta = 600$ . The following elastic material parameters were assumed:  $E = 38500$  MPa and  $\nu = 0.2$ . A characteristic length of micro-structure was  $l_c = 2$  mm. The non-local averaging was performed in the current configuration. The non-local coefficient was chosen as  $m = 2$  on the basis of other calculations. The tensile strength  $f_t$  was taken from a Gaussian (normal) distribution around the mean value 3.6 MPa with a standard deviation 0.05 MPa and a cut-off  $\pm 0.1$  MPa. To obtain a Gaussian distribution of the concrete strength, a polar form of so-called Box-Muller transformation was used (*Box and Muller* [30]).

The two-dimensional calculations were performed with FE meshes composed of 6908 (small-size beam) up to 51632 (large-size beam) quadrilateral elements composed of four diagonally crossed triangles to avoid volumetric locking. The maximum finite element size in the neighbourhood of the notch was not greater than  $3 \times l_c$  to achieve mesh-objective results (*Marzec et al.* [110], *Bobiński and Tejchman* [23]).

Table 4.1. Maximum vertical failure forces obtained in laboratory tests and numerical FE calculations

Beam	Beam height $D$ [mm]	Beam length $L$ [mm]	Failure vertical force (experiments) [N]	Calculated vertical failure force (elasto-plasticity) [N]	Calculated vertical failure force (damage mechanics) [N]
Small	80	320	3017	2871	2915
Medium	160	640	5350	5115	5175
Large	320	1280	8692	8524	8602
Small long	80	640	1237	1161	1137
Medium long	160	1280	1837	1954	2101

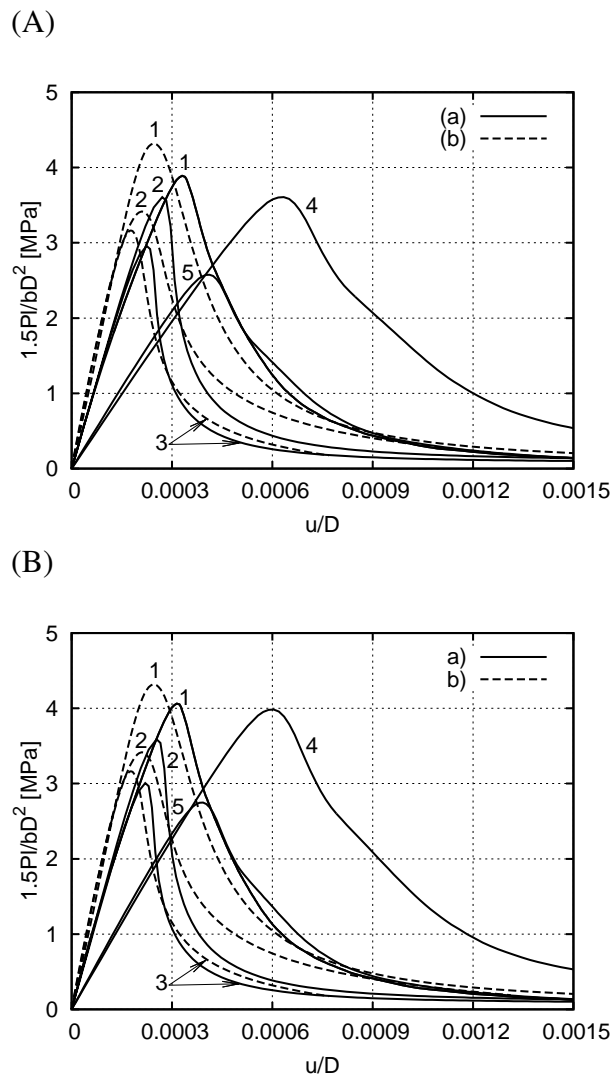


Figure 4.1. Calculated nominal strength  $1.5Pl/(bD^2)$  versus normalized beam deflection  $u/D$  ( $u$  – beam deflection,  $D$  – beam height): (sand concrete): (A) elasto-plasticity, (B) damage mechanics, (a) FE results, (b) experiments by Le Bellégo et al. (*Le Bellégo et al.* [97]): (1) small-size beam, (2) medium-size beam, (3) large-size beam, (4) small-size long beam, (5) medium-size long beam

The beam deformation was included by prescribing a vertical displacement at the mid-point of the beam top. For the solution of a non-linear equation of motion governing the response of a system of finite elements, the initial stiffness method was used with a symmetric elastic global stiffness matrix.

Figure 4.1 presents the numerical results of the nominal strength  $\sigma_N = 1.5Pl/(bD^2)$  for sand concrete beams compared to tests by Le Bellégo et al. (*Le Bellégo et al.* [97]). The results are in a satisfactory agreement with tests by Le Bellégo et al. (*Le Bellégo et al.* [97]) and with own experiments (Tab. 4.1). They are quantitatively similar with an elasto-plastic and a damage model. The deterministic size effect was realistically modelled in calculations. The calculated widths of the localized zone above the notch at  $u/D = 0.0005$  are: 6 mm and 7 mm (small-size beam), 7 mm and 7 mm (small-size long beam), 7 mm and 7 mm (medium-size beam), 6 mm and 7 mm (medium-size long beam) and 7 mm and 7 mm (large-size beam) within enhanced elasto-plasticity and damage mechanics, respectively (Fig. 4.2).

## 4.2. Reinforced concrete beams

Laboratory tests were carried out on five different short reinforced concrete beams without shear reinforcement and free at ends (*Walraven and Lehwalter* [168]). The geometry of the specimens is shown in Fig. 4.3. The beam length  $L$  varied between 680 mm and 2250 mm and the height  $h$  was between 200 mm and 1000 mm (the beams' width  $b$  was always 250 mm). The cylinder compressive strength of concrete was about 20 MPa. In turn, the cylinder splitting tensile strength of concrete was about 2 MPa. The maximum size of the aggregate in concrete was  $d_{max} = 16$  mm. The concrete cover measured from the bar centre to the concrete surface was 40 mm for the smallest beam and 70 mm for the largest one. In all tests, the span-to-depth ratio was  $a/d = 1$ . The reinforcement ratio of the specimens was 1.1%, so the failure by yielding of longitudinal steel bars was excluded in advance (yield strength of longitudinal reinforcement was 420 MPa). To obtain a geometrically similar cross-sectional area, various combinations of bar sizes were used (with diameters of 16, 18, 20 mm). The ratio between the width of the loading plate  $k$  and the effective depth  $d$  was kept constant ( $k/d = 0.25$ ), (Fig. 4.3). The beams were incrementally loaded by a vertical force applied at a mid-span of each beam. During loading, first, at about 40% of the failure load, bending cracks appeared. Afterwards, at about 45–50% of the failure load, the first inclined crack occurred. The beam failure took place in a gradual gentle way in shear compression by crushing concrete adjacent to the loading plate initiated by a formation of short parallel inclined cracks.

A pronounced size effect was observed, exemplified by the reduction of the nominal normalised shear strength  $v_u = V_u/(bdfc)$  with increasing effective cross sectional depth  $d$  in the range of the beam height  $h = 200 - 800$  mm:  $v_u = 0.23$  ( $h = 200$  mm),  $v_u = 0.15$  ( $h = 400$  mm),  $v_u = 0.13$  ( $h = 600$  mm),  $v_u = 0.10$  ( $h = 800 - 1000$  mm). The cracks developed significantly faster in the larger beams.

The geometry details of the reinforced concrete beams and shear failure forces  $V_u$  are given in Tab. 4.2.

To describe a deterministic size effect and pattern of cracks in short reinforced concrete beams without shear reinforcement subjected to mixed shear-tension failure, three different

enhanced continuum constitutive models for concrete (Chapter 2) were used: an isotropic elasto–plastic model with a Drucker–Prager criterion in compression and with a Rankine criterion in tension, an isotropic damage model and an anisotropic smeared crack model.

Table 4.2. Beams' properties and failure loads

beam	$h$	$d$	$L$	$L_t$	$A_{st}$	number of	$f_c$	$V_u$
specimen	[mm]	[mm]	[mm]	[mm]	[mm <sup>2</sup> ]	steel bars	[N/mm <sup>2</sup> ]	[kN]
V711	200	160	320	680	606	3 $\phi$ 16	18.1	165
V022	400	360	720	1030	1020	4 $\phi$ 18	19.9	270
V511	600	560	1120	1380	1570	5 $\phi$ 20	19.8	350
V411	800	740	1480	1780	2040	2 (4 $\phi$ 18)	19.4	365
V211	1000	930	2250	1860	2510	2 (4 $\phi$ 18)	20.0	505

To simulate the behaviour of reinforcement, an associated elasto–perfect plastic constitutive law by von Mises was assumed. A bond–slip between concrete and reinforcement was considered according to Dörr (*Dörr* [51]) (Eq. 2.68). The computations were a continuation of other numerical studies of deterministic size effect in slender reinforced concrete beams without shear reinforcement subjected to bending under tensile failure (*Marzec et al.* [110]) which were carried out within both isotropic elasto–plasticity and isotropic damage mechanics using non–local softening. A good agreement between experiments and FE analyses with respect to a deterministic size effect and geometry of localized zones was achieved.

The two-dimensional FE calculations were performed with 4 reinforced concrete beams of Section 2.3 ( $h = 200 - 800$  mm). The regular meshes with 2720 ( $h = 200$  mm) up to 16560 ( $h = 800$  mm) quadrilateral elements composed of four diagonally crossed triangles were used to avoid volumetric locking. The maximum finite element height, 15 mm, and finite element width, 10 mm, were not greater than  $3 \times l_c$  ( $l_c = 5 - 20$  mm) to achieve mesh–objective results (*Marzec et al.* [110]). Two comparative 3D calculations were performed for the beam of  $h = 200$  mm. The mesh with 16320 eight–noded solid elements was used. The maximum sizes of finite elements were again not greater than  $3 \times l_c$  ( $l_c = 10 - 20$  mm).

The following elastic material parameters were assumed for concrete:  $E = 28900$  MPa (modulus of elasticity) and  $\nu = 0.20$  (Poisson's ratio). The cylinder compressive strength was given as  $f_c = 20$  MPa. The tensile strength was  $f_t = 2$  MPa. The deformation was induced by prescribing a vertical displacement at the mid–point of the beam top.

To investigate the effect of the bond stiffness, several numerical tests were carried out with a different value of  $\delta_0$  changing from 0.06 mm (*Dörr* [51]) up to 1.5 mm (*Haskett et al.* [70]), Figs. 2.16a and 2.18.

## Enhanced elasto–plastic model

Preliminary FE calculations have shown a certain effect of a characteristic length of micro–structure, tensile fracture energy, compressive fracture energy, softening rate in tension and compression (linear and non–linear) and stiffness of end–slip on both the nominal beam strength, width and spacing of localized zones (Tabs. 4.4 and 4.5). The beam strength increased

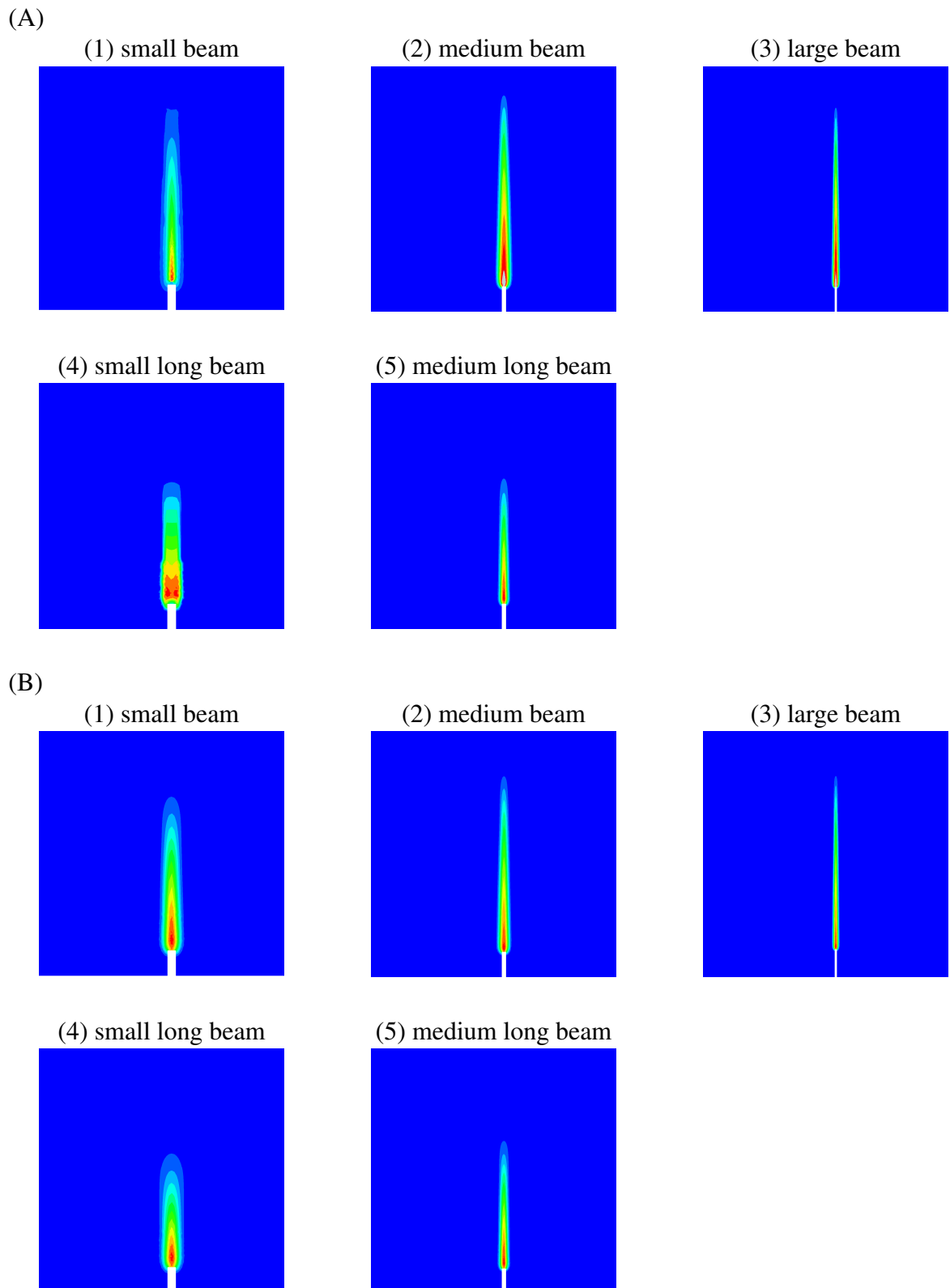


Figure 4.2. Distribution of the non-local: (A) softening parameter  $\bar{\kappa}$  (elasto-plasticity) and (B) strain measure  $\bar{\epsilon}$  (damage mechanics) above the notch from numerical calculations for: (1) small-size beam, (2) medium-size beam, (3) large-size beam, (4) small-size long beam, (5) medium-size long beam

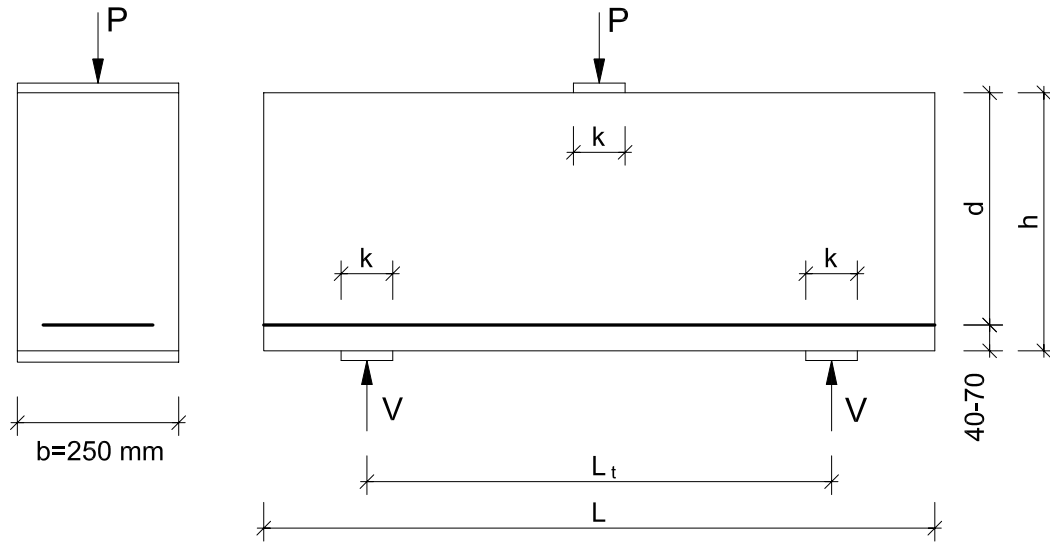


Figure 4.3. Geometry of reinforced concrete beams used in laboratory tests by Walraven and Lehwalter (Walraven and Lehwalter [168])

with increasing characteristic length, tensile fracture energy and compressive fracture energy. In turn, the spacing of localized zones increased with increasing characteristic length and softening rate, and decreasing tensile fracture energy, compressive fracture energy and bond stiffness. The calculated width of localized tensile and compressive zones increased with increasing characteristic length  $l_c$  and was equal approximately to  $(1.5 - 4) \times l_c$  with  $l_c = 5 - 20$  mm. The ultimate vertical force  $P$  was smaller for the 3D model by 5%.

On the basis of the preliminary calculations, the further analyses were performed with a 2D model, using a characteristic length of  $l_c = 5$  mm, a non-local parameter  $m = 2$ , and linear softening in tension and compression (Fig. 4.4). The tensile fracture energy was  $G_f = 50$  N/m and compressive fracture energy was  $G_c = 1500$  N/m. The tensile fracture energy was calculated as  $G_f = g_f \times w_f$ ;  $g_f$  – area under the entire softening function (with  $w_f \approx 4 \times l_c$  – width of tensile localized zones,  $l_c = 5$  mm). In turn, the compressive fracture energy was calculated as  $G_c = g_c \times w_c$ ; ( $g_c$  – area under the entire softening/hardening function up to  $\kappa_1 = 0.006$ ,  $w_c \approx 4 \times l_c$  – width of compressive localized zones,  $l_c = 5$  mm). The internal friction angle was  $\varphi = 14^\circ$  and the dilatancy angle was chosen as  $\psi = 8^\circ$ . The displacement  $\delta_0$  at which perfect slip occurred was 0.24 mm. The distribution of material parameters was uniform in all beams.

Figure 4.5 shows the calculated force–displacement curves ( $P$  – vertical force at the mid-point of the beam top,  $u$  – vertical displacement of this mid-point) for the beams of  $h = 200 - 800$  mm. The distribution of the non-local tensile softening parameter is depicted in Fig. 4.6 at the beam failure. In addition, the distribution of the non-local tensile softening parameter is shown at the normalised vertical force of  $V/(bdf_c) = 0.10$  as compared to the experimental crack pattern (Fig. 4.7).

The calculated failure forces are in a satisfactory agreement with the experimental ones (Tab. 4.2), but are always larger by 10–20% than the experimental ones (the differences increase with increasing beams' size). The geometry of localized zones is in satisfactory

agreement with experimental crack patterns (Fig. 4.7). The vertical and inclined long and short localized zones were numerically obtained. The experimental crack pattern was more non-symmetric. The widths of calculated tensile and compressive localized zones are about  $w_f = w_c = 4 \times l_c$ . In turn, the calculated average spacing  $s$  of main localized tensile zones is:  $s = 80$  mm ( $h = 200$  mm),  $s = 90$  mm ( $h = 400$  mm),  $s = 170$  mm ( $h = 600$  mm) and  $s = 150$  mm ( $h = 800$  mm).

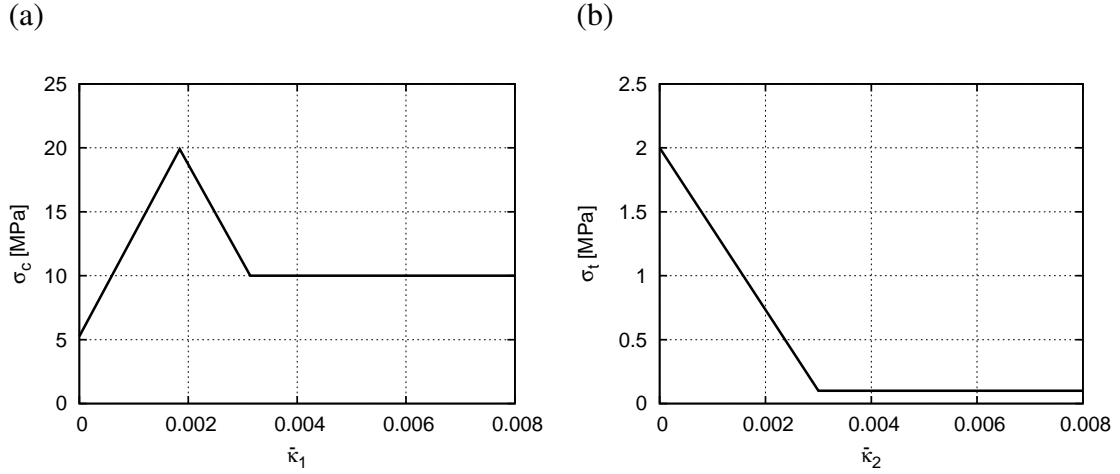


Figure 4.4. Assumed hardening/softening functions for FE-calculations: (a)  $\sigma_t = f(\kappa_2)$  in tension, (b)  $\sigma_c = f(\kappa_1)$  in compression ( $\sigma_t$  – tensile stress,  $\sigma_c$  – compressive stress,  $\kappa_i$  – hardening/softening parameter)

The calculated spacing of localized zones  $s$  was also compared with the average crack spacing according to by Lorrain et. al (Lorrain et. al [103]):

$$s = 1.5c + 0.1 \frac{\phi_s}{\rho} = 1.5 \times 32 + 0.1 \frac{16}{0.011} = 193 \text{ mm} \quad (h = 200 \text{ mm}), \quad (4.1)$$

$$s = 1.5c + 0.1 \frac{\phi_s}{\rho} = 1.5 \times 31 + 0.1 \frac{18}{0.011} = 210 \text{ mm} \quad (h = 400 \text{ mm}), \quad (4.2)$$

$$s = 1.5c + 0.1 \frac{\phi_s}{\rho} = 1.5 \times 30 + 0.1 \frac{20}{0.011} = 227 \text{ mm} \quad (h = 600 \text{ mm}), \quad (4.3)$$

$$s = 1.5c + 0.1 \frac{\phi_s}{\rho} = 1.5 \times 51 + 0.1 \frac{18}{0.011} = 240 \text{ mm} \quad (h = 800 \text{ mm}), \quad (4.4)$$

wherein  $\phi_s = 16 - 20$  mm is the mean bar diameter,  $\rho = 1.1\%$  denotes the reinforcement ratio and  $c = 30 - 51$  mm denotes the concrete cover. The calculated spacing of localized zones, 80 – 170 mm, is significantly smaller than these obtained with analytical formula by Eqs. 4.1 – 4.3 (193 – 240 mm).

### Enhanced smeared-crack and enhanced damage model

The following parameters were assumed in enhanced smeared crack and damage models:  $E = 28900$  MPa,  $\nu = 0.2$ ,  $\kappa_0 = 1E-4$ ,  $\alpha = 0.95$  and  $\beta = 500$  (damage approach Eq. 2.42),  $E = 28900$  MPa,  $\nu = 0.2$ ,  $\kappa_0 = 1E-4$ ,  $\alpha = 0.95$ ,  $\beta = 500$  and  $k = 10$  (damage approach Eq. 2.41),  $E = 28900$  MPa,  $\nu = 0.2$ ,  $\kappa_0 = 1E-4$ ,  $\alpha = 0.95$ ,  $\beta = 500$ ,  $\alpha_1 = 0.1$ ,  $\alpha_2 = 1.16$ ,  $\alpha_3 = 2.0$  and  $\gamma = 0.2$  (damage approach Eq. 2.44) and  $E = 28900$  MPa,  $\nu = 0.2$ ,  $p = 4.0$ ,

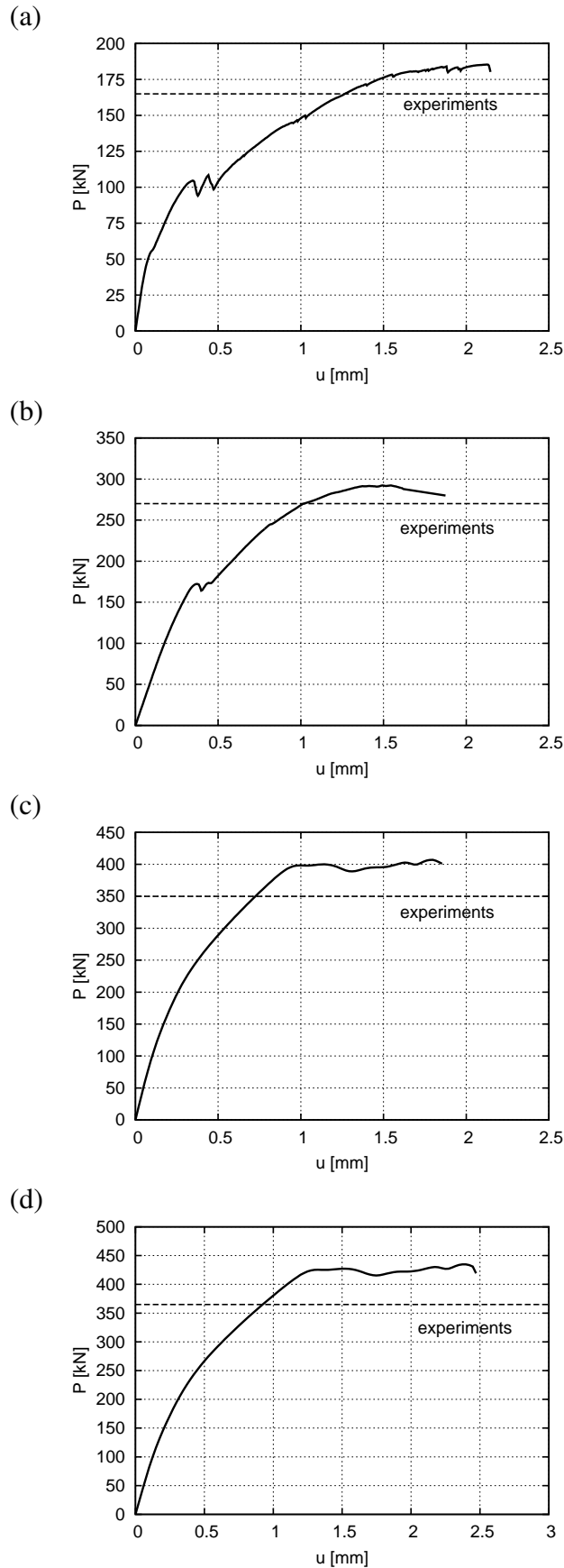


Figure 4.5. Calculated force–displacement curves within elasto–plasticity (as compared to the experimental maximum vertical force) for different beams: (A)  $h = 200$  mm, (B)  $h = 400$  mm, (C)  $h = 600$  mm, (D)  $h = 800$  mm ( $P$  – resultant vertical force,  $u$  – vertical displacement)

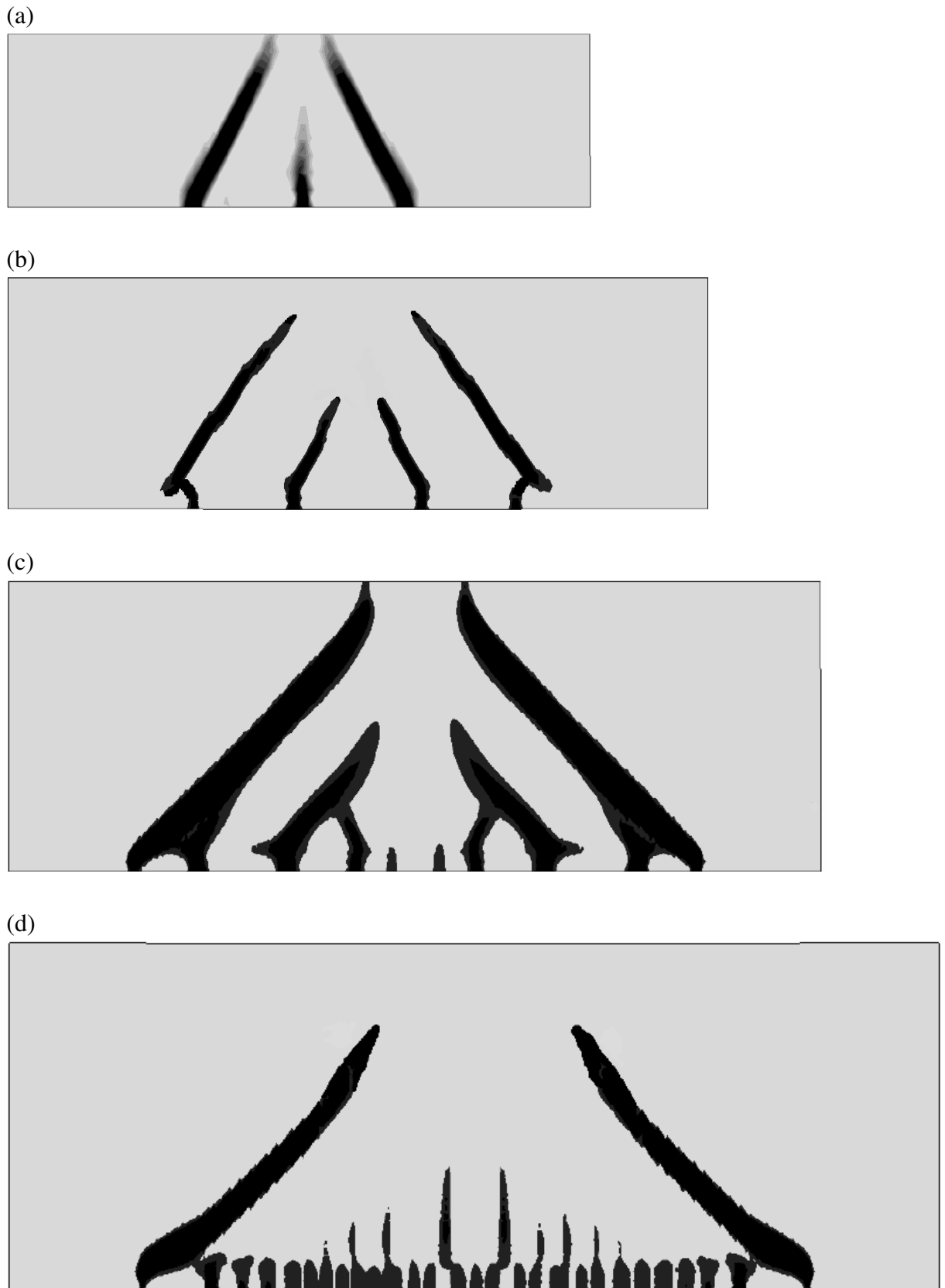


Figure 4.6. Distribution of calculated non-local tensile softening parameter within elasto-plasticity in beams at failure for different beams: (a)  $h=200$  mm, (b)  $h=400$  mm, (c)  $h=600$  mm, (d)  $h=800$  mm (note that the beams are not proportionally scaled)

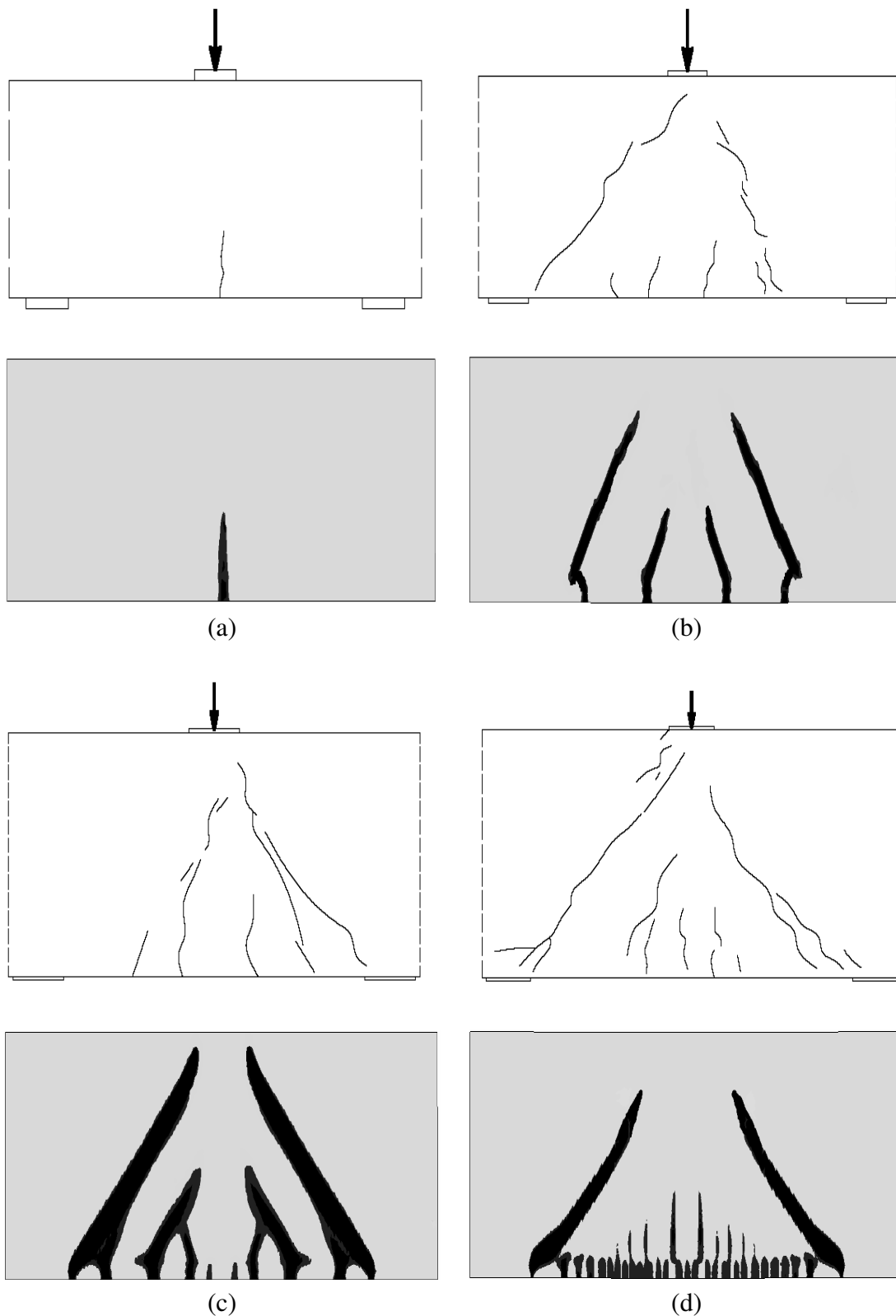


Figure 4.7. Comparison of distribution of the non-local tensile softening parameter within elasto-plasticity in short reinforced concrete beams at the normalised vertical force  $V/(bdfc) = 0.10$  with experimental crack patterns for different beams: (a)  $h = 200$  mm, (b)  $h = 400$  mm, (c)  $h = 600$  mm, (d)  $h = 800$  mm (note that the beams are not proportionally scaled)

$b_1 = 3.0$ ,  $b_2 = 6.93$ ,  $f_t = 2.0$  MPa,  $\epsilon_{su} = 0.006$  and  $\epsilon_{nu} = 0.006$  (smeared crack approach). The results are shown in Figs. 4.8 and 4.9 (smeared rotating crack model) and Figs. 4.10 and 4.11 (damage model). The results using fixed cracks and a rotation crack were similar.

The force–displacement curves are very similar as those obtained with an elasto–plastic model. The calculated forces at failure are always larger by 5 – 20% than the experimental ones. The calculated geometry of localized zones within a smeared crack approach is similar as this within elasto–plasticity except of beams with  $h > 400$  mm where the localized zones are more diffuse. The effect of crack type assumed in the model (fixed or rotating cracks) was insignificant. In turn, large discrepancies occur in the distribution of localized zones when using the damage model. The inclined localized zones were not obtained in FE analyses (only one vertical).

To obtain a better match with experiments more refined continuum models should be used at macro–level. A more advanced concrete model in compression can be implemented in elasto–plasticity (e.g. model by *Menetrey and Willam* [113]). In addition, the evolution of internal friction and dilatancy against plastic deformation can be taken into account. In the case of damage mechanics, anisotropy can be considered. Within a smeared crack approach, plastic crack strain can be added (*de Borst and Nauta* [42]). Other alternative to improve the FE results is to apply simple macro–continuum models to reinforced concrete elements considered at meso–scale (*Gitman et al.* [67], *Skarżyński and Tejchman* [151]).

### Deterministic size effect

Figure 4.12 shows a comparison between the calculated (Section 4.1) and experimental size effect (Chapter 3) for concrete beams subjected to three–point bending. The nominal strength  $1.5Pl/(bD^2)$  at failure as a function of the beam height  $D$  is analysed. In addition, the size effect law by Bažant (*Bažant and Planas* [16]) is enclosed.

The measured data of concrete beams of a similar geometry match well the size effect law by Bažant (*Bažant and Planas* [16]).

In turn, Figure 4.13 shows a comparison between the calculated and experimental size effect: the relative shear stress  $V/(bdf_c)$  at failure as a function of effective beam depth  $d$  for reinforced concrete beams under mixed shear–tension failure. In addition, the size effect law by Bažant (*Bažant and Planas* [16]) is enclosed.

The experimental and theoretical beam strength shows a strong parabolic size dependence and well match the size effect law by Bažant.

### 4.3. Conclusions

The following conclusions can be drawn from FE analyses with concrete beams at macro–level under tensile failure:

- Two simple isotropic continuum models within elasto–plasticity and damage continuum enhanced by a characteristic length of micro–structure are able to capture the width of localized zones and a deterministic size effect in concrete beams subjected to three–point bending.

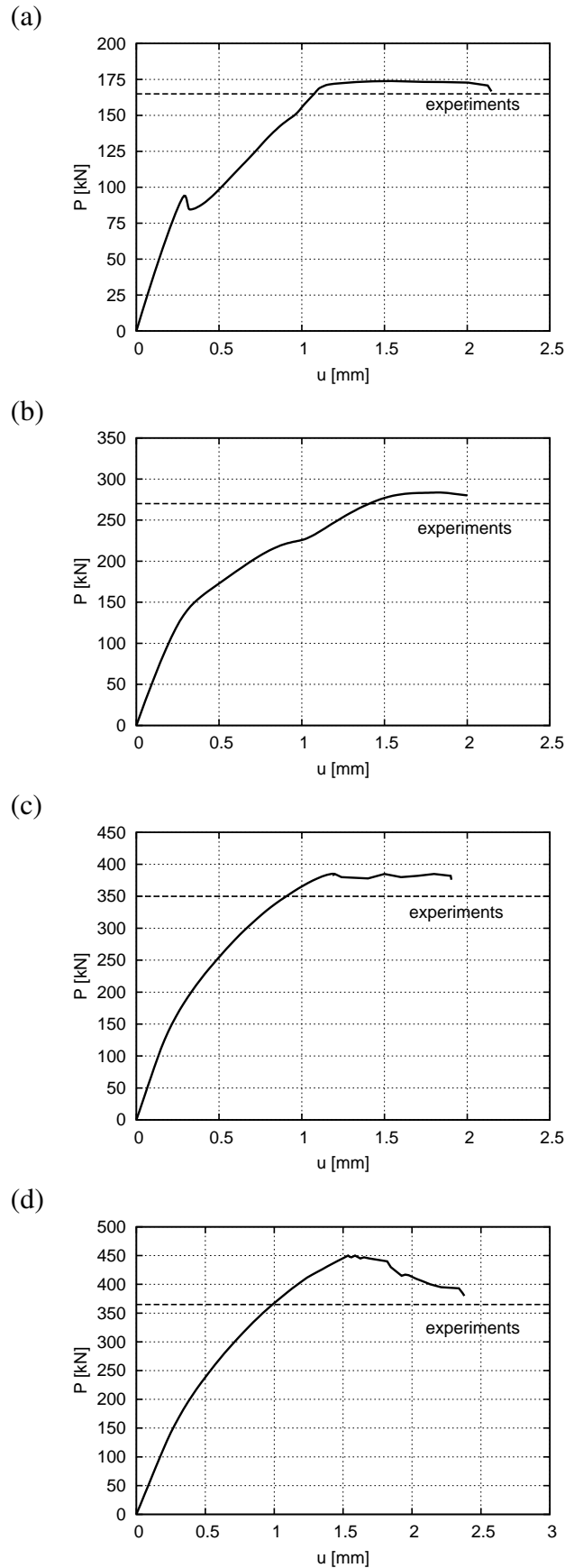


Figure 4.8. Calculated force–displacement curves with smeared crack approach (as compared to the experimental maximum vertical force) for different beams: (a)  $h = 200$  mm, (b)  $h = 400$  mm, (c)  $h = 600$  mm, (d)  $h = 800$  mm ( $P$  – resultant vertical force,  $u$  – vertical displacement)

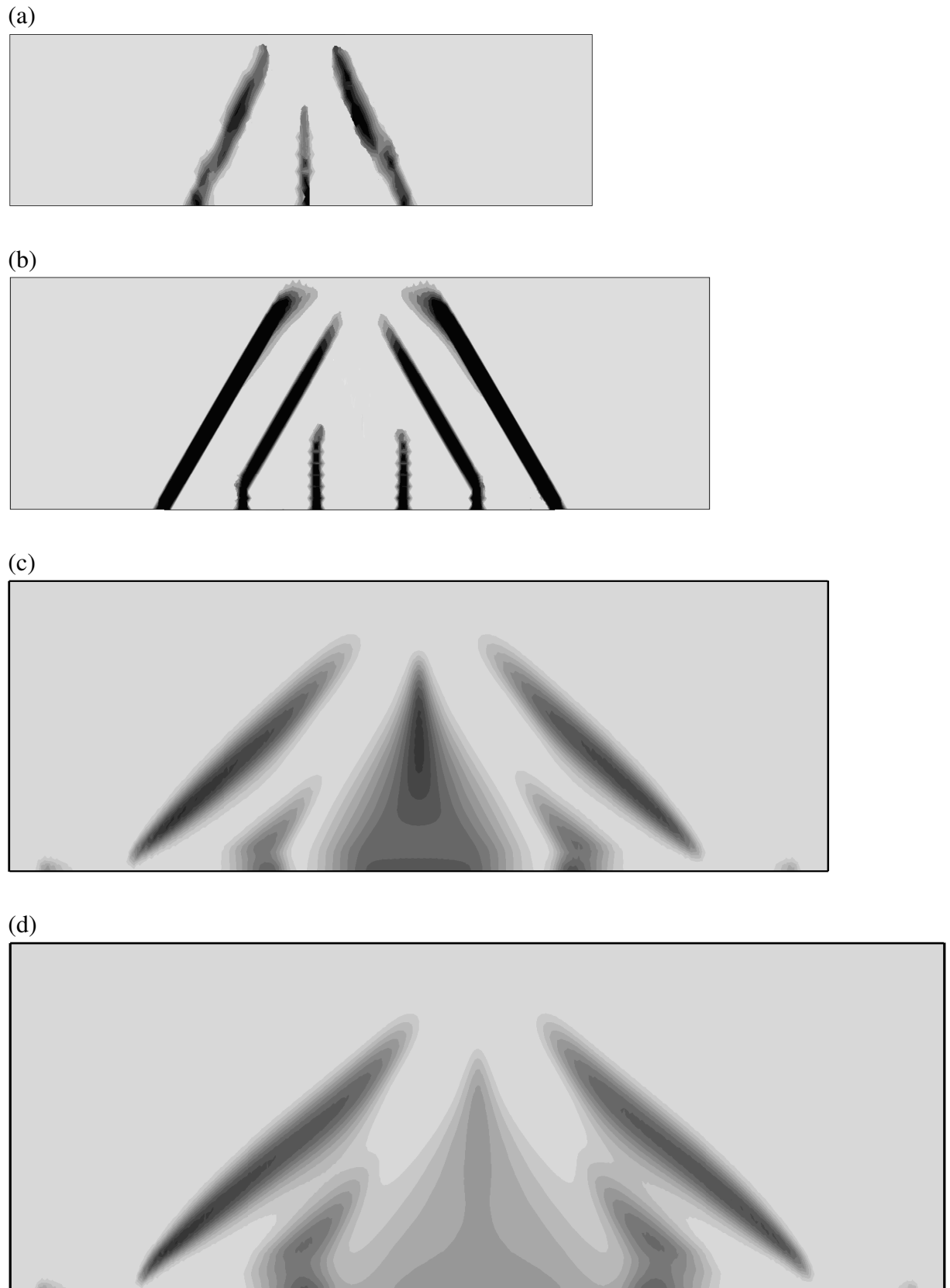


Figure 4.9. Distribution of calculated non-local strain measure with smeared crack approach in different beams at failure: (a)  $h = 200$  mm, (b)  $h = 400$  mm, (c)  $h = 600$  mm, (d)  $h = 800$  mm (note that the beams are not proportionally scaled)

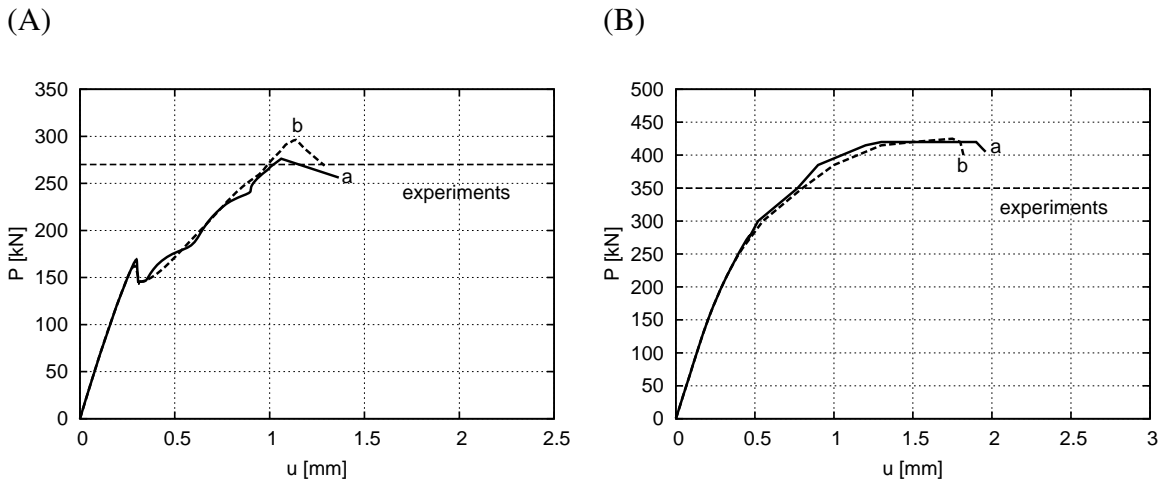


Figure 4.10. Calculated force–displacement curves within damage mechanics (as compared to the experimental maximum vertical force) for two beams: (A)  $h = 400$  mm, (B)  $h = 600$  mm ( $P$  – resultant vertical force,  $u$  – vertical displacement): (a) equivalent strain measure by Eq. 2.42, (b) equivalent strain measure by Eq. 2.44

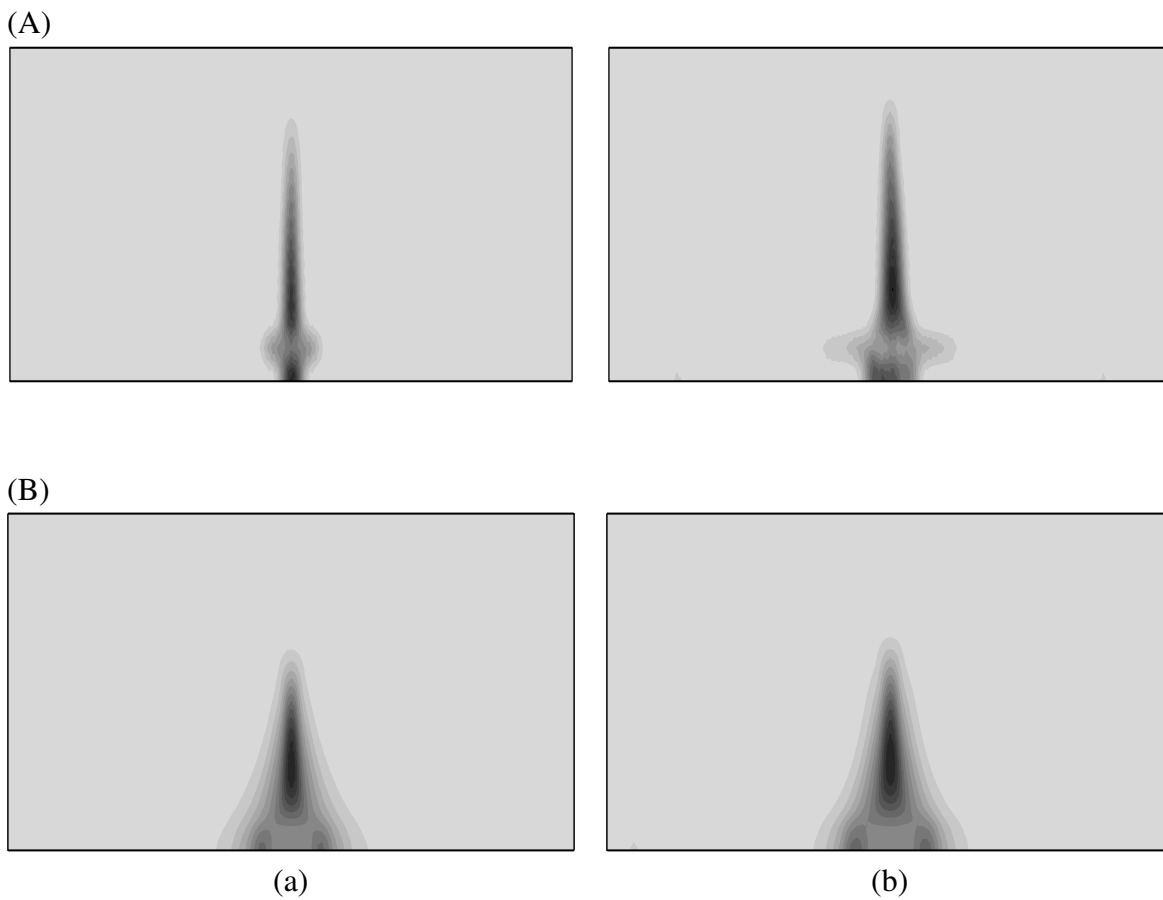


Figure 4.11. Distribution of the calculated non–local strain measure within damage mechanics in two beams at failure: (A)  $h = 400$  mm, (B)  $h = 600$  mm, (a) equivalent strain measure by Eq. 2.42, (b) equivalent strain measure by Eq. 2.44 (note that the beams are not proportionally scaled)

- The nominal strength of notched concrete beams during three–point bending increases with decreasing beam size.
- The calculated width of the localized zone is approximately equal to 6–7 mm (within elasto–plasticity) and 7 mm (within damage mechanics) with the characteristic length equal to 2 mm. It depends insignificantly on the beam size.
- The assumed characteristic length of micro–structure in continuum crack models has to be very small (i.e. 1–2 mm) to obtain a satisfactory agreement with experiments with respect to the width of a localized zone.

The following conclusions can be drawn: from FE analyses with reinforced concrete beams at macro–level under shear failure

- Three different simple continuum crack models enhanced by non–local softening are able to capture a deterministic size effect in short reinforced concrete beams without shear reinforcement.
- The calculated material strength was in a satisfactory agreement with experiments for 4 reinforced concrete beams of a different size using 3 different models. It was higher by 5–20% as compared to experimental ones.
- The geometry of localized zones was in a good agreement within elasto–plasticity, in a medium agreement within a smeared–crack approach and a completely false within isotropic damage mechanics.
- The calculated spacing of localized tensile zones increased with increasing characteristic length, softening rate and beam height and decreasing fracture energy and bond stiffness within elasto–plasticity. The tensile fracture energy was  $G_f = 50$  N/m and the compressive fracture energy was  $G_c = 1500$  N/m.
- The calculated and experimental spacing of localized zones was significantly smaller than this from analytical formulae.

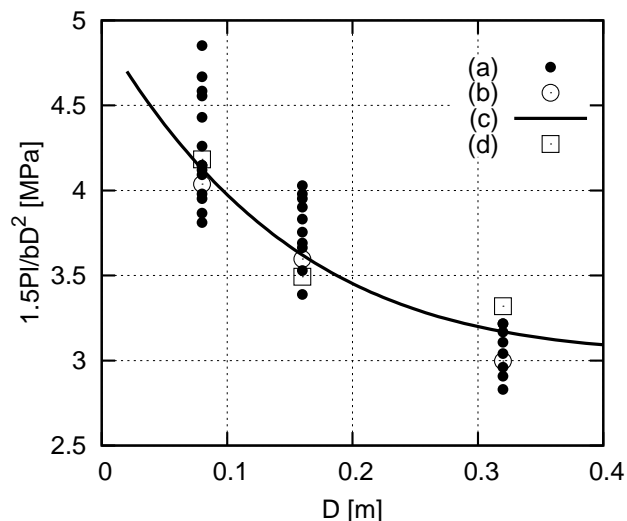


Figure 4.12. Calculated and measured size effect in nominal strength  $1.5Pl/(bD^2)$  versus beam height  $D$  for concrete beams of similar geometry (beams '1', '2' and '3': (a) own laboratory experiments, (b) own FE–calculations (elasto–plasticity), (c) size effect law by Bažant (Bažant [7]), Eq. 3.5, (d) experiments by Le Bellégo et al. (Le Bellégo et al. [97]))

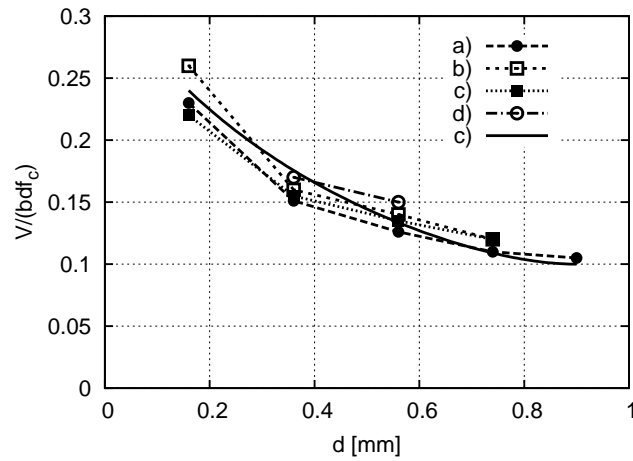


Figure 4.13. Calculated size effect in reinforced concrete beams from FE–analyses compared to experiments (*Walraven and Lehwalter* [168]) and to the size effect law by Bažant (*Bažant and Planas* [16]) ( $b$  – beam width,  $d$  – effective beam height,  $f_c$  – compressive strength of concrete,  $V_u$  – ultimate vertical force): (a) experiments, (b) FE–calculations (elasto–plasticity), (c) FE–calculations (smeared crack model), (d) FE–calculations (damage mechanics), (e) size effect law by Bažant

Table 4.3. Data summary of own laboratory experiments, FE–results and corresponding laboratory tests by *Le Bellęgo et al.* [97]

No.	Force small beam ( $D = 0.08$ m) [kN]	Force medium beam ( $D = 0.16$ m) [kN]	Force large beam ( $D = 0.32$ m) [kN]	Force small long beam ( $D = 0.08$ m) [kN]	Force medium long beam ( $D = 0.16$ m) [kN]
Experiments for sand concrete beams by <i>Le Bellęgo et al.</i> ( <i>Le Bellęgo et al.</i> [97])					
1	2.96	4.97	9.44	-	-
FE–results for sand concrete beams (elasto–plasticity)					
1	2.87	5.11	8.52	1.16	1.95
FE–results for sand concrete beams (damage mechanics)					
1	2.91	5.17	8.60	1.14	2.10
Own experiments with gravel (g) and sand (s) concrete beams					
1	2.81 (g)	5.21 (g)	8.42 (g)	1.12 (g)	1.74 (g)
2	2.83 (g)	4.62 (g)	8.27 (g)	1.41 (g)	1.95 (s)
3	2.95 (g)	5.07 (g)	8.84 (g)	1.20 (g)	1.82 (s)
4	2.75 (g)	5.45 (g)	8.05 (g)	1.25 (s)	-
5	2.71 (g)	5.25 (g)	9.15 (s)	1.08 (s)	-
6	2.93 (g)	5.55 (s)	8.65 (s)	1.15 (s)	-
7	2.87 (g)	5.34 (s)	9.01 (s)	1.18 (s)	-
8	2.91 (s)	5.62 (s)	9.15 (s)	1.51 (s)	-
9	3.26 (s)	5.66 (s)	-	-	-
10	3.03 (s)	5.73 (s)	-	-	-
11	3.24 (s)	-	-	-	-
12	3.45 (s)	-	-	-	-
13	3.15 (s)	-	-	-	-
14	3.32 (s)	-	-	-	-
15	2.95 (s)	-	-	-	-

Table 4.4. Summary of FE-input data

FE-simulation number	beam height $h$ [mm]	width of tensile localized zones $w_f$ [m]	tensile fracture energy $G_t$ [N/m]	width of compress. localized zones $w_c$ [m]	compressive fracture energy $G_c$ [N/m]	charact. length $l_c$ [mm]	bond model
1a		15	50	20	1500	5	
1b	200	15	50	20	1500	10	bs
1c		15	50	25	1750	20	
2a		15	100	20	1500	5	
2b	200	20	100	20	1500	10	bs
2c		40	100	25	1750	20	
3a		15	200	20	1500	5	
3b	200	35	200	25	1750	10	bs
3c		60	200	25	1750	20	
4a		15	50	15	1500	5	
4b	400	35	50	25	1750	10	bs
5a		20	100	15	1500	5	
5b	400	40	100	25	1750	5	bs
6a		15	50	15	1500	5	
6b	600	15	100	25	1750	5	bs
7a		15	50	15	1500	5	
7b	800	15	100	25	1750	5	bs
8a		15	50	20	1500	5	bs
8b		15	50	20	1500	5	bs ( $\delta_0 = 0.12$ mm)
8c	200	15	50	20	1500	5	bs ( $\delta_0 = 0.24$ mm)
8d		15	50	20	1500	5	bs ( $\delta_0 = 1.0$ mm)
9a		40	100	25	1750	10	bs
9b		40	100	25	1750	10	bs ( $\delta_0 = 0.12$ mm)
9c	400	40	100	25	1750	10	bs ( $\delta_0 = 0.24$ mm)
9d		40	100	25	1750	10	bs ( $\delta_0 = 1.0$ mm)
10a		15	50	20	1500	10	pb
10b	200	15	50	20	1500	10	bs
11a		40	100	25	1750	10	pb
11b	400	40	100	25	1750	10	bs
12a		15	50	15	900	5	
12b	200	15	50	20	1500	5	bs
12c		15	50	20	1800	5	
13a		15	50	20	900	10	
13b	400	35	50	25	1750	10	bs
13c		35	50	25	2250	10	
14a (3D)	200	35	50	25	1750	20	bs
14b (3D)	200	20	100	20	1400	10	bs
15 (3D)	200	35	50	25	1750	20	bs ( $\delta_0 = 1.0$ mm)

Table 4.5. Data summary of experiments, FE–results and analytical formulae (crack spacing)

FE-simulation number (Tab. 4.4)	beam height $h$ [mm]	failure vertical force (experiments) [kN]	failure vertical force (FEM) [kN]	spacing of localized zones from FEM $s$ [mm]	crack spacing by CEB–FIP model [34] [mm]	crack spacing by Lorrain et al. [103] [mm]
1a			182	105		
1b	200	165	185	105	270	193
1c			187	160		
2a			186	80		
2b	200	165	190	80	270	193
2c			193	160		
3a			190	105		
3b	200	165	192	105	270	193
3c			197	160		
4a			285	180		
4b	400	270	287	145	303	210
5a			291	60		
5b	400	270	295	90	303	210
6a			400	110		
6b	600	350	405	170	337	227
7a			425	85		
7b	800	365	435	150	303	240
8a			182	105		
8b			178	105		
8c	200	165	187	105	270	193
8d			175	105		
9a			295	145		
9b			296	145		
9c	400	270	297	145	270	193
9d			275	230		
10a			195	80		
10b	200	165	190	80	270	193
11a			305	145		
11b	400	270	295	180	303	210
12a			170	80		
12b	200	165	182	105	270	193
12c			185	80		
13a			275	360		
13b	400	270	295	145	303	210
13c			297	180		
14a			195	160		
14b	200	165	220	80	270	193
15	200	165	175	160	270	193



## Chapter 5

# Mesoscopic modelling of strain localization in concrete

This chapter deals with strain localization in concrete specimens subjected to uniaxial tension and investigations of localized zones in notched concrete beams subjected to quasi-static three-point bending. The material was described at the meso-scale as a random heterogeneous three-phase one. The simulations were carried out with the FEM using an isotropic damage constitutive model (with a Rankine failure type criterion and an exponential softening law) enhanced by a characteristic length of micro-structure  $l_c = 0.5$  mm by means of non-local theory (Eqs. 2.32, 2.37 and 2.42). The effect of a specimen size, random distribution of aggregate, aggregate density and shape, characteristic length on the width and shape of a localized zone and load displacement curves was investigated here. The existence of Representative Volume Element (RVE) was studied.

### 5.1. Determination of RVE with standard averaging approach

The intention of FE investigations is to determine the effect of a random distribution of aggregate, aggregate density, characteristic length and non-local range on both strain localization and stress-strain curves in concrete during uniaxial tension and to check the existence of the Representative Volume Element (RVE) (according to idea given by *Gitman et. al* [65]) using an enhanced damage for all individual phases (which naturally causes an overall material anisotropy) within a standard averaging approach (Skarżyński and Tejchman [151]).

The FE investigations were performed with concrete described as a three-phase material composed of cement matrix, aggregate and interfacial transition zones (ITZ) between the cement matrix and aggregate. The aggregate grains were assumed to be of a circular shape and were randomly distributed in a homogeneous cement matrix according to a sieve curve (Fig. 5.1). They were generated according to the method given by Eckardt and Konke (*Eckardt and Könke* [54]). First, a grading curve was chosen. Next, certain amounts of particles with defined diameters  $d_1, d_2, \dots, d_n$  were generated according to this curve. The size of aggregate inclusions varied from  $d_{min} = 2.5$  mm up to  $d_{max} = 5$  mm. The circles were randomly placed in the prescribed area starting with the largest ones and preserving a certain mutual distance (*van Mier et al.* [166]):

$$D > \frac{D_1 + D_2}{2}, \quad (5.1)$$

where  $D$  is the distance between two neighbouring particle centres and  $D_1, D_2$  are the diameters of two particles. In the next step, the generated particle structure was overlaid with an irregular mesh of 8000–12000 quadrilateral elements composed of four diagonally crossed triangles to avoid volumetric locking. The finite elements belonging to cement matrix, aggregate inclusions and bond zones, respectively, had their own properties (Tab. 5.1). It was

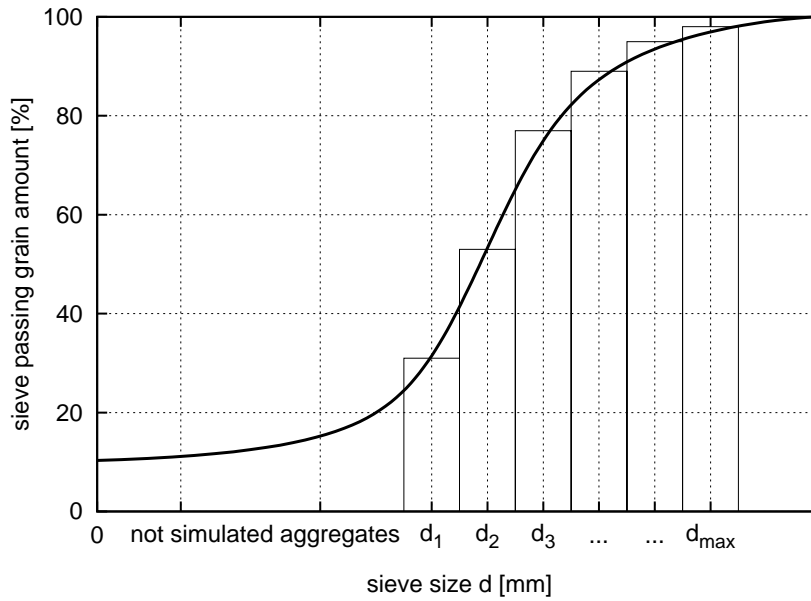


Figure 5.1. Approximation of the grading curve with discrete number of aggregate sizes

Table 5.1. Material properties assumed for FE calculations

Material properties	Inclusions	Matrix	ITZ
Young's modulus $E$ [MPa]	30000	25000	20000
Poisson's ratio $\nu$ [-]	0.2	0.2	0.2
Crack initiation strain $\kappa_0$ [-]	0.5	8E-5	5E-5
Residual stress level $\alpha$ [-]	0.95	0.95	0.95
Slope of softening $\beta$ [-]	200	200	200

assumed that the inclusions and bond zones had the highest and the lowest stiffness, respectively (Tab. 5.1). The elements in the cement matrix were taken twice as small as a characteristic length of micro-structure. In turn, the size of bond zone elements, 0.25 mm (equal to  $0.1 \times d_{min}$ ), was smaller than the size of cement matrix elements.

The calculations were carried out with periodic boundary conditions and material periodicity to avoid the effect of walls (*van der Sluis* [164], *Gitman* [65]). In the first case, the positions of nodes along corresponding specimen boundaries were the same before and after deformation. This is illustrated in Fig. 5.2, where an arbitrary periodically deformed unit cell under uniaxial extension conditions is shown. The deformation of each boundary pair is the same and the stresses are opposite in sign for each pair. The displacement boundary conditions are:

$$\begin{aligned}
 u_{12} - u_4 &= u_{11} - u_1 \\
 u_{22} - u_1 &= u_{21} - u_2, \\
 u_3 - u_2 &= u_2 - u_1
 \end{aligned}
 \tag{5.2}$$

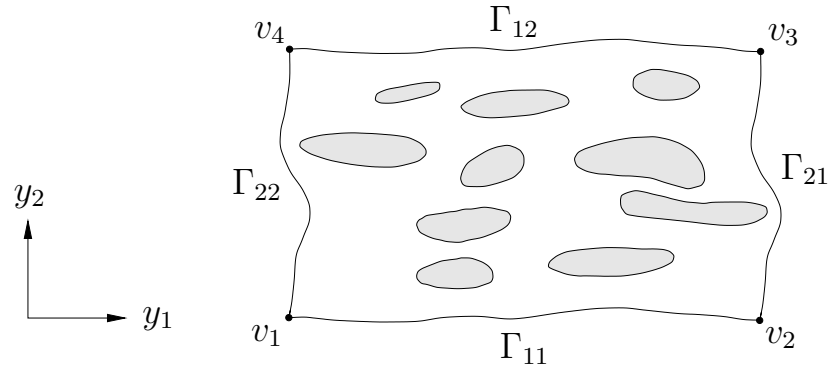


Figure 5.2. Periodically deformed unit cell with boundaries  $\Gamma_R$  and nodes  $v_i$  (van der Sluis [164])

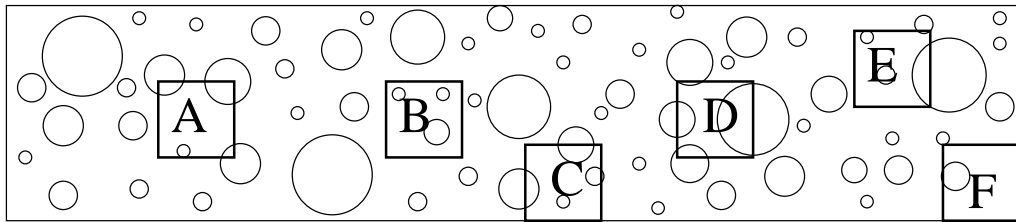


Figure 5.3. Distribution of different unit cells in a concrete specimen (Gitman [65])

where  $u_{ij}$  is the displacement for any material point along the boundary  $\Gamma_{ij}$  and  $u_i$  is the node displacement. From the periodicity equations (Eq. 5.2) can be observed that the independent entities are  $\Gamma_{11}$ ,  $\Gamma_{21}$ ,  $u_1$ ,  $u_2$  and  $u_4$  whereas the tied dependent entities are  $\Gamma_{22}$ ,  $\Gamma_{12}$  and  $u_3$ .

In addition, to eliminate wall effects, the periodicity of the material was assumed (Gitman [65]). According to its definition, the RVE should represent any part of the material. Figure 5.3 presents samples different unit cells A – F in a concrete specimen. The cells A, B, D and E are valid in the context of material periodicity. However, the cells C and F experience wall-effects since some edges are crossed by inclusions. In the calculations, we avoided inclusions penetrating through the unit cell boundaries by letting them re-appear at the opposite edge (Fig. 5.4).

To analyse the existence and size of the RVE, a two-dimensional uniaxial tension tests (Fig. 5.5) were performed with a quadratic concrete specimen representing a unit cells (Figs. 5.6–5.8) with periodicity of boundary conditions and material. For periodic boundary conditions, the displacements were suppressed in the node ‘ $v_1$ ’ (Figs. 5.2 and 5.5). Furthermore, in the node ‘ $v_2$ ’, a non-zero displacement was prescribed in a horizontal direction in while the displacement a vertical direction was suppressed. The displacement components of the node ‘ $v_3$ ’ and ‘ $v_4$ ’ were free and tied together.

First, concrete specimens of five different size were investigated (a characteristic length of micro-structure was  $l_c = 0.5$  mm). The smallest and the largest unit cells were  $10 \times 10$  mm<sup>2</sup> and  $25 \times 25$  mm<sup>2</sup>, respectively (Fig. 5.6). For each specimen, five different stochastic realisations were performed (Fig. 5.7) with an aggregate density  $\rho$  kept constant ( $\rho = 30\%$ ,  $\rho = 45\%$  and  $\rho = 60\%$ ) (Fig. 5.8). Next, the calculations were carried out with a different characteristic length of micro-structure varying between  $l_c = 0.1 - 2.0$  mm. Later, the effect of the aggregate density ( $\rho = 30\%$ ,  $\rho = 45\%$  and  $\rho = 60\%$ ) on strain localization was inves-

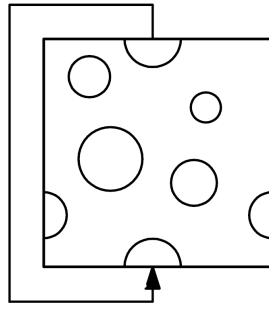


Figure 5.4. Simulation of material periodicity

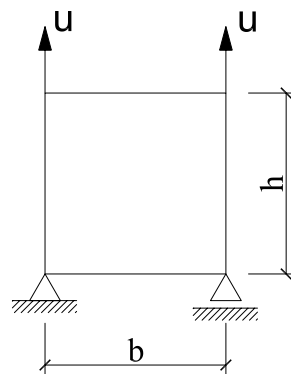
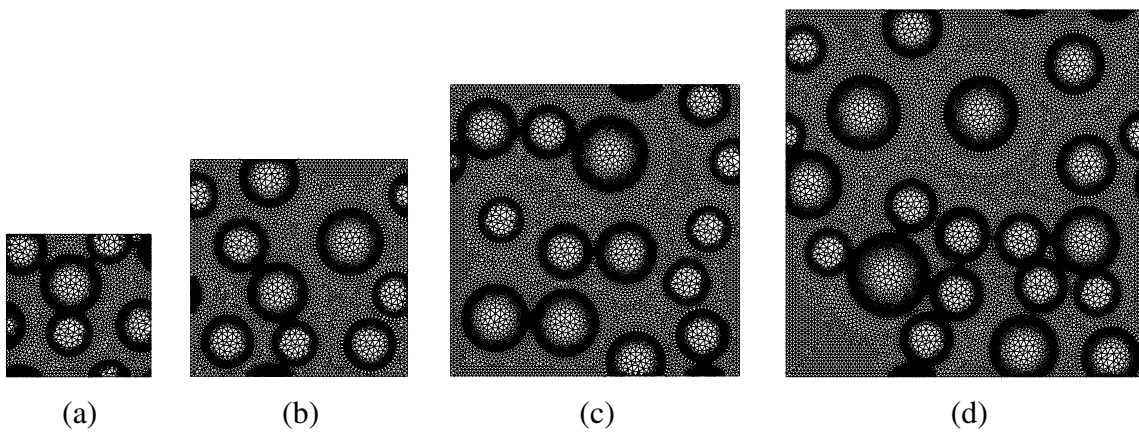
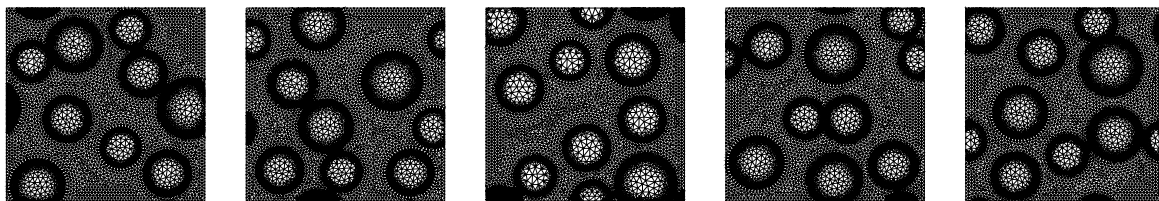


Figure 5.5. Uniaxial tension test (schematically)

Figure 5.6. Concrete specimens of a different size: (a)  $10 \times 10 \text{ mm}^2$ , (b)  $15 \times 15 \text{ mm}^2$ , (c)  $20 \times 20 \text{ mm}^2$ , (d)  $25 \times 25 \text{ mm}^2$  (aggregate density  $\rho = 30\%$ )Figure 5.7. Different distributions of aggregate for a concrete specimen of  $15 \times 15 \text{ mm}^2$  (aggregate density  $\rho = 30\%$ )

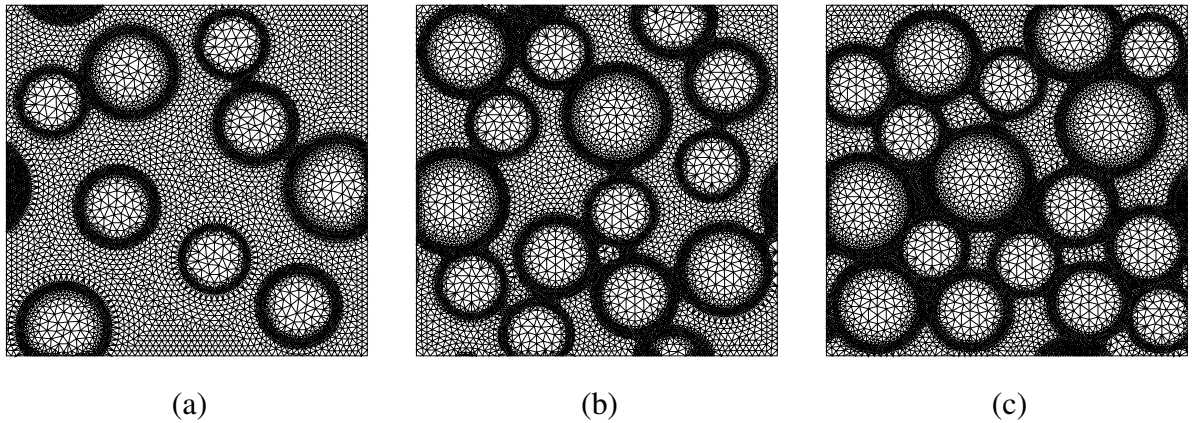


Figure 5.8. Concrete specimens for different aggregate density  $\rho$ : (a)  $\rho = 30\%$ , (b)  $\rho = 45\%$ , (c)  $\rho = 60\%$

tigated ( $l_c = 0.5$  mm). In the final comparative calculations, non-locality was prescribed to the cement matrix only.

The averaging was performed in the entire material domain. The homogenized stress and strain are defined in two dimensions as:

$$\langle \sigma \rangle = \frac{f_y^{int}}{b}, \quad (5.3)$$

$$\langle \varepsilon \rangle = \frac{u}{h}, \quad (5.4)$$

where  $f_y^{int}$  denotes the sum of all nodal internal forces in 'y' direction along the top edge of the specimen (Fig. 5.5),  $u$  is the prescribed displacement applied in 'y' direction, and  $b$  and  $h$  are the width and height of the specimen.

Figures 5.9–5.11 present the stress–strain relationships for various specimen sizes and random distributions of aggregates with material constants from Tab. 5.1 ( $l_c = 0.5$  mm). The aggregate density was  $\rho = 30\%$ ,  $\rho = 45\%$  or  $\rho = 60\%$ , respectively. In turn, the influence of the specimen size on the evolution of the stress–strain curves for different aggregate densities is demonstrated in Fig. 5.12. The results evidently show that the stress–strain curves are the same independently of the specimen size, aggregate density and distribution of inclusions in an elastic regime only (almost up to the peak). However, they are completely different in a softening regime after the peak is reached. An increase of the specimen size causes an increase of material brittleness. The differences in the evolution of stress–strain curves in a softening regime are caused by strain localization contributing to loss of material homogeneity (Fig. 5.13). Strain localization in the form of a localized zone propagates between aggregates and can be strongly curved. The width of the calculated zone is about  $w_c = (4 \times l_c) = 2$  mm (with  $l_c = 0.5$  mm).

The results indicate that the RVE can be determined in a linear–elastic regime only. However, it cannot be determined in a softening regime due to strain localization (*Gitman et al.* [66]). The fact of a non-existence of the RVE has to be taken into account in a multi-scale approach in order to maintain the objectivity of results with respect to a cell size.

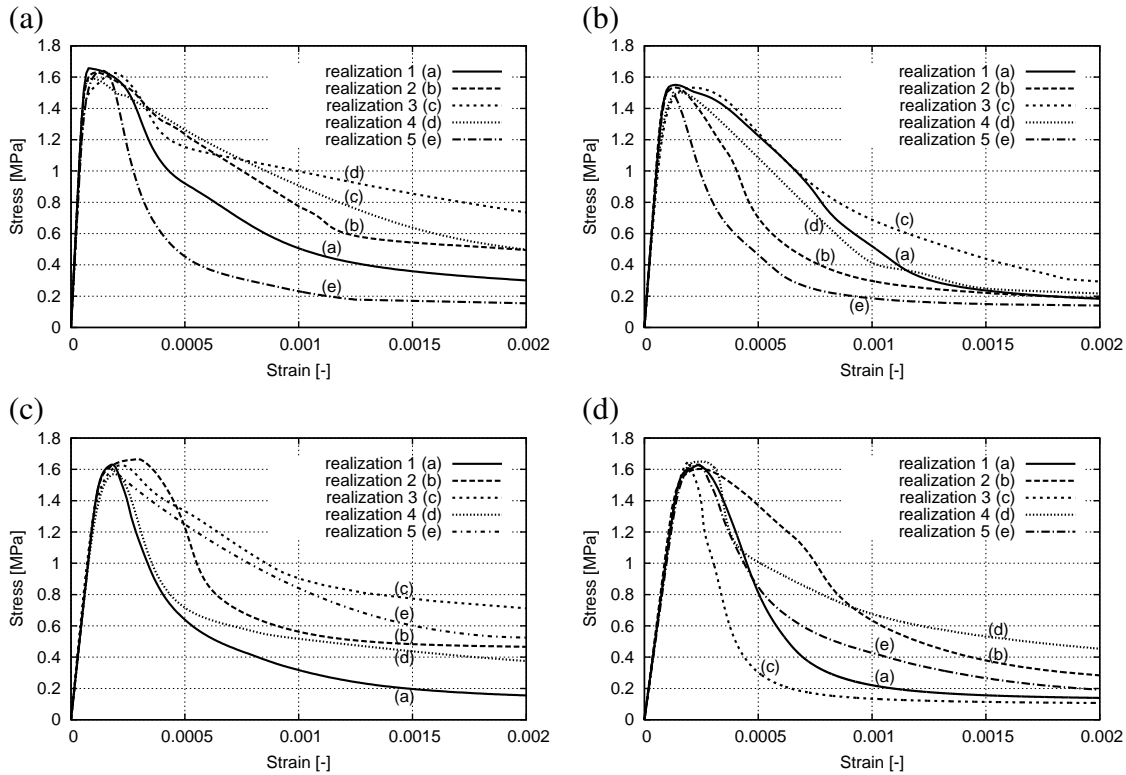


Figure 5.9. Stress–strain curves with various sizes of concrete specimen and random distributions of aggregate: (a)  $10 \times 10 \text{ mm}^2$ , (b)  $15 \times 15 \text{ mm}^2$ , (c)  $20 \times 20 \text{ mm}^2$ , (d)  $25 \times 25 \text{ mm}^2$  (characteristic length  $l_c = 0.5 \text{ mm}$ , aggregate density  $\rho = 30\%$ )

The effect of a characteristic length of micro-structure on the stress–strain curve and strain localization is shown in Figs. 5.14–5.17. Figures 5.14 and 5.16 demonstrate the influence of  $l_c$  on the evolution of stress–strain curves with two different specimen sizes:  $10 \times 10 \text{ mm}^2$  and  $25 \times 25 \text{ mm}^2$ , respectively. In turn, Figs. 5.15 and 5.17 present the distribution of a non–local softening strain measure for various  $l_c$  changing between 0.1 mm and 2.0 mm.

With increasing characteristic length, both specimen strength and width of a localized zone increase. On the other hand, softening decreases and material behaves more ductile. Thus, a pronounced deterministic size effect occurs (Bobiński *et al.* [28]). The width of a localized zone is about  $w_c = 4 \times l_c$  independently of  $l_c$ . A localized zone propagating in a cement matrix between aggregates is strongly curved with  $l_c = 0.25 \text{ mm}–1.0 \text{ mm}$ , whereas becomes more straight for  $l_c > 1.0 \text{ mm}$  (Fig. 5.17e).

The width of a localized zone,  $w_c = 4 – 8 \text{ mm}$ , with  $l_c = 1.0 – 2.0 \text{ mm}$  [ $l_c = (0.2 – 0.4) \times d_{max}$ ] is in good accordance with the measured width of the localized zone, 3.5 mm–5.5 mm, on a surface of notched concrete beams subject to bending by means of a DIC technique (Skarżyński *et al.* [150]). However, this numerical outcome is in contrast with a statement by Bažant and Novak (Bažant and Novak [11]) that a characteristic length is about  $3 \times d_{max}$ .

Figure 5.18 demonstrates the effect of the aggregate density on the stress–strain curves for two specimen sizes:  $20 \times 20 \text{ mm}^2$  and  $25 \times 25 \text{ mm}^2$ , respectively ( $\rho = 30\%$ ,  $\rho = 45\%$ ,  $\rho = 60\%$ , with  $l_c = 0.5 \text{ mm}$ ).

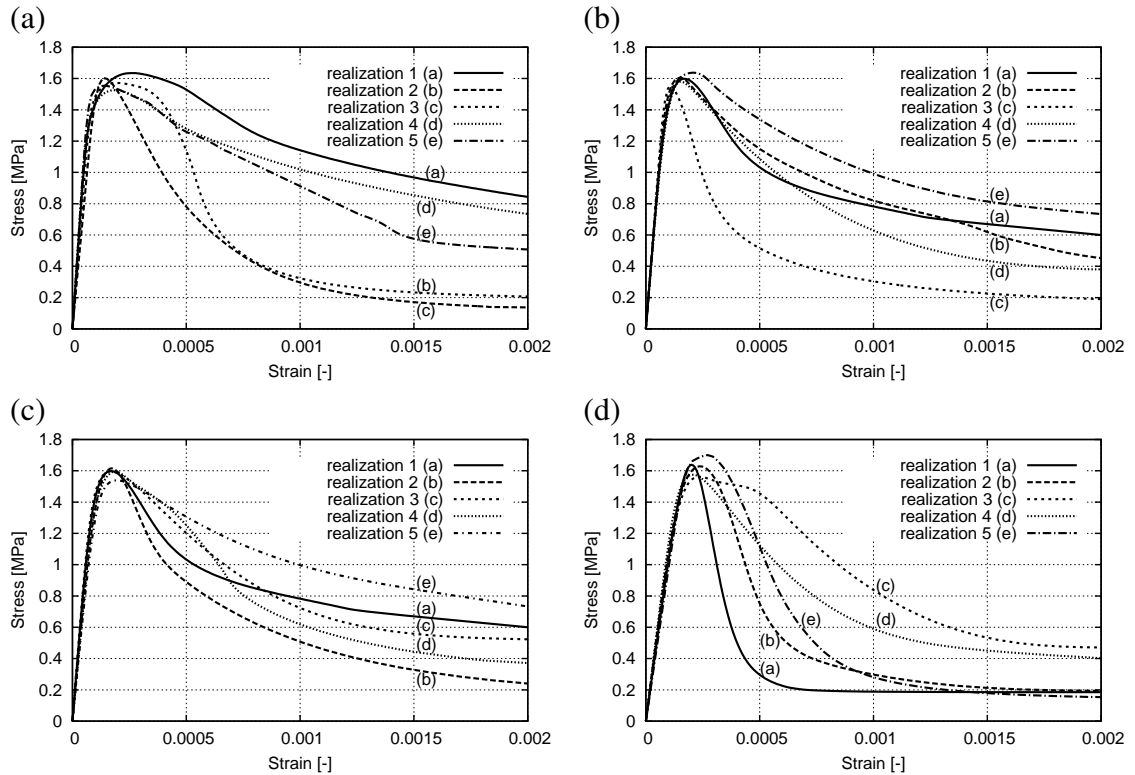


Figure 5.10. Stress–strain curves with various sizes of concrete specimen and random distributions of aggregate: (a)  $10 \times 10 \text{ mm}^2$ , (b)  $15 \times 15 \text{ mm}^2$ , (c)  $20 \times 20 \text{ mm}^2$ , (d)  $25 \times 25 \text{ mm}^2$  (characteristic length  $l_c = 0.5 \text{ mm}$ , aggregate density  $\rho = 45\%$ )

A localized zone is also influenced by an aggregate spacing. With increasing aggregate density, a localized zone becomes slightly narrower (Fig. 5.19). This means that a characteristic length of micro-structure may not be related to the aggregate size only but also to the grain size of the cement matrix (Skarżyński *et al.* [150]). Figure 5.20 shows the influence of the range of non-locality on the stress-strain relationship. In contrast to studies where the non-locality was prescribed to all three phases of concrete, here, a cement matrix was solely assumed to be non-local due to fact that strain localization occurred only there. A characteristic length was once more  $l_c = 0.5 \text{ mm}$ .

The effect of the non-locality range on results turned out to be insignificant since the range of averaging (Eq. 2.56) slightly decreased (Figs. 5.20 and 5.21).

## 5.2. Determination of RVE with non-standard averaging approaches

The FE two-dimensional investigations were performed with concrete described as a three-phase material composed of cement matrix, aggregate and interfacial transition (contact) zones between the cement matrix and aggregate (the material constants each phase are given in Tab. 5.1). The interface was assumed to be the weakest component (Lilliu and van Mier [99]) and its width was equal  $50 \mu\text{m}$  (He [72]). For the sake of simplicity, the aggregate shape was assumed in the form of circles. The number of triangular finite elements was 4000 (the smallest specimen) – 100000 (the largest specimen). The size of triangular finite elements was:  $s_a = 0.5 \text{ mm}$  (aggregate),  $s_{cm} = 0.25 \text{ mm}$  (cement matrix) and  $s_{ITZ} = 0.05$

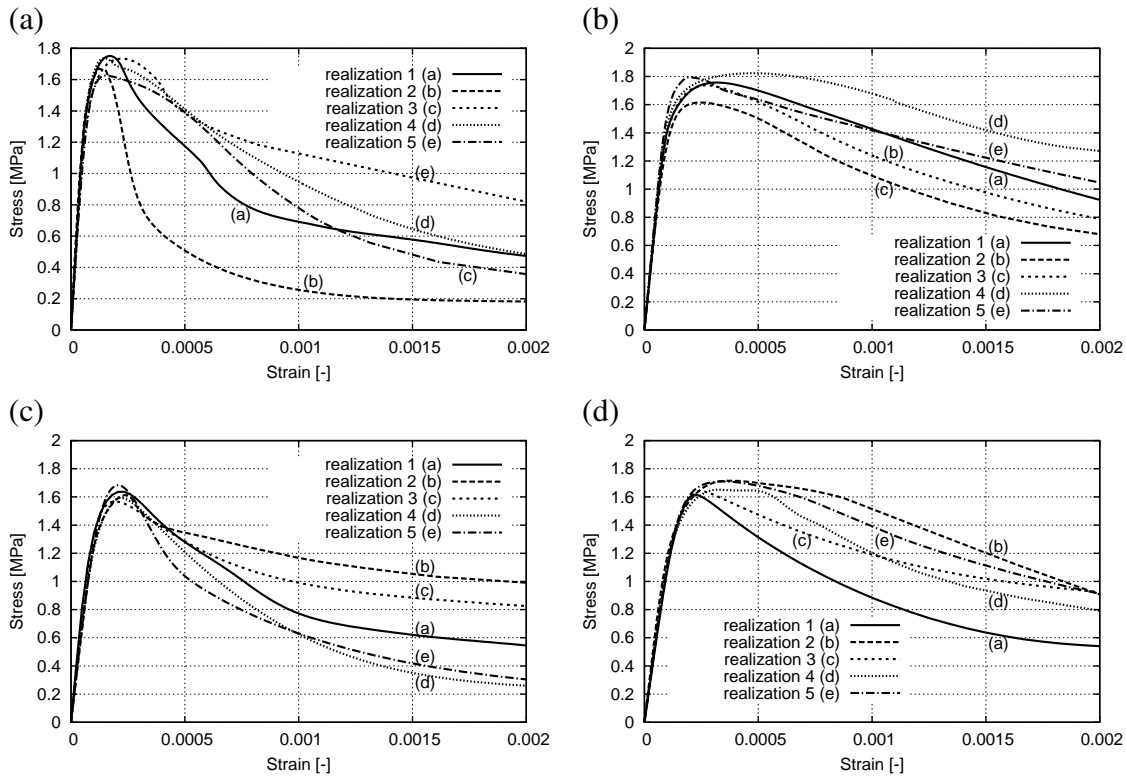


Figure 5.11. Stress–strain curves with various sizes of concrete specimen and random distributions of aggregate: (a)  $10 \times 10 \text{ mm}^2$ , (b)  $15 \times 15 \text{ mm}^2$ , (c)  $20 \times 20 \text{ mm}^2$ , (d)  $25 \times 25 \text{ mm}^2$  (characteristic length  $l_c = 0.5 \text{ mm}$ , aggregate density  $\rho = 60\%$ )

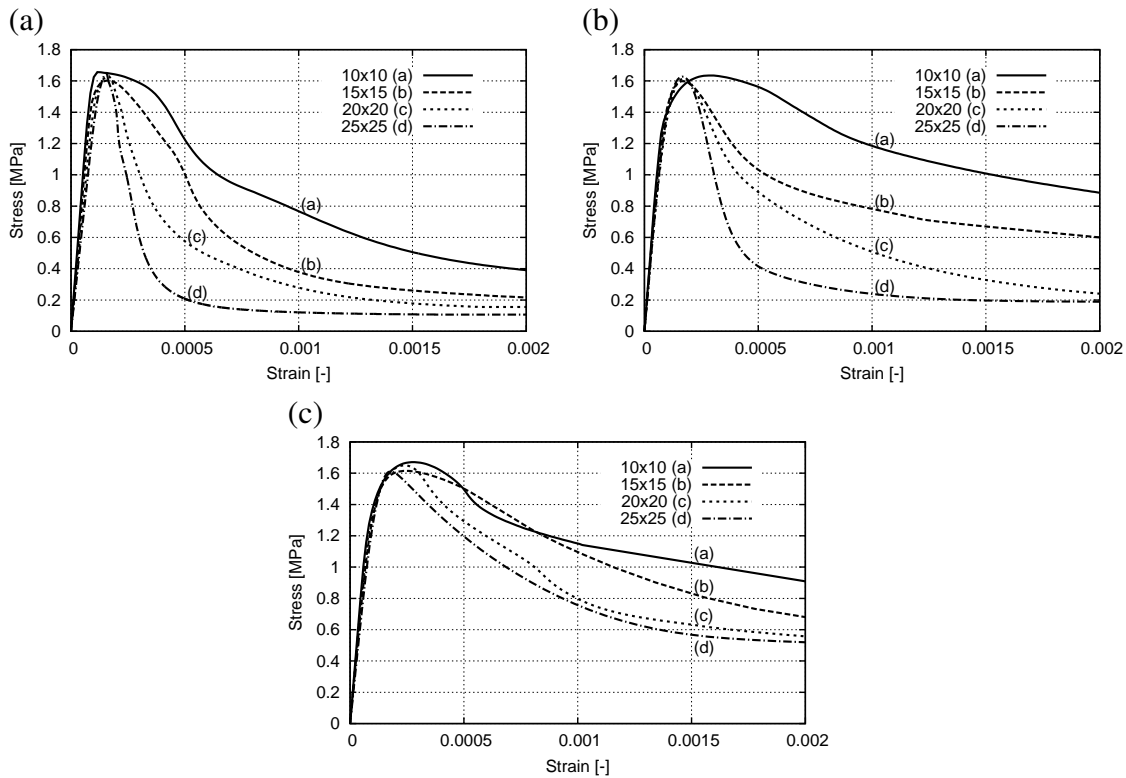


Figure 5.12. Stress–strain curves with various sizes of concrete specimen and aggregate densities  $\rho$ : (a)  $\rho = 30\%$ , (b)  $\rho = 45\%$ , (c)  $\rho = 60\%$  (characteristic length  $l_c = 0.5 \text{ mm}$ )

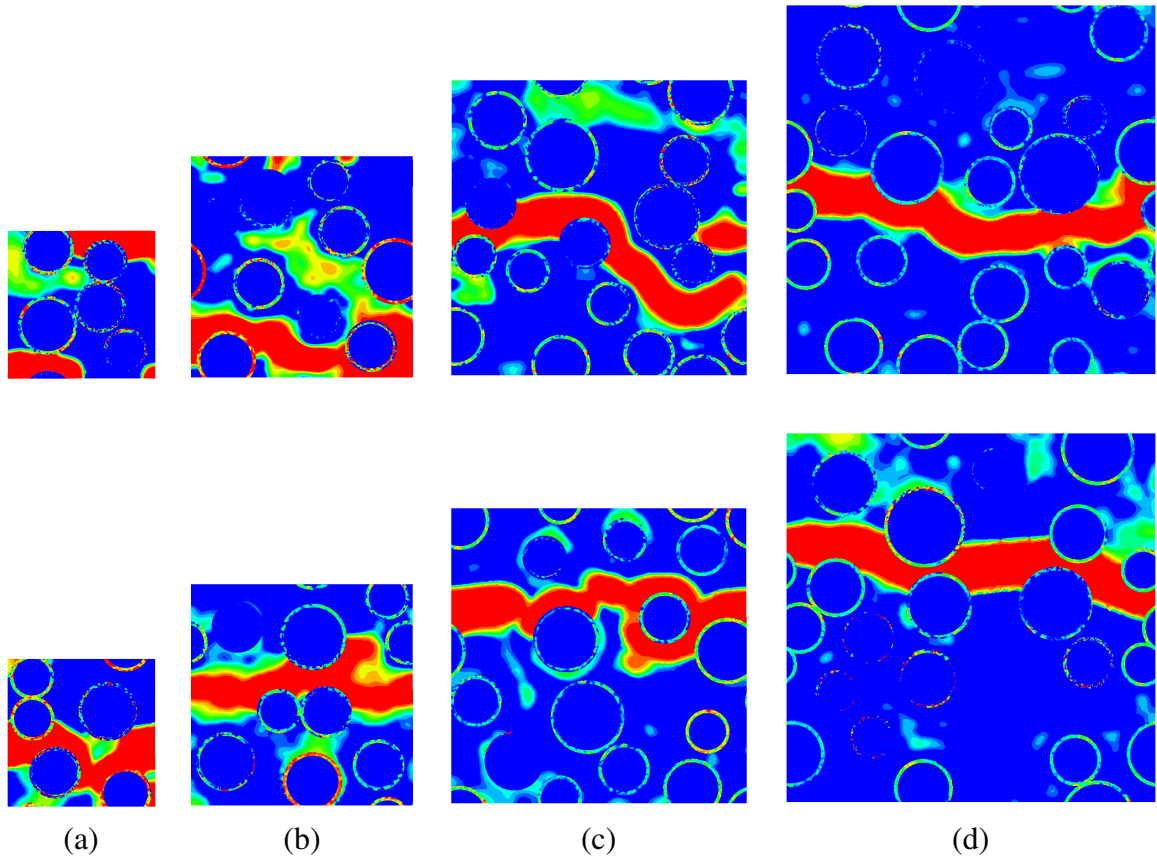


Figure 5.13. Distribution of non-local softening strain measure for two different random distributions of aggregate: (a)  $10 \times 10 \text{ mm}^2$ , (b)  $15 \times 15 \text{ mm}^2$ , (c)  $20 \times 20 \text{ mm}^2$ , (d)  $25 \times 25 \text{ mm}^2$  (characteristic length  $l_c = 0.5 \text{ mm}$ , aggregate density  $\rho = 30\%$ )

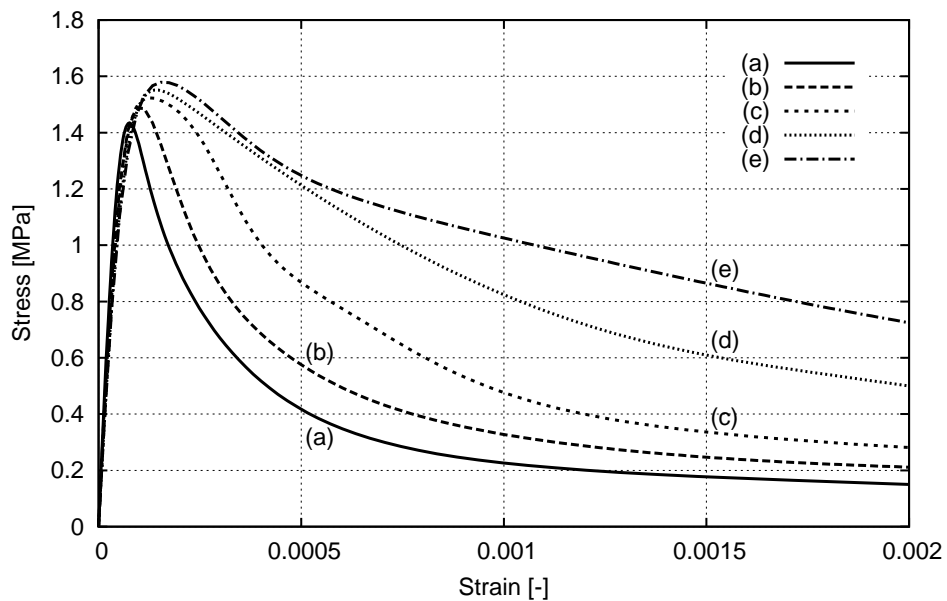


Figure 5.14. Stress-strain curves for different values of a characteristic length: (a)  $l_c = 0.1 \text{ mm}$ , (b)  $l_c = 0.25 \text{ mm}$ , (c)  $l_c = 0.5 \text{ mm}$ , (d)  $l_c = 1.0 \text{ mm}$ , (e)  $l_c = 2.0 \text{ mm}$  (specimen size  $10 \times 10 \text{ mm}^2$ , aggregate density  $\rho = 30\%$ )

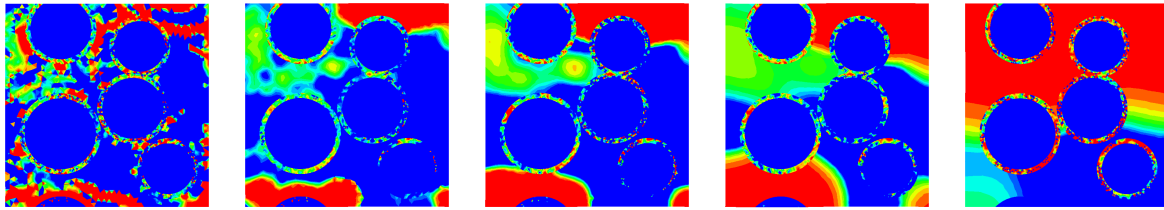


Figure 5.15. Distribution of non-local softening strain measure for different values of a characteristic length: (a)  $l_c = 0.1$  mm, (b)  $l_c = 0.25$  mm, (c)  $l_c = 0.5$  mm, (d)  $l_c = 1.0$  mm, (e)  $l_c = 2.0$  mm (specimen size  $10 \times 10$  mm<sup>2</sup>, aggregate density  $\rho = 30\%$ )

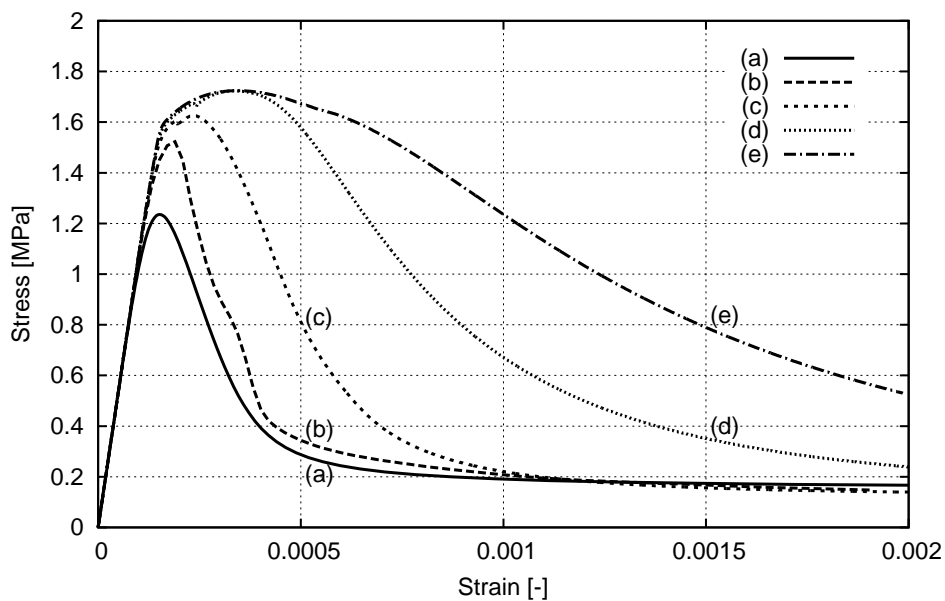


Figure 5.16. Stress-strain curves for different values of a characteristic length: (a)  $l_c = 0.1$  mm, (b)  $l_c = 0.25$  mm, (c)  $l_c = 0.5$  mm, (d)  $l_c = 1.0$  mm, (e)  $l_c = 2.0$  mm (specimen size  $25 \times 25$  mm<sup>2</sup>, aggregate density  $\rho = 30\%$ )

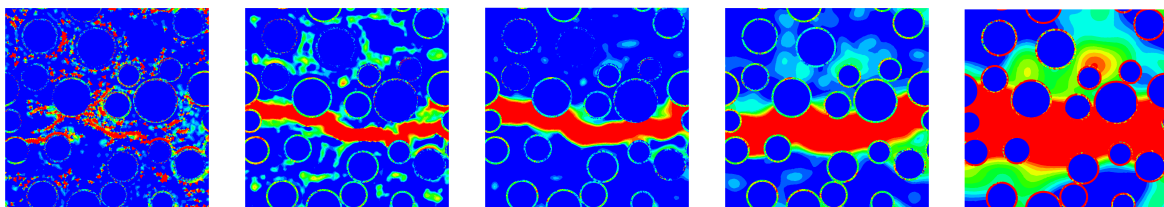


Figure 5.17. Distribution of non-local softening strain measure for different values of a characteristic length: (a)  $l_c = 0.1$  mm, (b)  $l_c = 0.25$  mm, (c)  $l_c = 0.5$  mm, (d)  $l_c = 1.0$  mm, (e)  $l_c = 2.0$  mm (specimen size  $25 \times 25$  mm<sup>2</sup>, aggregate density  $\rho = 30\%$ )

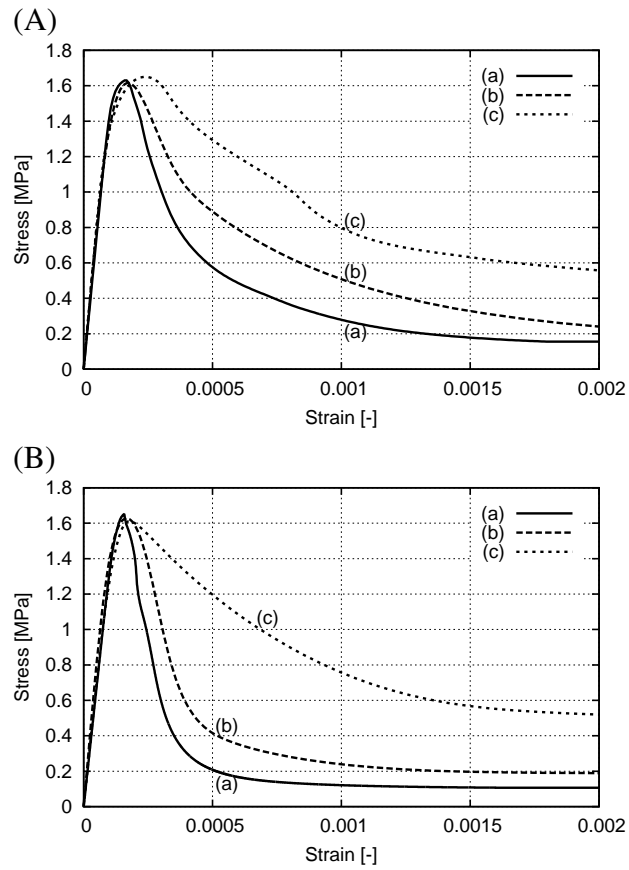


Figure 5.18. Stress–strain curves for different aggregate densities: (a)  $\rho = 30\%$ , (b)  $\rho = 45\%$ , (c)  $\rho = 60\%$  and cell sizes (A)  $20 \times 20 \text{ mm}^2$ , (B)  $25 \times 25 \text{ mm}^2$  ( $l_c = 0.5 \text{ mm}$ )

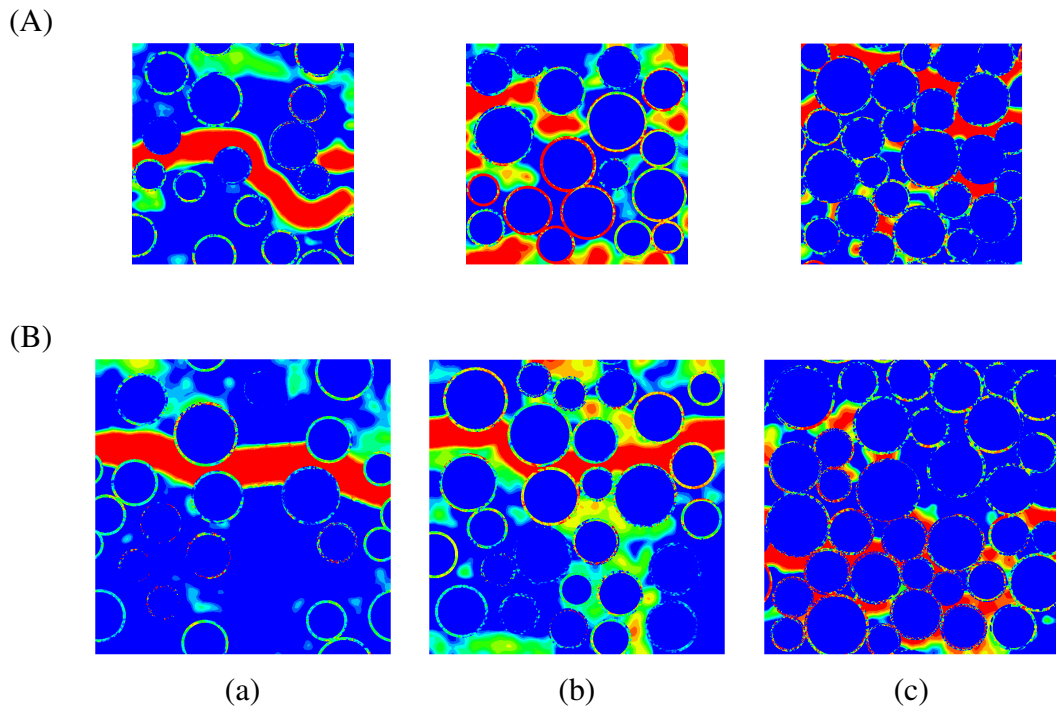


Figure 5.19. Distribution of non–local softening strain measure for two different aggregate densities: (a)  $\rho = 30\%$ , (b)  $\rho = 45\%$ , (c)  $\rho = 60\%$  and cell sizes (A)  $20 \times 20 \text{ mm}^2$ , (B)  $25 \times 25 \text{ mm}^2$  ( $l_c = 0.5 \text{ mm}$ )

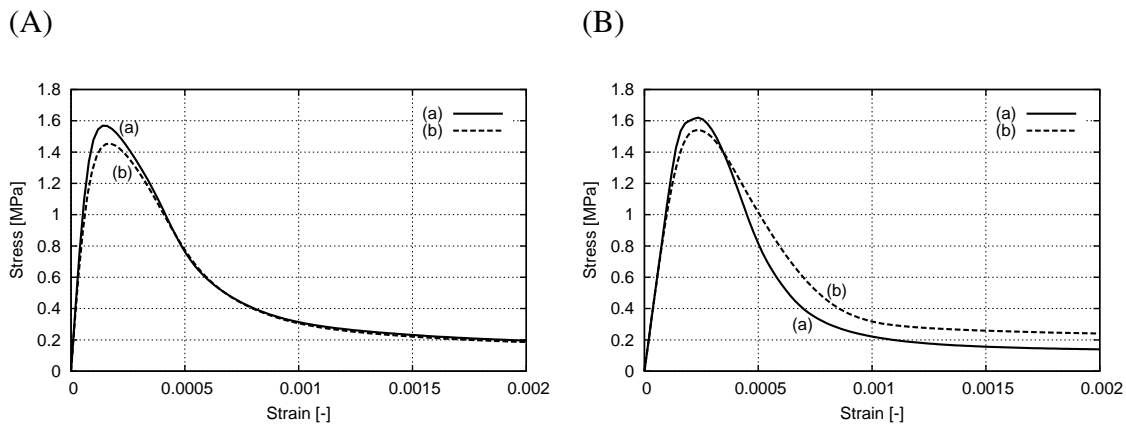


Figure 5.20. Stress–strain curves for two different specimen sizes: (A)  $15 \times 15 \text{ mm}^2$ , (B)  $25 \times 25 \text{ mm}^2$  with (a) non–locality prescribed to three phases and (b) non–locality prescribed to cement matrix (aggregate density  $\rho = 30\%$ , characteristic length  $l_c = 0.5 \text{ mm}$ )

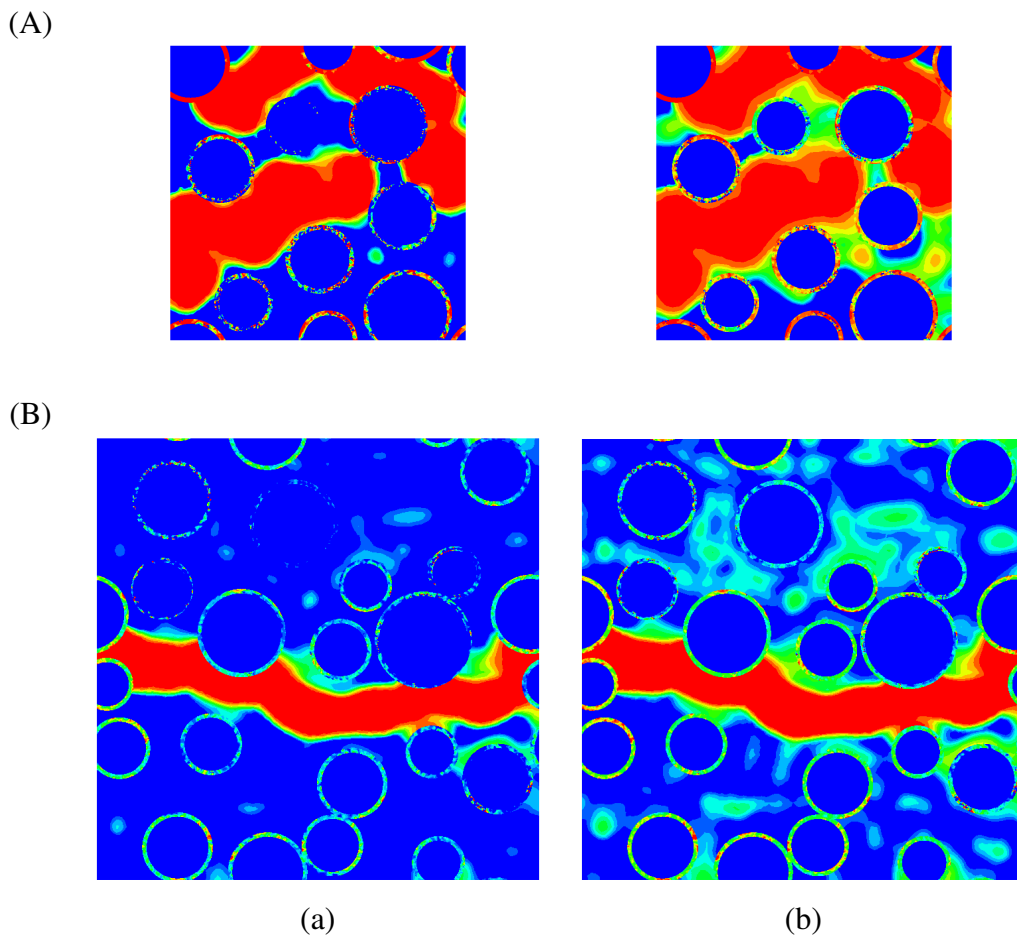


Figure 5.21. Distribution of non–local softening strain measure for two different specimen sizes: (A)  $15 \times 15 \text{ mm}^2$ , (B)  $25 \times 25 \text{ mm}^2$  with (a) non–locality prescribed to three phases and (b) non–locality prescribed to cement matrix (aggregate density  $\rho = 30\%$ , characteristic length  $l_c = 0.5 \text{ mm}$ )

mm (interface). To analyse the existence and size of RVE under tension, a two-dimensional uniaxial tension test (Fig. 5.5) was again performed with a quadratic concrete specimen representing a unit cell with periodicity of boundary conditions and material periodicity (Figs. 5.4 and 5.22). The unit cells of six different sizes were investigated:  $5 \times 5 \text{ mm}^2$ ,  $10 \times 10 \text{ mm}^2$ ,  $15 \times 15 \text{ mm}^2$ ,  $20 \times 20 \text{ mm}^2$ ,  $25 \times 25 \text{ mm}^2$  and  $30 \times 30 \text{ mm}^2$  respectively (Fig. 5.23). For each specimen, three different stochastic realisations were performed with an aggregate density  $\rho = 30\%$  (results for  $\rho = 45\%$  and  $\rho = 60\%$  showed the same trend). The characteristic length of micro-structure was assumed to be  $l_c = 1.5 \text{ mm}$  (Chapter 3).

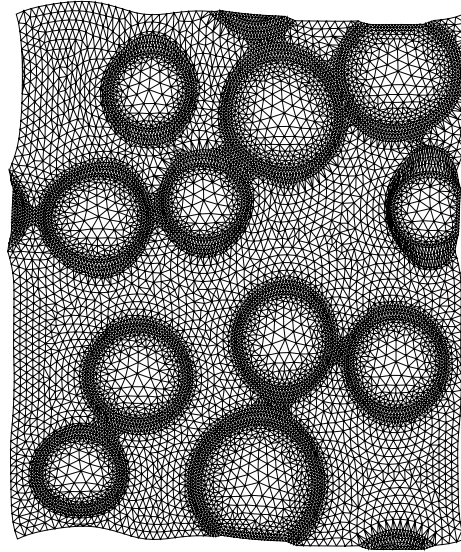


Figure 5.22. Deformed three-phase concrete with periodicity of boundary conditions and material periodicity

First similar calculations as in Section 5.1 were carried out using a standard averaging approach for comparative purposes. Figure 5.24 presents the stress-strain relationships for various specimen sizes and random distributions of aggregate with material constants from Tab. 5.1 ( $l_c = 1.5 \text{ mm}$ ). In the first case, the aggregate distribution was similar and in the second case it was random in different unit cells. The results show that the stress-strain curves are the same solely in an elastic regime independently on the specimen size, aggregate density and aggregate distribution. However, they are completely different at the peak and in the softening regime. An increase of the specimen size causes strength decrease and an increase of material brittleness (softening rate) (Fig. 5.24). The differences in the evolution of stress-strain curves in a softening regime are caused by strain localization (in the form of a curved localized zone propagating between aggregates Figs. 5.25 and 5.26) contributing to loss of material homogeneity (due to the fact that strain localization is not scaled with increasing specimen size). The width of a calculated localized zone is approximately  $w_c = 3 \text{ mm} = 2 \times l_c = 12 \times s_{cm}$  (unit cell  $5 \times 5 \text{ mm}^2$ ),  $w_c = 5 \text{ mm} = 3.33 \times l_c = 20 \times s_{cm}$  (unit cell  $10 \times 10 \text{ mm}^2$ ) and  $w_c = 6 \text{ mm} = 4 \times l_c = 24 \times s_{cm}$  (unit cells larger than  $10 \times 10 \text{ mm}^2$ ).

Figure 5.27 presents the expectation value and standard deviation of the fracture energy  $G_f$  versus the specimen height  $h$  for three different realisations. The fracture energy  $G_f$  was calculated as the area under the stress-strain curves  $g_f$  multiplied by the width of a localized

zone  $w_c$ :

$$G_f = g_f \times w_c = \left( \int_a^b \langle \sigma \rangle d \langle \varepsilon \rangle \right) \times w_c, \quad (5.5)$$

The integration limits  $a_1$  and  $a_2$  are 0 and 0.001, respectively (Fig. 5.24). The fracture energy decreases with increasing specimen size, i.e. a strong size dependence of RVE exists since a localized zone does not scale with its size

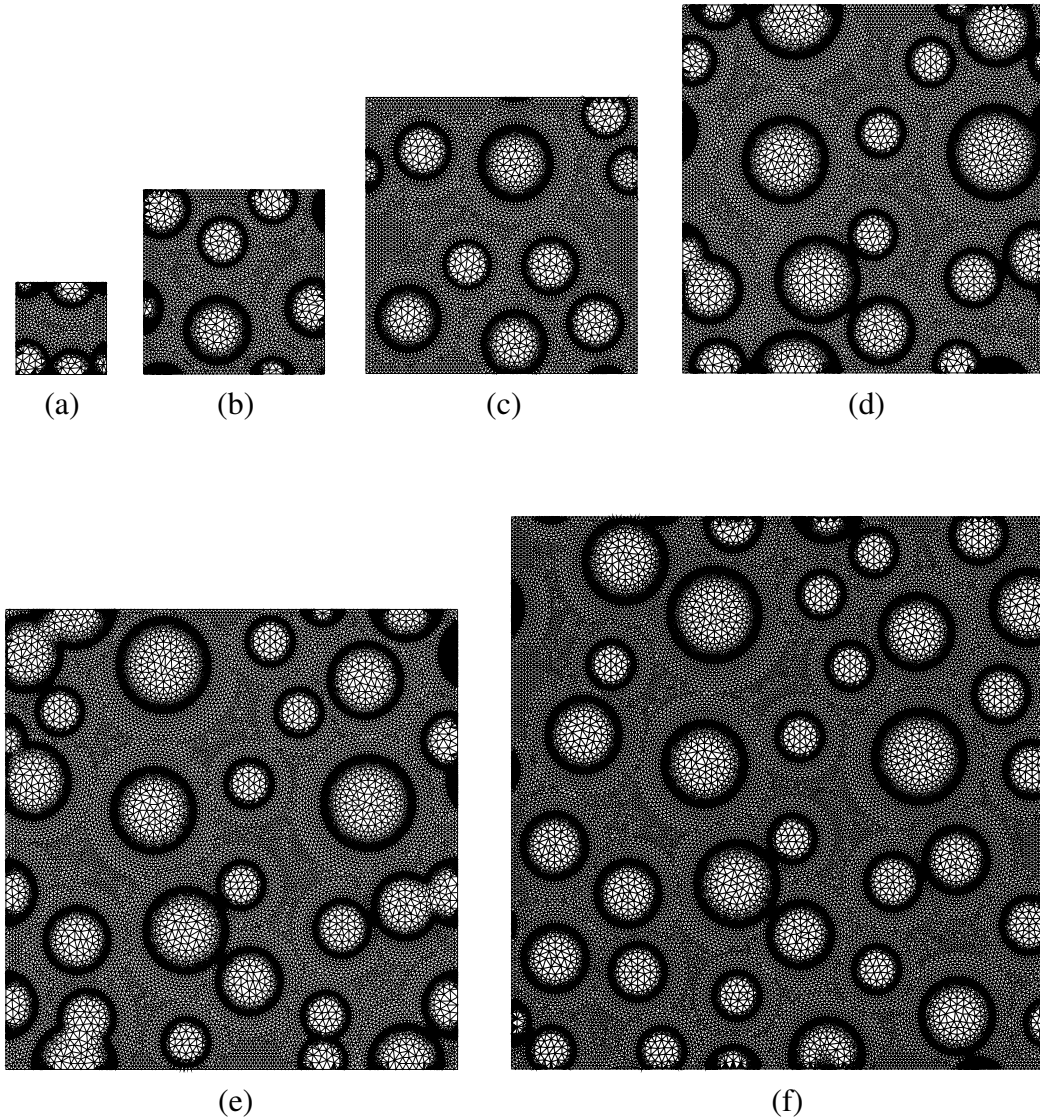


Figure 5.23. Concrete specimens of different size: (a)  $5 \times 5 \text{ mm}^2$ , (b)  $10 \times 10 \text{ mm}^2$ , (c)  $15 \times 15 \text{ mm}^2$ , (d)  $20 \times 20 \text{ mm}^2$ , (e)  $25 \times 25 \text{ mm}^2$ , (f)  $30 \times 30 \text{ mm}^2$  (aggregate density  $\rho = 30\%$ )

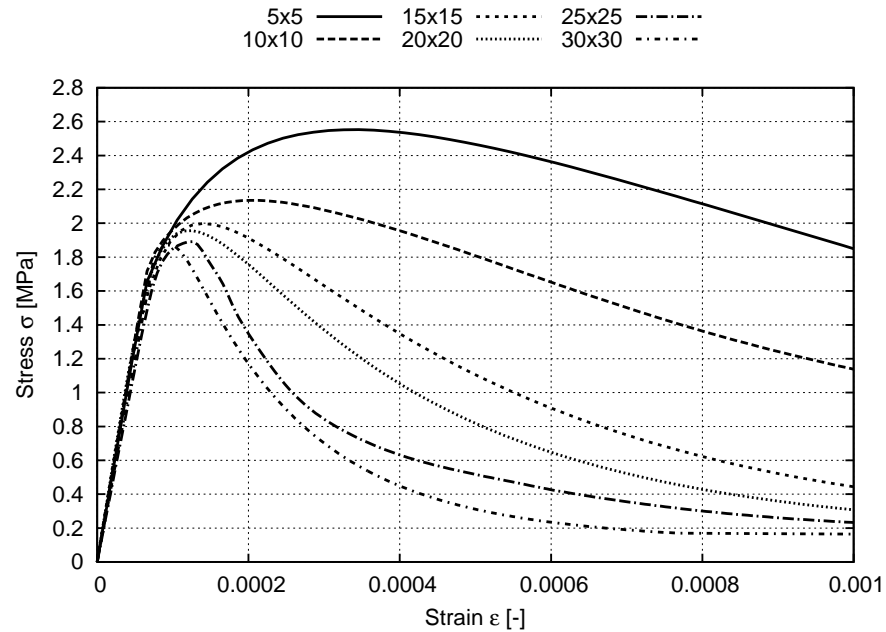
Next, the homogenized stress and strain were averaged over the localized domain only according to Verhoosel et al. (Verhoosel et al. [167]) and Nguyen et al. (Nguyen et al. [124]):

$$\langle \sigma \rangle = \frac{1}{A_z} \int_{A_z} \sigma_m dA_z, \quad (5.6)$$

$$\langle \varepsilon \rangle = \frac{1}{A_z} \int_{A_z} \varepsilon_m dA_z, \quad (5.7)$$

where  $A_z$  is the localized zone area (on the basis of a distribution of the equivalent strain measure) and  $\sigma_m$  and  $\varepsilon_m$  are the meso-stress and meso-strain respectively. Thus, a linear material behaviour is simply swept out and an active plastic response is solely taken into account.

(a)



(b)

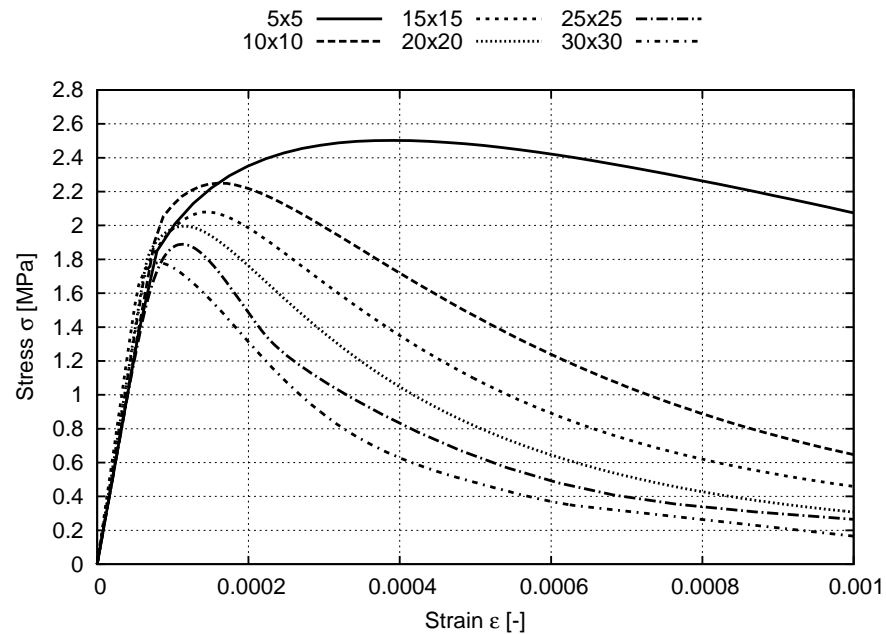


Figure 5.24. Stress–strain curves for various sizes of concrete specimens and two different random distributions of aggregate (a) and (b) using standard averaging procedure (characteristic length  $l_c = 1.5$  mm, aggregate density  $\rho = 30\%$ )

Figure 5.28 presents the stress–strain relationships for various specimen sizes and two random aggregate distributions of aggregates with material constants from Tab. 5.1 ( $l_c = 1.5$  mm) for the calculated localized zones of Figs. 5.25 and 5.26. The stress–strain curves in a softening regime (for the unit cells larger than  $10 \times 10$  mm<sup>2</sup>) are in a vary good accordance with respect to their shape. In this case, the statistically representative volume element exists and is equal to  $15 \times 15$  mm<sup>2</sup>. Figure 5.29 presents the expectation value and standard deviation of the fracture energy  $G_f$  versus the specimen height  $h$  for three different realisations. The integration limits were  $a_1 = 0$  and  $a_2 = 0.004$  (Fig. 5.28). The fracture energy decreases with increasing specimen size approaching an asymptote when the cell size is  $15 \times 15$  mm<sup>2</sup>. With increasing characteristic length, both specimen strength and width of a localized zone increase. On the other hand, softening decreases and material behaves more ductile (Skarżyński and Tejchman [151]). Taking these two facts into account, a varying characteristic length related to the reference specimen size (assumed as  $15 \times 15$  mm<sup>2</sup> or  $30 \times 30$  mm<sup>2</sup>) was introduced according to the formula:

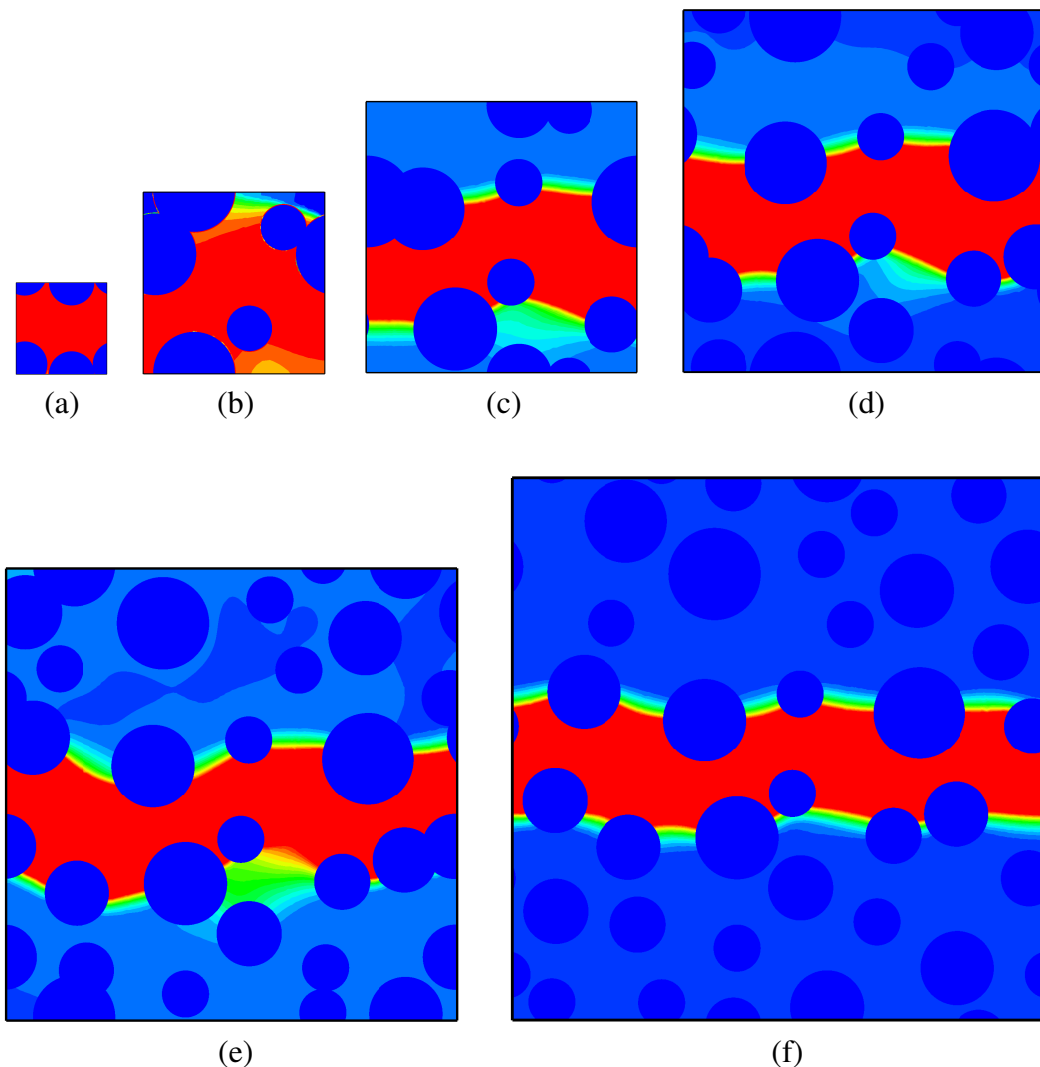


Figure 5.25. Distribution of non–local softening strain measure for various specimen sizes and stress–strain curves of Fig. 5.24a using standard averaging procedure (characteristic length  $l_c = 1.5$  mm, aggregate density  $\rho = 30\%$ )

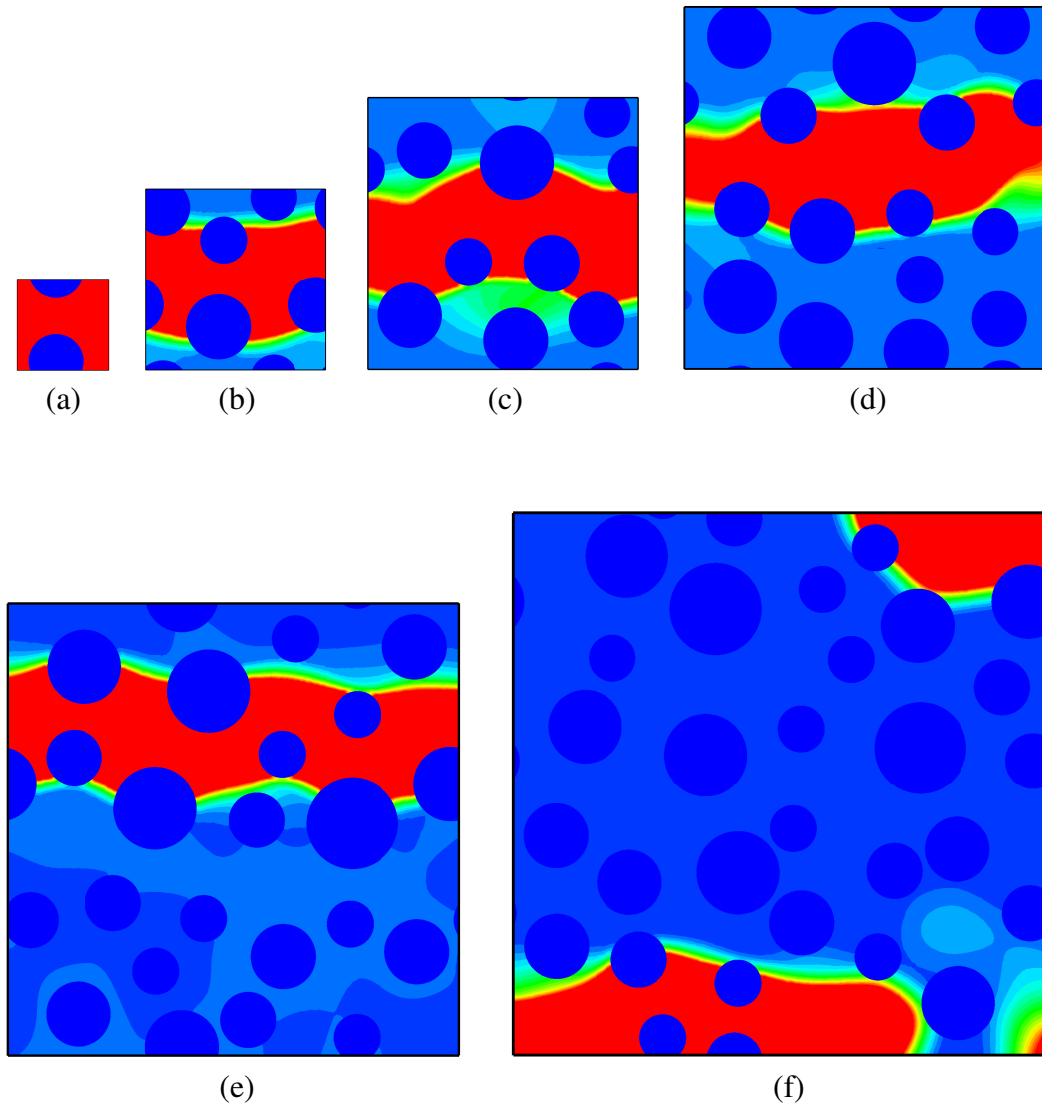


Figure 5.26. Distribution of non-local softening strain measure for various specimen sizes and stress-strain curves of Fig. 5.24b using standard averaging procedure (characteristic length  $l_c = 1.5$  mm, aggregate density  $\rho = 30\%$ )

$$l_c^v = l_c^{15 \times 15} \times \frac{h \text{ [mm]}}{15 \text{ [mm]}}, \quad (5.8)$$

$$l_c^v = l_c^{30 \times 30} \times \frac{h \text{ [mm]}}{30 \text{ [mm]}}, \quad (5.9)$$

where  $l_c^{15 \times 15} = l_c^{30 \times 30} = 1.5$  mm is a characteristic length for the reference unit cell  $15 \times 15$  mm<sup>2</sup> or  $30 \times 30$  mm<sup>2</sup> and  $h$  is the cell height. A larger unit cell than  $30 \times 30$  mm<sup>2</sup> can be also used (the width of a localized zone in the reference unit cell cannot be too strongly influenced by boundary conditions as e.g. the cell size smaller than  $10 \times 10$  mm<sup>2</sup>). The stress-strain relationship for various specimen sizes and various characteristic lengths are shown in Figs. 5.30 and 5.31. A characteristic length varies between  $l_c = 0.5$  mm for the unit cell  $5 \times 5$  mm<sup>2</sup> and  $l_c = 3.0$  mm for the unit cell  $30 \times 30$  mm<sup>2</sup> according to Eq. 5.8 and between  $l_c = 0.25$  mm for the unit cell  $5 \times 5$  mm<sup>2</sup> and  $l_c = 1.5$  mm for the unit cell  $30 \times 30$  mm<sup>2</sup> according to Eq. 5.9.

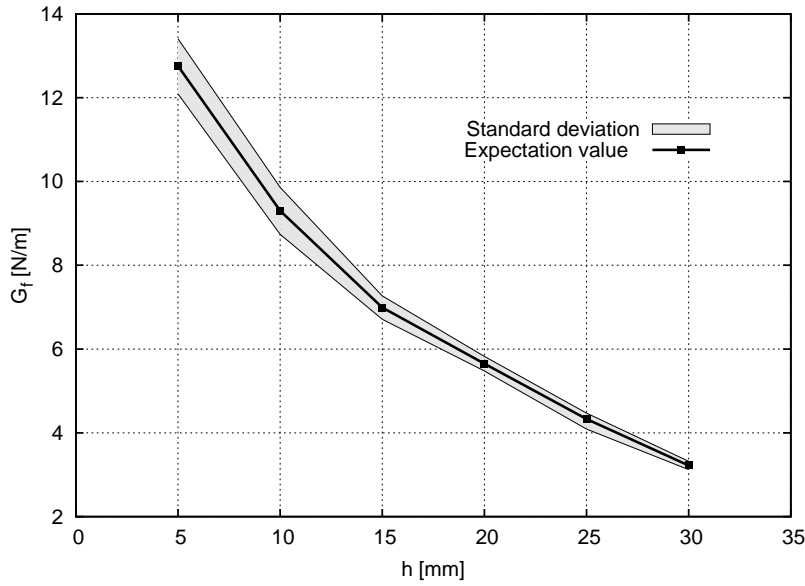


Figure 5.27. Expected value and standard deviation of fracture energy using standard averaging (aggregate density  $\rho = 30\%$ )

The width of a calculated localized zone (for the reference unit cell  $15 \times 15 \text{ mm}^2$ ) is approximately  $w_c = 4 \times l_c = 8 \times s_{cm} = 2 \text{ mm}$  (unit cell  $5 \times 5 \text{ mm}^2$ ),  $w_c = 4 \times l_c = 16 \times s_{cm} = 4 \text{ mm}$  (unit cell  $10 \times 10 \text{ mm}^2$ ),  $w_c = 4 \times l_c = 24 \times s_{cm} = 6 \text{ mm}$  (unit cell  $15 \times 15 \text{ mm}^2$ ),  $w_c = 4 \times l_c = 32 \times s_{cm} = 8 \text{ mm}$  (unit cell  $20 \times 20 \text{ mm}^2$ ),  $w_c = 4 \times l_c = 40 \times s_{cm} = 10 \text{ mm}$  (unit cell  $25 \times 25 \text{ mm}^2$ ),  $w_c = 4 \times l_c = 48 \times s_{cm} = 12 \text{ mm}$  (unit cell  $30 \times 30 \text{ mm}^2$ ) (Figs. 5.32 and 5.33). The width of a calculated localized zone (for the reference unit cell  $30 \times 30 \text{ mm}^2$ ) is approximately  $w_c = 4 \times l_c = 4 \times s_{cm} = 1 \text{ mm}$  (unit cell  $5 \times 5 \text{ mm}^2$ ),  $w_c = 4 \times l_c = 8 \times s_{cm} = 2 \text{ mm}$  (unit cell  $10 \times 10 \text{ mm}^2$ ),  $w_c = 4 \times l_c = 12 \times s_{cm} = 3 \text{ mm}$  (unit cell  $15 \times 15 \text{ mm}^2$ ),  $w_c = 4 \times l_c = 16 \times s_{cm} = 4 \text{ mm}$  (unit cell  $20 \times 20 \text{ mm}^2$ ),  $w_c = 4 \times l_c = 20 \times s_{cm} = 5 \text{ mm}$  (unit cell  $25 \times 25 \text{ mm}^2$ ),  $w_c = 4 \times l_c = 24 \times s_{cm} = 6 \text{ mm}$  (unit cell  $30 \times 30 \text{ mm}^2$ ) (Figs. 5.34 and 5.35). A localized zone is scaled with the specimen size. Owing to that the material does not lose its homogeneity and its response during softening is similar for the unit cell  $15 \times 15 \text{ mm}^2$  and larger ones. Thus, the size of the representative volume element is again equal to  $15 \times 15 \text{ mm}^2$ .

The expectation value and standard deviation of the unit fracture energy  $g_f = G_f/w_c$  versus the specimen height  $h$  are demonstrated in Fig. 5.36. With increasing cell size, the value of  $g_f$  stabilizes for the unit cell  $15 \times 15 \text{ mm}^2$ .

### 5.3. Conclusions

The results of FE simulations under tensile loading of softening quasi-brittle materials with a heterogeneous three-phase structure revealed the following points:

- the Representative Volume Element (RVE) cannot be defined in quasi-brittle materials as concrete due to strain localization connected to softening. This fact has to be taken into account when using a multi-scale approach to maintain the objectivity of results with respect to a cell size. The RVE can be found in homogeneous materials only,

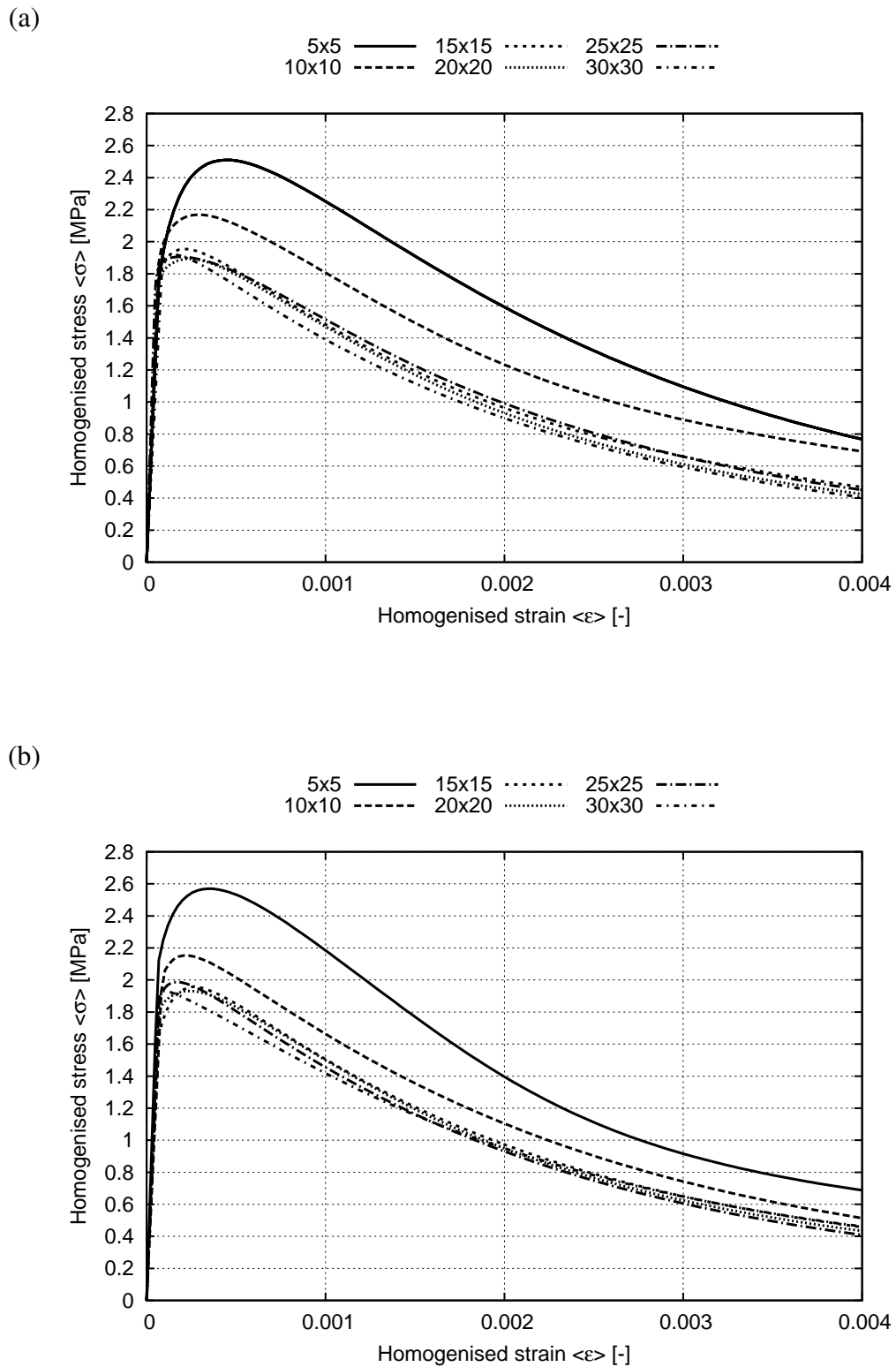


Figure 5.28. Stress–strain curves for various sizes of concrete specimens and two different random distributions of aggregate (a) and (b) using failure averaging procedure (characteristic length  $l_c = 1.5$  mm, aggregate density  $\rho = 30\%$ )

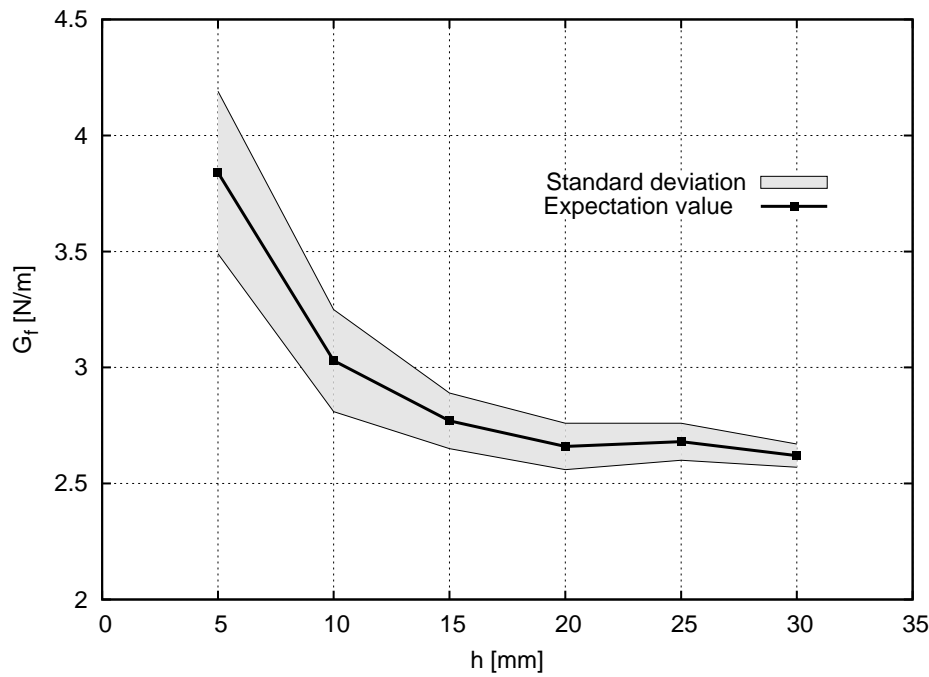


Figure 5.29. Expected value and standard deviation of fracture energy using failure averaging (aggregate density  $\rho = 30\%$ )

- the Representative Volume Element (RVE) cannot be defined in quasi-brittle materials with a standard averaging approach (over the entire domain) due to occurrence of localized zone which width is not scaled with the specimen size. The shape of stress-strain curve depends on the unit cell size beyond the elastic region,
- the representative volume element (RVE) can be defined in quasi-brittle materials using both a failure zone averaging approach and a varying characteristic length approach. In the first case, the averaging is performed in the damage domain and in the second case, a characteristic length is scaled with the specimen size. The size of a two-dimensional statistically representative volume element is approximately equal to  $15 \times 15 \text{ mm}^2$ .
- with increasing characteristic length of micro-structure  $l_c$ , both material strength and width of a localized zone grow but material softening decreases. The width of a localized zone is about  $w_c = 4 \times l_c$ . The localized zone can be strongly curved with a small  $l_c$ ,
- the width of the localized zone increases with decreasing aggregate density.

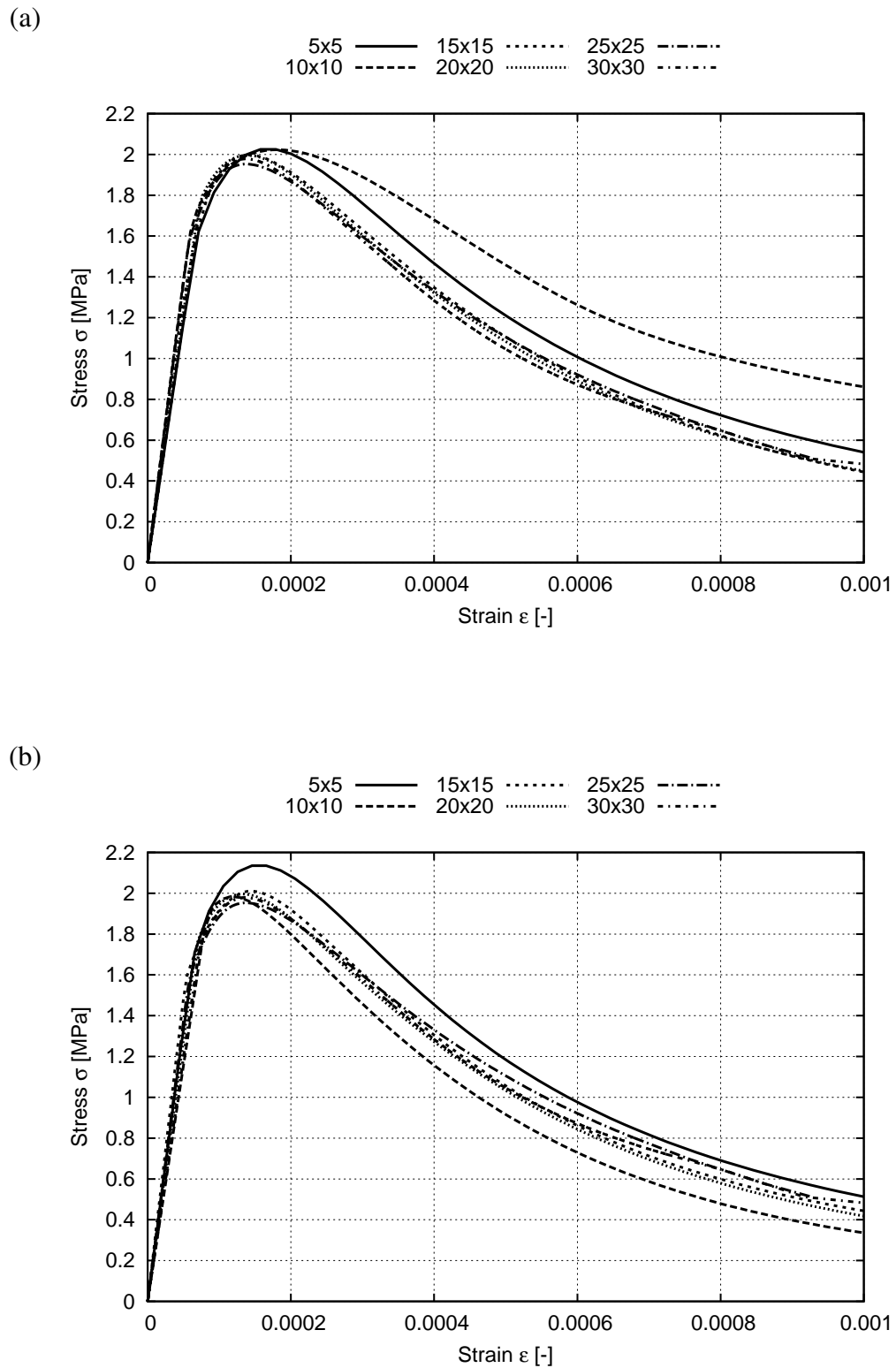


Figure 5.30. Stress–strain curves for various sizes of concrete specimens and two different random distributions of aggregate (a) and (b) using varying characteristic length averaging approach (reference size  $15 \times 15 \text{ mm}^2$ , characteristic length according to Eq. 5.8, aggregate density  $\rho = 30\%$ )

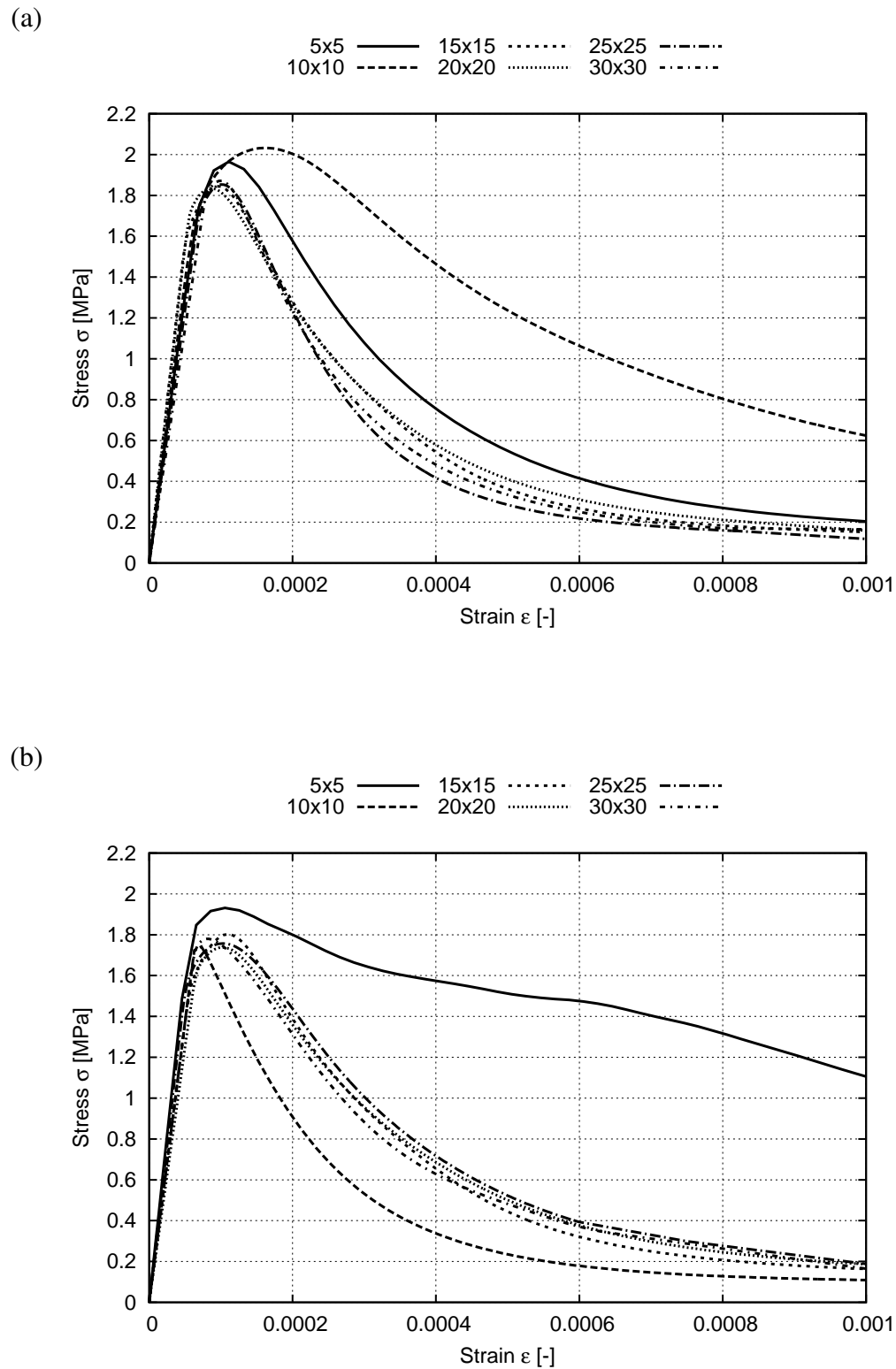


Figure 5.31. Stress–strain curves for various sizes of concrete specimens and two different random distributions of aggregate (a) and (b) using varying characteristic length averaging approach (reference size  $30 \times 30 \text{ mm}^2$ , characteristic length according to Eq. 5.9, aggregate density  $\rho = 30\%$ )

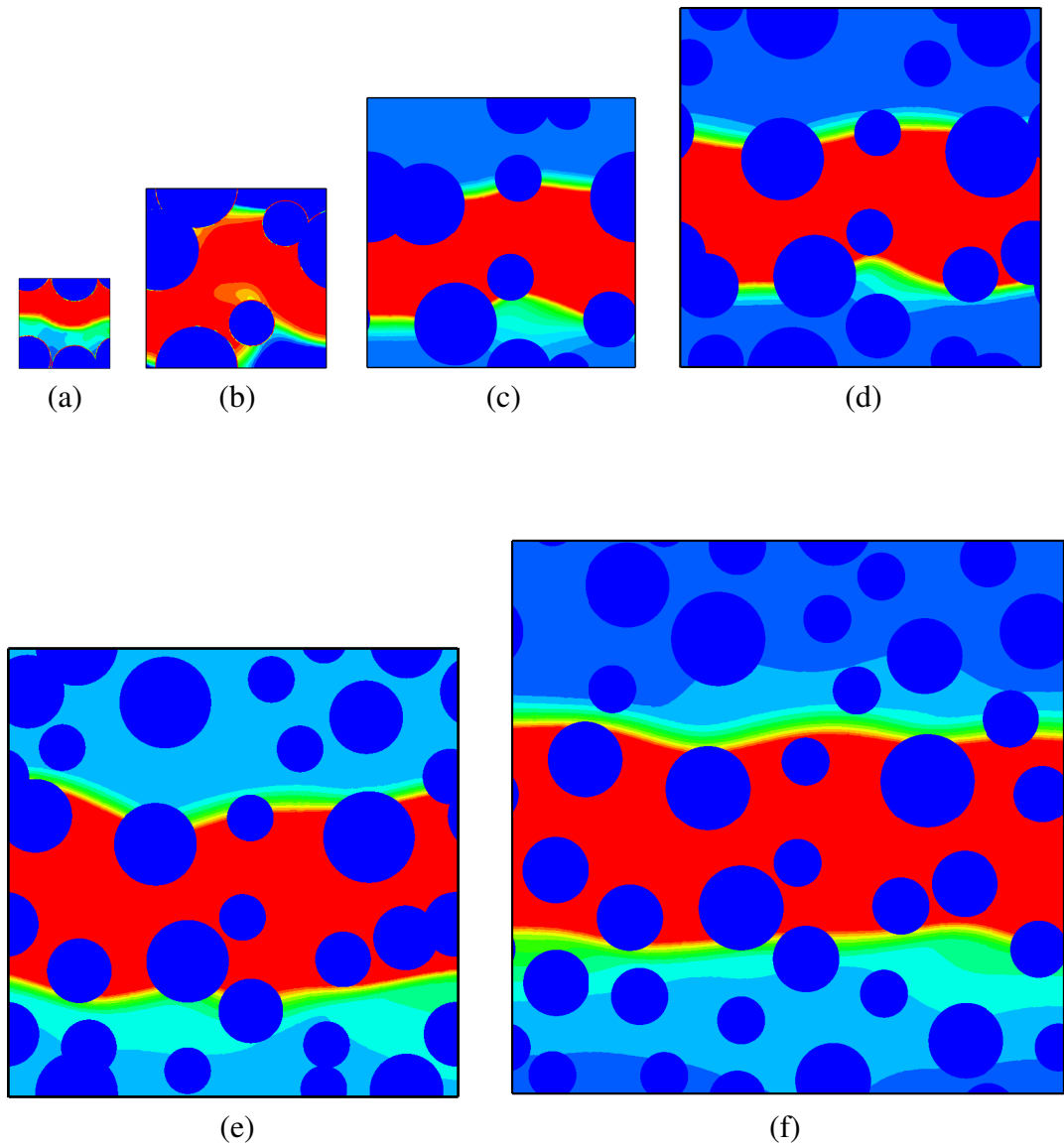


Figure 5.32. Distribution of non-local softening strain measure for various specimen sizes and stress-strain curves of Fig. 5.30a using varying characteristic length averaging approach (reference size  $15 \times 15 \text{ mm}^2$ , characteristic length according to Eq. 5.8, aggregate density  $\rho = 30\%$ )

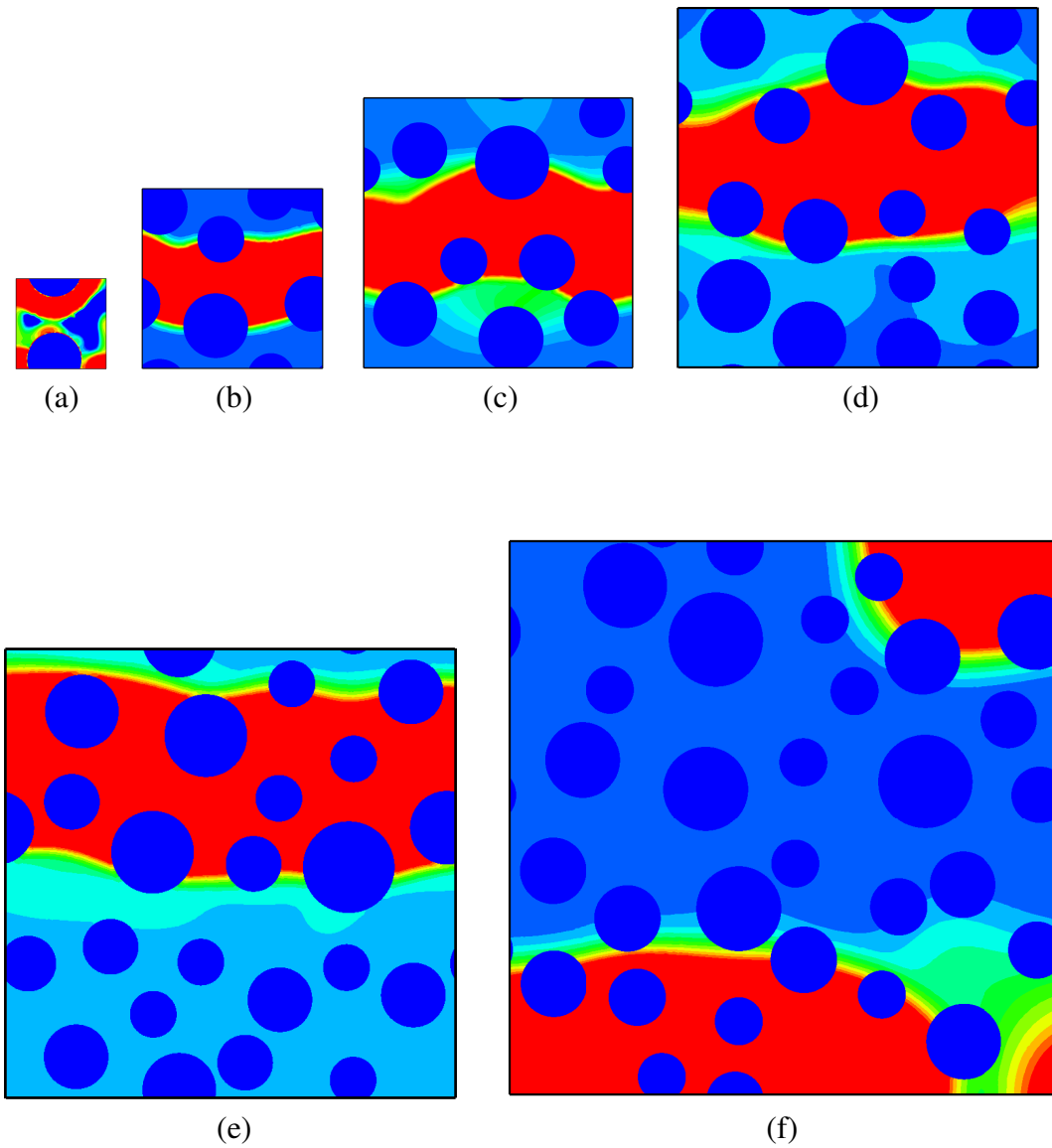


Figure 5.33. Distribution of non-local softening strain measure for various specimen sizes and stress-strain curves of Fig. 5.30b using varying characteristic length averaging approach (reference size  $15 \times 15 \text{ mm}^2$ , characteristic length according to Eq. 5.8, aggregate density  $\rho = 30\%$ )

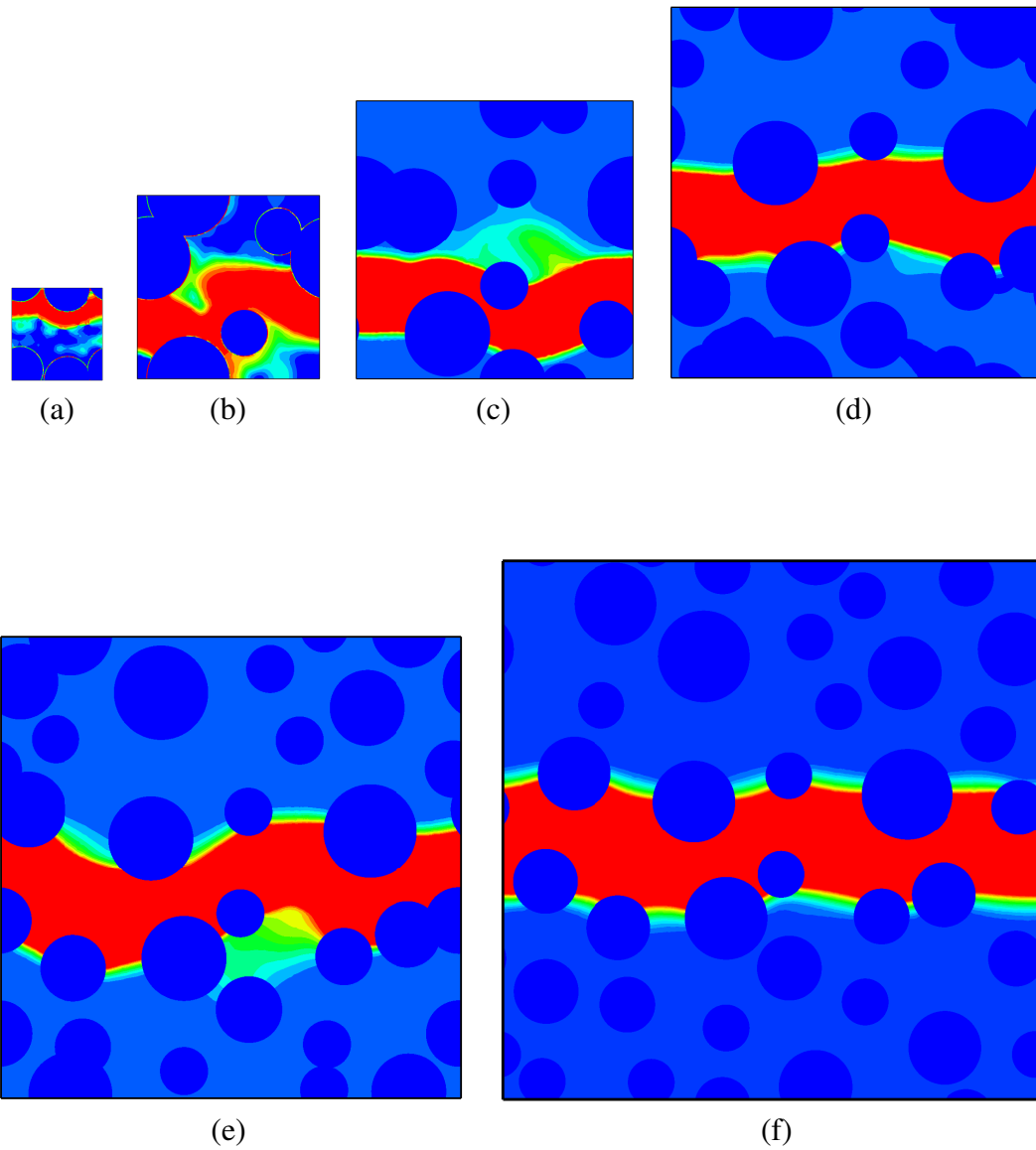


Figure 5.34. Distribution of non-local softening strain measure for various specimen sizes and stress-strain curves of Fig. 5.31a using varying characteristic length averaging approach (reference size  $30 \times 30 \text{ mm}^2$ , characteristic length according to Eq. 5.9, aggregate density  $\rho = 30\%$ )

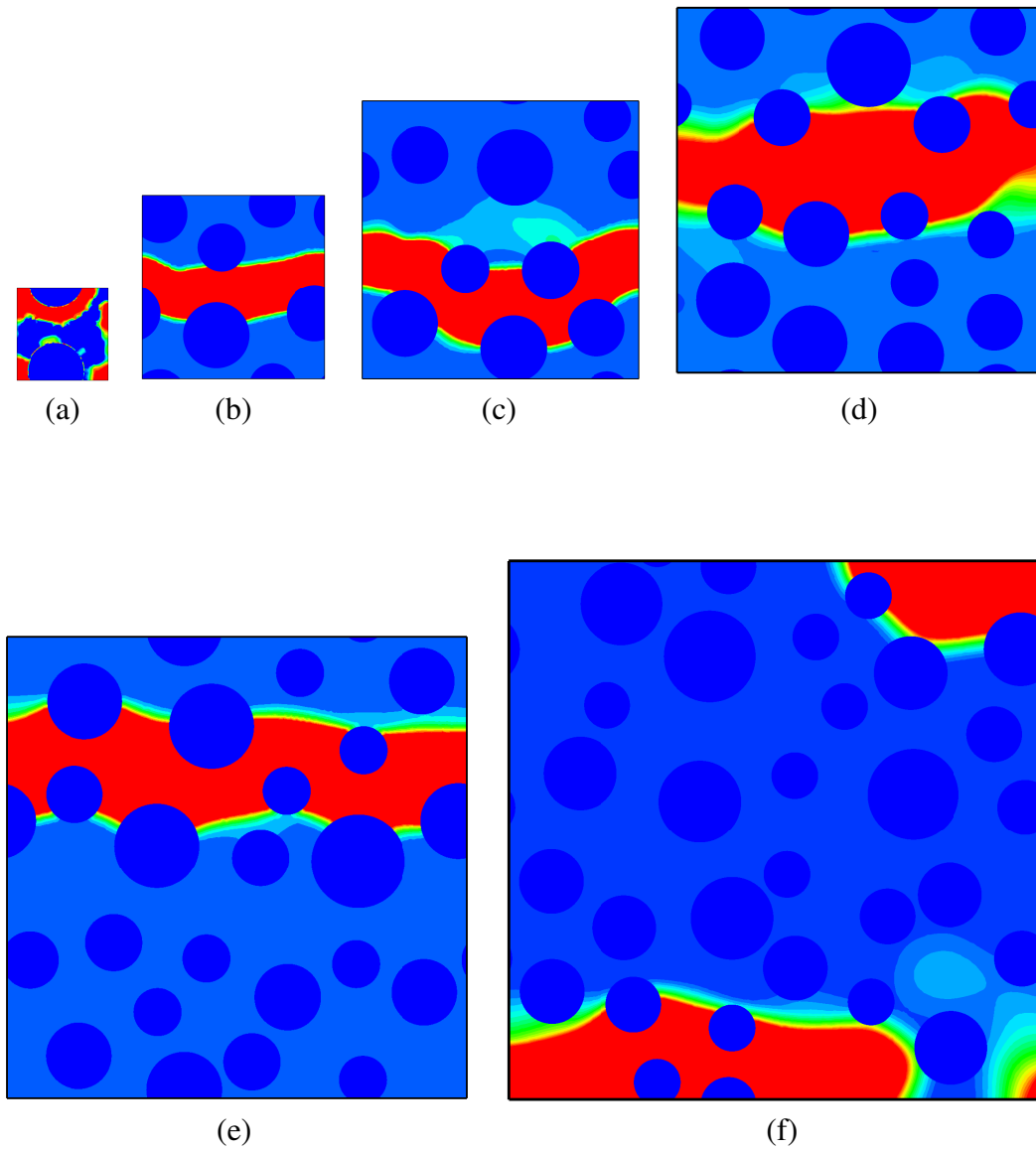
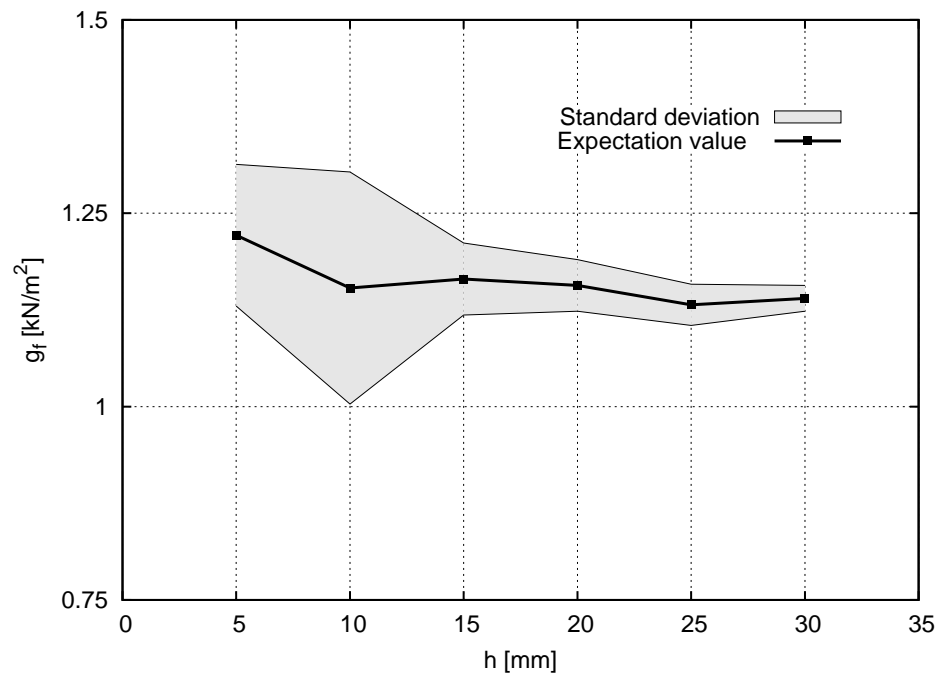


Figure 5.35. Distribution of non-local softening strain measure for various specimen sizes and stress-strain curves of Fig. 5.31b using varying characteristic length averaging approach (reference size  $30 \times 30 \text{ mm}^2$ , characteristic length according to Eq. 5.9, aggregate density  $\rho = 30\%$ )

(a)



(b)

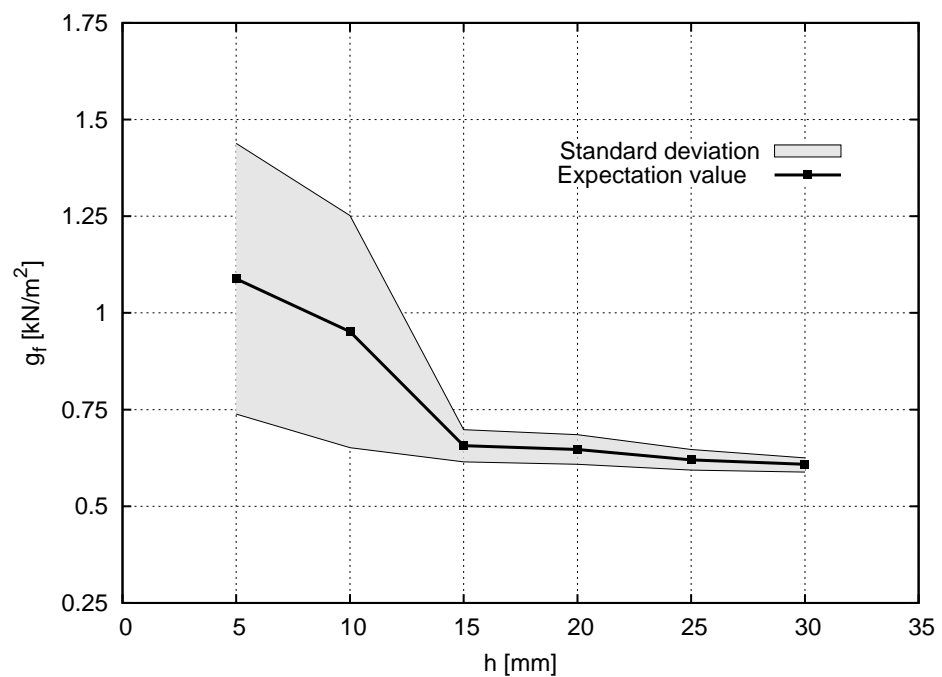


Figure 5.36. Expected value and standard deviation of fracture energy using standard averaging: (a) reference size  $15 \times 15 \text{ mm}^2$ , (b) reference size  $30 \times 30 \text{ mm}^2$  (aggregate density  $\rho = 30\%$ )



## Chapter 6

# Macroscopic – mesoscopic modelling of strain localization

This Chapter describes investigations on strain localization at meso-scale in notched concrete beams subjected to quasi-static three point bending. The simulations were carried out with FEM using isotropic damage constitutive model (with a Rankine failure type criterion and an exponential softening law) enhanced by a characteristic length of micro-structure by means of a non-local theory (Eqs. 2.32, 2.37 and 2.42). Concrete was modelled as a random heterogeneous three-phase material. The effect of the beam size, aggregate distribution, aggregate density, aggregate shape, aggregate size and characteristic length on the width and shape of a localized zone and load-displacement curve was numerically investigated. The numerical results were compared with own laboratory tests results using Digital Image Correlation (Chapter 3), the tests by Le B llego et al. (*Le B llego et al.* [97]) and the size effect law by Ba zant (*Ba zant* [7]).

If the meso-structure of concrete is taken into account, such FE modelling is connected with a very large number of finite elements. To practically solve this problem, a macro-meso connection is used. It is done in a direct way, where a region with strain localization is considered at the meso-scale and a remaining region at the macro-level using a constitutive model. Alternatively, a computational homogenization is made using a multi-scale approach (*Gitman et al.* [67], *Geers et al.* [61], *Kaczmarczyk et al.* [85]). In this approach, the macro-meso connection is used as a constitutive equation on the macro-level. Thus, instead of an explicit formulation of the stress-strain relation, the data from the meso-level is taken into account. The idea of such technique is as follows: the strain from the macro-level goes in the form of boundary conditions to the meso-level, where a heterogeneous material behaviour is modelled, after which the reaction forces to boundary conditions are transformed by means of a homogenization technique (by changing the macro-level constitutive tangent stiffness) as stresses back to the macro-level. Different models for concrete can be used at meso-scale, e.g. discrete (interface element models (*Carol et al.* [33]), lattice approaches (*Kozicki and Tejchman* [95]), discrete element models DEM (*Donze et al.* [50])) or continuum models (with cohesive elements (*Kaczmarczyk et al.* [85]), enhanced by a characteristic length of micro-structure (*Gitman et al.* [67]) or using discontinuities (*Belytschko et al.* [20, 19])).

The combined macro-mesoscopic simulations are similar to a multi-scale approach using a Coupled Volume method where the size of a macro-element equals the size of a meso-cell (to avoid the assumption of any size of RVE) (*Gitman et al.* [67]). However, they are significantly faster because there is no need to move from one to another level.

## 6.1. Input data

Two-dimensional numerical simulations of experiments with notched concrete beams subjected to quasi-static three-point bending (Fig. 3.10) were performed. The deformation was induced by prescribing a vertical displacement at the mid-point of the beam top. Concrete on meso-scale was considered as a three-phase material encompassing cement matrix, aggregate and interfacial transition zones (ITZ) between cement matrix and aggregate (Fig. 6.1). Aggregate was randomly distributed in cement matrix according to a sieve curve. Similarly as in experiments, two different concrete mixes were analysed: sand and gravel concrete (Fig. 3.11). To reduce the number of aggregates in calculations, the size of inclusions varied from  $d_{min} = 0.5$  mm up to  $d_{max} = 3$  mm in sand concrete and from  $d_{min} = 2$  mm up to  $d_{max} = 8$  mm in gravel concrete. Aggregate had mainly a circular shape for the sake of simplicity. The width of ITZs was assumed to be 0.25 mm (*Gitman et al.* [66]). Aggregate was generated according to the method given by Eckardt and Könke (*Eckardt and Könke* [54]). The aggregate density was  $\rho = 30\%$ ,  $\rho = 45\%$  or  $\rho = 60\%$ . The FE-meshes including 12000–1600000 triangular elements were assumed. The calculations were carried out with one set of material parameters for usual concrete, which was prescribed to finite elements corresponding to a specified concrete phase (Tab. 6.1). The interface was assumed to be the weakest component (*Lilliu and van Mier* [99], *Kozicki and Tejchman* [95]). The size of finite elements was:  $s_a = 0.5$  mm (aggregate),  $s_{cm} = 0.5$  mm (cement matrix) and  $s_{ITZ} = 0.1$  mm (interface).

The following numerical calculation program was assumed. First, three beams of a different size were modelled to be as totally homogeneous (as one-phase material). Afterwards, a small-size beam ( $80 \times 320$  mm<sup>2</sup>) of gravel concrete was modelled: as a partially homogeneous and partially heterogeneous with a meso-section in the notch neighbourhood and as an entirely heterogeneous at meso-scale. The width of a heterogeneous meso-scale section  $b_{ms}$  varied between  $D/2$  (40 mm) and  $D$  (80 mm) ( $D$  – beam height). These analyses allowed us to determine a representative width of a required heterogeneous region close to the notch.

Next, the effect of different parameters was studied in a small-size beam. Finally, calculations were carried out with partially heterogeneous beams of a different size to determine a deterministic size effect.

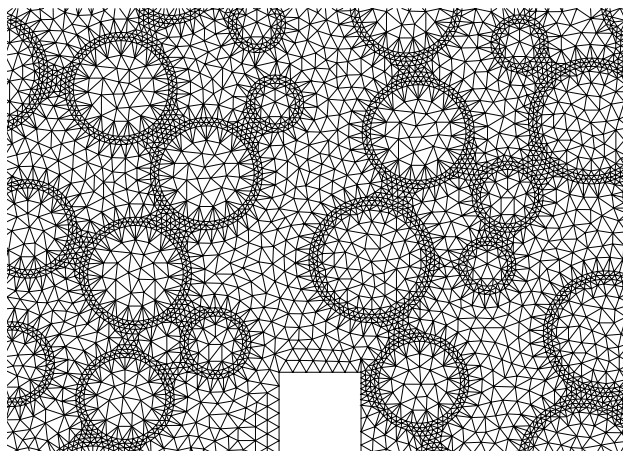


Figure 6.1. Three-phase concrete in the neighbourhood of the notch: aggregate of round shape, cement matrix and interfacial transition zones (ITZ)

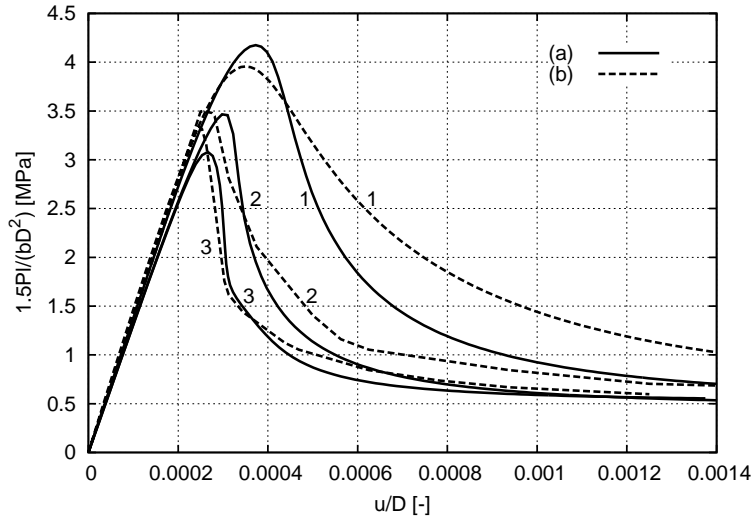


Figure 6.2. Calculated and experimental nominal strength  $1.5Pl/(bD^2)$  versus normalised beam deflection  $u/D$  ( $u$ –beam deflection,  $D$ –beam height): (a) FE–results, (b) experiments by Le Bellégo et al. (Le Bellégo et al. [97]): (1) small–size beam, (2) medium–size beam, (3) large–size beam (homogeneous one–phase material,  $l_c^M = 2$  mm)

Table 6.1. Material properties assumed for FE calculations of concrete beams on meso–scale

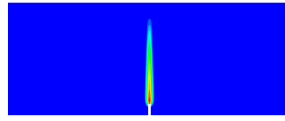
Material parameters	Inclusions	Cement matrix	ITZ
Young’s modulus $E$ [MPa]	40000	35000	20000
Poisson’s ratio $\nu$ [-]	0.2	0.2	0.2
Crack initiation strain $\kappa_0$ [-]	0.5	1E–4	7E–5
Residual stress level $\alpha$ [-]	0.95	0.95	0.95
Slope of softening $\beta$ [-]	200	200	200

Three–five different stochastic realisations were usually performed for the same case. The width of the localized zone above the notch in all beams was measured at the deflection of  $u = 0.15$  mm on the basis of the non–local softening strain measure  $\bar{\epsilon}$  (Eq. 2.63). As the cut–off value,  $\bar{\epsilon}_{min} = 0.025$  was always assumed at the maximum mid–point value of  $\bar{\epsilon}_{max} = 0.08 - 0.13$ .

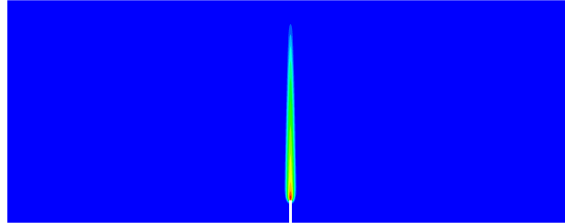
## 6.2. Numerical results

Figure 6.2 presents the numerical results of the nominal strength  $\sigma_N = 1.5Pl/(bD^2)$  of three different concrete beams versus the normalised deflection  $u/D$  ( $P$  – vertical force,  $u$  – beam deflection,  $D$  – beam height,  $b$  – beam width,  $l = 3 \times D$  – beam span) as compared to laboratory tests by Le Bellégo et al. (Le Bellégo et al. [97]). Concrete was treated as an entirely homogeneous one–phase material with the following material constants:  $E = 38500$  MPa,  $\nu = 0.2$ ,  $\kappa_0 = 1.3 \times 10^{-4}$ ,  $\alpha = 0.95$ ,  $\beta = 400$ ,  $l_c^M = 2$  mm (where  $l_c^M$  denotes the macroscopic characteristic length). Totally, 12000–92000 triangular elements were assumed. In turn, Fig. 6.3 shows the distribution of a non–local softening strain measure in beams.

(a)



(b)



(c)

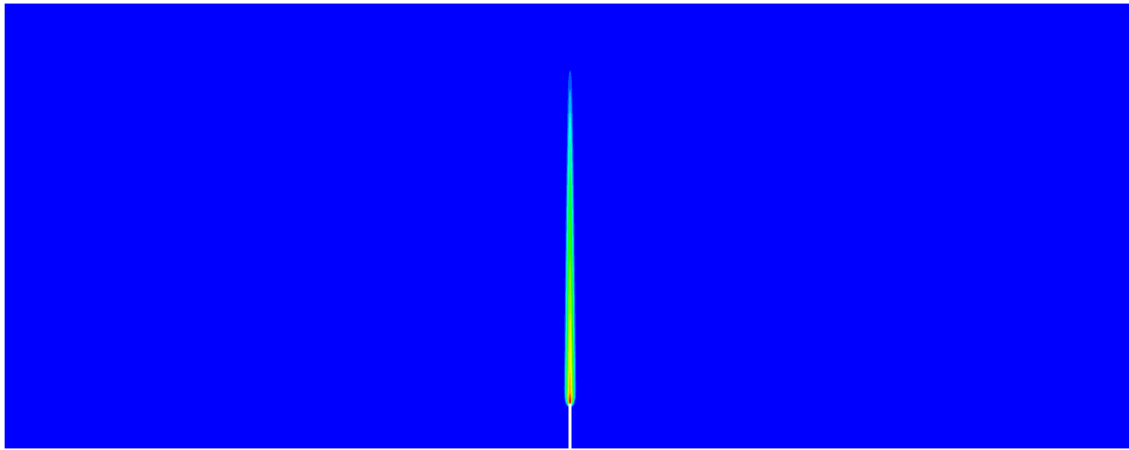


Figure 6.3. Distribution of non-local strain measure above the notch from numerical calculations (at  $u/D = 0.005$ ): (a) small-size beam, (b) medium-size beam, (c) large-size beam (homogeneous one phase material,  $l_c^M = 2$  mm)

The numerical results of strength are in a satisfactory agreement with tests by Le Bellégo et al. (*Le Bellégo et al.* [97]). The deterministic size effect was realistically described (nominal strength and material ductility increase with decreasing beam size). The width of a localized zone above the notch is about  $w_c = 6$  mm ( $u/D = 0.0005$ ) and approximately corresponds to the measured maximum value of  $w_c = 5.5$  mm by DIC (Fig. 3.17). However, in contrast to experiments, the calculated localized zones are always straight. Even an assumption of a stochastic distribution of tensile strength near the notch did not significantly affect their shape Fig. 6.4 (*Bobniński et al.* [28]).

Figure 6.5 demonstrates the load–deflection curves obtained for two different aggregate distributions to determine a realistic width of a meso-scale region close to the notch (to reduce computation time). Concrete was treated in a meso-scale as a random three-phase heterogeneous material with circularly-shaped aggregate using material constants from Tab. 6.1. In the remaining region, material was homogeneous one-phase material ( $E = 38500$  MPa,  $\nu = 0.2$ ,  $\kappa_0 = 1.3 \times 10^{-4}$ ,  $\alpha = 0.95$ ,  $\beta = 400$ ). The beam size was  $80 \times 320$  mm<sup>2</sup>. The width

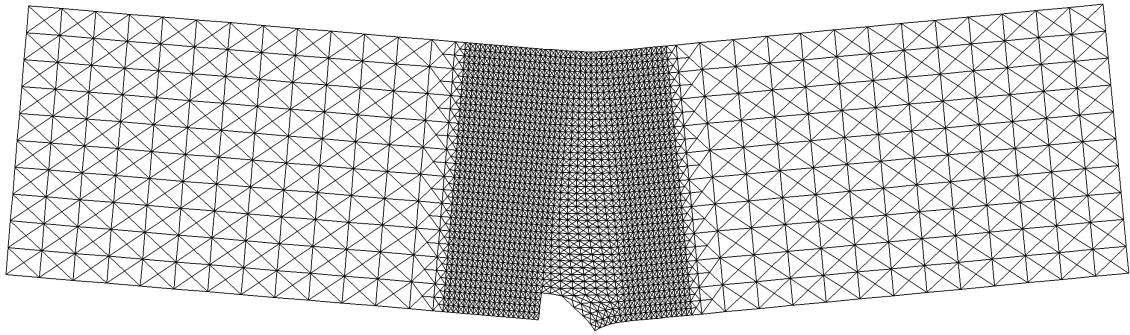


Figure 6.4. Deformed FE mesh for a small-size beam  $80 \times 320 \text{ mm}^2$  with random spatially correlated distribution of tensile strength (Bobiński *et al* [28])

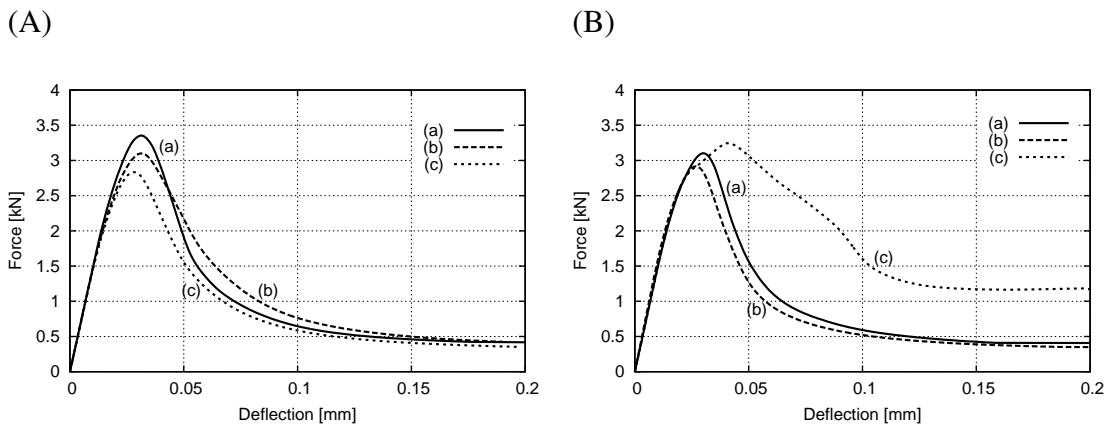


Figure 6.5. Calculated force–deflection curves for two different random distributions of aggregate in small-size beam of gravel concrete ( $d_{50} = 2 \text{ mm}$ ,  $d_{max} = 8 \text{ mm}$ ,  $l_c^m = 1.5 \text{ mm}$ ): (a) entirely heterogeneous, (b) partially heterogeneous beam with width of meso-scale section of  $b_{ms} = 80 \text{ mm}$ , (c) partially heterogeneous beam with width of the meso-scale section of  $b_{ms} = 40 \text{ mm}$

of a meso-scale region was  $b_{ms} = 40 \text{ mm}$  or  $b_{ms} = 80 \text{ mm}$  (Fig. 6.6). Totally 65000–110000 finite elements were assumed. The characteristic length was  $l_c^m = 1.5 \text{ mm}$  and the aggregate density was  $\rho = 30\%$ . An entirely heterogeneous beam with 365000 elements served as the reference beam. For comparison, a stochastic distribution of aggregate was always the same in a meso-scale section. Figure 6.7 shows the distribution of a non-local softening parameter above the notch.

The results show that the effect of the width of the meso-scale region on the results can be significant if  $b_{ms} < D/2$  (Figs. 6.5B and 6.7B). However, when the width of the meso-scale region close to the notch equals  $b_{ms} = D = 80 \text{ mm}$ , the results of forces and strains with an entirely and a partially heterogeneous beam are similar. In further calculations to save computational time, a representative meso-scale section was assumed to be always equal to the beam height  $b_{ms} = D$  (i.e. 80 mm for a small-size beam, 160 mm for a medium-size beam and 320 mm for a large-size beam).

The effect of the aggregate distribution on the load–deflection diagram and strain localization is shown in Figs. 6.8–6.11 (beam size  $80 \times 320 \text{ mm}^2$ ) with material constants from Tab. 6.1 ( $l_c^m = 1.5 \text{ mm}$ ). The aggregate density was  $\rho = 30\%$  or  $\rho = 45\%$  for sand concrete

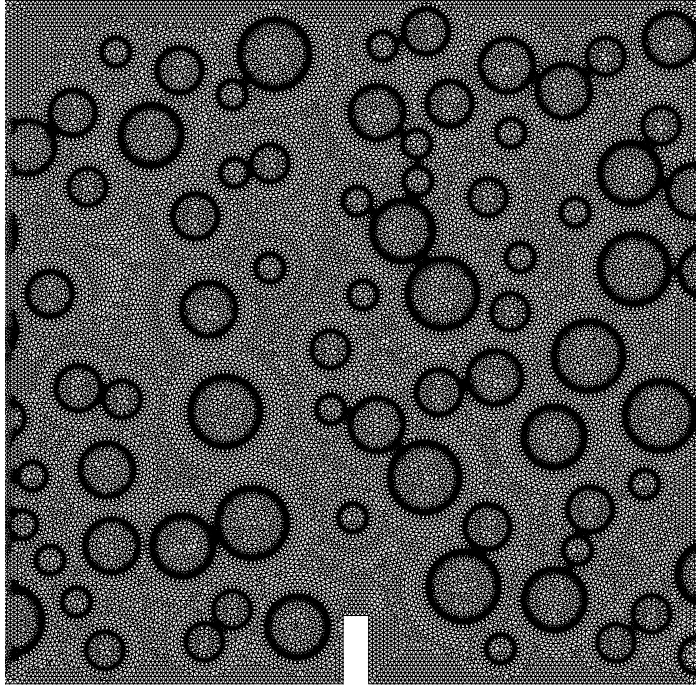


Figure 6.6. FE-mesh used for calculations (small-size beam  $80 \times 320 \text{ mm}^2$ ) in the meso-scale region ( $b_{ms} = D$ ,  $\rho = 30\%$ )

( $d_{50} = 0.5 \text{ mm}$  and  $d_{max} = 3 \text{ mm}$ ) and for gravel concrete ( $d_{50} = 2 \text{ mm}$  and  $d_{max} = 8 \text{ mm}$ ) respectively.

The load–displacement curves are the same in an almost entire elastic regime independently of the distribution of inclusions. However, they can be significantly different after the peak is reached (Figs. 6.8 and 6.10) due to a localized zone propagating between aggregate distributed at random. The localized zone is always non-symmetric and curved. The width of the calculated localized zone is approximately  $w_c = (4 \times l_c^m) = 6 \text{ mm}$  ( $\rho = 30\%$ ) and  $w_c = (3 \times l_c^m) = 4.5 \text{ mm}$  ( $\rho = 45\%$ ) independently of  $d_{50}$ , what is in agreement with own experiments (Figs. 3.15 and 3.16). Calculated localized zone creates at  $u/D = 0.0002$  and its width linearly increases during deformation (as in the experiment).

Figures 6.12–6.14 demonstrate the effect of the aggregate size and aggregate density in sand concrete ( $d_{50} = 0.5 \text{ mm}$  and  $d_{max} = 3 \text{ mm}$ ) and gravel concrete ( $d_{50} = 2 \text{ mm}$  and  $d_{max} = 8 \text{ mm}$ ) for a small-size beam ( $80 \times 320 \text{ mm}^2$ ) using aggregate density  $\rho = 30\%$ ,  $\rho = 45\%$  and  $\rho = 60\%$  ( $l_c^m = 1.5 \text{ mm}$ ). With increasing maximum aggregate and aggregate density, beam strength slightly increases (by 10–25%, Fig. 6.13). The width of a localized zone does not depend on the maximum aggregate size  $d_{max}$ . This outcome is in contrast to statements by Pijauder–Cabot and Bažant (*Pijauder–Cabot and Bažant* [136]) and Bažant and Oh (*Bažant and Oh* [12]) wherein the width of the localized zone was estimated to be about  $3 \times d_{max}$ . It is also in contrast to experimental results by Mihashi and Nomura (*Mihashi and Nomura* [118]) who have shown that the width of a localized zone in the case of normal concrete increases with increasing aggregate size. The width of the localized zone is influenced by aggregate density; the localized zone becomes narrower with increasing aggregate density:  $w_c = 6 \text{ mm}$  at  $\rho = 30\%$ ,  $w_c = 4.5 \text{ mm}$  at  $\rho = 45\%$ ,  $w_c = 3 \text{ mm}$  at  $\rho = 60\%$ ). The calculated results of  $w_c$  compare well with the experimental ones (Fig. 3.17). This means that a characteristic length

of micro-structure may be also related to the grain size of cement matrix. The shape of a localized zone is affected by  $d_{50}$  ( $d_{max}$ ) and  $\rho$  (in particular for  $\rho = 60\%$ ).

The effect of the aggregate shape in a small-size beam ( $80 \times 320 \text{ mm}^2$ ) of sand ( $d_{50} = 0.5 \text{ mm}$  and  $d_{max} = 3 \text{ mm}$ ) and gravel concrete ( $d_{50} = 2 \text{ mm}$  and  $d_{max} = 8 \text{ mm}$ ) is shown in Figs. 6.15 and 6.17 ( $\rho = 30\%$ ,  $\rho = 45\%$ ,  $\rho = 60\%$ ,  $l_c^m = 1.5 \text{ mm}$ ). The results with circular-shaped and angular-shaped aggregate (Fig. 6.16) are compared. The beam strength is slightly higher for beams with angular-shape aggregate (up to 10%), Fig. 6.15. However, the shape of the localized zone and material softening are significantly affected by the aggregate shape (Fig. 6.17).

The effect of the characteristic length of micro-structure on the load-deflection diagram and strain localization is shown in Figs. 6.18–6.21 using the same stochastic distribution of aggregate. Figures 6.18 and 6.20 demonstrate the influence of  $l_c$  on the evolution of load-deflection curves for two different mixes: sand concrete ( $d_{50} = 0.5 \text{ mm}$  and  $d_{max} = 3 \text{ mm}$ ) with aggregate density  $\rho = 30\%$ , and gravel concrete ( $d_{50} = 2 \text{ mm}$  and  $d_{max} = 8 \text{ mm}$ ) with aggregate density  $\rho = 45\%$ , respectively.

In turn, Figs. 6.19 and 6.21 present the distribution of a non-local softening strain measure above the notch for various  $l_c$  changing between 0.1 mm and 5.0 mm. With increasing characteristic length, both beam strength and width of the localized zone obviously increase. The material softening decreases and material becomes more ductile. A pronounced deterministic size effect occurs. The localized zone propagating in a cement matrix between aggregate grains is strongly curved at  $l_c^m = 0.1 - 2.5 \text{ mm}$ , whereas it becomes more straight at  $l_c^m > 2.5 \text{ mm}$ . The width of the localized zone,  $w_c = (3 - 4) \times l_c^m = 4.5 - 6.0 \text{ mm}$  with  $l_c^m = 1.5 \text{ mm}$  and  $\rho = 30 - 45\%$ , ( $l_c^m = 0.5 \times d_{max}$  for sand concrete and  $l_c^m = 0.2 \times d_{max}$  for gravel concrete), is in good accordance with the experimental width of the localized zone on the surface of notched beams (3.5–5.5 mm, Fig. 3.17).

The effect of the beam size is presented in Figs. 6.22 and 6.23. Figure 6.22 shows the numerical results of the nominal strength  $\sigma_N = 1.5Pl/(bD^2)$  versus the normalised deflection  $u/D$  for three different concrete beams compared to tests by Le Bellęgo et al. (*Le Bellęgo et al.* [97]). Concrete was treated as a one-phase material with a heterogeneous three-phase close to the notch ( $b_{ms} = D$ ) with material constants from Tab. 6.1. The following amount of finite elements was used: 110000 (small-size beam), 420000 (medium-size beam) and 1600000 (large-size beam). In turn, Fig. 6.23 presents the distribution of non-local softening strain measure in beams. The calculations were carried out with gravel concrete  $d_{max} = 8 \text{ mm}$ , aggregate density  $\rho = 30\%$  and characteristic length  $l_c^m = 1.5 \text{ mm}$ .

The results are in a satisfactory agreement with tests by Le Bellęgo et al. (*Le Bellęgo et al.* [97]). The deterministic size effect is realistically modelled in calculations. The width of the localized zone above the notch at  $u/D = 0.0005$  is 6 mm for all beam sizes. The localized zone propagating between aggregate is always strongly curved, what satisfactory reflects the experimental results (Figs. 3.15 and 3.16).

Figure 6.24 shows a comparison between the measured and calculated size effect for concrete beams. In addition, the results of a deterministic size effect law by Bažant (*Bažant and Planas* [16], *Bažant* [7]) are enclosed (which is valid for structures with pre-existing notches) (Eq. 3.5).

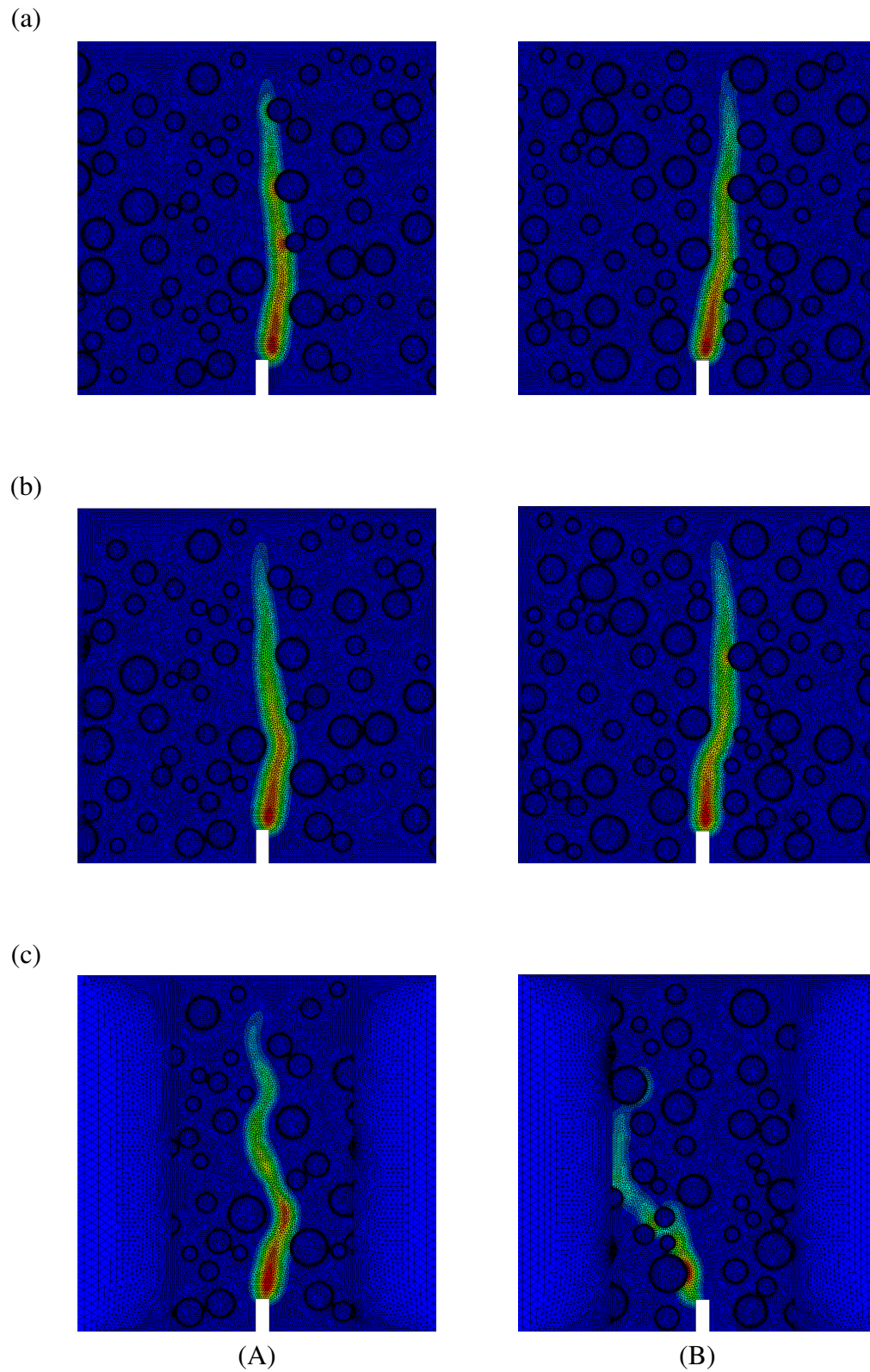


Figure 6.7. Calculated distribution of non-local strain measure above the notch (small-size beam  $80 \times 320$  mm,  $l_c^m = 1.5$  mm) for gravel concrete ( $d_{50} = 2$  mm,  $d_{max} = 8$  mm): (a) entirely heterogeneous beam, (b) partially heterogeneous beam with width of meso-scale section of  $b_{ms} = 80$  mm, (c) partially heterogeneous beam with width of the meso-scale section of  $b_{ms} = 40$  mm

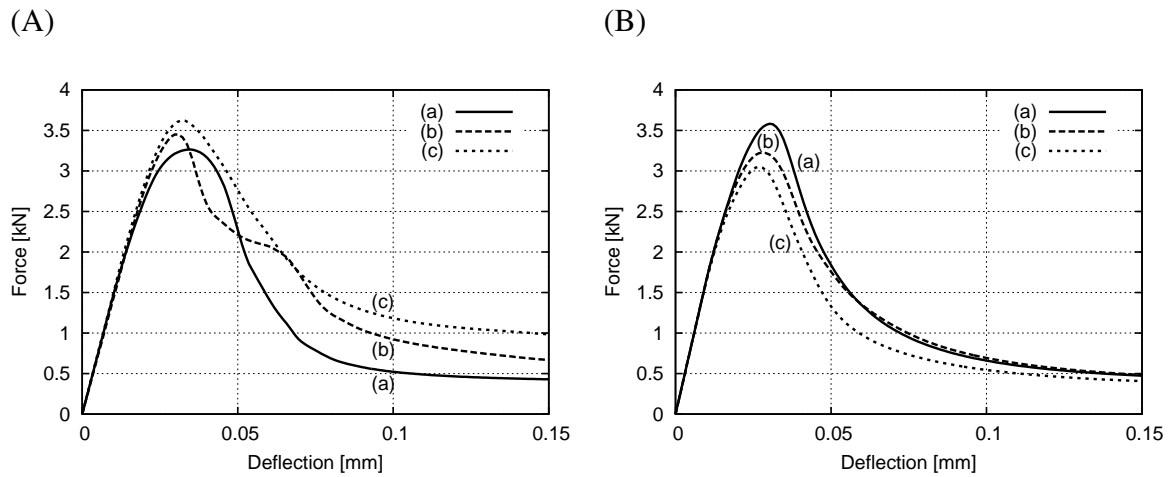


Figure 6.8. Calculated load–deflection curves for two concrete mixes and three random distributions of aggregate (curves (a), (b), (c)) in a small–size beam  $80 \times 320 \text{ mm}^2$  ( $l_c^m = 1.5 \text{ mm}$ ,  $\rho = 30\%$ ): (A) sand concrete ( $d_{50} = 0.5 \text{ mm}$ ,  $d_{max} = 3 \text{ mm}$ ), (B) gravel concrete ( $d_{50} = 2 \text{ mm}$ ,  $d_{max} = 8 \text{ mm}$ )

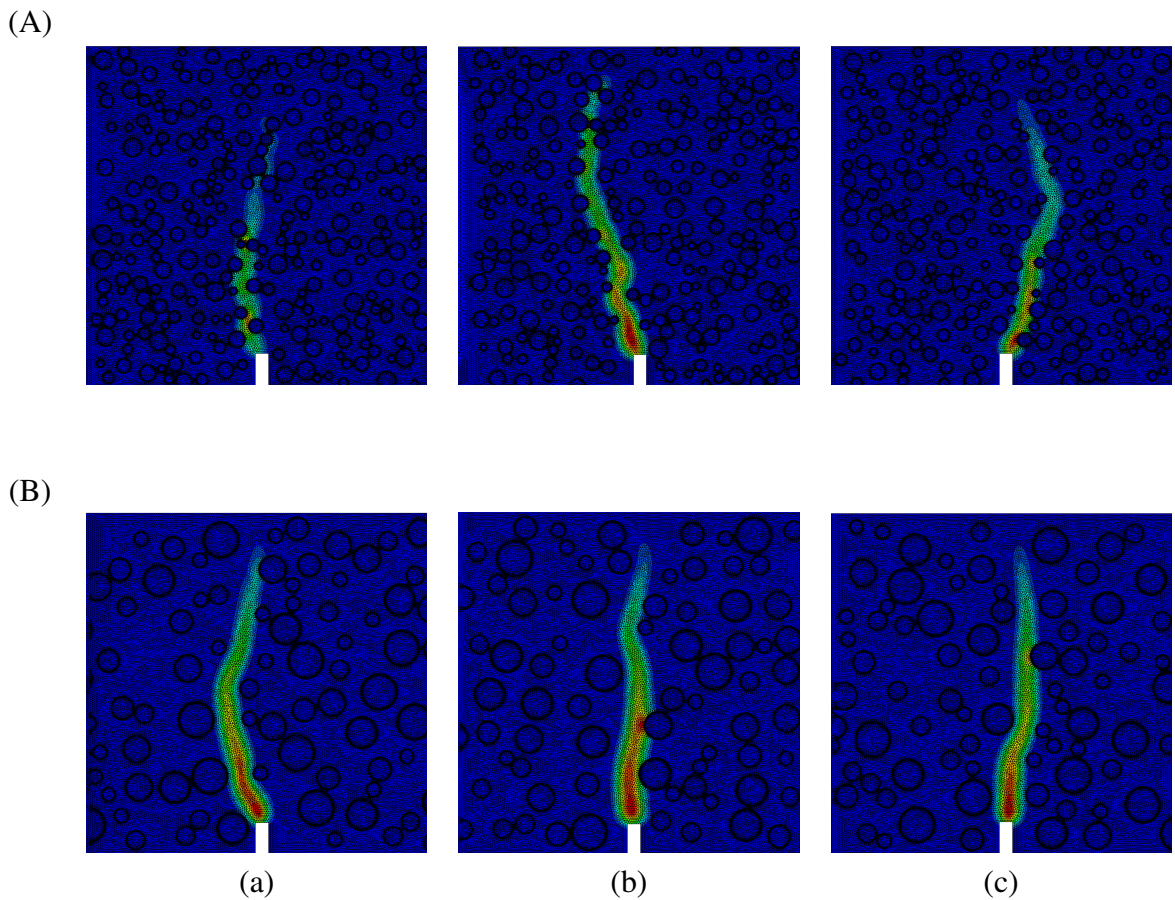


Figure 6.9. Calculated distribution of non–local strain measure for various concrete mixes and three random distributions of aggregate: (a), (b), (c) in small–size beam corresponding to load–deflection curves of Fig. 6.8 ( $l_c^m = 1.5 \text{ mm}$ ,  $\rho = 30\%$ ): (A) sand concrete ( $d_{50} = 0.5 \text{ mm}$ ,  $d_{max} = 3 \text{ mm}$ ), (B) gravel concrete ( $d_{50} = 2 \text{ mm}$ ,  $d_{max} = 8 \text{ mm}$ )

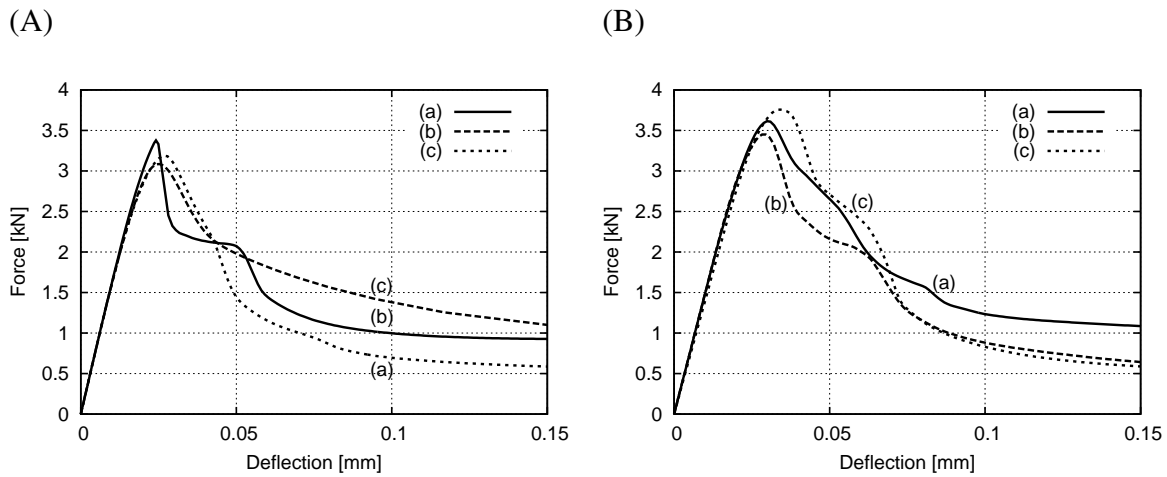


Figure 6.10. Calculated load–deflection curves for two concrete mixes and three random distributions of aggregate (curves (a), (b), (c)) in a small–size beam  $80 \times 320$  mm<sup>2</sup> ( $l_c^m = 1.5$  mm,  $\rho = 45\%$ ): (A) sand concrete ( $d_{50} = 0.5$  mm,  $d_{max} = 3$  mm), (B) gravel concrete ( $d_{50} = 2$  mm,  $d_{max} = 8$  mm)

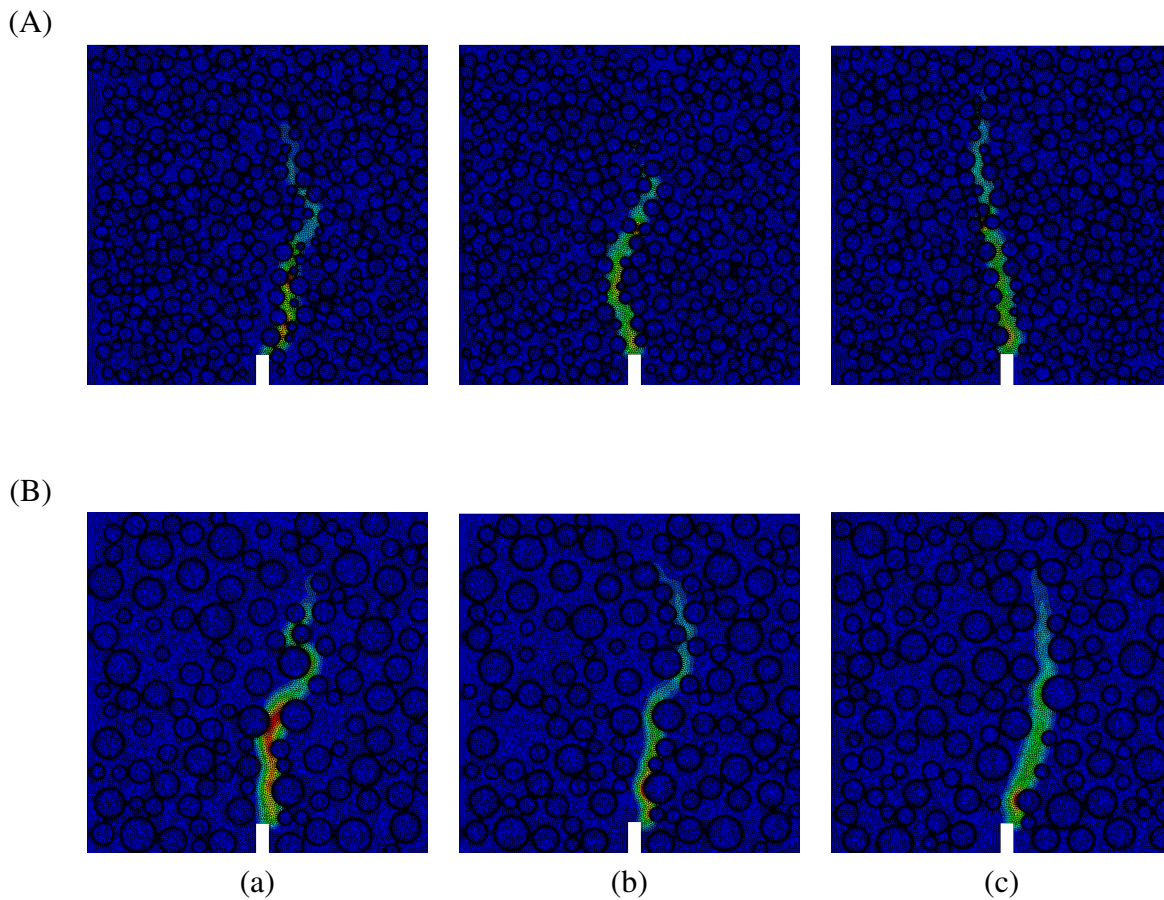


Figure 6.11. Calculated distribution of non–local strain measure for various concrete mixes and three random distributions of aggregate: (a), (b), (c) in small–size beam corresponding to load–deflection curves of Fig. 6.10 ( $l_c^m = 1.5$  mm,  $\rho = 45\%$ ): (A) sand concrete ( $d_{50} = 0.5$  mm,  $d_{max} = 3$  mm), (B) gravel concrete ( $d_{50} = 2$  mm,  $d_{max} = 8$  mm)

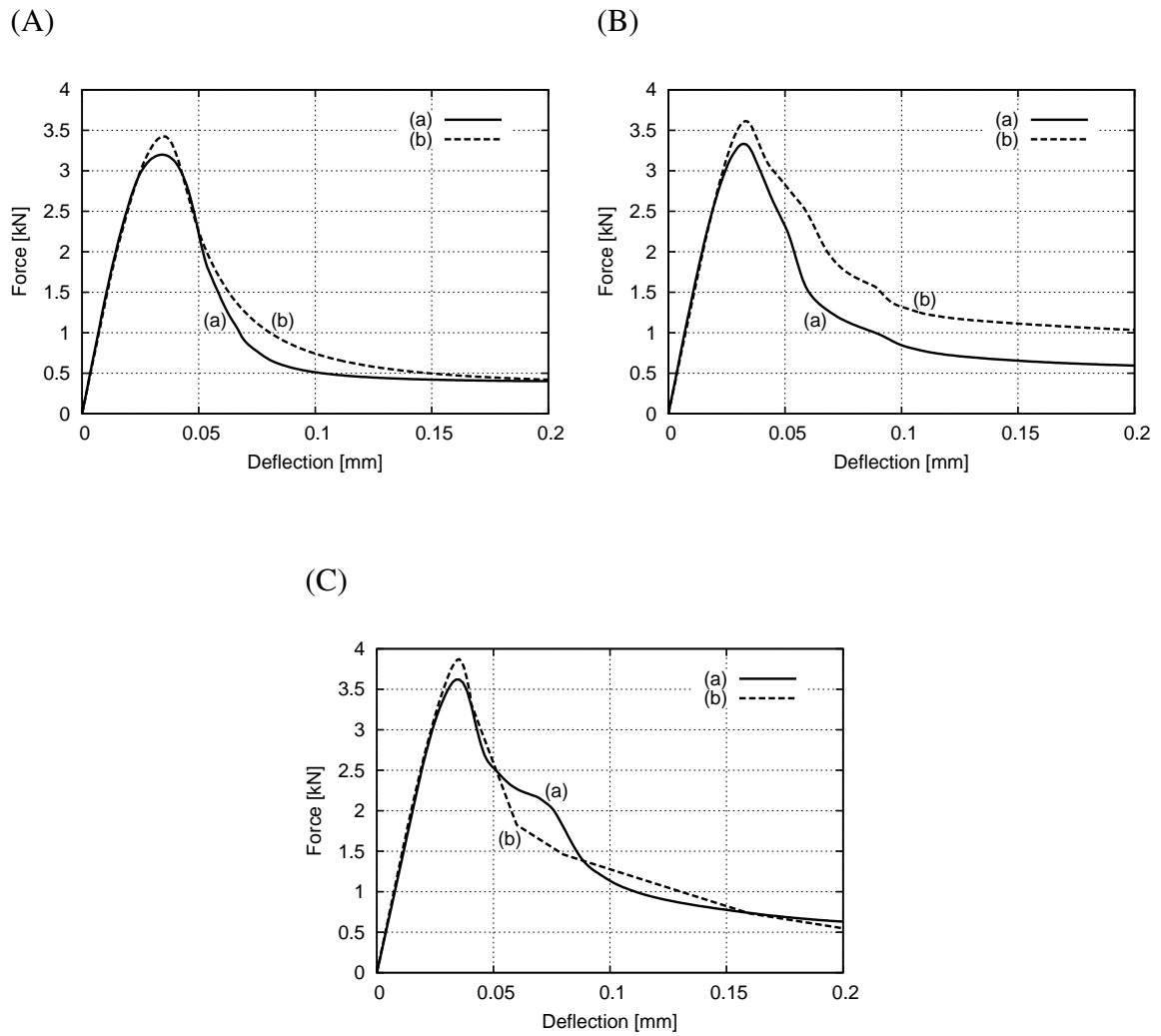


Figure 6.12. Calculated load–deflection curves for different aggregate densities (small–size beam  $80 \times 320 \text{ mm}^2$ ): (A)  $\rho = 30\%$ , (B)  $\rho = 45\%$ , (C)  $\rho = 60\%$ , (a) sand concrete ( $d_{50} = 0.5 \text{ mm}$ ,  $d_{max} = 3 \text{ mm}$ ), (b) gravel concrete ( $d_{50} = 2 \text{ mm}$ ,  $d_{max} = 8 \text{ mm}$ )

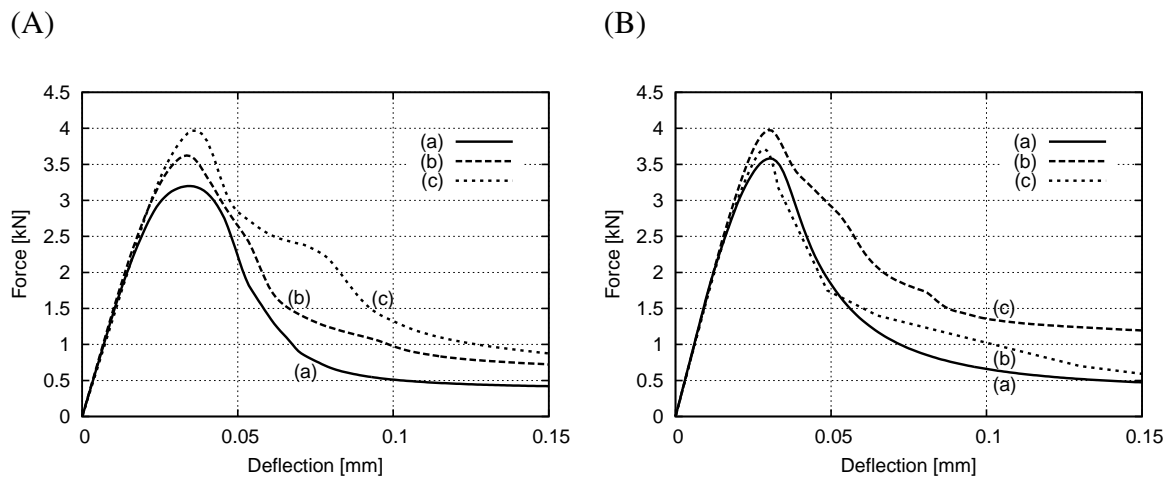


Figure 6.13. Calculated load–deflection curves (small–size beam  $80 \times 320 \text{ mm}^2$ ): (A) sand concrete ( $d_{50} = 0.5 \text{ mm}$ ,  $d_{max} = 3 \text{ mm}$ ), (B) gravel concrete ( $d_{50} = 2 \text{ mm}$ ,  $d_{max} = 8 \text{ mm}$ ), (a)  $\rho = 30\%$ , (b)  $\rho = 45\%$ , (c)  $\rho = 60\%$

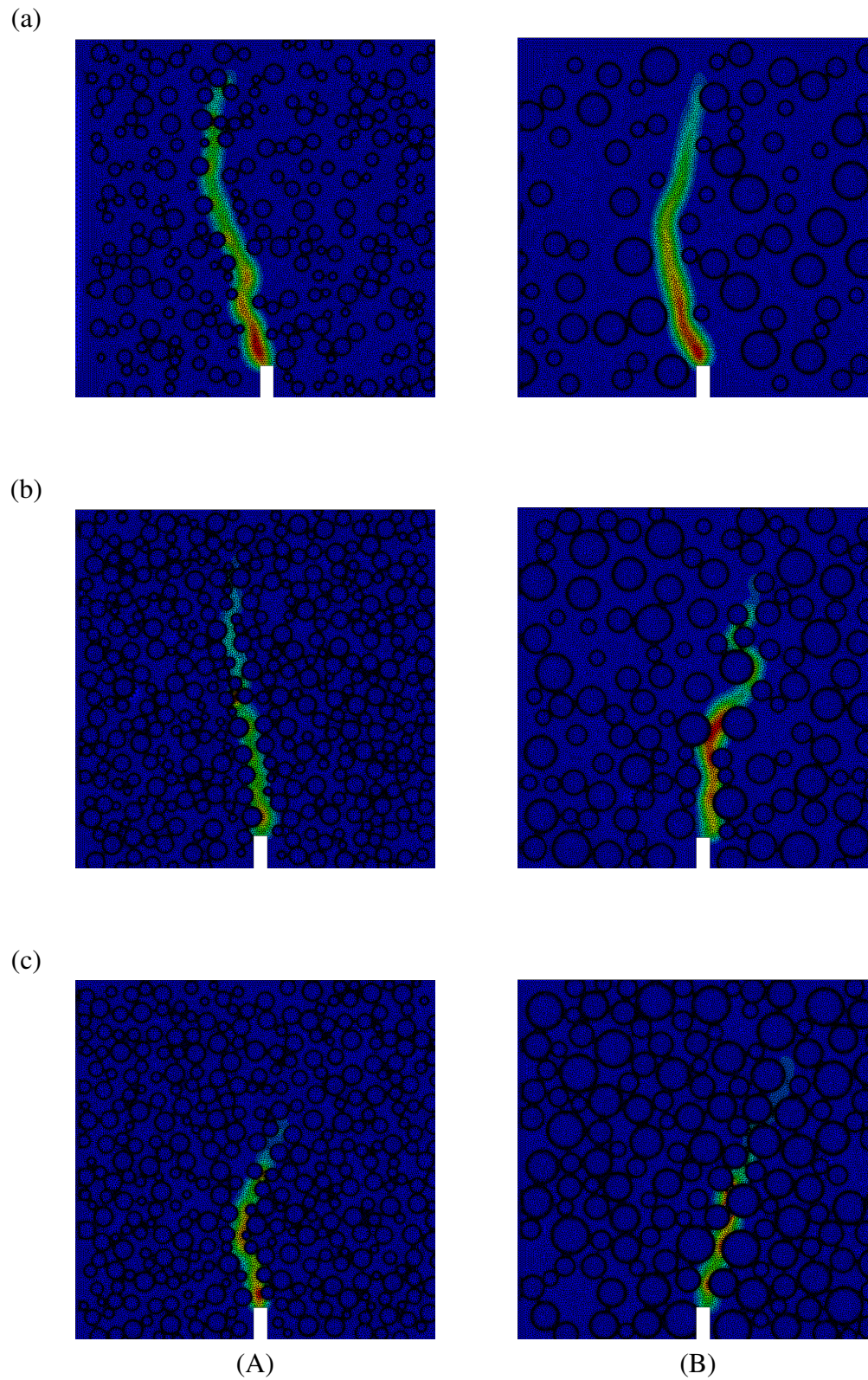


Figure 6.14. Calculated distribution of non-local strain measure for different aggregate densities (small-size beam  $80 \times 320 \text{ mm}^2$ ): (a)  $\rho = 30\%$ , (b)  $\rho = 45\%$ , (c)  $\rho = 60\%$ , (A) sand concrete ( $d_{50} = 0.5 \text{ mm}$ ,  $d_{max} = 3 \text{ mm}$ ), (B) gravel concrete ( $d_{50} = 2 \text{ mm}$ ,  $d_{max} = 8 \text{ mm}$ )

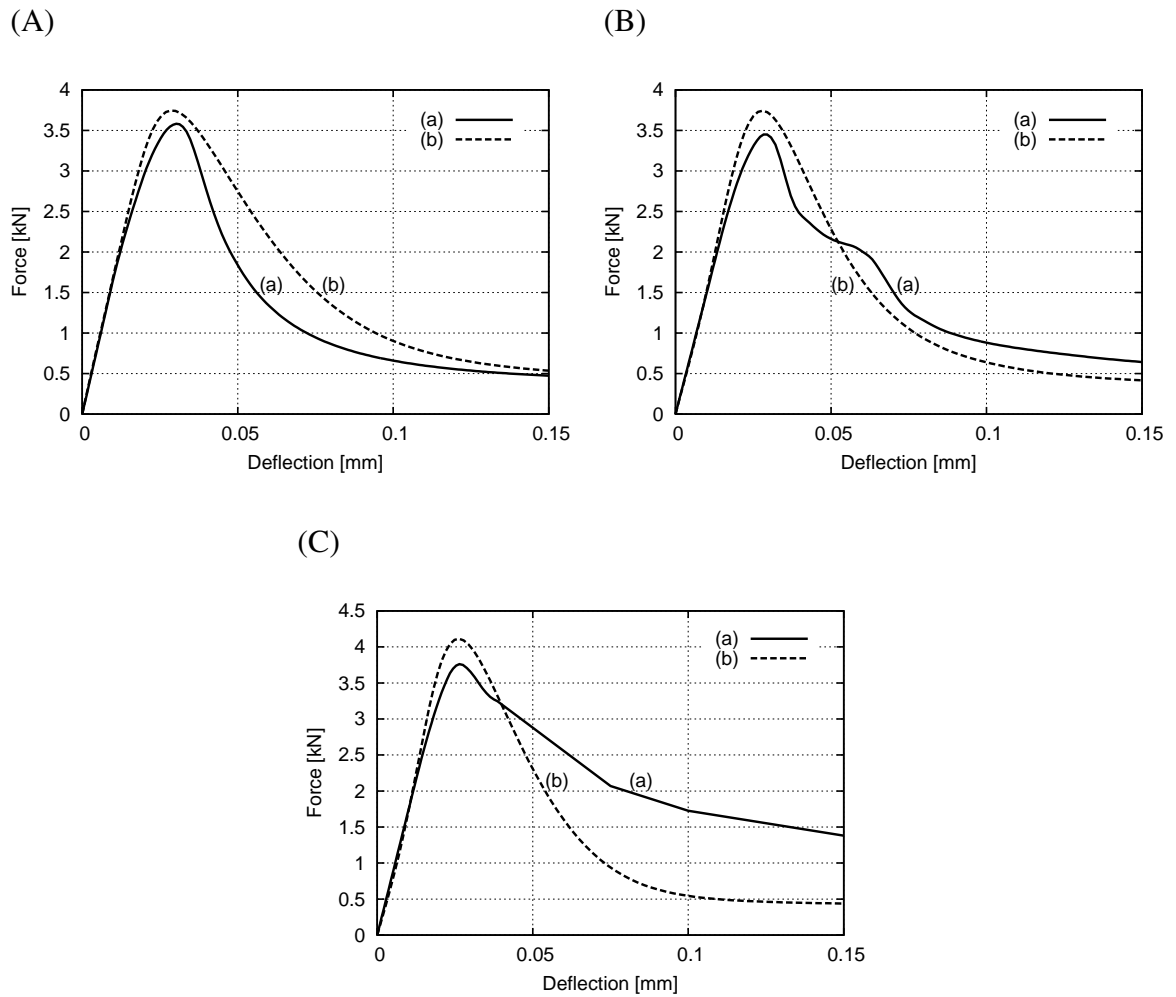


Figure 6.15. Calculated load–deflection diagrams (small–size beam  $80 \times 320 \text{ mm}^2$ ): (a) aggregate of circular shape, (b) aggregate of angular shape for different aggregate densities: (A)  $\rho = 30\%$ , (B)  $\rho = 45\%$ , (C)  $\rho = 60\%$  ( $l_c^m = 1.5 \text{ mm}$ )

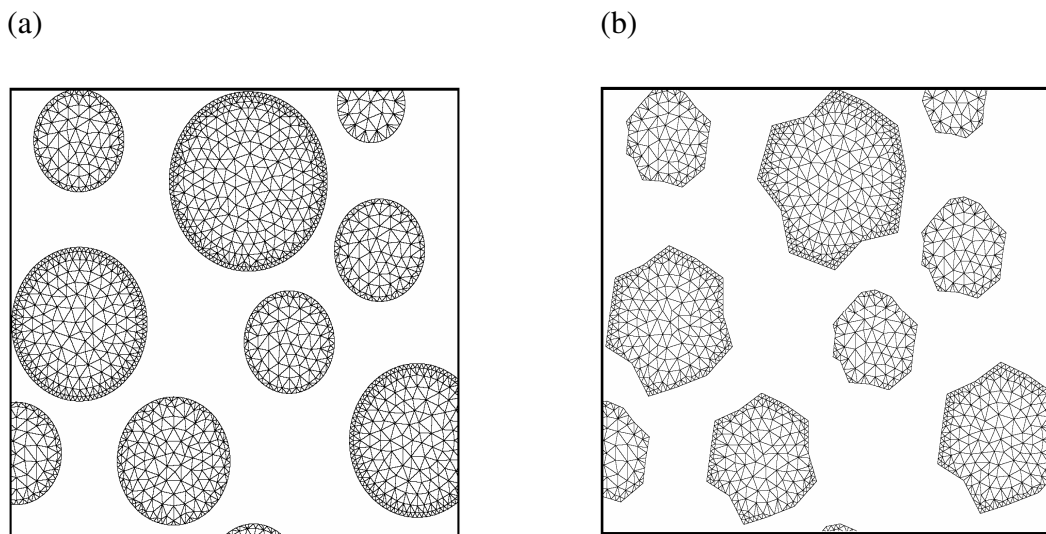
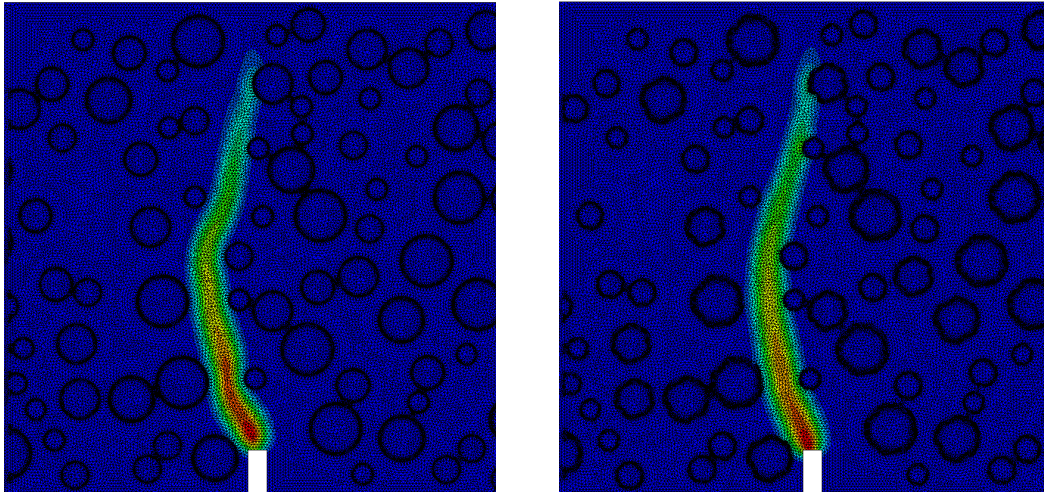
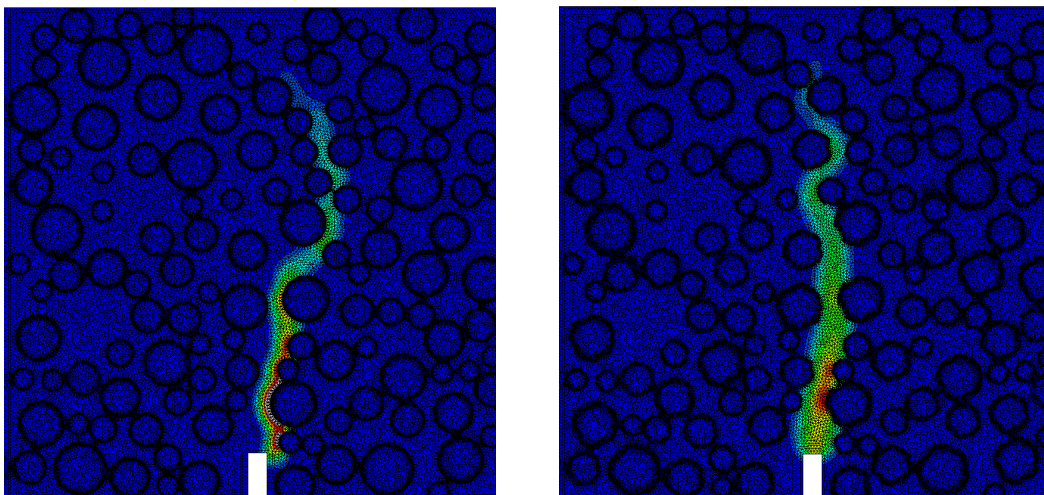


Figure 6.16. Shape of aggregate used in calculations ( $\rho = 30\%$ ): (a) circular aggregate, (b) angular aggregate

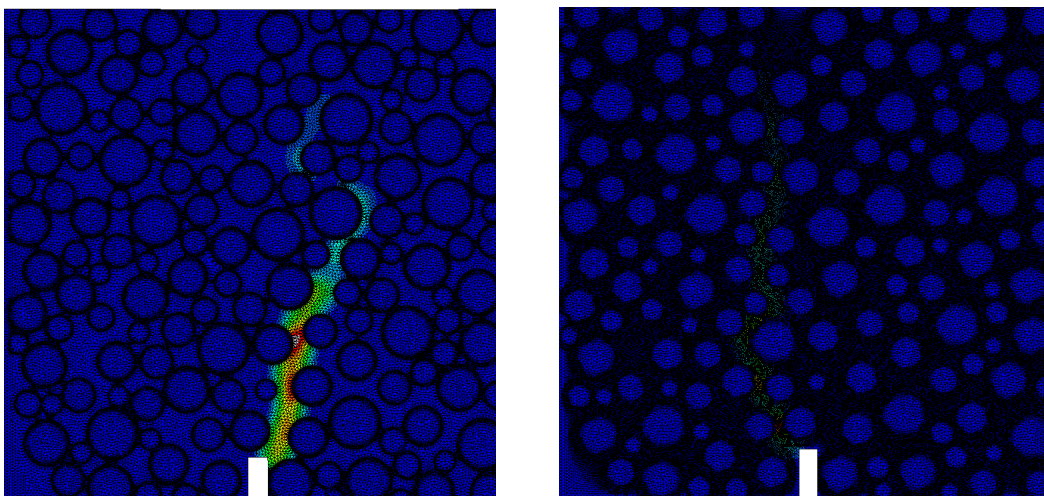
(a)



(b)



(c)



(A)

(B)

Figure 6.17. Calculated distribution of non-local strain measure above notch (small-size beam  $80 \times 320 \text{ mm}^2$ ): (A) aggregate of circular shape, (B) aggregates of angular shape, (a)  $\rho = 30\%$ , (b)  $\rho = 45\%$ , (c)  $\rho = 60\%$  ( $l_c = 1.5 \text{ mm}$ )

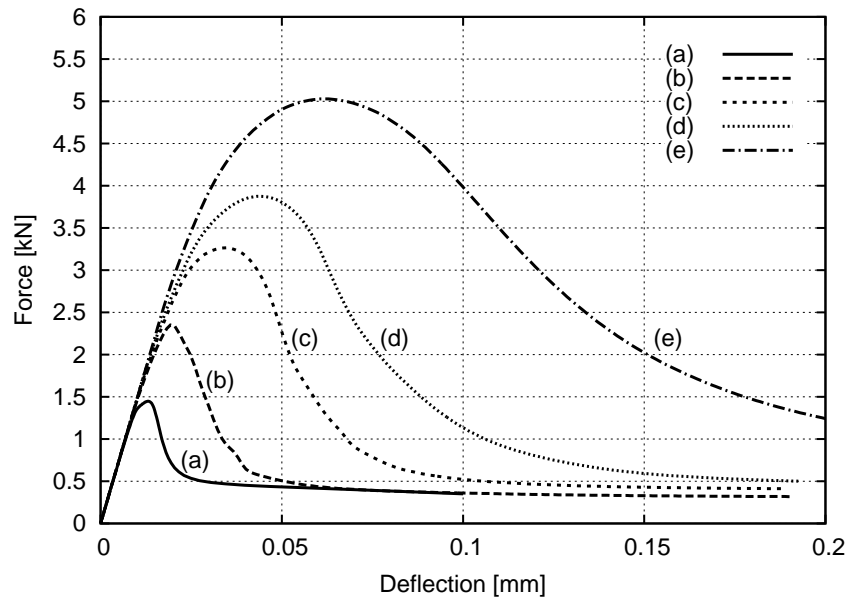


Figure 6.18. Calculated load–deflection curves for different characteristic lengths: (a)  $l_c^m = 0.1$  mm, (b)  $l_c^m = 0.5$  mm, (c)  $l_c^m = 1.5$  mm, (d)  $l_c^m = 2.5$  mm, (e)  $l_c^m = 5.0$  mm (small–size beam  $80 \times 320$  mm<sup>2</sup>, sand concrete  $d_{50} = 0.5$  mm,  $d_{max} = 3$  mm, aggregate density  $\rho = 30\%$ )

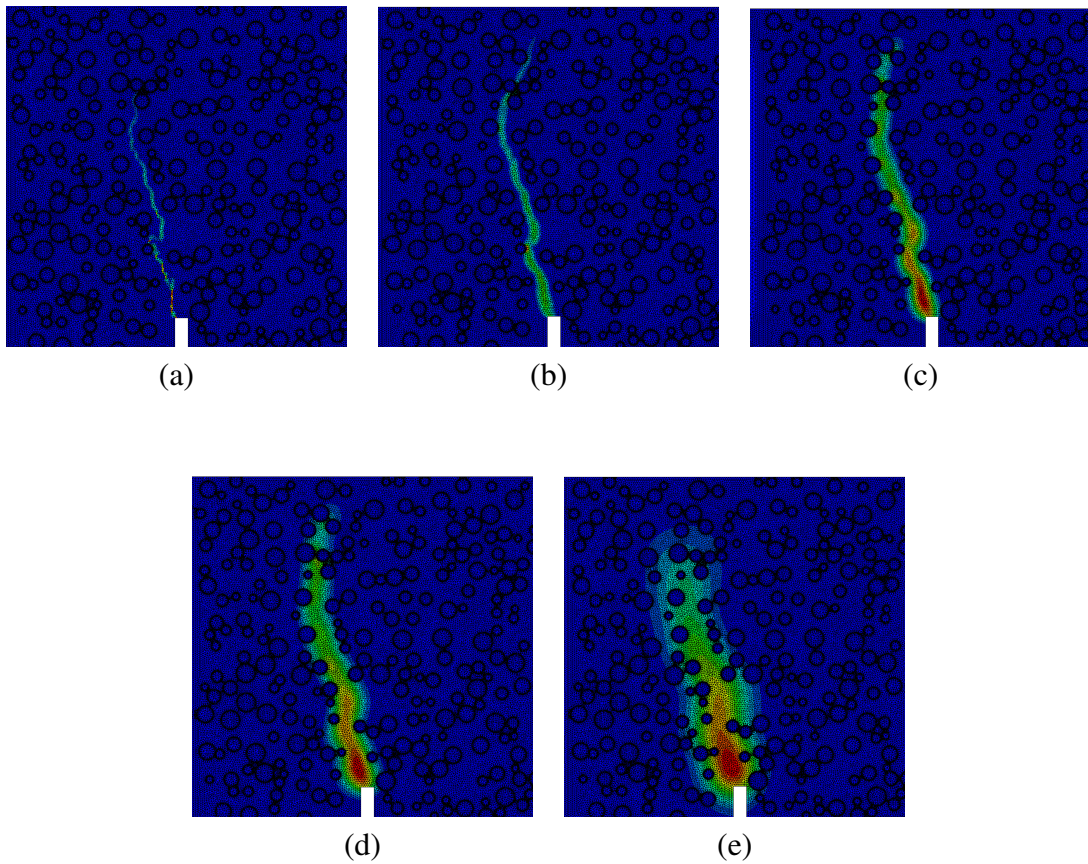


Figure 6.19. Calculated distribution of non–local strain measure for different characteristic lengths: (a)  $l_c^m = 0.1$  mm, (b)  $l_c^m = 0.5$  mm, (c)  $l_c^m = 1.5$  mm, (d)  $l_c^m = 2.5$  mm, (e)  $l_c^m = 5.0$  mm (small–size beam  $80 \times 320$  mm<sup>2</sup>, sand concrete  $d_{50} = 0.5$  mm,  $d_{max} = 3$  mm, aggregate density  $\rho = 30\%$ )

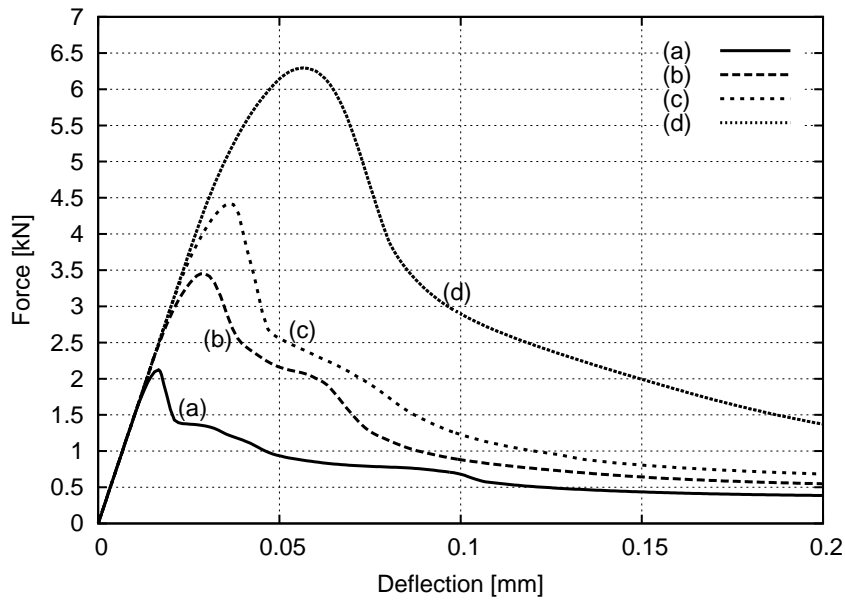


Figure 6.20. Calculated load–deflection curves for different characteristic lengths: (a)  $l_c^m = 0.5$  mm, (b)  $l_c^m = 1.5$  mm, (c)  $l_c^m = 2.5$  mm, (d)  $l_c^m = 5.0$  mm (small–size beam  $80 \times 320$  mm<sup>2</sup>, gravel concrete  $d_{50} = 2$  mm,  $d_{max} = 8$  mm, aggregate density  $\rho = 45\%$ )

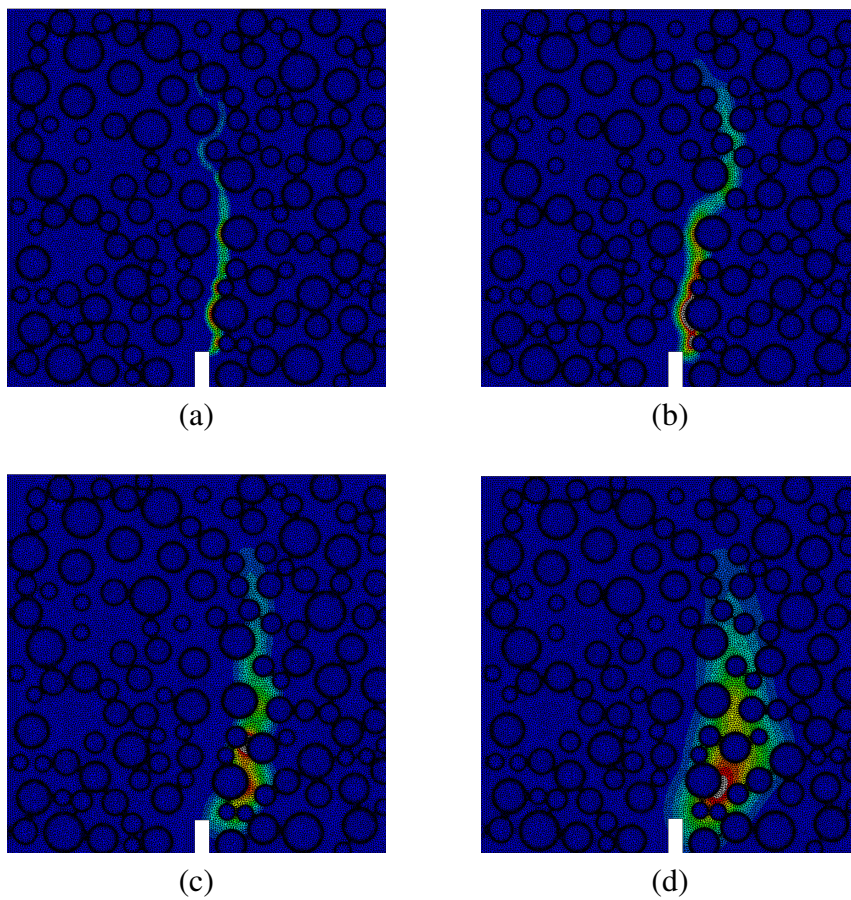


Figure 6.21. Calculated distribution of non–local strain measure for different characteristic lengths: (a)  $l_c^m = 0.5$  mm, (b)  $l_c^m = 1.5$  mm, (c)  $l_c^m = 2.5$  mm, (d)  $l_c^m = 5.0$  mm (small–size beam  $80 \times 320$  mm<sup>2</sup>, gravel concrete  $d_{50} = 2$  mm,  $d_{max} = 8$  mm, aggregate density  $\rho = 45\%$ )

To find the parameters  $B$  and  $D_0$ , a non-linear least squares Marquardt–Lavenberg algorithm was used. The experimental and theoretical beam strength shows a strong parabolic size dependence. The experimental and numerical results match quite well the size effect law by Bažant (Bažant and Planas [16]).

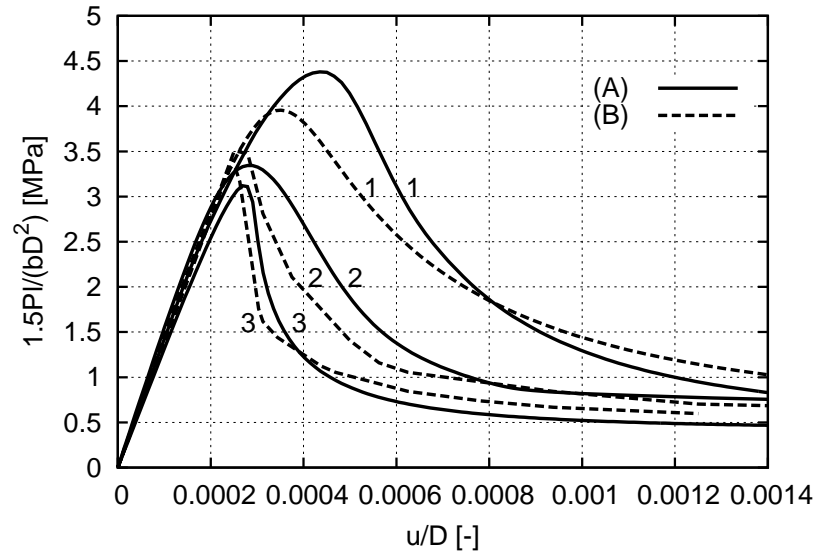


Figure 6.22. Calculated nominal strength  $1.5Pl/(bD^2)$  versus normalised beam deflection  $u/D$  ( $u$  – beam deflection,  $D$  – beam height): (A) FE–results, (B) experiments by Le Bellėgo et al. (Le Bellėgo et al. [97]): (1) small–size beam, (2) medium–size beam, 3) large–size beam (three–phase random heterogeneous material close to notch  $b_{ms} = D$ ,  $\rho = 30\%$ ,  $l_c^m = 1.5$  mm)

### 6.3. Conclusions

A meso–scale numerical model was used in this Chapter to analyse strain localization in concrete. The following conclusions can be drawn:

- material micro–structure on meso–scale has to be taken into account in calculations of strain localization to obtain a proper shape of a localized zone,
- the calculated strength, width and geometry of localized zones are in a satisfactory agreement with experimental measurements when the characteristic length is about  $l_c^m = 1.5$  mm,
- the width of the localized zone above the notch is about  $2 - 4 \times l_c^m$ . It increases with decreasing aggregate density from  $2 \times l_c^m$  ( $\rho = 60\%$ ), up to  $4 \times l_c^m$  ( $\rho = 30\%$ ). It increases also with increasing characteristic length. It is not affected by the aggregate size, aggregate roughness and beam height,
- beam strength increases with increasing characteristic length, aggregate density and aggregate roughness and decreasing beam height. It depends also on the aggregate distribution,
- material softening is strongly influenced by the characteristic length, aggregate density, aggregate roughness and beam height,
- the localized zone above the notch is strongly curved with  $l_c^m = 1.0 - 2.5$  mm,
- the characteristic length of micro–structure is probably related to the grain size of cement matrix

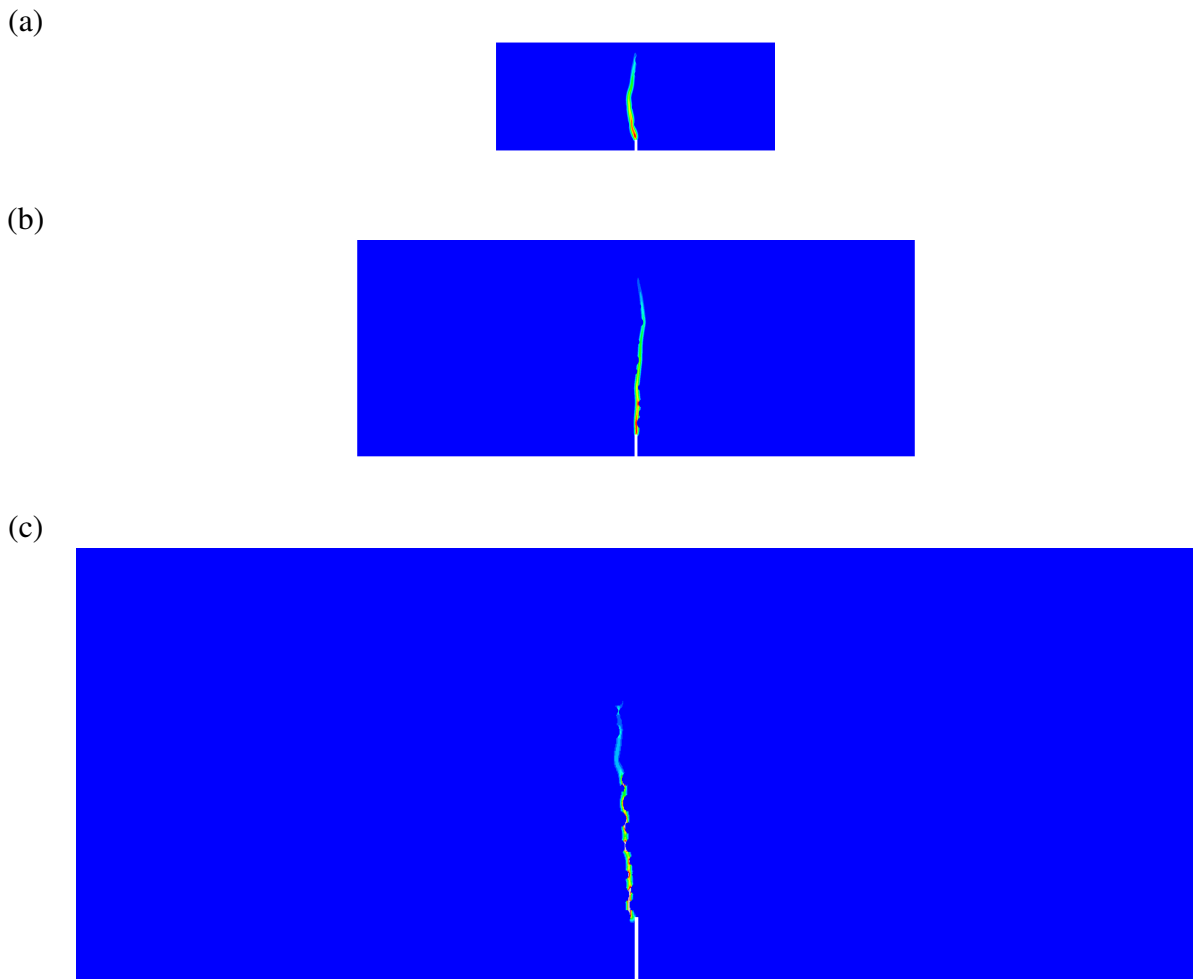


Figure 6.23. Calculated distribution of non-local strain measure above the notch from numerical calculations (at  $u/D = 0.0005$ ): (a) small-size beam, (b) medium-size beam, (c) large-size beam (three-phase random heterogeneous material close to notch  $b_{ms} = D$ ,  $\rho = 30\%$ ,  $l_c^m = 1.5$  mm)

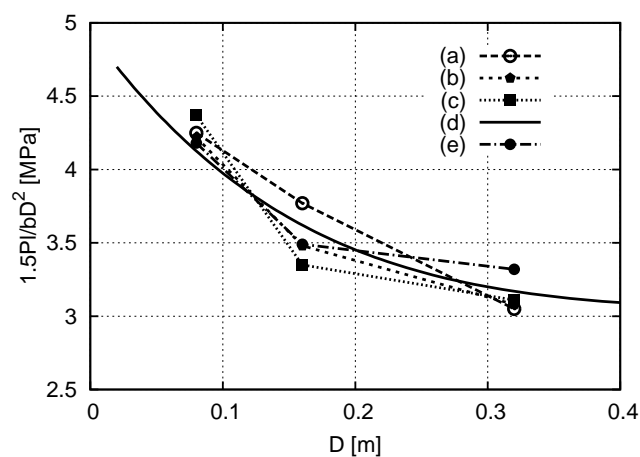


Figure 6.24. Calculated and measured size effect in nominal strength  $1.5Pl/(bD^2)$  versus beam height  $D$  for concrete beams of a similar geometry (small-, medium- and large-size beam): (a) own laboratory experiments, (b) own FE-calculations (homogeneous one-phase material), (c) own FE-calculations (heterogeneous material close to the notch  $b_{ms} = D$ ), (d) size effect law by Bažant (Bažant [7]), (e) experiments by Le Bellégo et al. (Le Bellégo et al. [97])

---

The calculation time using PC with Duo Processor E6320 and 3.5 GB RAM was:

- 146556 seconds (the entire beam considered at the meso–scale with approximately 350000 elements),
- 6340 seconds (the beam considered at the macro–meso scale with approximately 80000 elements),
- 30 seconds (the entire beam considered at the macro–scale with approximately 1000 elements).



## Chapter 7

# Final conclusions and future work

The following conclusions can be derived from the experiments with notched concrete beams with a different geometry:

- The Digital Image Correlation technique is a very effective optical technique to determine the displacement field on the surface of concrete with a high accuracy and without any physical contact with the surface.
- The width of a localized zone on the concrete surface of notched beams does not depend on the beam dimensions and concrete mix. Its maximum size (on the concrete surface) lies between 3.5 mm and 5.5 mm (on the basis of experimental results obtained using DIC technique). It means that the characteristic length of micro-structure  $l_c$  may not always be related to the aggregate size. It can be supposed that  $l_c$  may be more related to the aggregate spacing or cement particle size than to the aggregate size.
- The nominal strength of notched concrete beams during three-point bending increases with decreasing beam height and beam span.

The following conclusions can be derived from FE calculations with notched concrete beams with a different geometry:

- An isotropic continuum damage model with non-local softening is able to capture the mechanism of evolution of strain localization in concrete elements during tension and bending treated as a heterogeneous three-phase material.
- The results of FE simulations under tensile loading of softening quasi-brittle materials with a heterogeneous three-phase structure revealed that the Representative Volume Element (RVE) cannot be defined in quasi-brittle materials as concrete with a standard averaging approach (over the entire domain) due to occurrence of a localized zone which width is not scaled with the specimen size. The shape of stress-strain curve depends on the unit cell size beyond the elastic region. This fact has to be taken into account when using a multi-scale approach to maintain the objectivity of results with respect to a cell size.
- The representative volume element (RVE) can be defined in quasi-brittle materials using both alternative averaging methods like: a failure zone averaging approach and a varying characteristic length approach. In the first case, the averaging is performed in the damage domain and in the second case, a characteristic length is scaled with the specimen size. The size of a two-dimensional statistically representative volume element is approximately equal to  $15 \times 15 \text{mm}^2$ . Two novel methods allow to determine a size of the so-called representative volume element (RVE) which is one of the most important parameters in homogenization-based multi-scale models. Investigations of the existence and size determination of the RVE also proved that with increasing characteristic length of micro-structure  $l_c$ , both material strength and width of a localized zone grow but material softening decreases.
- The localized zone can be strongly curved with a small  $l_c$ , the width of the localized zone increases with decreasing aggregate density. The material micro-structure on the

meso-scale has to be taken into account in calculations of strain localization to obtain a proper shape.

- The calculated strength, width and geometry of localized zones are in a satisfactory agreement with experimental measurements when a characteristic length is about  $l_c^m = 1.5$  mm. The width of the localized zone above the notch is about  $2 - 4 \times l_c^m$  and it increases with decreasing aggregate density from  $2 \times l_c^m$  ( $\rho = 60\%$ ), up to  $4 \times l_c^m$  ( $\rho = 30\%$ ). It also increases with increasing characteristic length but it is not affected by the aggregate size, aggregate roughness and beam height. The beam strength increases with increasing characteristic length, aggregate density, aggregate roughness and decreasing beam height. It also depends on the aggregate distribution. Material softening is strongly influenced by the characteristic length, aggregate density, aggregate roughness and beam height.

The research work will be continued. The laboratory tests will be performed with notched and unnotched concrete beams subjected to three-point bending using mixes with different density, size, shape and roughness of aggregate and size of cement particles. In experiments, the crack mouth opening displacement (CMOD) will be controlled to capture material brittleness after the peak. To determine the width of a localized zone inside beams, elastic waves will also be used (*Skarżyński et al.* [150]).

The size of the Representative Volume Element (RVE) in concrete under mixed-mode failure conditions using two alternative non-standard averaging strategies will be numerically studied with concrete as a random heterogeneous material composed of three phases: aggregate, cement matrix and bond.

The 3D mesoscopic analyses will be performed for beams to capture more realistically micro-structure of concrete and a related size effect. The effect of aggregate roughness, shape and size and the effect of the grain size in cement matrix will be also analysed to identify a characteristic length of micro-structure. The full aggregate distribution curve will be implemented.

To numerically capture a continuous-discontinuous character of failure, continuum crack models with non-local softening will be initially connected with cohesive elements (*Bobinski and Tejchman* [27]) and later with strong discontinuities (*Oliver et al.* [126]).

Finally, a two-scale approach will be used with mesoscopic RVE elements in integration points. Alternatively, both scales will be linked by means of a Coupled Volume multi-scale approach, where the size of a macro-element equals the size of a meso-cell (to avoid the assumption of any size of RVE).

# Bibliography

- [1] *Abaqus. Theory Manual, Version 5.8.* Hibbit, Karlsson & Sorensen Inc., 1998.
- [2] ADRIAN, R. J. Particle–Imaging Techniques for Experimental Fluid Mechanics. *Annual Review of Fluid Mechanics* 23 (1991), 261–304.
- [3] AKKERMAN, J. Rotationsverhalten von Stahlbeton–Rahmenecken. *Dissertation* (2000), Universität Fridericiana zu Karlsruhe.
- [4] ASFERG, P. N., POULSEN, P. N., AND NIELSEN, L. O. Modelling of crack propagation in concrete applying to XFEM. *Computational Modelling of Concrete Structures EURO–C* (eds. N. Bicanic, R. de Borst, H. Mang and G. Meschke) (2006), 33–42.
- [5] ASKES, H., AND SLUYS, L. J. A classification of higher–order strain gradient models in damage mechanics. *Archives of Applied Mechanics* 53(5-6) (2003), 448–465.
- [6] BAO, G., HUTHINSON, J. W., AND MCMEEKING, R. M. Plastic reinforcement of ductile materials against plastic flow and creep. *Acta Metallurgica et Materialia* 39(8) (1991), 1871–1882.
- [7] BAŽANT, Z. P. Probability distribution of energetic–statistical size effect in quasi–brittle fracture. *Probabilistic Engineering Mechanics* 19 (2004), 307–319.
- [8] BAŽANT, Z. P., AND BHAT, P. D. Endochronic theory of inelasticity and failure of concrete. *ASCE Journal of Engineering Mechanics* 102(4) (1976), 701–722.
- [9] BAŽANT, Z. P., AND JIRASEK, M. Nonlocal integral formulations of plasticity and damage: survey of progress. *ASCE Journal of Engineering Mechanics* 128(11) (2002), 1119–1149.
- [10] BAŽANT, Z. P., AND LIN, F. Non–local yield limit degradation. *International Journal for Numerical Methods in Engineering* 35 (1988), 1805–1823.
- [11] BAŽANT, Z. P., AND NOVAK, D. Stochastic models for deformation and failure of quasibrittle structures: recent advantages and new directions. *Computational Modelling of Concrete Structures EURO–C* (eds. N. Bicanic, R. de Borst, H. Mang and G. Meschke) (2003), 583–598.
- [12] BAŽANT, Z. P., AND OH, B. H. Crack band theory for fracture of concrete. *Materials and Structures (RILEM)* 16(93) (1983), 155–177.
- [13] BAŽANT, Z. P., AND OŽBOLT, J. Nonlocal microplane model for fracture, damage and size effect in structures. *ASCE Journal of Engineering Mechanics* 116(11) (1990), 2485–2505.
- [14] BAŽANT, Z. P., PANG, S. D., VORECHOVSKY, M., AND NOVAK, D. Energetic–statistical size effect simulated by SFEM with stratified sampling and crack band mode. *International Journal for Numerical Methods in Engineering* 71(11) (2008), 1297–1320.
- [15] BAŽANT, Z. P., AND PIJAUDER-CABOT, G. Measurements of characteristic length of non–local continuum. *ASCE Journal of Engineering Mechanics* 115(4) (1989), 755–767.
- [16] BAŽANT, Z. P., AND PLANAS, J. Fracture and size effect in concrete and other quasi–brittle materials. *CRC Press LLC* (1998).
- [17] BAŽANT, Z. P., AND SHIEH, C. L. Endochronic model for nonlinear triaxial behaviour of concrete. *Nuclear Engineering and Design* 47(2) (1978), 305–315.
- [18] BEDNARSKI, T. *Mechanika plastycznego plynienia w zarysie.* Wydawnictwo Naukowe PWN, Warszawa, 1995.
- [19] BELYTSCHKO, T., GRACIE, R., AND VENTURA, G. A review of extended / generalized finite element methods for material modeling. *Modelling and Simulation in Materials Science and Engineering* 17(4) (2009), 1–24.

- [20] BELYTSCHKO, T., MOES, N., USUI, S., AND PARIMI, C. Arbitrary discontinuities in finite elements. *International Journal for Numerical Methods in Engineering* 50(4) (2001), 993–1013.
- [21] BHANDARI, A. R., AND INOUE, J. Experimental study of strain rates effects on strain localization characteristics of soft rocks. *Soils and Foundations* 45(1) (2005), 125–140.
- [22] BOBIŃSKI, J. Implementacja i przykłady zastosowań nieliniowych modeli betonu z nielokalnym osłabieniem. *Praca doktorska* (2006), Politechnika Gdańsk.
- [23] BOBIŃSKI, J., AND TEJCHMAN, J. Numerical simulations of localization of deformation in quasi-brittle materials within non-local softening plasticity. *Computers and Concrete* 1(4) (2004), 433–455.
- [24] BOBIŃSKI, J., AND TEJCHMAN, J. Modelling of concrete behaviour with a non-local continuum damage approach. *Archives of Hydro-Engineering and Environmental Mechanics* 52(2) (2005), 85–102.
- [25] BOBIŃSKI, J., AND TEJCHMAN, J. Modelling of size effects in concrete using elasto-plasticity with non-local softening. *Archives of Civil Engineering* 52(1) (2006), 7–35.
- [26] BOBIŃSKI, J., AND TEJCHMAN, J. FE – simulations of cracks in concrete under mixed mode conditions. *The 17<sup>th</sup> International Conference on Computer Methods in Mechanics CMM – 2007* (2007).
- [27] BOBIŃSKI, J., AND TEJCHMAN, J. Quasi-static crack propagation in concrete with cohesive elements under mixed-mode conditions. *Proceedings 5<sup>th</sup> European Congress on Computational Methods in Applied Sciences and Engineering ECCOMAS 2008* (2008).
- [28] BOBIŃSKI, J., TEJCHMAN, J., AND GÓRSKI, J. Notched concrete beams under bending – calculations of size effects within stochastic elasto-plasticity with non-local softening. *Archives of Mechanics* 61(3–4) (2009), 283–307.
- [29] BORINO, G., FAILLA, B., AND PARRINELLO, F. A symmetric nonlocal damage theory. *International Journal of Solids and Structures* 40(13–14) (2003), 3621–3645.
- [30] BOX, G. E. P., AND MULLER, M. E. A note of the generation of random normal deviates. *The Annals of Mathematical Statistics* 29 (1958), 610–611.
- [31] BRINKGREVE, R. B. J. Geomaterial models and numerical analysis of softening. *PhD Thesis* (1994), Delft University of Technology.
- [32] CABALLERO, A., CAROL, I., AND LOPEZ, C. M. 3D meso-mechanical analysis of concrete specimens under biaxial loading. *Fatigue and Fracture of Engineering Materials and Structures* 30(9) (2007), 877–886.
- [33] CAROL, I., LOPEZ, C. M., AND ROA, O. Micromechanical analysis of quasi-brittle materials using fracture-based interface elements. *International Journal for Numerical Methods in Engineering* 52 (2001), 193–215.
- [34] CEB-FIB. Model code 1990 for concrete structures. 228, 1–205.
- [35] CECOT, W. Adaptive FEM analysis of selected visco-plastic problems. *Computer Methods in Applied Mechanics and Engineering* 196 (2007), 3859–3870.
- [36] CECOT, W., AND RACHOWICZ, W. Adaptive solution of problems modeled by unified state variable constitutive equations. *Computer Assisted Mechanics and Engineering Sciences* 7 (2000), 479–492.
- [37] CHEN, J., YUAN, H., AND KALKHOF, D. A non-local damage model for elastoplastic materials based on gradient plasticity theory. *Report Nr. 01-13, Paul Scherrer Institut* (2001), 1–130.
- [38] CHRISTMAN, T., NEEDLEMAN, A., AND SURESH, S. An experimental and numerical study of deformation in metal-ceramic composites. *Acta Metallurgica* 37(11) (1989), 3029–3050.
- [39] CUSATIS, G., BAŽANT, Z. P., AND CEDOLIN, L. Confinement-shear lattice model for concrete damage in tension and compression: I. Theory. *ASCE Journal of Engineering Mechanics* (2003), 1439–1448.

- [40] D'ADDETTA, G. A., KUN, F., AND RAMM, E. On the application of a discrete model to the fracture process of cohesive granular materials. *Granular Matter* 4(2) (2002), 77–90.
- [41] DE BORST, R., MÜHLHAUS, H., PAMIN, J., AND SLUYS, L. J. Computational modelling of localization of deformation. *Proceedings of the third International Conference on Computational Plasticity* (eds. D. R. J. Owen, E. Onate and E. Hinton) (1992), 483–508.
- [42] DE BORST, R., AND NAUTA, P. Non-orthogonal cracks in a smeared finite element model. *Engineering with Computers* 2(3) (1985), 35–46.
- [43] DE BORST, R., AND PAMIN, J. Some novel developments in finite element procedures for gradient-dependent plasticity. *International Journal for Numerical Methods in Engineering* 39(14) (1996), 2477–2505.
- [44] DE BORST, R., PAMIN, J., AND GEERS, M. On coupled gradient-dependent plasticity and damage theories with a view to localization analysis. *European Journal of Mechanics A/Solids* 18(6) (1999), 939–962.
- [45] DE VREE, J. H. P., BREKELMANS, W. A. M., AND VAN GILS, M. A. J. Comparison of nonlocal approaches in continuum damage mechanics. *Computers and Structures* 55(4) (1995), 581–588.
- [46] DEN UIJL, J. A., AND BIGAJ, A. A bond model for ribbed bars based on concrete confinement. *Heron* 41(3) (1996), 201–226.
- [47] DERSCH, H. Testing interpolator quality. URL: <http://www.all-in-one.de/dersch/> (1999).
- [48] DI PRISCO, C., IMPOSIMATO, S., AND AIFANTIS, E. C. A visco-plastic constitutive model for granular soils modified according to non-local and gradient approaches. *International Journal for Numerical and Analytical Methods in Geomechanics* 26 (2002), 121–138.
- [49] DI PRISCO, M., AND MAZARS, J. Crush-crack: a non-local damage model for concrete. *Mechanics of Cohesive-Frictional Materials* 1(4) (1996), 321–347.
- [50] DONZE, F. V., MAGNIER, S. A., DAUDEVILLE, L., MARIOTTI, C., AND DAVENNE, L. Numerical study of compressive behavior of concrete at high strain rates. *Journal for Engineering Mechanics* 25(10) (1999), 1154–1163.
- [51] DÖRR, K. Ein Beitrag zur Berechnung von Stahlbetonscheiben unter besonderer Berücksichtigung des Verbundverhaltens. *PhD Thesis* (1980), Darmstadt Universität.
- [52] DRAGON, A., AND MRÓZ, Z. A continuum model for plastic-brittle behaviour of rock and concrete. *International Journal for Engineering Science* 17(2) (1979), 121–137.
- [53] DRUGAN, W. J., AND WILLIS, J. R. A. A micromechanics-based nonlocal constitutive equation and estimates of representative volume element size for elastic composites. *Journal of the Mechanics and Physics of Solids* 44(4) (1996), 497–524.
- [54] ECKARDT, S., AND KÖNKE, C. Simulation of damage in concrete structures using multiscale models. *Computational Modelling of Concrete Structures EURO-C* (eds. N. Bicanić, R. de Borst, H. Mang and G. Meschke) (2006), 77–84.
- [55] EHLERS, W., AMMANN, M., AND DIEBELS, S. h-Adaptive FE methods applied to single- and multiphase problems. *International Journal for Numerical Methods in Engineering* 54(2) (2002), 219–239.
- [56] EVESQUE, P. Fluctuations, correlations and representative elementary volume (REV) in granular materials. *Powders and Grains* 11 (2000), 6–17.
- [57] FEENSTRA, P. H., AND DE BORST, R. A composite plasticity model for concrete. *International Journal of Solids and Structures* 33(5) (1996), 707–730.
- [58] FERRARA, L., AND DI PRISCO, M. Mode I fracture behaviour in concrete: nonlocal damage modeling. *ASCE Journal of Engineering Mechanics* 127(7) (2001), 678–692.
- [59] FEYEL, F., AND CHABOCHE, J. L. FE2 multiscale approach for modelling the elastoviscoplastic behaviour of long fiber SiC/Ti composite materials. *Computer Methods in Applied Mechanics and Engineering* 183 (2000), 309–330.
- [60] GEERS, M. G. D. Experimental analysis and computational modelling of damage and fracture. *PhD thesis* (1997), Eindhoven University of Technology.

- [61] GEERS, M. G. D., KOUZNETSOVA, V., AND BREKELMANS, W. A. M. Multi-scale computational homogenization: trends & challenges. *Journal of Computational and Applied Mathematics* 234(7) (2010), 2175–2182.
- [62] GHOSH, S., LEE, K., AND MOORTHY, S. Multiple scale analysis of heterogeneous elastic structures using homogenisation theory and Voronoi cell finite element method. *International Journal for Solids and Structures* 32(1) (1995), 27–62.
- [63] GHOSH, S., LEE, K., AND MOORTHY, S. Two scale analysis of heterogeneous elastic–plastic materials with asymptotic homogenization and Voronoi cell finite element model. *Computer Methods in Applied Mechanics and Engineering* 132 (1–2) (1996), 63–116.
- [64] GHOSH, S., LEE, K., AND RAGHAVAN, P. A multi-level computational model for multi-scale damage analysis in composite and porous materials. *International Journal for Solids and Structures* 38 (2001), 2335–2385.
- [65] GITMAN, I. M. Representative volumes and multi-scale modelling of quasi-brittle materials. *PhD Thesis* (2006), Delft University of Technology.
- [66] GITMAN, I. M., ASKES, H., AND SLUYS, L. J. Representative volume: Existence and size determination. *Engineering Fracture Mechanics* 74(16) (2007), 2518–2534.
- [67] GITMAN, I. M., ASKES, H., AND SLUYS, L. J. Coupled-volume multi-scale modelling of quasi-brittle material. *European Journal of Mechanics A/Solids* 27(3) (2008), 302–327.
- [68] GODYCKI-ĆWIRKO, T. *Mechanika Betonu*. Arkady, 1982.
- [69] GUEDES, J. M., AND KIKUCHI, N. Preprocessing and postprocessing for materials based on the homogenization method with adaptive finite element methods. *Computer Methods in Applied Mechanics and Engineering* 83 (1990), 143–198.
- [70] HASKETT, M., OEHLERS, D. J., AND MOHAMED ALI, M. S. Local and global bond characteristics of steel reinforcing bars. *Engineering Structures* 30(2) (2008), 376–383.
- [71] HÄUSSLER-COMBE, U., AND PRÖCHTEL, P. Ein dreiaxiales Stoffgesetz für Betone mit normaler und hoher Festigkeit. *Beton- und Stahlbetonbau* 100(1) (2005), 52–62.
- [72] HE, H. Computational modelling of particle packing in concrete. *PhD Thesis* (2010), Delft University of Technology.
- [73] HILL, R. On macroscopic effects of heterogeneity in elastoplastic media at finite strain. *Mathematical Proceedings of the Cambridge Philosophical Society* 95 (1984), 481–494.
- [74] HORDIJK, D. A. Local approach to fatigue of concrete. *PhD Thesis* (1991), Delft University of Technology.
- [75] HSIEH, S. S., TING, E. C., AND CHEN, W. F. Plasticity–fracture model for concrete. *International Journal for Solids and Structures* 18(3) (1982), 181–187.
- [76] HUGHES, T. J. R., AND WINGET, J. Finite rotation effects in numerical integration of rate constitutive equations arising in large-deformation analysis. *International Journal for Numerical Methods in Engineering* 15 (1980), 1862–1867.
- [77] IBRAHIMBEGOVIĆ, A., MARKOVIĆ, D., AND GATUINGT, F. Constitutive model of coupled damage–plasticity and its finite element implementation. *European Journal of Computational Mechanics* 12(4) (2003), 381–405.
- [78] JIRASEK, M. Nonlocal models for damage and fracture: comparison and approaches. *International Journal of Solids and Structures* 8(5–6) (1998), 683–707.
- [79] JIRASEK, M., AND MARFIA, S. Non-local damage model based on displacement averaging. *International Journal for Numerical Methods in Engineering* 63(1) (2005), 77–102.
- [80] JIRASEK, M., AND ROLSHOVEN, S. Comparison of integral-type nonlocal plasticity models for strain-softening materials. *International Journal of Engineering Science* 41 (2003), 1553–1602.
- [81] JIRASEK, M., AND ZIMMERMANN, T. Analysis of rotating crack model. *ASCE Journal of Engineering Mechanics* 124(8) (1998), 842–851.
- [82] KACHANOV, L. M. *Introduction to continuum damage mechanics*. Martinus Nijhoff Publishers, 1986.

- [83] KACZMARCZYK, Ł. Micro-to-macro transitions of macrostructure for the first order and second order continuum. *15<sup>th</sup> Inter-Institute Seminar for Young Researcher* (2005), Budapest.
- [84] KACZMARCZYK, Ł. Numeryczna analiza wybranych problemów mechaniki ośrodków niejednorodnych. *Praca doktorska* (2006), Politechnika Krakowska.
- [85] KACZMARCZYK, Ł., PEARCE, C. J., BICANIĆ, N., AND DE SOUZA NETO, E. Numerical multiscale solution strategy for fracturing heterogeneous materials. *Computer Methods in Applied Mechanics and Engineering* 199 (2009), 1100–1113.
- [86] KANIT, T., FOREST, S., GALLIET, I., MOUNOURY, V., AND JEULIN, D. Determination of the size of the representative volume element for random composites: statistical and numerical approach. *International Journal of Solids and Structures* 40 (2003), 3647–3679.
- [87] KLISIŃSKI, M., AND MRÓZ, Z. Description of inelastic deformation and degradation for concrete. *International Journal of Solids and Structures* 24(4) (1988), 391–416.
- [88] KOIDE, H., AKITA, H., AND TOMON, M. Size effect on flexural resistance due to bending span of concrete beams. *Fracture Mechanics of Concrete Structures (eds. H. Mihashi and K. Rokugo)* (1998), 2121–2130.
- [89] KOMPFFNER, T. A. Ein finites Elementmodell für die geometrisch und physikalisch nichtlineare Berechnung von Stahlbetonschalen. *PhD Thesis* (1983), University of Stuttgart.
- [90] KOTSOVOS, M. D., AND NEWMAN, J. B. Generalized stress-strain relations for concrete. *ASCE Journal of Engineering Mechanics* 104(4) (1978), 845–856.
- [91] KOUZNETSOVA, V., BREKELMANS, W. A. M., AND BAAIJENS, F. P. T. An approach to micro-macro modeling of heterogeneous materials. *Computational Mechanics* 27 (2001), 37–48.
- [92] KOUZNETSOVA, V. G. Computational homogenization for the multi-scale analysis of multi-phase materials. *PhD Thesis* (2002), Eindhoven University of Technology.
- [93] KOUZNETSOVA, V. G., GEERS, M., AND BREKELMANS, W. A. M. Size of Representative Volume Element in a second-order computational homogenization framework. *International Journal for Multiscale Computational Engineering* 2(4) (2004), 575–598.
- [94] KOZICKI, J., AND TEJCHMAN, J. Experimental investigations of strain localization in concrete using Digital Image Correlation (DIC) technique. *Archives of Hydro-Engineering and Environmental Mechanics* 54(1) (2007), 3–24.
- [95] KOZICKI, J., AND TEJCHMAN, J. Modelling of fracture processes in concrete using a novel lattice model. *Granular Matter* 10(5) (2008), 377–388.
- [96] KUPFER, H., HILSDORF, H. K., AND RUSH, H. Behavior of concrete under biaxial stresses. *Journal of the American Concrete Institute* 66(8) (1969), 656–666.
- [97] LE BELLÉGO, C., DUBE, J. F., PIJAUDER-CABOT, G., AND GERARD, B. Calibration of nonlocal damage model from size effect tests. *European Journal of Mechanics A/Solids* 22(1) (2003), 33–46.
- [98] LEMAITRE, J., AND CHABOCHE, J. L. *Mechanics of solid materials*. Cambridge University Press, Cambridge UK, 1990.
- [99] LILLIU, G., AND VAN MIER, J. G. M. 3D lattice type fracture model for concrete. *Engineering Fracture Mechanics* 70(7–8) (2003), 927–941.
- [100] LIU, T. C. Y., NILSON, H., AND SLATE, F. O. Biaxial stress-strain relations for concrete. *ASCE Journal of the Structural Division* 98(5) (1972), 1025–1034.
- [101] ŁODYGOWSKI, T., AND PERZYNA, P. Numerical modelling of localized fracture of inelastic solids in dynamic loading process. *International Journal for Numerical Methods in Engineering* 40(22) (1997), 4137–4158.
- [102] LORET, B., AND PREVOST, J. H. Dynamic strain localisation in elasto-visco-plastic solids, Part 1. General formulation and one-dimensional examples. *Computer Methods in Applied Mechanics and Engineering* 83 (1990), 247–273.
- [103] LORRAIN, M., MAUREL, O., AND SEFFO, M. Cracking behavior of reinforced high-strength concrete tension ties. *ACI Structural Journal* 95(5) (1998), 626–635.

- [104] LOURENCO, P. Computational strategies for masonry structures. *PhD thesis* (1996), Delft University of Technology.
- [105] MAASART, T. J. Multi-scale modeling of damage in masonry structures. *PhD Thesis* (2003), Technical University Eindhoven.
- [106] MAIER, T. Numerische Modellierung der Entfestigung im Rahmen der Hypoplastizität. *PhD Thesis* (2002), University of Dortmund.
- [107] MAIER, T. Nonlocal modelling of softening in hypoplasticity. *Computers and Geotechnics* 30(7) (2003), 300–317.
- [108] MARCHER, T., AND VERMEER, P. A. Macro-modelling of softening in non-cohesive soils. *Continuous and Discontinuous Modelling of Cohesive-Frictional Materials* (eds: P. A. Vermeer et al.) (2001), 89–110.
- [109] MARZEC, I. Zastosowanie modelu sprężysto–plastycznego betonu z degradacją sztywności i nielokalnym osłabieniem do modelowania elementów betonowych cyklicznie obciążonych. *Praca doktorska* (2008), Politechnika Gdańsk.
- [110] MARZEC, I., BOBIŃSKI, J., AND TEJCHMAN, J. Simulations of spacing of localized zones in reinforced concrete beams using elasto–plasticity and damage mechanics with non–local softening. *Computers and Concrete* 4(4) (2007), 377–403.
- [111] MAZARS, J., AND PIAUDER-CABOT, G. Continuum damage theory–application to concrete. *ASCE Journal of Engineering Mechanics* 115(2) (1989), 345–365.
- [112] MEFTAH, F., AND REYNOUARD, J. M. A multilayered mixed beam element on gradient plasticity for the analysis of localized failure modes. *Mechanics of Cohesive-Frictional Materials* 3 (1998), 305–322.
- [113] MENETREY, P., AND WILLAM, K. J. Triaxial failure criterion for concrete and its generalization. *ACI Structural Journal* 92(3) (1995), 311–318.
- [114] MICHEL, J. C., MOULINEC, H., AND SUQUET, P. Effective properties of composite materials with periodic microstructure: a computational approach. *Computer Methods in Applied Mechanics and Engineering* 172 (1999), 109–143.
- [115] MIEHE, C., AND KOCH, A. Computational micro–to–macro transition of discretized microstructures undergoing small strain. *Archives of Applied Mechanics* 72 (2002), 300–317.
- [116] MIEHE, C., SCHOTTE, J., AND SCHRÖDER, J. Computational homogenization analysis in finite plasticity. Simulation of texture development in polycrystalline materials. *Computer Methods in Applied Mechanics and Engineering* 171 (1999), 387–418.
- [117] MIEHE, C., SCHOTTE, J., AND SCHRÖDER, J. Computational micro–macro transitions and overall moduli in the analysis of polycrystals at large strains. *Computational Materials Science* 16 (1999), 372–382.
- [118] MIHASHI, H., AND NOMURA, N. Correlation between characteristics of fracture process zone and tension–softening properties of concrete. *Nuclear Engineering and Design* 165(3) (1996), 359–376.
- [119] MOONEN, P., CARMELIET, J., AND SLUYS, L. J. A continuous–discontinuous approach to simulate fracture processes in quasi–brittle materials. *Philosophical Magazine* 88(28–29) (2008), 3281–3298.
- [120] MRÓZ, Z. Mathematical models of inelastic concrete behavior. *University Waterloo Press* (1973).
- [121] MÜHLHAUS, H. Scherfugenanalyse bei Granularen Material im Rahmen der Cosserat–Theorie. *Ingenieur Archive* 56 (1986), 389–399.
- [122] MÜHLHAUS, H., AND AIFANTIS, E. C. A variational principle for gradient plasticity. *International Journal of Solids and Structures* 28(7) (1991), 845–858.
- [123] NEEDLEMAN, A. Material rate dependence and mesh sensitivity in localization problems. *Computer Methods in Applied Mechanics and Engineering* 67 (1988), 69–85.
- [124] NGUYEN, V. P., VALLS, O. L., STROEVEN, M., AND SLUYS, L. J. Homogenization–based

- multiscale crack modeling: from micro diffusive damage to macro cracks. *Proc. IV European Conference on Computational Mechanics ECCM 2010, Paris* (2010), 1–8.
- [125] NILSEN, A. U., MONTEIRO, P. J. M., AND GJORV, O. E. Estimation of the elastic moduli of lightweight aggregate. *Cement and Concrete Research* 25(2) (1995), 276–280.
- [126] OLIVER, J., HUESPE, A. E., AND SANCHEZ, P. J. A comparative study on finite elements for capturing strong discontinuities: E-FEM vs. X-FEM. *Computer Methods in Applied Mechanics and Engineering* 195 (2006), 4732–4752.
- [127] ORTIZ, M., AND PANDOLFI, A. Finite-deformation irreversible cohesive elements for three-dimensional crack-propagation analysis. *International Journal for Numerical Methods in Engineering* 44 (1999), 1267–1282.
- [128] PALANISWAMY, R., AND SHAH, S. P. Fracture and stress-strain relationship of concrete under triaxial compression. *ASCE Journal of the Structural Division* 100(5) (1974), 901–916.
- [129] PAMIN, J. Gradient-dependent plasticity in numerical simulation of localization phenomena. *PhD thesis* (1994), Delft University of Technology.
- [130] PAMIN, J. Gradient-enhanced continuum models: formulation, discretization and applications. *Habilitation monograph* (2004), Cracow University of Technology.
- [131] PAMIN, J., AND DE BORST, R. Simulation of crack spacing using a reinforced concrete model with an internal length parameter. *Archives of Applied Mechanics* 68(9) (1998), 613–625.
- [132] PEDERSEN, R. R., SIMONE, A., AND SLUYS, L. J. An analysis of dynamic fracture in concrete with a continuum visco-elastic visco-plastic damage model. *Engineering Fracture Mechanics* 75(13) (2008), 3782–3805.
- [133] PEERLINGS, R. H. J. Enhanced damage modelling for fracture and fatigue. *PhD thesis* (1999), Delft University of Technology.
- [134] PEERLINGS, R. H. J., DE BORST, R., BREKELMANS, W. A. M., AND GEERS, M. G. D. Gradient-enhanced damage modelling of concrete fracture. *Mechanics of Cohesive-Frictional Materials* 3(4) (1998), 323–342.
- [135] PIETRUSZCZAK, S., JIANG, J., AND MIRZA, F. A. An elastoplastic constitutive model for concrete. *International Journal for Solids and Structures* 24(7) (1988), 705–722.
- [136] PIJAUDER-CABOT, G., AND BAŽANT, Z. P. Nonlocal damage theory. *ASCE Journal of Engineering Mechanics* 113(10) (1987), 1512–1533.
- [137] PIJAUDER-CABOT, G., HAIDAR, K., LOUKILI, A., AND OMAR, M. Ageing and durability of concrete structures. *Degradation and Instabilities in Geomaterials* (eds. F. Darve and I. Vardoulakis) (2004).
- [138] PIVONKA, P., OŽBOLT, J., LACKNER, R., AND MANG, H. A. Comparative studies of 3D-constitutive models for concrete: application to mixed-mode fracture. *International Journal for Numerical Methods in Engineering* 60(2) (2004), 549–570.
- [139] POLIZZOTTO, C., BORINO, G., AND FUSCHI, P. A thermodynamically consistent formulation of nonlocal and gradient plasticity. *Mechanics Research Communications* 25(1) (1998), 75–82.
- [140] RAFFAEL, M., WILLERT, C., AND KOMPENHAUS, J. Particle image velocimetry: A practical guide. *Berlin: Springer-Verlag* (2007), ISBN 3-540-63683-8.
- [141] RECHENMACHER, A. L. Grain-scale processes governing shear band initiation and evolution in sands. *Journal of the Mechanics and Physics of Solids* 54(1) (2006), 22–45.
- [142] RODRIGUEZ-FERRAN, A., MORATA, I., AND HUERTA, A. A new damage model based on non-local displacements. *International Journal of Analytical Methods in Geomechanics* 29(5) (2005), 473–493.
- [143] ROTS, J. G., AND BLAAUWENDRAAD, J. Crack models for concrete, discrete or smeared? Fixed, multi-directional or rotating? *Heron* 34 (1) (1989), 1–59.
- [144] RUCKA, M., AND WILDE, K. Guided waves in steel rails – experimental works and wavelet signal processing. *Key Engineering Materials* 347 (2007), 115–120.

- [145] SCHLANGEN, E., AND GARBOCZI, E. J. Fracture simulations of concrete using lattice models: computational aspects. *Engineering Fracture Mechanics* 57(2–3) (1997), 319–332.
- [146] SENGUL, O., TASDEMIR, C., AND TASDEMIR, M. A. Influence of aggregate type on mechanical behavior of normal- and high-strength concretes. *ACI Materials Journal* 99(6) (2002), 528–533.
- [147] SIMO, J. C., AND JU, J. Strain- and stress-based continuum damage models – I. formulation. *International Journal for Solids and Structures* 23(7) (1987), 821–840.
- [148] SIMONE, A., WELLS, G. N., AND SLUYS, L. J. From continuous to discontinuous failure in a gradient-enhanced continuum damage model. *Computer Methods in Applied Mechanics and Engineering* 192(41–42) (2003), 4581–4607.
- [149] SKARŻYŃSKI, Ł., SYROKA, E., RUCKA, M., WILDE, K., AND TEJCHMAN, J. Measurements of fracture zones in concrete using Digital Image Correlation and elastic wave technique. *Proceedings 6<sup>th</sup> International Conference AMCM'2008 (Analytical Models and New Concepts in Concrete and Masonry Structures)* (2008), 243–244.
- [150] SKARŻYŃSKI, Ł., SYROKA, E., AND TEJCHMAN, J. Measurements and calculations of the width of the fracture process zones on the surface of notched concrete beams. *Strain* (2008), doi: 10.1111/j.1475–1305.2008.00605.x.
- [151] SKARŻYŃSKI, Ł., AND TEJCHMAN, J. Mesoscopic modelling of strain localization in concrete. *Archives of Civil Engineering* LV 4 (2009), 503–526.
- [152] SŁOMIŃSKI, C., NIEDOSTATKIEWICZ, M., AND TEJCHMAN, J. Application of particle image velocimetry (PIV) for deformation measurement during granular silo flow. *Powder Technology* 173(1) (2007), 1–18.
- [153] SLUYS, L. J. Wave propagation, localisation and dispersion in softening solids. *PhD Thesis* (1992), Delft University of Technology.
- [154] SLUYS, L. J., AND DE BORST, R. Dispersive properties of gradient-dependent and rate-dependent media. *Mechanics of Materials* 18(2) (1994), 131–149.
- [155] SMIT, R. J. M., BREKELMANS, W. A. M., AND MEIJER, H. E. H. Prediction of the mechanical behavior of nonlinear heterogeneous systems by multi-level finite element modeling. *Computer Methods in Applied Mechanics and Engineering* 155(1–2) (1998), 181–192.
- [156] STRÖMBERG, S., AND RISTINMAA, M. FE-formulation of nonlocal plasticity theory. *Computer Methods in Applied Mechanics and Engineering* 136 (1999), 127–144.
- [157] TEJCHMAN, J. Influence of a characteristic length on shear zone formation in hypoplasticity with different enhancements. *Computers and Geotechnics* 31(8) (2004), 595–611.
- [158] TEJCHMAN, J., HERLE, I., AND WEHR, J. FE-studies on the influence of initial void ratio, pressure level and mean grain diameter on shear localisation. *International Journal for Numerical and Analytical Methods in Geomechanics* 23 (1999), 2045–2074.
- [159] TEJCHMAN, J., AND WU, W. Numerical study on pattering of shear bands in Cosserat continuum. *Acta Mechanica* 99(1–4) (1993), 61–74.
- [160] TERADA, K., AND KIKUCHI, N. Nonlinear homogenization method for practical applications. *Computational Methods in Micromechanics (eds. S. Ghosh and M. Ostoja-Starzewski)* (1995), 1–16.
- [161] TERADA, K., AND KIKUCHI, N. A class of general algorithms for multi-scale analysis of heterogeneous media. *Computer Methods in Applied Mechanics and Engineering* 190 (2001), 5427–5464.
- [162] TRUKOZKO, A., AND ZIJL, W. Complementary finite element method applied to the numerical homogenization of 3D absolute permeability. *Communications in Numerical Methods in Engineering* 18 (2002), 31–41.
- [163] VAN DER SLUIS, O. Effective properties of a viscoplastic constitutive model obtained by homogenisation. *Mechanics of Materials* 31 (1999), 743–759.
- [164] VAN DER SLUIS, O. Homogenisation of structured elastoviscoplastic solids. *PhD Thesis* (2001), Eindhoven University of Technology.

- [165] VAN MIER, J. G. M. Microstructural effects on fracture scaling in concrete, rock and ice. *IUTAM Symposium on Scaling Laws in Ice Mechanics and Ice Dynamics* (eds. J. P. Dempsey and H. H. Shen) (2001), 171–182.
- [166] VAN MIER, J. G. M., SCHLANGEN, E., AND VERVUURT, A. Lattice type fracture models for concrete. *Continuum Models for Material and Microstructure* (editor H. B. Mühlhaus, John Wiley & Sons) (1995), 341–377.
- [167] VERHOOSSEL, C. V., REMMERS, J. J. C., AND GUTIERREZ, M. A. A partition of unity–based multiscale approach for modelling fracture in piezoelectric ceramics. *International Journal for Numerical Methods in Engineering* 82(8) (2010), 966–994.
- [168] WALRAVEN, J., AND LEHWALTER, N. Size effects in short beams loaded in shear. *ACI Structural Journal* 91(5) (1994), 585–593.
- [169] WHITE, D. J., TAKE, W. A., AND BOLTON, M. D. Soil deformation measurement using particle image velocimetry (PIV) and photogrammetry. *Geotechnique* 53(7) (2003), 619–631.
- [170] WINNICKI, A. Viscoplastic and internal discontinuity models in analysis of structural concrete. *Habilitation monograph* (2007), Cracow University of Technology.
- [171] WINNICKI, A., PEARCE, C. J., AND BICANIĆ, N. Viscoplastic Hoffman consistency model for concrete. *Computers and Concrete* 79 (2001), 7–19.
- [172] ZBIB, H. M., AND AIFANTIS, C. E. A gradient–dependent flow theory of plasticity: application to metal and soil instabilities. *Applied Mechanics Reviews* 42(11) (1989), 295–304.
- [173] ZHOU, F., AND MOLINARI, J. F. Dynamic crack propagation with cohesive elements: a methodology to address mesh dependency. *International Journal for Numerical Methods in Engineering* 59 (2004), 1–24.
- [174] ZHOU, W., ZHAO, J., LIU, Y., AND YANG, Q. Simulation of localization failure with strain–gradient–enhanced damage mechanics. *International Journal for Numerical and Analytical Methods in Geomechanics* 26 (2002), 793–813.
- [175] ZIMMERMANN, S., KLEINMAN, C. S., AND HORDIJK, D. A. Multi–scale modeling of concrete–like composites. In *9<sup>th</sup> International Conference on Mechanical Behaviour of Materials* (2003).



# List of publications

## Publications in journals from ISI Master Journal List (2)

1. SKARŻYŃSKI, Ł., SYROKA, E., AND TEJCHMAN J. Measurements and calculations of the width of the fracture process zones on the surface of notched concrete beams, *Strain*, doi: 10.1111/j.1475-1305.2008.00605.x, 2008 (32 punkty na liście Ministerstwa Nauki),
2. SKARŻYŃSKI, Ł., AND TEJCHMAN, J. Calculations of fracture process zones on mesoscale in notched concrete beams subjected to three–point bending, *European Journal of Mechanics A/Solids*, **29**, 746-760, 2010 (32 punkty na liście Ministerstwa Nauki).

## Publications in reviewed journals (2)

1. SKARŻYŃSKI, Ł., AND TEJCHMAN, J. Mesoscopic modelling of strain localization in concrete, *Archives of Civil Engineering*, LV, **4**, 2009 (6 punktów na liście Ministerstwa Nauki),
2. SKARŻYŃSKI, Ł., I TEJCHMAN, J. Obliczenia MES zginanych belek betonowych na poziomie skali mezo, *Inżynieria Morska i Geotechnika*, **2**, 353-360, 2010 (6 punktów na liście Ministerstwa Nauki).

## Conference proceedings (7)

1. SKARŻYŃSKI, Ł., SYROKA, E., RUCKA, M., WILDE, K., AND TEJCHMAN, J. Measurements of fracture process zones in concrete using Digital Image Correlation and elastic wave technique, *Proceedings 6<sup>th</sup> International Conference AMCM'2008 (Analytical Models and New Concepts in Concrete and Masonry Structures)*, June 9–11, 2008, Łódź, Poland, pp. 243–244,
2. SYROKA, E., SKARŻYŃSKI, Ł., AND TEJCHMAN, J. Simulations of strain localization in reinforced concrete elements using elasto-plastic and damage mechanics with non-local softening, *Proceedings 6<sup>th</sup> International Conference AMCM'2008 (Analytical Models and New Concepts in Concrete and Masonry Structures)*, June 9–11, Łódź, Poland, pp. 245–246, 2008
3. SKARŻYŃSKI, Ł., AND TEJCHMAN, J. FE modelling of brittle materials at mesoscale, *Proceedings 18<sup>th</sup> International Conference on Computer Methods in Mechanics CMM'2009*, May 18–21, Zielona Góra, Poland, pp. 417–448, 2009
4. BOBIŃSKI, J., MAJEWSKI, T., SKARŻYŃSKI, Ł., SYROKA, E., AND TEJCHMAN, J. FE modelling of strain localization in large reinforced concrete elements within elasto–plasticity

- with non–local softening, *Proceedings 18<sup>th</sup> International Conference on Computer Methods in Mechanics CMM'2009*, May 18–21, Zielona Góra, Poland, pp. 129–130, 2009
5. SKARŻYŃSKI, Ł., AND TEJCHMAN, J. A meso–macro modelling of concrete, *Proceedings X International Conference on Computational Plasticity, Fundamentals and Applications Complas'2009*, September 2–4, Barcelona, Spain, 2009
  6. SKARŻYŃSKI, Ł., AND TEJCHMAN, J. Multiscale modelling of concrete beams subjected to three–point bending, *Proceedings Computational modelling of Concrete Structures Euro–C 2010* (eds. N. Bicanic, R. de Borst, H. Mang and G. Meschke), March 15–18, Rohrmoos/Schladming, Austria, pp. 703–710, 2010
  7. SKARŻYŃSKI, Ł., AND TEJCHMAN, J. Multiscale modelling of concrete beams subjected to three–point bending, *Proceedings IV European Conference on Computational Mechanics*, May 16–21, Palais de Congress, Paris, France, 2010.

## Streszczenie

Praca doktorska przedstawia wyniki badań lokalizacji odkształceń w betonie. Zrozumienie mechanizmu powstawania stref lokalizacji jest niezwykle ważne, ponieważ są one prekursorami ostatecznego zarysowania i zniszczenia betonowych elementów. Realistyczny opis szerokości i rozstawu stref lokalizacji jest istotny do określenia wytrzymałości materiału w wierzchołku i w obszarze pokrytycznym aby zapewnić bezpieczeństwo konstrukcom inżynierskim.

Doświadczenia laboratoryjne zostały przeprowadzone w celu określenia szerokości i kształtu strefy lokalizacji na powierzchni naciętych belek betonowych podczas quasi–statycznego trzypunktowego zginania. Do pomiaru dwuwymiarowych przemieszczeń na powierzchni belek zastosowano bezinwazyjną metodę cyfrowej korelacji obrazów. W doświadczeniach przyjęto belki o różnej geometrii.

Obliczenia numeryczne wykonano metodą elementów skończonych na poziomie skali makro, mezo oraz makro–mezo dla elementów betonowych i żelbetowych. Do opisu lokalizacji odkształceń na poziomie skali makro, w długich belkach betonowych podczas zniszczenia od rozciągania i krótkich belkach zbrojonych podczas zniszczenia od ścinania, użyto trzech różnych ciągłych modeli konstytutywnych dla betonu: sprężysto–plastycznego z izotropowym wzmocnieniem i osłabieniem (z kryterium Druckera–Pragera w ściskaniu i kryterium Rankine’a w rozciąganiu), izotropowego modelu z degradacją sztywności z jednym skalarem zniszczenia i anizotropowego modelu rysy rozmytej z rysami nieobrotowymi i rysą obracającą się. Dla właściwego opisu lokalizacji odkształceń, modele ciągłe zostały rozszerzone o długość charakterystyczną mikrostruktury przy zastosowaniu teorii nielokalnej. W ten sposób rozpatrywane problemy brzegowe były matematycznie dobrze postawione.

Mezoskopowe obliczenia metodą elementów skończonych wykonano dla elementu betonowego podczas jednoosiowego rozciągania. Beton został opisany jako stochastyczny niejednorodny materiał trzyfazowy składający się z cementu, kruszywa i stref kontaktu pomiędzy cementem a kruszywem. Zastosowano izotropowy model z degradacją sztywności i nielokalnym osłabieniem. Analizowano koncept reprezentatywnego objętościowego elementu w betonie przy użyciu standardowej metody uśredniania. Dodatkowo, zaproponowano dwie alternatywne niestandardowe metody uśredniania do określenia reprezentatywnego objętościowego elementu w betonie podczas jednoosiowego rozciągania.

Na zakończenie wykonano obszerne obliczenia MES przy zastosowaniu połączonego podejścia makro–mezoskopowego dla betonowych belek zginanych. Do obliczeń ponownie zastosowano izotropowy model z degradacją sztywności i nielokalnym osłabieniem. Zbadano numerycznie wpływ wymiaru belek, rozkładu kruszywa, zagęszczenia kruszywa, kształtu kruszywa i długości charakterystycznej na szerokość i kształt strefy lokalizacji oraz krzywą

obciążenie–przemieszczenie. Obliczenia makro–mezoskopowe były zgodne z wynikami własnych doświadczeń laboratoryjnych.

# Acknowledgements

The research printed in this dissertation has been carried out in the framework of a doctoral studies at the Faculty of Civil and Environmental Engineering of the Gdańsk University of Technology. The numerical calculations were performed on supercomputers of the Academic Computer in Gdańsk TASK.

Scientific research in 2010 has been carried out as a part of the project: “Innovative resources and effective methods of safety improvement and durability of buildings and transport infrastructure in the sustainable development” financed by the European Union.

I would like to express my sincere gratitude to my supervisor Prof. Jacek Tejchman for his guidance, help and support throughout four years of research. I would like to thank him for constant encouragements in numerical research and laboratory experiments.

I would like to thank all my colleagues and friends from the Gdańsk University of Technology, in particular, Jerzy Bobiński, Ireneusz Marzec and Jan Kozicki for their willingness to help in numerical modelling. I certainly would like to thank Eugeniusz Grześ for providing the excellent conditions for laboratory tests. Furthermore, I would like to express my acknowledgements to my room-mate Tomasz Majewski for a perfect co-working and social atmosphere.

I wish to express my gratitude to my parents for their inexpressible and unconditional support. Last but certainly not least, I deeply thank my wife Diana for her devoted participation in my research life, encouraging help, understanding and patience.

Łukasz Skarżyński

# Curriculum vitae

Name: Łukasz Skarżyński

Date of birth: 25.07.1982

Place of birth: Ostrołęka, Poland



- Sept. 1997 – June 2001      4<sup>th</sup> High School in Olsztyn with maths / physics and advanced English education programme
- Sept. 2001 – June 2006      Master degree in Engineering, Department of Bridge Structures, Faculty of Civil and Environmental Engineering, Gdańsk University of Technology, Poland, under supervision of Prof. Kazimierz Wysiatycki. Graduation thesis: *Project of strengthening of one-span arc-bridge over the Narew river in Ostrołęka.*
- Sept. 2004 – November 2006      Bachelor degree in Engineering, Department of Highway Engineering, Faculty of Civil and Environmental Engineering, Gdańsk University of Technology, Poland, under supervision of dr eng. Bohdan Dołżycki Graduation thesis: *The pavement condition visual assessment of Jaškowa Dolina in Gdańsk.*
- Sept. 2006 – Sept. 2010      PhD researcher in Faculty of Civil and Environmental Engineering, Gdańsk University of Technology, Poland, under supervision of Prof. Jacek Tejchman. Research topic: *Macroscopic and mesoscopic modelling of strain localization in concrete*